Functional studies of Frataxin : relations with metal homeostasis and oxidatives stress

Thi-Hong-Liên Han

▶ **To cite this version:**

Thi-Hong-Liên Han. Functional studies of Frataxin : relations with metal homeostasis and oxidatives stress. Other. Université Sorbonne Paris Cité, 2016. English. NNT : 2016USPCC288 . tel-01929004

HAL Id: tel-01929004
https://theses.hal.science/tel-01929004

Submitted on 20 Nov 2018

UNIVERSITE SORBONNE PARIS CITE

UNIVERSITE PARIS.DIDEROT

Ecole Doctorale 388 : Chimie Physique et Chimie Analytique de Paris Centre

Laboratoire ITODYS – UMR 7086

THESE DE DOCTORAT

Spécialité : Physico-chimie

HAN Thi Hong Lien

Titre

Etudes de la fonction de la frataxine :

Relations avec l'homéostasie métallique et le stress oxydant.

Thèse dirigée par Nguyet-Thanh Ha-Duong

Soutenue le 12 octobre 2016

Jury

Mme Anne-Laure Bulteau	Rapportrice
M. Peter Faller	Rapporteur
M. Jean-Michel Camadro	Examinateur
M. Jean-Michel El Hage Chahine	Co-directeur
Mme Nguyet-Thanh Ha Duong	Directrice de thèse
Mme Sylvie Michel	Examinatrice

À mes parents

REMERCIEMENTS

Je tiens à remercier **Nguyêt-Thanh HA-DUONG**, ma directrice de thèse qui m'a encadrée tout au long de mes trois années de thèse. Je te remercie pour ta patience, ta disponibilité, nos nombreuses discussions sur la science et également sur la vie quotidienne. Merci de m'avoir toujours comprise et encouragée pour que je grandisse et évolue. Pour moi, tu es non simplement un « cô-giáo » mais une grande amie que j'ai la chance de connaître.

Un grand remerciement à **Jean-Michel EL HAGE CHAHINE**, mon co-directeur de thèse qui est aussi chef de l'équipe « Métaux, Chélateur, Protéine ». Je te remercie de m'avoir accueillie au sein de l'équipe. Tous tes conseils, tes explications ainsi que tes connaissances de la physicochimie m'ont beaucoup apportée.

J'exprime ma sincère reconnaissance à **Jean-Michel CAMADRO**, notre collaborateur à l'Institut Jaques Monod. Ces travaux de thèse ne pourraient jamais être achevés sans les suggestions de ton côté, tes idées de recherche, tes expériences ainsi que tes connaissances très approfondies sur les études de l'ataxie de Friedreich et la frataxine.

J'adresse mes remerciements à l'ensemble des membres du jury : **Anne-Laure BULTEAU, Peter FALLER, et Sylvie MICHEL** d'avoir accepté de juger mon travail

Mes travaux de thèse ont été effectués au sein dulaboratoire ITODYS et l'Institut Jaques Monod. Je remercie **François Maurel** - le directeur du laboratoire ITODYS et **Giuseppe Baldacci** - le directeur de l'Institut Jaques Monod de m'avoir accueillie dans vos laboratoires. Je remercie **Pierre-François Quenin, Brigitte Eftassiou, Brigitte Delavaquerie et Äyméric Noël** pour tous vos aides administratifs et informatiques pendant mes trois années de thèse. Je remercie aussi les équipes de techniciens des deux instituts pour leurs aides indispensables.

J'ai pu bénéficier du programme de bourses de l'Université des Sciences et des Technologies de Hanoï qui m'a financée pendant trois ans. Je tiens à remercier

c'est en France que nous nous sommes rencontrés ! Je vous remercie d'avoir embellit mes trois années alors que j'étais éloignée de ma famille.

Je terminerai par la gratitude que je voue à ma famille, mes parents, ma grande sœur et mon petit frère et qui sont toujours à mes côtés et m'encouragent. Enfin, merci à toi, Nam, pour tout ton soutien, ton réconfort de près ou loin, merci simplement pour ta présence à mes côtés.

TABLE OF CONTENTS

CHAPTER I: Bibliography

List of abbreviations

Δ*yfh1*:   yeast strain depleted of frataxin

Δ*hFxn:*   mammalian cells depleted of frataxin

δ-ALA: δ-aminolevulinic acid

ACN: acetonitrile

BL21(DE3):   competent cells *E. coli*

CyaY: bacterial frataxin homologue

CIA: cytosolic iron-sulfur cluster assembly

CV: column volume (chromatography)

Dfh: *Drosophila* frataxin homologue

DN: dentate nuclei

DRG: dorsal root ganglia

ESI: electrospray ionization

FA: Friedreich's ataxia

FAD: Flavin adenine dinucleotide

FXN: gene which encodes frataxin (mammalian)

GSH: reduced glutathione

hFxn: mammalian frataxin

IPTG: Isopropyl β-D-1-thiogalactopyranoside

ISP: iron-sulfur proteins

ISC: iron-sulfur cluster

ISD11:   cysteine desulfurase –interacting protein (mammalian)

Isd11:	cysteine desulfurase –interacting protein (yeast)
ISCU:	iron-sulfur cluster assembly scaffold (mammanlian)
Isu1:	iron-sulfur cluster assembly scaffold (yeast)
ITC:	Isothermal titration calorimetric
K_d:	Dissociation constant
K_m:	Michealis Menten constant
k_{obs} :	observed rate constant of forward reaction
k_{-obs} :	observed rate constant of backward reaction
LB:	Luria Bertani medium
LBE5052:	Auto induction medium
MALDI:	matrix-assisted laser desorption/ionization
MCK:	muscle creatine kinase (mouse)
MWCO:	molecular weight cut-off
NFS1:	cysteine desulfurase
NTA:	nitriolotriacetic acid
OD600:	optical density at 600 nm
OXPHOS:	oxidative phosphorylation
PAGE:	Polyacrylamide gel electrophoresis contains
PDB:	protein data bank
ROS:	reactive oxygen species
SDS:	sodium dodecyl sulfate
SOD:	Superoxide dismutase
SOD1:	Copper, zinc superoxide dismutase

SOD2:	Manganese superoxide dismutase
Tau (τ):	relaxation time
TB:	Terrific Broth medium
TCA:	Trichloroacetic acid
TFA:	Trifluoroacetic acid
WST-1:	(2-(4-Iodophenyl)-3-(4-nitrophenyl)-5-(2,4-disulfophenyl)-2H-tetrazolium monosodium salt
XO:	Xanthine oxidase
Yfh1:	yeast frataxin homologue (*S. cerevisieae*)
Yhb1:	yeast flavohemoglobin (*S. cerevisieae*)

CHAPTER I. BIBLIOGRAPHY

1. Friedreich's ataxia

1.1. Clinical features

Ataxia means a neurological sign consisting of the lack in voluntary coordination of muscle movements that includes gait abnormality. Friedreich's ataxia (FA) is the most prevalent form of hereditary ataxia in the Caucasian population (Martelli and Puccio 2014). FA was initially described by Nikolaus Friedreich. Clinical features as ataxia, dysarthria, sensory loss, muscle weakness, scoliosis, foot deformation and cardiac symptoms were present, and the age of onset was around puberty (Table I.1). Often as young as teenagers, patients become wheelchair-bound and unable to independently perform daily activities. This disease is the consequence of a mutation localized in the region 9q13 of chromosome, which induces the abnomalities in cellular metabolism and manifests in different tissues under a diversity of clinical features.

Table I.1: Clinical features of Friedreich's ataxia

Clinical features of Friedreich's ataxia
Progressive ataxia (legs, arms, and speech)
Areflexia (up-going toe sign)
Dysarthria
Atrophy of the spinal cord
Loss of position and vibratory sense
Extensor plantar responses
Heart disease (abnormalities on ECG)
Vision loss
Eye movements (fixation instability)
Hearing loss
Foot deformity
Scoliosis
Diabetes

1.1.1. Neuropathology

Friedreich's ataxia is a neurodegenerative disorder involving both the peripheral and central nervous systems. FA neuropathology includes atrophy of the dorsal root ganglia (DRG) with a progressive destruction of the larger neurons and thicker myelinated axons, which accounts for the thinning of the dorsal root and sensory nerve neuropathy. The impact of DRG degeneration on the downstream structures of the spinal cord and brainstem underlies secondary damage, with atrophy of the Clarke and dorsal column, gracile and cuneate nucleus and spinocerebellar tract. Atrophy of Betz cells and the cortico-spinal tract is the second purely intrinsic central nervous system lesion of FA (Koeppen A. H. and Mazurkiewicz 2013).

1.1.2. Cardiac system

Besides the typical neurological involvement, FA is also associated with a progressive hypertrophic cardiomyopathy (thickening of ventricular walls). The common cause of death in FA patients is arrhythmias or cardiac failure. The cardiac morphology of patients with FA is variable. The cardiac symptoms may develop early in life but the degree and timing of cardiac involvement correlates poorly with the level of neurological disability. The histological changes in the left ventricle mainly consist of cellular hypertrophy, diffuse fibrosis, and focal myocardial necrosis (Weidemann et al. 2013).

1.1.3. Skeletal muscle

FA patients are wheelchair dependent and unable to perform daily activities. Clinically, they show progressive and symmetrical loss of muscle strength particularly affecting the lower limbs. Morphological and histological studies of patients muscle biopsy indicated atrophy in the neurogenic muscle as well as the absence of muscle regeneration. They also showed reduced capillary density in skeletal muscle, which may be the result of the immobility as a consequence of ataxia (Nachbauer et al. 2012).

1.2. Cellular metabolism

1.2.1. Genetic mechanism

Patients with FA have guanine-adenine-adenine (GAA) trinucleotide repeat expansion in the first intron of *FXN* gene located in chromosome 9q13 (Campuzano et al. 1996), which

encoded for a mitochondrial protein so-called frataxin (Figure I.1). This protein is highly conserved during the evolution. It has been found in all organisms from bacteria to mammalian. Thus, in order to study this disease, the FA type mutant or complete deletion mutant has been created in multiple models from *E. coli* to human cell lines. Herein, the nomenclature of different frataxin homologues is unified as below:

- Bacteria frataxin homologue: CyaY
- Yeast frataxin: Yfh1
- Drosophile frataxin: Dfh
- Mammalian frataxin: hFxn
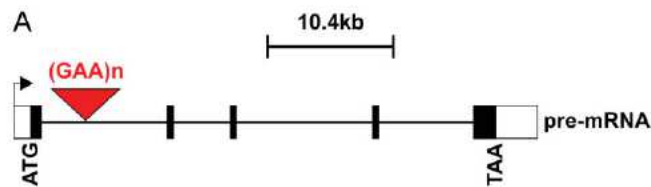
Figure I.1: **FXN gene in the 9q13 chromosome.**

In healthy individuals, the number of repeats ranges from 6-36, whereas in FA patients, it is in the 70-1700 range, most commonly in 600-900 (Campuzano et al. 1996, Pandolfo and Pastore 2009). The length of (GAA) repeat expansion inversely correlates with the ages of onset and the severity of the disease. Long expansion leads to an early onset, severe clinically illness and death in young adult life, whereas patients with short expansion have a later onset and milder signs, some even are not diagnosed during their life time (Koeppen A. H. 2011). In 96 % of patient, this repeat expansion is homozygous, but in 2-4 % of patients it is heterozygous with missense mutations present in the coding region of one allele and expansion in the other. Until now, 44 different mutations have been described in FA heterozygous form, including point mutations, as well as insertion or deletion mutations (Figure I.2a) (follow Human Gene Mutation Database, Cardiff, UK). No patient homozygous for point mutations has been described (Galea et al. 2016).

The GAA expansion leads to silence mRNA transcription through a mechanism involving modifications of the chromatin structure of the locus, resulting in expression of a structurally and functionally normal frataxin but at levels that are estimated at ~5-30 % of normal

(Gottesfeld 2007). The missense mutations can lead to an amino acid residue change (Figure I.2b).
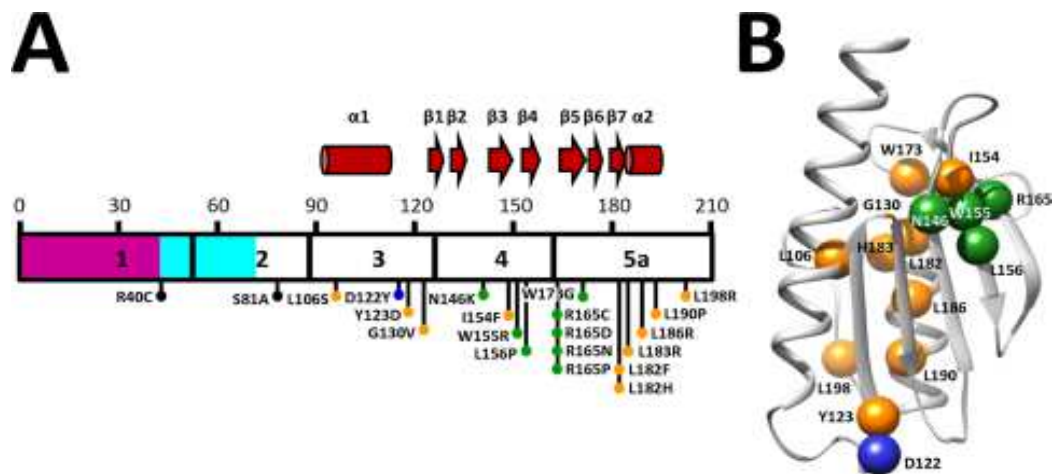
Figure I.2: **Diseases-associated FXN point mutations and corresponding positions in human frataxin molecule.** *(A) Exons 1 to 5a are numbered and delineated within the frataxin sequence. The mitochondrial transit peptide is colored purple, the intermediate N-terminal tail is light blue, and mature frataxin is white. Secondary structure motifs are shown above the sequence, where the α-helices are illustrated as cylinders and β-strands as arrows. Black dots represent residues at sites cleaved during frataxin maturation (B) Illustration of human frataxin molecule highlights residues that are mutated in FA (Galea et al. 2016).*

In most cases, heterozygous patients are clinically indistinguishable from patients that are homozygous for the GAA expansion, but a few missense mutations in compound heterozygous patients cause atypical or milder clinical presentations (Cossée et al. 1999) (Gellera et al. 2007). It was shown in knockout animal model that the complete absence of frataxin leads to early embryonic death (Cossée et al. 2000).

The nuclear-encoded human frataxin protein is synthesized in the nucleus as a 210 amino acid precursor (23 kDa) with an N-terminal mitochondrial-targeting sequence and it undergoes two steps of cleavage to achieve activity site. The insufficient level of frataxin in mitochondria causes defects in mitochondrial and cellular metabolism as: iron-sulfur cluster synthesis, heme synthesis and anti-oxidative stress. Most of these alterations concern "made-in mitochondrion" processes, thus the mitochondria-rich tissues such as the heart and the brain are most affected. The levels of *FXN* mRNA and frataxin protein show specificity for tissue that partially correlates with tissue-specific effects of its deletion pathology (Table I.2).

Table I.2: Tissue-specific FA pathology (Anzovino et al. 2014).

Alteration	Heart	Neurons	Skeletal muscle
Cytosolic iron deficiency	Yes	?	No
Mitochondrial iron loading	Yes	No	No
Perturbed iron-sulfur cluster synthesis	Yes	Yes	?
Autophagy/apotosis	Yes	Yes	?
Oxydative stress	?	Yes	?
Inflammatory response	?	Yes	?

1.2.2. Perturbation in mitochondrial processes

The deficiency of frataxin causes mitochondrial dysfunction (Vázquez-Manrique et al. 2005), (Gonzalez-Cabo and Palau 2013), which has a direct effect on the pathophysiology of the disease. The mitochondria are long known as the powerhouses of the cell. They generate ATP by oxidative phosphorylation *via* respiration chain (complexes I-IV). The generation of reactive oxygen species (ROS) is closely associated with ATP production so mitochondria are considered as the major source of ROS. Mitochondrion is also known as a major site for the metabolism of transition metals, including iron, which is essential for metabolic processes critical for cell viability. Important processes such as [Fe-S] cluster assembly and heme biosynthesis occur in this organelle. The dysfunction of mitochondria in FA patients or FA models organisms involves all the processes listed above.

1.2.2.1. *Transition metal homeostasis*

1.2.2.1.1. Physiological condition

Transition metal ions are particularly required for the correct function of all mitochondrial machineries. They are frequently used as cofactors for enzymes and oxygen-carrying proteins that take advantage of their propensity to gain and lose single electron. These metalloproteins participate in all vital processes of mitochondria as ATP production or detoxification of ROS.

As the majority of mitochondrial proteins, the metalloproteins are encoded by nuclear DNA and imported into the organelle as apo- and unfolded proteins. Iron, copper, manganese and

zinc are inserted into peptides during the folding or post-translation process. Hence, mitochondria have its own mechanism of storage corresponding to each metal (Atkinson and Winge 2009, McCormick et al. 2015).

(i) Fe:

The mitochondrion is a major site of cellular iron utilization, and inversely, iron influences many aspects of mitochondrial metabolism. Iron is imported into mitochondria from cytosol by crossing the inner mitochondrial membrane through the mitochondrial iron importers (mitoferrins Mrs3/4). Within the mitochondrion, iron participates in three major metabolic pathways: (i) iron-sulfur cluster (ISC) assembly, (ii) heme biogenesis and (iii) mitochondrial iron storage. All of these processes give mitochondrion a central role in modulating iron homeostasis.

(a) Iron-sulfur cluster

(b) Heme b
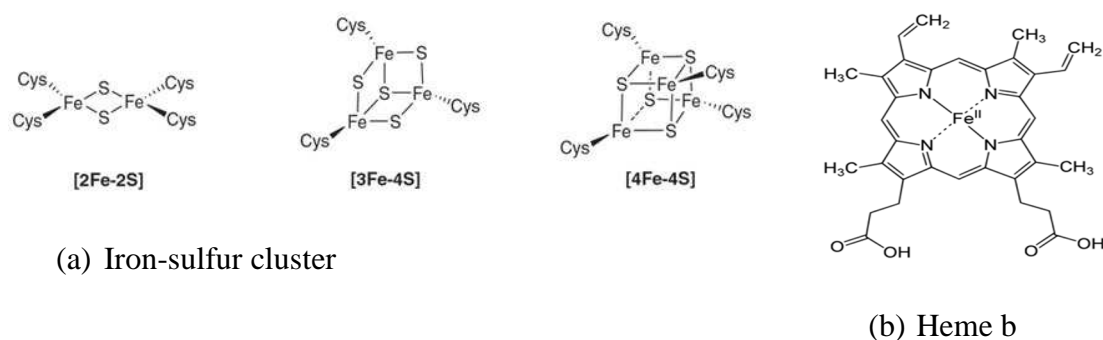
*Figure I.3: **Iron prosthetic groups.***

-   **[Fe-S] cluster biogenesis:** Iron sulfur clusters (ISC) (Fig I.3a) are ancient and vital prosthetic groups that are found in a wide range of proteins in the mitochondria, cytosol and nucleus. Many of these proteins play major roles in the metabolism, such as catalysis, electron-transfer in redox reactions and regulation of gene expression. ISC assembly machineries include at least 10 proteins. That comprise essentially protein scaffold, sulfur donor, electron transporter, iron chaperone and cluster transporter. Importantly, mammalian ISC biogenesis occurs in two different but functionally connected compartments: mitochondrial (ISC system) and extra-mitochondrial (CIA system). The inorganic *de novo* [Fe-S] cluster is synthesized within the mitochondrion by ISC assembly apparatus. They are then inserted into mitochondrial apo-proteins or passed through a process which generates an unknown molecule (X-S) that is exported by the ABC transporter Atm1 to the cytosol to

support the cytosol iron sulfur cluster proteins (ISP) biogenesis and to be utilized elsewhere (Figure I.4) *(Lill et al. 2015)*.

A

B
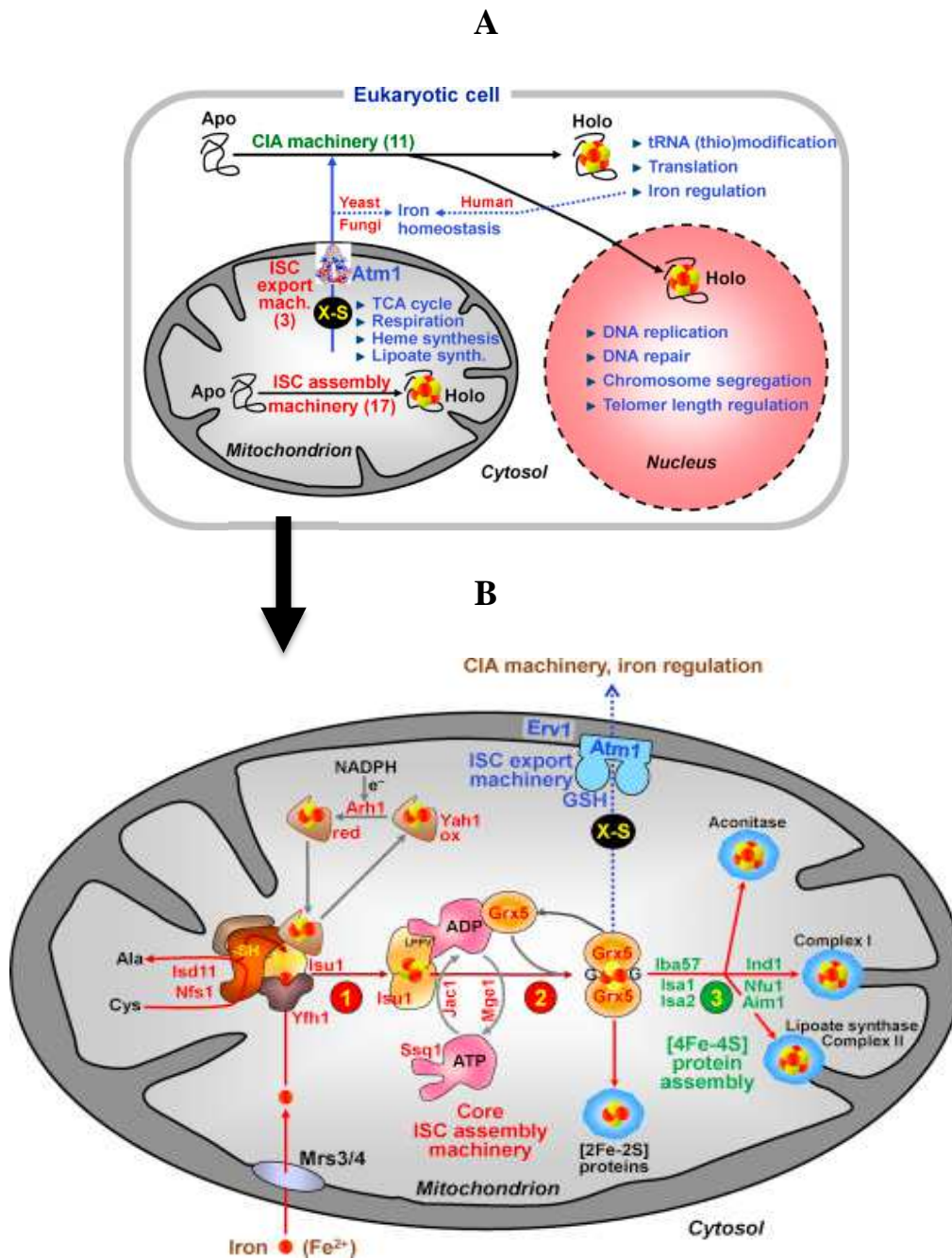
Figure I.4: ***Illustration of [Fe-S] cluster (ISC) biogenesis in eukaryote cells****. (**A**) Three distinct machineries assist the maturation of Fe/S proteins in non-green eukaryotes. The mitochondrial ISC assembly machineries consist of 17 known proteins and mature all organelle ISPs. The ISC system cooperates with the ISC export machinery and the CIA machinery, which is in charge for the biogenesis of cytosolic and nuclear ISPs. The central component of ISC export machinery is the mitochondrial inner membrane ABC transporter Atm1, which exports a sulfur- and glutathione containing compound of still unknown identify (X-S) to the cytosol (**B**) The current model for mitochondrial ISC assembly machinery. The ISC assembly occurs in three distinct steps. **Step 1**: The*

*de novo [2Fe-2S] cluster is assembled in the scaffold protein Isu1 with the participation of cysteine desulfurase complex Nfs1-Isd11 as sulfur supplier, an electron donor ferredoxin Yah1 and frataxin Yfh1 with unknown function. Iron for this step is imported from cytosol by mitoferrins Mrs3/4. **Step 2**: [2Fe-2S] cluster is released from Isu1. The cluster is transferred from Isu1 to mitochondrial glutaredoxin Grx5 that binds the [2Fe-2S] group in a glutathione dependent manner. The dedicated Hsp70 chaperone Ssq1 bind to the conserved LPPV motif of Isu1(ATP-hydrolysis dependent association) and facilitate the transfer of [2Fe-2S] from Isu1 to Grx5. Jac1 is a co-chaperone which assists the recruitment of Ssq1 to Isu1. The ADP-ATP exchange by Mge1 helps to dissociate Ssq1 from Isu1 and thus closes the chaperone cycle. From here, the Grx5-bound [2Fe-2S] clusters are transmitted to one of three pathways: (i) be transferred to mitochondrial apo-proteins without further assistance; (ii) pass through an unknown process which generates a sulfur or possibly glutathione-containing molecule (X-S) that is exported by the ABC transporter Atm1 to the cytosol to support the cytosol ISPs biogenesis; and (iii) shift to the third step. **Step 3**: All mitochondrial [4Fe-4S] proteins are assembled. Specialized ISC factors [Iba57-Isa1-Isa2] first facilitate the synthesis of [4Fe-4S] cluster from Grx5-bound [2Fe-2S] cluster. Then, the target specific insertion of [4Fe-4S] cluster into apo-proteins is archieved by various dedicated ISC targeting factors (Ind1, Nfu1, Aim1). (Lill et al. 2015)*

- **Heme biogenesis:** Heme is a prosthetic group that contains a metal, iron is the most common, in the central position of porphyrin ring (Fig I. 3b). Iron atom can uptake or release another smaller ligand *e.g.* O_2. Heme is an essential cofactor of important proteins, such as hemoglobin and myoglobin. The heme biosynthetic pathway includes eights enzymes, it begins and ends in mitochondria but the intermediate steps occur in the cytoplasm (Ponka 1997). In the final step, an iron atom is inserted into protoporphyrin IX by ferrochelatase. In the case of iron unavailability or deficiency, it is replaced by Zn(II) to form Zn-protoporphyrin, which can be an indicator for iron deficiency diseases. Ferrochelatase requires one [2Fe-2S] cluster to govern its catalytic activity, it is possible that any disruption in ISC synthesis would also adversely affect the heme synthesis (Anzovino et al. 2014).

- **Mitochondrial iron storage:** Iron excess from heme or ISC synthesis is sequestered by mitochondrial ferritin (Levi et al. 2001). Since reactive oxygen species are generated in mitochondria, it is essential that iron is stored in an inert form to prevent adventitious redox cycling reactions (Richardson Des R. et al. 2010). Ferritin stores iron by inducing its oxidation and deposes it inside the cavity in a ferric oxo-hydroxide core, which is structurally similar to the mineral ferrihydrite. Ferritin is highly expressed in tissues with high metabolic activity and oxygen consumption, such as testis, brain, and heart. Non-ferritin iron or labile iron pool is reactive and probably toxic for cell. Mitochondria from iron-sufficient cells contain labile iron in low-molecular-mass complexes at about 100-150 μM (McCormick et al. 2015).

The three pathways described above contribute to mitochondria the role of a gatekeeper for iron metabolism. Every disruption in these pathways can affect iron homeostasis in both mitochondria and cytoplasm.

(ii) Cu:

Copper is required within the mitochondrion for the function of two metalloproteins: Cytochrome c oxidase (CcO) and Cu-Zn superoxide dismutase (SOD1). CcO locates in the inner membrane. CcO is the terminal complex in respiratory chains, which reduces O_2 to two water molecules and transfers two protons into intermembrane space. Two subunits Cu_A and Cu_B of CcO containing copper are encoded by mitochondrial genome. Hence, the insertion of Cu certainly occurs in intermembrane space. SOD1 is localized and functionalized mainly in cytosol, with however 1-5 % is found in the intermembrane space. It is one of three common superoxide dismutases that catalytically convert superoxide to oxygen and hydrogen peroxide. SOD1 contains copper and zinc, where copper plays enzymatic role and zinc stabilizes the structure of protein. SOD1 is imported into mitochondrial as apo-protein; the metalation of SOD1 depends on a copper chaperone Ccs1.

There is very little, if any, free Cu within the cells. Copper is bound to proteins or complexed to glutathione or other small molecules. McCormick *et al.,* have indicated that 22 % of total mitochondrial copper (~16 μM of 71 μM) exist in a complex with an unknown low-molecular mass molecule (CuL). But the remaining question is whether the copper metalation of SOD1 and CcO is supplied by this CuL or from the cytosol (McCormick et al. 2015).The mechanism of copper import into the mitochondrion is unknown. Recently, Cobine PA *et al.* identified in yeast model two proteins of the mitochondria carrier family involving in mitochondrial copper import Pic2 and Mrs3. Mrs3 is an iron carrier that suggests a connection between copper and iron homeostasis (Vest et al. 2013, Vest et al. 2016). These studies also gave evidences for the direct interaction between CuL and Pic2/Mrs3.

Subsequently, copper is an important trace element for redox activity. It can also induce the generation of ROS *via* Fenton-like reaction. Therefore, cellular uptake, storage as well as copper export necessitate a tight regulation in order to guarantee sufficient copper supply for copper-containing enzyme but also to prevent copper-induced oxidative stress.

(iii) Mn:

In yeast, the only known function of Mn(II) in mitochondria is that of a cofactor in superoxide dismutase SOD2, the matrix superoxide dismutase. In contrast to Cu-dependent superoxide dismutase, SOD2 plays essential role in anti-oxidative stress since the complete loss of the enzyme SOD2 results in neonatal lethality in mice (Li Yibing et al. 1995) that cannot be rescued by CuZnSOD (Copin et al. 2000). Mammalian mitochondria contain the second Mn enzyme, which is type II arginase. It catalyzes the synthesis of ornithine and may regulate the production of NO by nitric oxide synthase (Topal et al. 2006).

Mitochondrial Mn labile pool exists majorly as a complex with an 1100 Da molecular weight (~2 μM) (McCormick et al. 2015). The mechanism of metalation for MnSOD is unknown. Apo-SOD2 has specific affinity to FeII. In iron excess condition, SOD2 risks to be irreversibly inactivated by the mismetalation of iron into apo-SOD2.

(iv) Zn:

Zinc is the most commonly utilized metal cofactors (9 % of all enzymes). In mitochondria, zinc is the catalytic cofactor of a range of proteases, which include inner membrane associated protease (mAAA, iAAA, Oma1 proteases of the inner membrane, and the intermembrane space protease Atp23) and mitochondrial processing protease (functions in cleavage of the N-terminal mitochondrial targeting sequences); Zn(II) is likely associated with the yeast mitoribosome. The dominant non-protein zinc in mitochondrial is at ~110 μM (McCormick et al. 2015). A subunit of cytochrome c oxidase (Cox4) and SOD1 require Zn for is stability.

1.2.2.1.2. Impairment of metal metabolism in FA model

Early characterization of the pathophysiology in individuals with FA provided obvious evidence of a link between frataxin deficiency and cellular metal metabolism dysregulation (Table I.3). However, their occurrences depend on the nature of the tissues.

Table I.3: Mitochondrial metals: function and the impaired metabolism in FA model.

Metal	Functions	Metabolism in FA
Fe	- Respiratory chain with 4 enzymes complexes I, II, III, IV - [Fe-S] cluster synthesis	- Reduce in ATP generation. - Deficiency in [Fe-S] cluster protein activity. - Zn-protoporphyrin IX is formed instead

	- Heme synthesis - Ferritin storage	of heme. - Iron accumulation in non-ferritin form.
Cu	- CuZn-superoxide dismutase (SOD1) – intermembrane space (IMS). - Cytochrome c oxidase (CcO) - inner membrane proteins, complex IV of respiratory chain.	- SOD1 is highly induced but decreased in activity (oxidative damage and lack of Cu for the metalation). - Reduce in activity of CcO.
Mn	MnSOD (SOD2) – superoxide dismutase in mitochondrial matrix.	Increase in protein amount but decrease in activity of SOD2.
Zn	- Cofactor of proteinases - Required structural stability SOD1 and Cox4, a subunit of CcO	Uncharacterized

In cardiac tissues, studies on autopsies of FA patients reported independent proofs of mitochondrial iron overload. The accumulation of iron in cardiomyocytes is restricted to small regions and progresses from granules in heart fibers to coarse aggregates in phagocytized cardiomyocytes (Lamarche et al. 1980). Cytosolic and mitochondrial ferritin, which are marker of iron excess, co-localize extensively in heart tissues. Hepcidine, a hepatic hormone controls systemic iron distribution, has been found in non-hepatic tissues including heart, which is an indicator of iron dysmetabolism (Koeppen A. H. et al. 2012). Rotig *et al.* was the first group to report the deficient activity of the ISC proteins of mitochondrial respiratory complexes I-III and aconitase in FA heart biopsies but not in other tissues (Rotig et al. 1997). The impairment of ATP synthesis in calf muscle and reduced biochemical activities of complex I and IV in the skeletal of FA patients were also reported. However, it was suggested that they were due to a quantitative decrease in the number of mitochondria rather than a selective mitochondrial dysfunction (Nachbauer et al. 2012).

However, iron overload does not occur typically in the nervous system. Dorsal root ganglion (DRG) are a primary target of FA with a remarkable lesion (Koeppen A. H. and Mazurkiewicz 2013). The assay of total Fe in DRG of FA patients was not increased. The accumulation of ferritin was only found in satellite cells surrounding dying DRG neurons (Koeppen A. H. et al. 2009). DRG in FA retained Zn and Fe rather than discharging them into the circulating blood (Koeppen Arnulf H et al. 2013). In physiological conditions, dentate

nucleus (DN) is an iron-rich structure that contains relatively high amounts of copper and zinc. The net amount of Fe, Cu or Zn does not increase or decrease significantly in the DN of FA patients, but the distributions of these metals are changed in affected DN. The Cu and Zn rich regions broaden and overlap extensively with the Fe-rich region. Copper is supposed to exist mainly in protein-bound forms in the DN of FA. The atrophy of the DN in FA correlates with Cu and Zn redistribution rather than with Fe dysregulation only (Koeppen A. H. et al. 2007, Koeppen A. H. et al. 2012).

A conditional mouse locally depleted frataxin within the heart and skeletal muscle, named the muscle creatine kinase (MCK) conditional - hFxn null mice (herein referred to as MCK-hFxn-knockout (KO) mice) is an effective model to study extensively the cellular mechanism of FA. Similar to patient cardiac tissues, mitochondrial iron accumulation as phosphorus and sulphur iron, cytosolic iron deficiency and low levels of cytosolic ferritin has been observed in MCK-hFxn-KO mouse (Huang et al. 2009, Puccio et al. 2001, Whitnall et al. 2008, Whitnall et al. 2012). However, no detectable iron deposits were observed in the complete hFxn-KO mouse or in the central nervous system of the 'neuron-specific' hFxn-KO mouse models (Santos et al. 2010). Also in yeast strain lack of yeast frataxin homolog ($\Delta yfh1$), iron was found in amorphous nanoparticles of ferric phosphate in mitochondria (Babcock et al. 1997, Foury and Cazzalini 1997, Lesuisse et al. 2003).

The inactivated iron-sulfur cluster proteins (ISPs) were found in cardiomyocytes of MCK-hFxn-KO mouse (Puccio et al. 2001) and $\Delta yfh1$ (Foury 1999, Rotig et al. 1997). Importantly, it was emphasized that the inactivation of iron-sulfur enzymes is the early phenomenon and intra-mitochondrial iron accumulation is the later (Poburski et al. 2016, Puccio et al. 2001, Stehling et al. 2004). FA patients do not manifest anaemia when frataxin expression is reduced, but heme production is attenuated (Huang et al. 2009). The enzymes involved in heme synthesis are altered (Boddaert et al. 2007, Yoon and Cowan 2004). Zn-protoporphyrine IX is formed instead of heme in $\Delta yfh1$ (Lesuisse et al. 2003).

The absence of frataxin in the heart and skeletal muscle leads to iron loading in liver, spleen and kidney because of the induction of hepcidin, hepatic hormone of iron metabolism (Whitnall et al. 2012). Biochemical studies on the iron metabolism of MCK-hFxn-KO mouse showed two alterations. First, there are the global down-regulation of molecules involved in ISC biogenesis, iron storage and heme synthesis while up-regulation of cytosolic heme catabolism. Second, the expression of molecules involved in cellular and mitochondrial iron

uptake tends to an increase in iron uptake targeting mitochondria, as well as a decrease in iron release (Huang et al. 2009). This implies a systemic perturbation of iron metabolism.

In contrast to the eukaryotic systems, a complete loss of the bacterial frataxin ortholog *(ΔcyaY)* does not exhibit a typical phenotype. It does not exhibit any modification in iron content or in the sensitivity to oxidant (Li D.S. et al. 1999).

Despite tissue-specific variations in frataxin-mediated iron handling, the dysregulation of iron metabolism due to frataxin deficiency remains the most prominent feature.

1.2.2.2. Mitochondrial redox control and oxidative stress

1.2.2.2.1. Generation of ROS/RNS in healthy mitochondrion

Redox dependent processes affect most cellular functions. Mitochondria are in the center of these processes as they generate reactive species (RS) that drive redox-sensitive events and respond to RS-mediated changes in the cellular redox state. Reactive species are not only harmful they are also important signaling molecules with potential therapeutic effect. The term reactive species relates to many kinds, such as reactive oxygen species (ROS: $O_2^{\bullet-}$, H_2O_2, $OH^{\bullet-}$), RS of nitrogen (RNS), carbon, sulfur and halogen, etc. Herein, we only mention ROS and RNS, the two most important RS in biological system. The components of RNS and ROS are listed in Figure I.5.
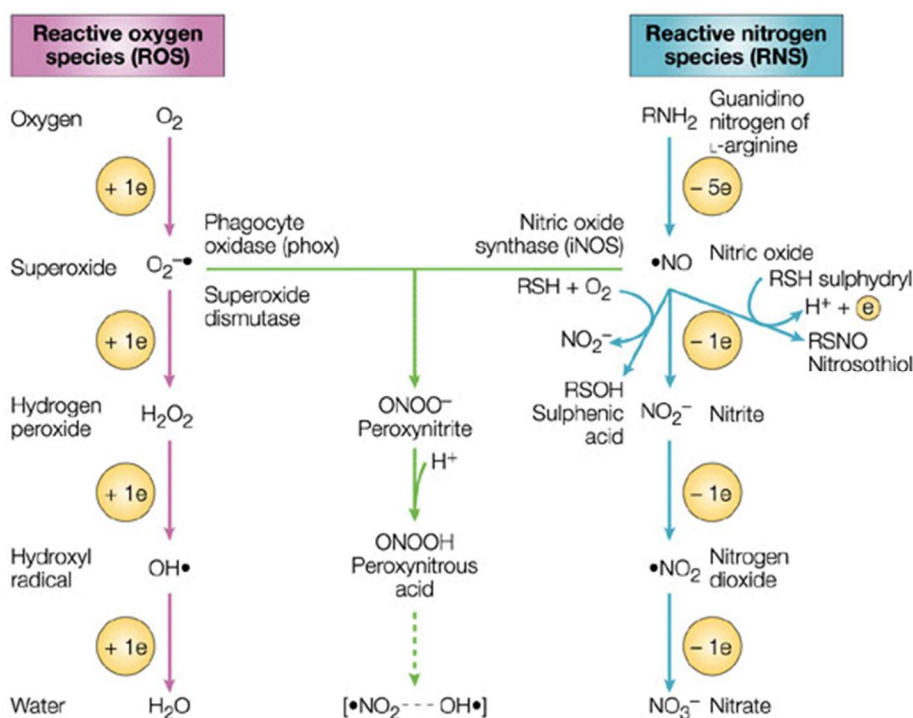
*Figure I.5: **Reactive oxygen and nitrogen intermediate production in mammalian cells.** ROS include superoxide anion ($O_2^{\bullet-}$)- the one electron reduction product of oxygen, hydrogen peroxide (H_2O_2), hydroxyl radical ($OH^{\bullet-}$). Nitric oxide (NO) is generated from the conversion of L-arginine to L-citrulline. The reduction step-by-step of NO generates nitrite (NO_2^{-}, nitrogen dioxide ($NO_2^{\bullet}$) and nitrate (NO_3^{-}). The reaction of NO with cysteine sulphydryl (R-SH) can result in either S-nitrosylation (R-SNO) or oxidation to the sulphenic acid (R-SOH). In reaction with superoxide anion, the highly reactive radical would be formed, include peroxynitrite anion ($ONOO^{-}$) and peroxynitrous acid (ONOOH). ONOOH spontaneously decomposes through a series of species that resemble the reactive radical hydroxyl ($OH^{\bullet}$) and nitrogen dioxide ($NO_2^{\bullet}$) (Fang 2004).*

(i) Reactive oxygen species (ROS)

In living organism, under aerobic condition, 90 % of the consumed oxygen is reduced directly to water by 4 electrons per O_2 molecule, catalyzed by cytochrome c oxidase – the complex IV in electron transport chain. The 10% is reduced systematic as detailed in ROS branch in figure I.5, the incompletely reduced products including $O_2^{\bullet-}$ (superoxide anion), H_2O_2 (hydrogen peroxide), $OH^{\bullet-}$ (hydroxyl radical) are called reactive oxygen species (ROS) (Fang 2004, Lushchak 2014).

In mitochondria, about 1-2 % of molecular oxygen is converted to superoxide anion during the oxidative phosphorylation by complexes I and III of the electron-transport chain, where 70% of $O_2^{\bullet-}$ are from the Q cycle (ubiquinol QH2 $\Leftrightarrow$ ubiquinone Q) as a part of electron transfer to complex III (Figure I.6). This superoxide can be released into the mitochondrial matrix or intermembrane space since the complex III- coenzyme Q10 binding site localize within the inner membrane (Handy and Loscalzo 2012).
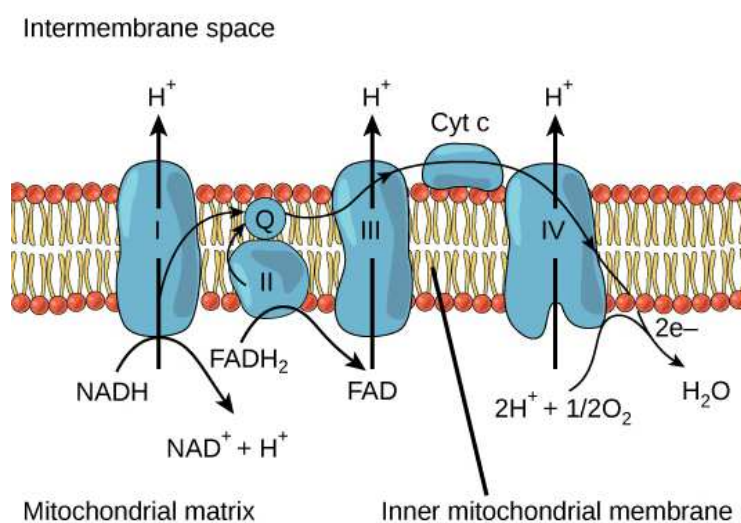
*Figure I.6: **Complexes I-IV** - the respiratory chains on the inner membrane of mitochondria.*

Superoxide radical is not a particularly strong reductant or oxidant (Abreu and Cabelli 2010). In physiological conditions, it seems unreactive with the amino acids. It is however highly reactive with some transition metal complexes, such as Cu, Mn, Fe because of the Haber-Weiss reaction (equation I.1). The damages induced by superoxide anion $O_2^{\bullet-}$ are more important on soluble metalloproteins such as [Fe-S] proteins (equations I.2 & I.3). Nevertheless, $O_2^{\bullet-}$ is converted into hydrogen peroxide H_2O_2 by superoxide dismutases (SODs). H_2O_2 is not a free radical but it is ROS as it is more reactive than an oxygen molecule, it can react with reduced cations of transition metal as Fe^{2+} or Cu^+ in Fenton-like reaction (equation I.4) and generates hydroxyl radical $OH^{\bullet-}$ and hydroxyl anion HO^-. Hydrogen peroxide and others ROS/RNS can furthermore inhibit aconitase - an ISC enzyme of Kreb's cycle, thus slow down glucose consumption, respiration and ATP synthesis (Brazzolotto et al. 1999, Gardner 1997, Lushchak 2014). H_2O_2 excess is scavenged by catalase- a heme containing protein (Handy and Loscalzo 2012).

Haber-Weiss reaction: $\qquad$ $Fe^{3+} + O_2^{\bullet-} \rightarrow Fe^{2+} + O_2$ $\qquad\qquad$ (I.1)

Inactivation [Fe-S] cluster: $\quad$ $[4Fe\text{-}4S]^{2+} + O_2^{\bullet-} \rightarrow [4Fe\text{-}4S]\text{-}OO^{\bullet}$ $\qquad$ (I.2)

$\qquad\qquad\qquad\qquad$ $[4Fe\text{-}4S]\text{-}OO^{\bullet} + 2\,H^+ \rightarrow [3Fe\text{-}4S] + H_2O_2 + Fe^{3+}$ $\qquad$ (I.3)

Fenton reaction: $\qquad\qquad$ $Fe^{2+}_{(aq)} + H_2O_2 \rightarrow Fe^{3+}_{(aq)} + OH^-_{(aq)} + OH^{\bullet-}$ $\qquad$ (I.4)
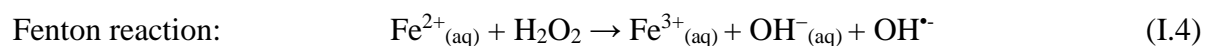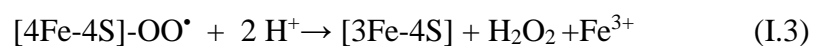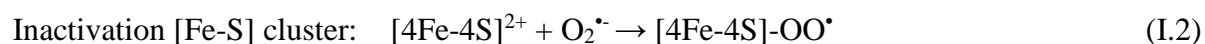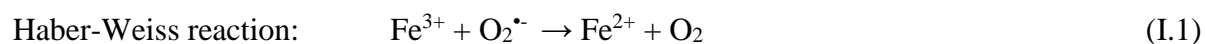
Hydroxyl radical can acquire one more electron and a proton to yield H_2O. In biological systems, this reaction mainly occurs through the substraction of hydrogen atom from proteins, lipids or DNA (Stadtman and Levine 2003).

It has been established that 90 % of ROS are produced in mitochondria (Herrero et al. 2008). Every post-translational modification of mitochondrial subunits can either promote or attenuate the generation of ROS. The other sources of ROS include: diverse oxidases (xanthine oxydases, NADPH oxidase, etc.) and the auto-oxidation of different small molecules (epinephrine, norepinephrine and xenobiotics, etc.) (Lushchak 2014).

(ii) Reactive nitrogen species (RNS)

In mammals, NO is mainly synthesized by nitric oxide synthases (NOS) through the conversion of L-arginine to NO and L-citrulline (Knowles and Moncada 1994). The physiological roles of NO depend on its local concentrations, it plays multiple roles in the

nervous system and glial regulated pathways. Under physiological conditions, it contributes to regulating proliferation, survival, and differentiation of neurons. Nitric oxide is involved in synaptic activity, neural plasticity, and cognitive function (i.e., memory). The imbalance nitric oxide metabolism can contribute to neuronal cell death and various neurodegenerative disorders (as Alzheimer's diseases, Parkinson's diseases etc.) (Bradley and Steinert 2016).

An increase in the production of NO during the neuroinflammation in the presence of ROS, especially superoxide anion, yields highly reactive peroxynitrite ($ONOO^-$). Peroxynitrite can react directly with proteins that contain transition metal centers. Therefore, it can modify proteins such as hemoglobin, myoglobin, and cytochrome c by oxidizing ferrous heme into its corresponding ferric forms. Peroxynitrite may also be able to change protein structure through the reaction with various amino acids in the peptide chain. The most common reaction is tyrosine nitration (nitrotyrosination Tyr $\Leftrightarrow$ Tyr-NO_3) which is considered as a biomarker of nitrosative stress. In another hand, NO itself can be added covalently into a cysteine thiol/sulfhydryl (RSH) (S-nitrosylation RSH $\Leftrightarrow$ R-SNO) (Figure I.5). All of these reactions affect protein structure and function, cause changes in the catalytic activity of enzymes, alter cytoskeletal organization, and impair cell signal transduction (Castro et al. 2011).

1.2.2.2.2. Oxidative defense mechanism

As the excess of reactive species (RS) can induce unexpected changes in the structure and function of biomolecule, it is then necessary for RS to be kept in a range compatible with normal cellular function. The imbalance between the production of ROS/RNS and the protection against ROS/RNS is defined as "oxidative stress" and/or "nitrosative stress". The oxidative/nitrosative stress induces damage to DNA and RNA (incorporation of an oxidized base during DNA polymerization, or oxidization of the integrated base), proteins (protein-protein cross-linking, fragmentations, unfolding, etc.) and lipid (formation of lipid peroxides (LOOH) which can also damage DNA and protein). Hence, the RS steady-state level must be strictly controlled.
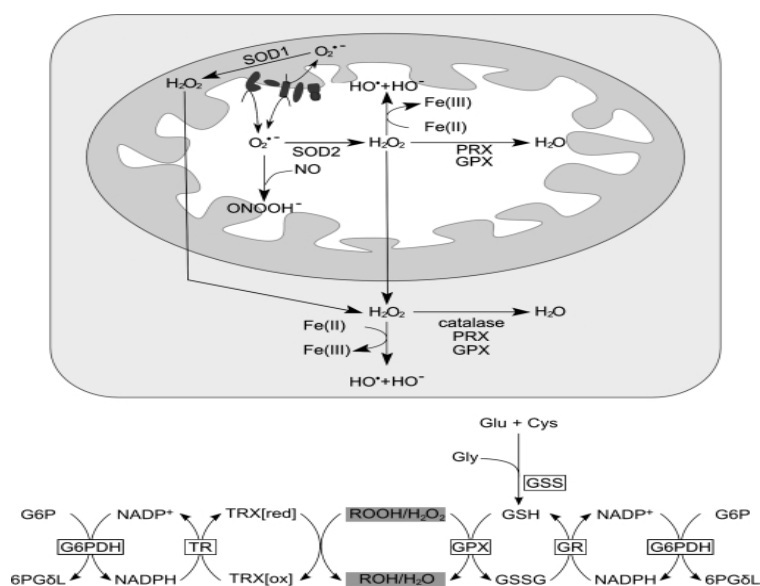
Figure I.7: ***ROS/RNS production and cellular antioxidant defense enzymes***. *Copper-dependent superoxide dismutase (SOD1), which locates in intermembrane space, is responsible for the dismutation of superoxide anion while manganese-dependent superoxide dismutase (SOD2) achieves the same purpose in the mitochondrial matrix. These processes generate hydrogen peroxide (H_2O_2) which can react with labile iron pool and produce OH^- and $OH^\cdot$. H_2O_2 and other peroxides are detoxified by glutathione peroxidases (GPXs), which oxidize glutathione. Glutathione (GSH/GSSG) is a tripeptide synthesized in two steps from glutamic acid, cysteine, and glycine. GSSG is reduced to GSH by glutathione reductase (GR) by using electrons from NADPH. NADPH is regenerated by the pentose phosphate pathway enzymes, glucose 6-phosphate dehydrogenase (G6PDH), and 6-phosphogluconate dehydrogenase. Other enzymes that scavenge H_2O_2 and peroxides are catalases and peroxiredoxins (PRXs). Peroxiredoxins can also scavenge $ONOO^-$. The cellular thiol redox status is maintained by the thioredoxin (TRX)/thioredoxin reductase (TR) and glutathione/glutaredoxin systems by reducing the oxidized sulfhydryl groups of proteins (Santos et al. 2010).*

Living organisms possess multilevel and complicated antioxidant system operating either to eliminate RS, or minimize their negative effects (Figure I.7). Antioxidants can be classified according to their molecular mass: low molecular mass (< 1000 Da) and high molecular mass (> 1000 Da).

The group of low molecular mass antioxidants includes molecules such as vitamins C (ascorbic acid) and E (tocopherol), carotenoids, anthocyanins, polyphenols, and uric acid. Most of them are supplied as food or supplement components. However, the most important antioxidant in this group is glutathione (GSH) (L-γ-glutamyl-L-cysteinylglycine), a tripeptide synthesized in most living organisms from glutamic acid, cysteine, and glycine. GSH is used to control RS level either *via* direct interaction, or serving as a cofactor for RS-detoxifying enzymes (*e.g.* glutathione-dependent peroxidases). High molecular mass antioxidant group

includes enzymes such as: superoxide dismutase SOD, catalase and glutathione-dependent peroxidase, etc. (Indo et al. 2015).

(i)   GSH and glutathione-dependent antioxidants

Under the conditions of oxidative/nitrosative stress, the thiols in cysteine residues (-SH) within proteins are among the most susceptible oxidant-sensitive targets that can undergo various reversible and irreversible redox alterations affecting protein activity or structure (Figure I.8). The tripeptide glutathione is present in cells at the millimolar concentrations (~1–10 mM). It shows high negative redox potential (high electron-donating capacity). It is the reason for which GSH can protect protein thiol groups from oxidation either directly as a free radical scavenger, or indirectly as co-substrate for a number of important enzymatic systems. Glutathione can also form a mixed-disulfide bridge with an accessible free thiol group on a protein (S-glutathionylation- P-SSG). Glutathionylated proteins may thus be used as a biomarker for oxidative stress.

Glutathione-dependent peroxidases (GPx) reduce H_2O_2 to form GSSG, and also lipid peroxides (L-OOH) – a reactive species (equation I.5 & I.6).

$$2GSH + H_2O_2 \rightarrow GSSG + 2H_2O \qquad\qquad (I.5)$$

$$2GSH + LOOH \rightarrow LOH + GSSG + H_2O \qquad\qquad (I.6)$$
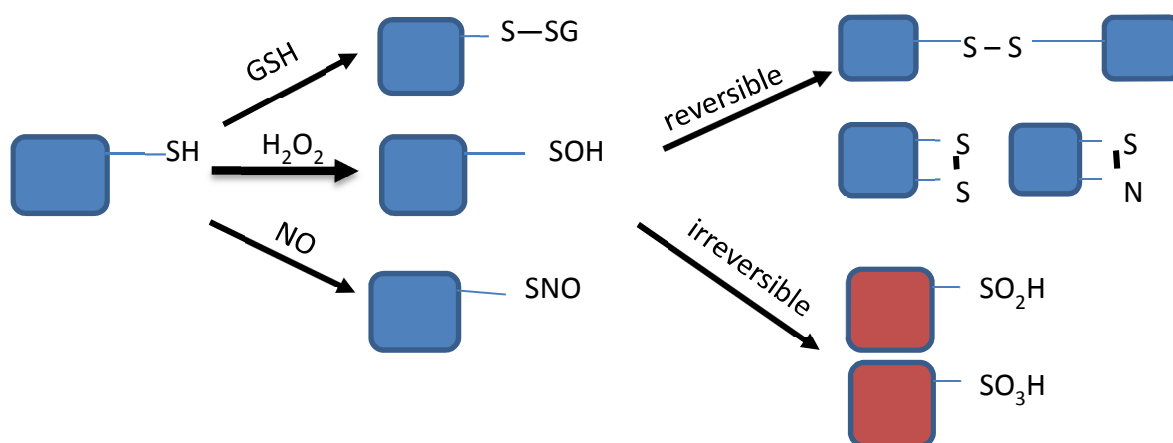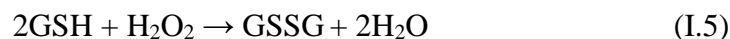
*Figure I.8: **Illustration of the modification of proteins thiol groups under oxidative/nitrosative stress.***

The reduced form of glutathione, GSH, is the quantitatively most important buffering system against oxidative stress in mammals. The physiological intracellular milieu is a reducing

environment with a GSH/GSSG ≥ 100. Maintaining optimal GSH/GSSG ratios in the cell is critical to cell survival and is important for regulating the redox state of protein thiols. In mitochondria, this ratio is higher than in cytosol, which minimizes protein glutathionylation by thiol disulfide exchange (Lushchak 2014). The concentration of reduced GSH and ratio GSH/GSSG allow evaluating the buffering capacity of medium.

(ii)   SODs

SOD family consists of metalloproteins, whose active site uses copper-zinc, manganese, iron, or nickel, are ubiquitous components of cellular antioxidant system. These proteins catalyze the dismutation of $O_2^{\bullet-}$ to oxygen and hydrogen peroxide. All known SODs require a redox active transition metal in the active site in order to accomplish the catalytic breakdown of superoxide anion. A generic mechanism for the metalloenzyme dependent dismutation steps is below (equation I.7 & I.8).

$$M^{(n+1)+}\text{-SOD} + O_2^{\bullet-} \rightarrow M^{n+}\text{-SOD} + O_2 \qquad\qquad (I.7)$$

$$M^{n+}\text{-SOD} + O_2^{\bullet-} + 2H^+ \rightarrow M^{(n+1)+}\text{-SOD} + H_2O_2 \qquad (I.8)$$
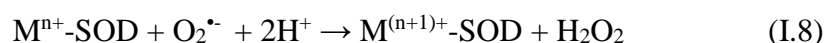
(*) M= Cu, Mn, Fe, Ni

CuZn-dependent SOD (SOD1) and Mn-dependent SOD (SOD2) are the only members of SOD family found within mitochondria (Culotta et al. 2006). SOD1 is an intracellular enzyme, which localizes throughout the cell cytoplasm, nucleus and microsomes; in mitochondria it has been detected only in intermembrane space. Whereas, MnSOD is the only mitochondrial matrix superoxide dismutase. SOD2 has a more crucial role in the inactivation of mitochondrial superoxide anion than SOD1. Indeed, SOD2 deficiency causes early neonatal death in knockout mice while the total absence of SOD1 does not (Li Yibing et al. 1995). Both SOD1 and SOD2 are imported into the mitochondria as apo-peptide and must undergo a step of post-translation coupled with the metalation.

The structure and function of SOD1 and SOD2 will be discussed in details in chapter IV.

1.2.2.2.3. <u>FA cases</u>

A similarity of phenotypes between FA and the ataxia of vitamin E deficiency led to envisage a probably relation between FA and oxidative stress. Furthermore, in the most common five mitochondrial diseases related to oxidative stress, FA is the most cited (Hayashi and

Cortopassi 2015). On the other hand, although anti-oxidative therapie (discussed in **1.3**) can reduce the symptoms of FA, they never can cure the disease (Santos et al. 2010). Therefore, the involvement of oxidative stress in FA remains controversal. The main research related to the oxidative deal with three aspects: (i) the evidences of oxidative damage in FA patients as well as in frataxin depletion models; (ii) increase of ROS/RNS production; (iii) FA models become highly sensitive to oxidative stress.

(i)   Oxidative stress markers

The loss of mitochondrial function and the appearance of the markers of oxidative damage in nearly all FA models have been examined. Products of DNA oxidative damage have been found in urine (Schulz et al. 2000); both mitochondrial and nuclear DNA damage are detected in peripheral blood cells (Haugen et al. 2010); shortened telomere and abnormal glutathionylation have been reported by study autopsy (Anjomani Virmouni et al. 2015). By investigating different human cell lines with FA, the increased level of glutathionylated cytoskeletal proteins was found in fibroblast and spinal cord of patients with FA together with a significant rise of dynamic tubulin and neurofilaments (Sparaco et al. 2009).

Frataxin deficient pancreatic islets in mice show decreased proliferation and increased apoptosis due to the increased ROS (Ristow et al. 2003). The disruption of frataxin expression in murine hepatocytes reduces life span and develops multiple hepatic tumors. Also, biomarkers of lipid oxidation and oxidized glutathione (GSSG) were found to be significantly high in liver specimen (Thierbach et al. 2005). In mice mutant with the (GAA) repeat expansion, oxidized proteins were found in cerebrum, cerebellum, heart and skeletal muscle and increased lipid peroxidation was also detected in cerebrum and heart samples (Al-Mahdawi et al. 2006). In yeast models, frataxin depletion led to the oxidization of mitochondrial proteins, mitochondrial DNA lesions and accumulations and nuclear DNA damage (Karthikeyan et al. 2003). Furthermore, frataxin deficiency had little effect when yeast cells were grown anaerobically, but a shift to aerobic growth resulted in loss of aconitase activity and oxidative protein damage (Bulteau et al. 2007). Moreover, oxidative stress in $\Delta yfh1$ mutants increased the proportion of fragmented mitochondria as compared to wild type (Lefevre et al. 2012).

(ii)   Increased ROS/RNS production

The increase of ROS as superoxide and hydrogen peroxide was reported in FA lymphoblasts by use of fluorescent probes (Napoli et al. 2006) and in frataxin-depletion pancreatic islets (Ristow et al. 2003).

The increased generation of ROS in FA was suggested to be a result of deficiency in ISC biosynthesis and iron accumulation. Indeed, in mitochondria of FA models, hydrogen peroxide H_2O_2 is overproduced because of the insufficient activity of complexes I-III of the oxidative phosphorylation chain and cytosolic aconitase. Iron is also overloaded in FA mitochondria in non-protein iron pool. The presence of H_2O_2 together with iron accumulation favor the Fenton-like reaction that generates ROS (equation I.4) (Babcock et al. 1997, Calabrese et al. 2005, Napoli et al. 2006, Radisky et al. 1999).

Conversely, this hypothesis can be contradicted by the following results. A study reported that the iron accumulated in frataxin deficient yeast is in an oxidized and insoluble form and thus unable to participate in Fenton-like reaction (Seguin et al. 2011). Recently, a time-resolved functional analysis on modified murine fibroblast revealed that a full depletion of frataxin induced a massive increase in ROS production before the iron accumulation. This result excludes away the primary role of iron overload for oxidative stress (Poburski et al. 2016).

(iii)   Increase oxidant sensitivity and oxidant protection deficiency

The increase of oxidant sensitivity has been shown by independent studies in various model: FA patient cells (Wong et al. 1999), yeast (Santos et al. 2010), *C. elegans* (Vázquez-Manrique et al. 2005), *Drosophila* (Runko et al. 2008), mouse (Al-Mahdawi et al. 2006). In these studies, the depletion of frataxin aggravates the sensitivity to a variety of pro-oxidants, including H_2O_2 and other peroxides as well as iron. The mechanism of the aggravation is complex. However a critical aspect is that the defense against oxidative stress is altered in FA models.

Biochemical studies have shown the impairment of glutathione homeostasis in FA patients' blood plasma and lymphocytes, FA mouse model, DRG cells and frataxin deficient *S. cerevisiae*. It was found that free reduced glutathione (GSH) decreased while glutathionyl-protein increased in blood of patients with Friedreich's ataxia (Piemonte et al. 2001) or in fibroblast (Pastore A. et al. 2003). Mouse neuronal cell lines with reduced amount of frataxin

showed that glutathione imbalance progressively increases with a significant rise of all oxidized forms of glutathione, including protein bound one (Carletti et al. 2014). The isolated mitochondria from Δ*yfh1* cells and lymphoblasts of FA patients showed evidence for a severe mitochondrial glutathione-dependent oxidative stress, with a low GSH/GSSG ratio (1.7 within the mitochondria Δ*yfh1*), and thiol modifications of key mitochondrial enzymes (Bulteau et al. 2012).

A continuous oxidative damage due to an impaired response to oxidative stress may contribute further to mitochondrial dysfunction and cell degeneration in FA. As mentioned before, SODs are the most important defenses against ROS as they catalyze the disproportionation of superoxide anion to hydrogen peroxide. Their activity requires however redox active metal ions. In heart cells of MCK-*hFxn* KO mouse, MnSOD expression was induced early but reduced when respiratory chain enzyme activities are extremely decreased and iron accumulation is visible in mitochondria. Similarly, Δ*hFxn* cerebellum has a lower MnSOD expression level (Seznec et al. 2005). In frataxin-deficient mouse model of FA, microarray and neurotic growth experiments in DRG tissue identified decreased transcripts encoding the antioxidants, including peroxiredoxins, glutaredoxins, and glutathione S-transferase (Shan et al. 2013). In Δ*yfh1* cells, both of CuZnSOD and MnSOD are highly induced but their specific activity (meaning dividing the enzymatic activity with the protein amount) is decreased. CuZnSOD activity can be restored in copper supplement medium. Whereas, the matrix mitochondrial MnSOD is always inactivated even in manganese supplemented culture (Irazusta et al. 2010).

1.3.   Pharmacotherapy for Friedreich ataxia

Currently, there is no treatment for FA as no drug therapy showed any efficacy in slowing disease progression. The palliative and symptomatic treatments, such as β-blockers, angiotensin-converting-enzyme inhibitors, surgery for cardiac manifestations and physical therapy are applied only to improve the quality of life. A number of active ingredients are under investigation since the identification of the frataxin responsible gene. The current efforts in developing therapeutic strategies deal with three approaches: iron chelators, antioxidants and/or stimulants of mitochondrial biogenesis, and frataxin level modifiers (Table I.4).

1.3.1. Iron chelators

Dysregulation of metabolic iron and its accumulation in mitochondria are typical hallmark of FA patients. Several iron chelators that target to the mitochondria have been avaluated including deferoxamine and deferiprone. They successfully protected the mitochondria and reduced ROS damage to mitochondrial proteins. However, the utilization of iron chelators presents an important risk mainly because of many side effects such as the decrease of the mRNA levels of both aconitase and frataxin (Pandolfo and Hausmann 2013).

1.3.2. Antioxidants and/or stimulant of mitochondrial biogenesis

Even if the role of oxidative stress in FA pathology remains controversial, it is clear that patients with FA present increased oxidative stress, resulting in DNA damage (Schulz et al. 2000), increased levels of lipid peroxidation (Abeti et al. 2015), and impaired ROS defenses (Irazusta et al. 2010). A lot of work has been done in evaluating the potential of antioxidants in FA therapy.

Until now, the first drug who reached phase III in clinical trials is Idebenone, an analogue of Co-enzyme Q10 (Figure I.8). Co-enzyme Q10 is a small lipophilic molecule present within the inner mitochondrial membrane in association with the electron transport chain (ETC) complexes, which transfers electrons between complexes I and II, and from oxidation of fatty acids and branched chain amino acids to complex III resulting in the ultimate production of ATP (Figure I.9).

Co-enzyme Q$_{10}$

Idebenone

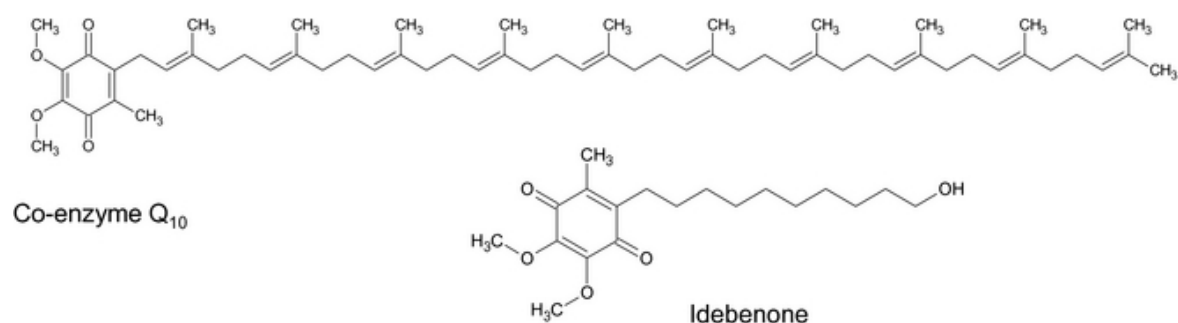*Figure I.9: **Chemical structures of co-enzyme Q10 and Idebenone.** They show the common reducible benzoquinone nucleus and lipophilic side chains.*

Idebedone can act as an electron carrier within the ETC and has similar antioxidant properties to co-enzyme Q10. Idebenone has been reported to increase oxidative phosphorylation and aerobic respiration (Meier and Buyse 2009), to improve intracellular markers of ROS damage

and FA symptoms, to decrease oxidative stress, lipid peroxidation and to slow the progression of heart diseases (Rustin et al. 1999, Schulz et al. 2000). However, in 2011, Idebenone failed its Phase III trial because it was found not to significantly improve lifespan and cardiac outcomes in patients. Idebenone is currently not licensed in Europe or the United States for use in FA. Therefore, further works are being undertaken with other CoQ10 analogs but no study has yet been performed in FA patients (Parkinson et al. 2013).

1.3.3. Frataxin level modifiers

One of the most promising treatment strategies for FA therapy is to increase the intracellular content of frataxin, thus preventing the cascade of protein deficiency that leads to the clinical syndrome. The level of frataxin expression can be increased by the compounds that combat the FXN gene silencing and/or a delivery system which introduce frataxin to cells.

Erythropoietin (EPO) is a 30 400 Da glycoprotein that was initially recognized as a regulator of red cell production. rHuEPO, which has the same biological effects as endogenous erythropoietin, is a 165 amino acid glycoprotein synthesized by recombinant DNA technology. Sturm *et al*., 2005 was the first group to report that rHuEPO can increase the quantity of frataxin, in addition to its classical neuro- and cardio protective effects (Sturm et al. 2005). It is suggested that EPO promotes the translation of mRNA into frataxin without a concurrent rise in frataxin mRNA level (Acquaviva et al. 2008). Other compounds have also shown success in increasing frataxin protein levels, such as histone deacetylase inhibitors BML-201 and 106. These two compounds are in pre-clinical phase (Richardson Timothy E. et al. 2013).

In addition, varieties of systems that allow the introduction of frataxin or vector expressing human FXN have been developed. For example, transactivator of transcription (TAT) from the human immunodeficiency virus (HIV) is a short peptide able to efficiently guide the delivery of fused proteins across cellular and intracellular membranes. TAT fusion proteins containing a mitochondrial targeting sequence can translocate through the mitochondrial membranes, with appropriate processing and persistence of the fusion protein within mitochondria. A TAT/h-frataxin fusion protein able to localize within the mitochondria is currently being developed and tested in mammalian model. Also, gene therapy is being experienced with several successful applications (Evans-Galea et al. 2014).

Table I.4: Active ingredients under investigation for FA therapy.

Agent	Groups	(+) Effects, (-) Side effects	Present stage
Idebenone	Antioxidant Analogue of Co Q10	(+) as free radical scavenger. (+) facilitate electron transport in ETC, thus enhance ATP production. (-) adequately improve cardiac outcomes in patients.	Phase III (failed in phase III study since 2011)
Mitoquinone	Antioxidant Analogue of CoQ10 specifically targeting at mitochondria	(+) decrease oxidative damage; 800 times more potent in preventing cellular death than idebenone (-) does not enhance ATP production.	Phase II
Deferiprone Deferoxamine	Iron chelator	(+) detoxify labile iron pool (-) side effects: agranulocytosis, musculoskeletal pain, dizziness, nausea vomiting, gastrointestinal discomfort and elevated hepatic enzymes, etc. (-) Decrease mRNA levels of both frataxin and aconitase (deferoxamine); and activity of aconitase (deferiprone).	Phase II
17β-Estradiol (E2) and methylene blue (MB)	Combination of antioxidant and iron chelator	(+) E2: neuroprotective effects; attenuate ROS, prevent lipids and proteins damage; stabilize mitochondrial membrane potential, maintain activity of ETC chain, aerobic respiration and favorable balance of anti/pro apoptotic proteins. (+) MB: neuroprotection and antioxidant (similar to idebenone)	Preclinical
Erythropoietin	Increase frataxin expression	(+) Promoting the translation of mRNA into frataxin without a concurrent rise in frataxin mRNA level.	Phase II
Pioglitazone	Stimulant mitochondrial	Agonist of the peroxisome proliferator-activated receptor gamma (+) increase fatty acid oxidation and mitochondrial function; decrease ROS accumulation and inflammation.	Phase III
Adeno-associated virus vector	Gene-therapy		Preclinical
TAT-frataxin fusion protein	Mitochondrial targeting frataxin		Preclinical

2. Frataxin and functions hypothesis

2.1. Structure

Frataxin is a small globular protein, highly conserved in most organisms from prokaryotes to eukaryotes, in eukaryote cells it locates in the mitochondrion. All frataxin orthologues have an unique fold that combines two terminal α-helices to form one plane, five antiparallel β-strands that construct the second plane of the protein and a sixth (or seventh in hFxn) β-strand that intersects the planes to give an overall planar "α–β sandwich" structure motif (Figure I.10) (Bencze et al. 2006).
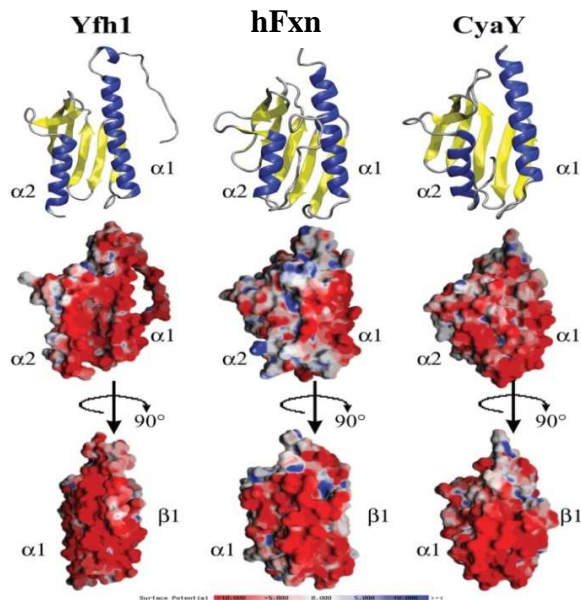
*Figure I.10: **Frataxin's structure**. Top: ribbon diagram for yeast, human and bacterial frataxin. Middle: electropotential plots for proteins in same orientation. Bottom: electropotential plots for proteins rotated −90 degrees around the y-axis compared to top display. Structure figures made using solution structures of Yfh1 (PDB ID# 2GA5), hFxn (PDB ID# 1LY7) and CyaY (PDB ID# 1SOY) frataxins. The negatively charged amino acids are red, the neutrally charged ones are grey and the positively charges ones are blue* (Bencze et al. 2006)

The strong structural similarity between frataxin orthologues results from the fact that these proteins share an extremely high degree of amino acid sequence similarity (Figure I.11). Various biochemical studies have reported the importance of conserved residues in both of two regions: the α1/β1 acidic ridge and the conserved β-sheet surface in stabilizing structure as well as in frataxin's functions (Bencze et al. 2007, Dhe-Paganon et al. 2000).
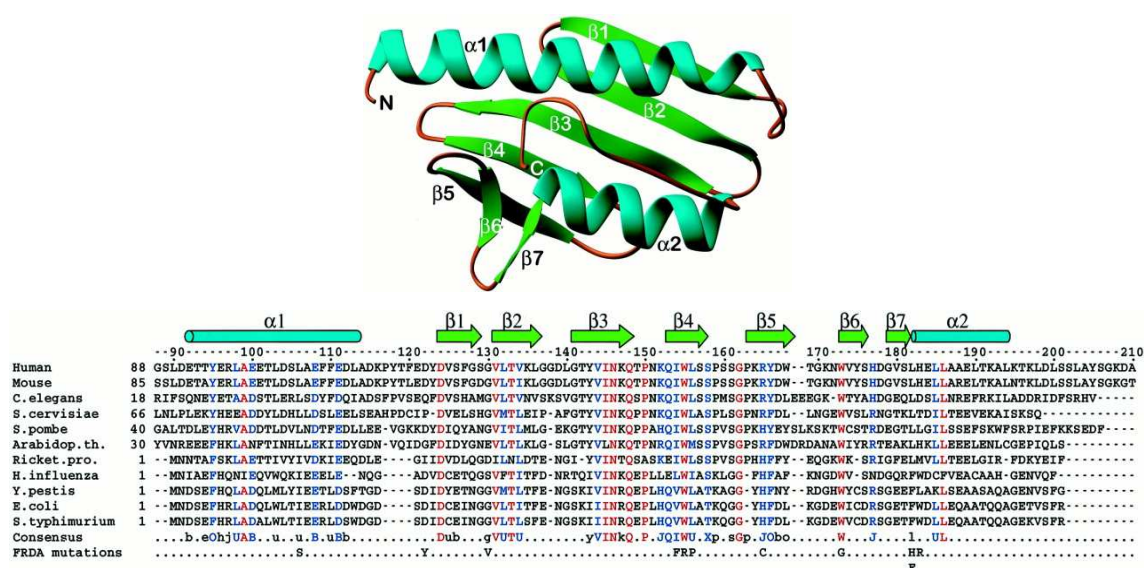
Figure I.11: **Structure-based sequence alignment of human frataxin with homologues from prokaryotes and other eukaryotes**. *Elements of secondary structure are denoted by turquoise cylinders (α helices) and green arrows (β strands). Identical residues are red. Highly conserved residues are blue (Dhe-Paganon et al. 2000).*

A large number of the highly conserved amino acids including a subset of aspartic acid and glutamic acid residues are located in the N-terminal region of the protein which is also exposed surface of the [α1- β1] interface. In physiological condition, these residues generate a negatively charged surface that covers roughly a quarter of frataxin's total accessible surface (Dhe-Paganon et al. 2000). The acidic residues which have critical role in iron-binding have been identified in most of frataxin orthologues as: E18/E19/D22 in CyaY (Adinolfi et al. 2002, Nair et al. 2004, Pastore C. et al. 2007b); D31/D35/ /D28/H32 in Yfh1 (Cook et al. 2006, Foury et al. 2007, He et al. 2004); D122/L113/D115 in hFxn (Bencze et al. 2007, Dhe-Paganon et al. 2000). The acidic ridge in α1- β1 interface are also reported to be necessary for frataxin - ferrochelatase interaction (D104, E108, E111, D122, D124 in hFxn) (Bencze et al. 2007) and holoYfh1 – Isu1 (the ISC scaffold proteins) (Cook et al. 2010). This acidic ridge is not only the site for functional interaction, but is also involved in frataxin's stability. Indeed, it was observed that these charged residues increase the binding ability but decrease molecular stability, illustrates interestingly a trade-off between activity and stability (Correia et al. 2010, Sanfelice et al. 2014). The conservation of these acidic patches suggests that the negatively charged amino acids can be the key for determining frataxin's function.

The second putative functional region of the protein is a large flat surface, which is formed by the 5-7 antiparallel β-strands. This β-sheet surface is nearly neutral because it conserves a collection of mostly uncharged residues. In physiological condition, the internal hydrophobic

core is important for the protein's stability. Furthermore, the exposed hydrophobic surface is supposed to be involved in the binding of frataxin to its functional partners as the components of [Fe-S] cluster assembly *via* V144, N146, Q148, Q153, W155, L156 and R165 (human numbering) (Bridwell-Rabb et al. 2011, Leidgens et al. 2010, Wang and Craig 2008). Importantly, the identical conserved W155 is reported to be essential for functional binding between frataxin and ISC scaffold (Leidgens et al. 2010). Moreover, the mutation of this residue into arginine, which has been found as point mutation in some heterozygous FA patients, rather blocks completely the mitochondrial import of frataxin (Galea et al. 2016). The residues from 122 to 124 on β-sheet surface are also reported to play important role in functional interactions of Yfh1 (Correia et al. 2010).

The "α–β sandwich" motif structure consists of a layer of α-helices packed against an antiparallel β-sheet. The fold is quite robust, the proteins with this type of structure accommodate a range of functions: metal chaperone (ferredoxin-like fold of some cytosolic copper chaperones), proteinase inhibitor (serine protease inhibitor), host defense (interleukin-8, class I histocompatibility antigens), electron transfer and enzymes (biotin synthetase, aspartate transcarbamylase) etc. The active sites are distributed over the whole surface of the fold. Many of these proteins use the hydrophobic surfaces or the loops to bind to other proteins (Orengo and Thornton 1993).

2.2. Stability

In spite of their high degree of conservation, the mid-point of the thermal unfolding (Tm) of different frataxin orthologues are very different. The hFxn and CyaY are quite stable, they have melting points in ranges of 60 °C and 54 °C, respectively, while Yfh1 has melting point at 35 °C (Adinolfi et al. 2002, Adinolfi et al. 2004). In addition, Yfh1 is one of the few proteins whose cold denaturation can be observed at temperatures around the freezing point of water and at physiological pH without the presence of destabilizing agents (Pastore A. et al. 2007a). It is suggested that the weak stability of Yfh1 is due to two reasons. First, Yfh1 has a shorter C-terminal sequence compared to other orthologues, which does not provide an effective protection of the hydrophobic core (Adinolfi et al. 2004). Second, the surface of Yfh1 is exceptionally rich in negative charges and the distances between the negatively charged residues (E89, E103, D101, E112) are smaller than the ones in CyaY and hFxn. Thus the repulsion between these residues favors the entrance of the solvent into the hydrophobic core (Sanfelice et al. 2014). The nature of buffer (organic or phosphate) has minimal effect on

protein stability while the presence of salt generally increases the stability of the frataxin's fold, most pronounced in the case of Yfh1. The substantial increase in ionic strength induces the decrease in repulsions between the negatively charged residues (Adinolfi et al. 2004, Sanfelice et al. 2014, Vilanova et al. 2014).

Many cell free studies dealt with the oligomer form of Yfh1 (trimer or more). However very recently, Pastore and co-workers have reported that the protein is predominantly present in cell not as an aggregate but as a monomeric species (Popovic et al. 2015).

2.3. Hypothesis about function

Since the discovery of frataxin, a lot of hypothesis about its functions have been supposed. In FA models, a range of defect in iron homeostasis has been observed. Hence, most of the hypothesis about its functions concern the iron metabolism, such as iron storage, mitochondrial iron efflux control, iron chaperone and iron donor for [Fe-S] assembly and heme synthesis. Also, the depletion of frataxin induces the highly sensitivity towards oxidative stress, which implies that frataxin can possibly participate in antioxidant defense.

2.3.1. Iron-binding: iron storage and/or mitochondrial iron-uptake control

Indeed, iron overload occurs in the mitochondria in the absence of frataxin led to the hypothesis that frataxin control mitochondrial iron flux (Radisky et al. 1999). This led also to an extensive study of all the frataxin orthologues with Fe^{2+}/Fe^{3+}.

Initially, Yfh1 was reported to form a multimer that consists of about 60 subunits which can sequester ~13,000 atoms of iron, which is close to Fe/ferritin ratio implying for frataxin a role similar to that of ferritin in iron sequestration (Adamec et al. 2000). In addition, at $Fe^{2+}/$ Yfh1 molar ratios below of 0.5, Yfh1 was reported to have the ferroxidase activity, as ferritin (Park et al. 2002). In presence of iron, CyaY has been shown to form aggregations as yeast homologue, whereas no multimeric form was observed for human frataxin (Adinolfi et al. 2002, Bou-Abdallah et al. 2004).

However, iron storage function seems to be excluded since the oligomerization is not observed *in vivo* (Aloria et al. 2004, Seguin et al. 2010).

Now, it has been shown that monomeric frataxins bind iron with similar affinities but with different stoichiometries: hFxn binds six or seven iron ions K_d ~ 12–55 μM (Yoon and Cowan

2003), CyaY bind two ferrous with K_d ~ 4 μM (Bou-Abdallah et al. 2004), frataxin from *Drosophila* Dfh binds one ferrous iron K_d ~ 6 μM (Kondapalli et al. 2008) and monomeric Yfh1 binds two ferrous irons K_d ~ 2.5 μM (Cook et al. 2006).

It was also shown that the bacterial frataxin CyaY has low cation specificity and its binding with divalent or monovalent metal does not involve cavities or pockets, but exposed glutamates and aspartates (Pastore C. et al. 2007b).

2.3.2. In iron-sulfur cluster assembly

[Fe-S] cluster is critically required for the function of numerous proteins involved in a wide range of cellular activities as electron transport, regulatory sensing, photosynthesis, tRNA modification, DNA repair and regulation of gene expression, etc. The biogenesis of Fe–S clusters proteins *in vivo* is a multistep process that involves a complicated sequence of catalyzed protein–protein interactions and coupled conformational changes between the components of several dedicated multimeric complexes.

In bacteria, three distinctive systems involved in Fe-S cluster proteins biogenesis have been identified: NIF, ISC and SUF systems (Table I.5), whereas in eukaryotes, the scenario is more complicated since the Fe-S proteins are required in all distinct subcellular compartments. ISC biogenesis can be broadly understood in terms of two phases: the formation of Fe–S cluster, and the transfer of the intermediates to apo-protein recipients. In eukaryote cells, the *de novo* [2Fe-2S] cluster is assembled within the mitochondrion by the ISC machinery. [Fe-S] clusters for the ISPs in cytosol or other organelles are synthesized by cytosolic system (CIA). However, this depends functionally on mitochondrial ISC system (detailed in 1.2.2.1.1). The core step of Fe-S biogenesis in the mitochondria is essential to all subcellular Fe-S proteins (Figure I.12).
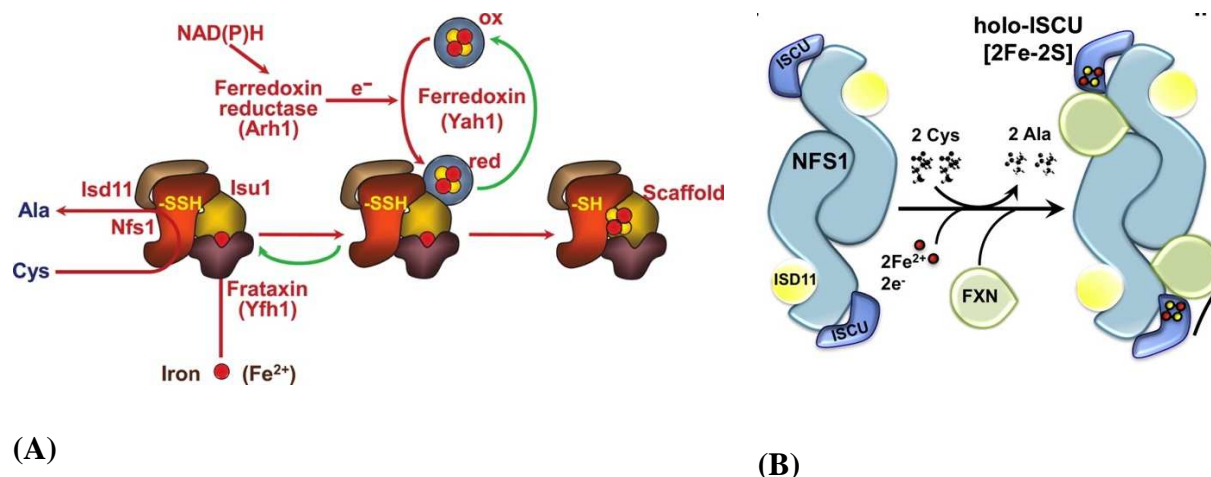
(A)

(B)

Figure I.12: **De novo [2Fe-2S] cluster formation on the scaffold protein Isu1.** *(A)* <u>Hypothesis A</u>: *The desulfurase complex Nfs1/Isd11 converts cysteine to alanine and releases sulfur which is transiently bound in form of a persulfide group on a conserved cysteine residue on Nfs1. After putative transfer to a cysteine residue on the scaffold protein Isu1 the sulfane sulfur is reduced to sulfide to allow for Fe/S cluster formation. Sulfur reduction is presumably mediated by the electron transport chain comprised of NAD(P)H, Arh1, and Yah1. Yah1 binds to Isu1 only in its reduced (red) but not oxidized (ox) state. The delivery of iron to Isu1 might involve frataxin (Yfh1) which is also needed for maximal desulfurase activity of Nfs1. (review by (Stehling et al. 2014))* **(B)** <u>Hypothesis B</u>: *Frataxin (FXN) is part of the core complex, potentially binding in a pocket-like region between NFS1 and ISCU. The cluster assembles upon ISCU when iron is provided together with the reducing equivalents that allow achievement of the final electronic configuration of the cluster. The source of iron for the nascent cluster remains to be identified, but proposed donors include frataxin or a complex of glutathione and glutaredoxin. Electrons are provided by ferredoxins (FDX1/2) and ferredoxin reductase (FDXR) (review by (Maio and Rouault 2015)*

The ISC system components in eukaryote are conserved through evolution. The nomenclature of ISC components in different models are listed in the table I. 5.

Table I.5: Inventory of mitochondrial de novo [Fe-S] ISC assembly factors

Prokaryotes name	**Yeast name**	**Human name**	**Putative functions**
IscU	Isu1/Isu2	ISCU	Scaffold protein
IscS	Nfs1	NFS1	Cysteine desulfurase: Sulfur supplier
	Isd11	ISD11	Structural stabilizer for cysteine desulfurase
Fdx	Yah1	FDX2	Electron transport
	Arh1	FDXR	Electron transport
CyaY	Yfh1	hFxn	Iron donor; Or enhance the entry of iron
			Regulator, stabilizer of ternary complex
			Activator of cysteine desulfurase
			Enhance S-S formation and/or S-S transfer

In general, the *de novo* synthesis of a [2Fe-2S] cluster is accomplished by a multiprotein complex with the cluster transiently bound on a protein scaffold Isu1 which provides the backbone structure for cluster assembly (Figure I.12). Cysteine desulfurase Nfs1 is the suppliers of sulfur by subtracting the element from L-cysteine through a persulfide intermediate by a pyridoxal-phosphate dependent mechanism. Isd11, which is not found in prokaryotes, is required for Nfs1 stability. The persulfide sulfur is transferred from Nfs1 to Isu1 likely involving the formation of persulfide group in one of three cysteine residues of the scaffold. The sulfur needs to be reduced from S^o to S^{2-}, the electrons required for this reduction are supplied by ferredoxin reductase Arh1 and ferredoxin Yah1 through an electron transport chain including NAD(P)H. The iron donor is always unidentified. The essential role of frataxin in ISC system was confirmed by the phylogenetic distribution (Huynen et al. 2001). Moreover, frataxin-deficient cells present the defect in mitochondrial Fe/S proteins (Chen et al. 2002, Foury 1999, Lutz et al. 2001, Rotig et al. 1997, Stehling et al. 2004). However, frataxin's exact functions are still subjects to controversy, which have been most extensively discussed. Various suggestions have been given as: iron donor/iron chaperone, enhancement the activity of Nfs1/Isd11 by exposing the active site, enhancement of the S-S bond transfer from Nfs1 to Isu1 or a regulator factor.

(i) Iron donor:

In the beginning, Yfh1 appears to interact with iron and also exhibits direct molecular interaction with the ISC components as Isu1, or Isu1/Nfs1/Isd11 complex in an iron-dependent manner (Gerber et al. 2003, Layer et al. 2006, Ramazzotti et al. 2004, Yoon and Cowan 2003). Similarly, holo-CyaY (preformed complex with iron) has been reported to give iron to IscU forming [2Fe-2S] cluster in presence IscS and cysteine (Layer et al. 2006). Significantly, apo-hFxn does not bind to ISCU, but holo-hFxn does, with a sub-micromolar binding affinity (Yoon and Cowan 2003).

Furthermore, the residues of Yfh1 which play critical roles in Yfh1-Isu1 interactions were identified. Consistently, the conserved acidic residues in [α1-β1] interface as D86, E89, D101 and E103, which are involved in the iron-binding sites, also have essential role in Isu1 binding (Cook et al. 2006, Foury et al. 2007) (purple residues in Figure I.13). Nevertheless, some other results compromised this hypothesis. The three residues 122-124 on β-sheet of Yfh1 are not involved in iron binding site, their alteration does not modify the affinity for iron neither, nor the stability of protein, however, this modification reduces the direct interaction

of Yfh1 with Isu1 as well as the activity of Yfh1 in the ISC assembly (Figure I.13) (Wang and Craig 2008). The mutation of W131 in Yfh1 (W155 in hFxn) – a conserved amino acid on β-sheet, which is not involved in iron binding, also weakens the association between Isu1 and Yfh1 (Leidgens et al. 2010).
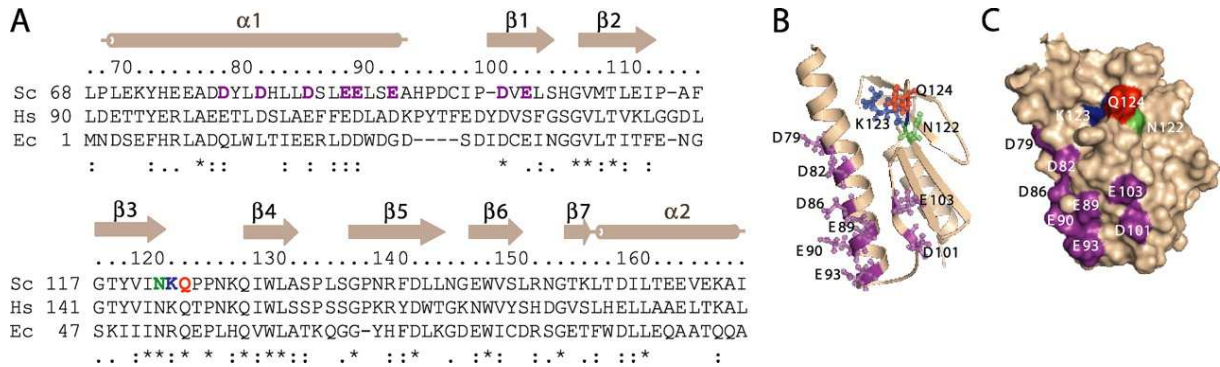

*Figure I.13: **Yfh1 structure**. (**A**): alignment of sequences corresponding to the α1-α2 region of Yfh1. S. cerevisiae, Yfh1 (Sc); Homo sapiens, frataxin (Hs); Escherichia coli, CyaY (Ec). Secondary structural elements and numbering referring to Yfh1 are above the sequences. Iron binding residues (purple), Asn-122 (green), Lys-123 (blue), Gln-124 (red) are indicated. Identical (*) and highly similar (:) residues are indicated. (**B**): Ribbon and (**C**): space-filled Yfh1 (Wang and Craig 2008).*

(ii)   Regulatory factor:

Many cell free studies on purified proteins have suggested that frataxin enhances the formation and transfer of persulfide, stabilizes the working complex and thereby improves the formation of ISC cluster in eukaryote cells.

The mechanism of persulfide formation and transfers from NFS1 to ISCU has been studied extensively. Actually, the sulfur is derived from the free amino acid cysteine by the cysteine desulfurase activity of NFS1. The enzyme binds the substrate cysteine in the pyridoxal phosphate-containing site, and a persulfide is formed on the active site cysteine residue of NFS1 in a manner depending on the accessory protein ISD11 which is also necessary for NFS1 stability. In bacteria, cysteine desulfurase activity is carried out by IscS, without an ISD11-similar partner. The "S-S" bond is then transferred to the scaffold ISCU, where it combines with iron to form the Fe-S cluster intermediate (Pandey et al. 2012).

Beside the direct molecular interaction of holo-frataxin with ISC scaffold proteins, hFxn was also described to bind ISD11. Contrary to hFxn-ISCU, this interaction is inhibited by iron but favored by nickel. The two conserved residues on β-sheet W155 and I154 are identified to be

necessary for hFxn-ISD11 binding (Shan et al. 2007). W155 is important for hFxn-ISCU binding as well. Barondeau's groups reported that frataxin binding improves the K_m for cysteine and the catalytic efficiency (k_{cat}/K_m) of NFS1. The presence of ferrous iron further stimulates this activation (Tsai and Barondeau 2010) (Figure I.14).
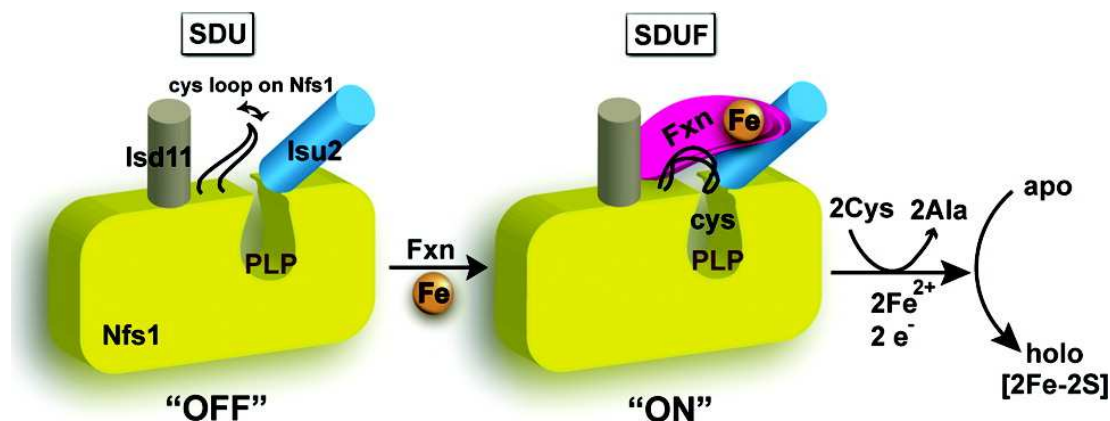

*Figure I.14: **Working model for hFxn activation of the Fe-S cluster assembly complex**. The NFS1 flexible loop is stabilized in a nonfunctional conformation for the NFS1-ISD11 (SD) complex or NFS1-ISD11-ISCU (SDU) complex. HFxn-SDU binding switches the NFS1 flexible loop from a nonfunctional to a catalytic conformation, which enhances substrate binding and lowers the K_m for cysteine. It also induces a conformational change in ISCU (Isu2) that facilitates the transfer of sulfur from NFS1 and thereby increases the cysteine turnover number (k_{cat}). Fe binding also induce a conformational change in ISCU that accelerates the transfer of sulfur from NFS1 to ISCU for Fe-S cluster biosynthesis (Tsai and Barondeau 2010).*

Similarly, in yeast model, Pandey *et al.* suggested that Nfs1 must undergo at least two conformational changes, one of which is mediated by Yfh1 to expose its "buried" substrate-binding sites, whereas the other is mediated by Isd11 to bring the bound substrate cysteine to the active site cysteine residue for persulfide formation. The Yfh1-Nfs1-Isd11 binding does not depend on iron, neither does Isu1 (Pandey et al. 2013).

HFxn also accelerates the formation of persulfide formation on NFS1 (Bridwell-Rabb et al. 2014) and enhances the rate of sulfur transfer from NFS1 persulfide to ISCU and to the small thiol-containing molecules such as DTT, L-cysteine and GSH. (Parent et al. 2015). Collin and co-workers showed that FXN stabilizes the quaternary complex ISCU/NFS1/ISD11/FXN and controls iron entry to the complex through activation of cysteine desulfurization. Moreover, the presence of FXN leads to a greater amount of [4Fe-4S] cluster per complex and to a transferable [4Fe-4S] cluster (Colin et al. 2013).
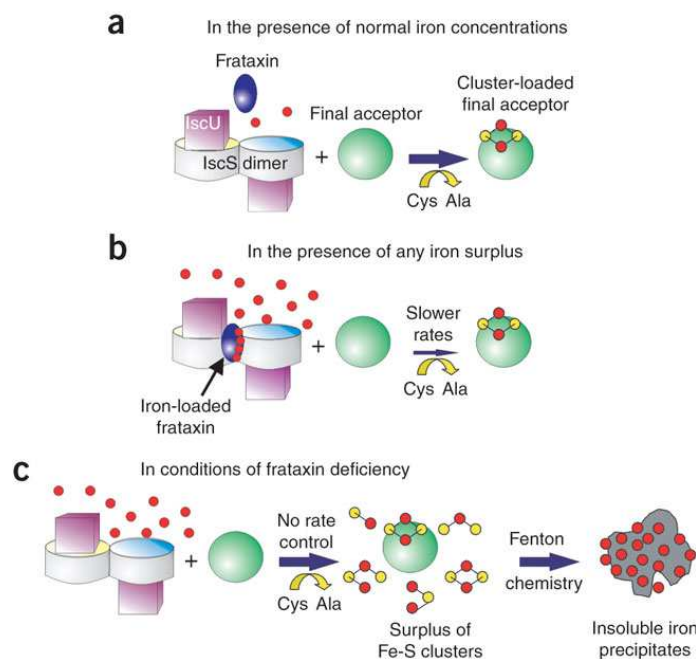
*Figure I.15: **Schematic model of the molecular mechanism of frataxin in the prokaryotic cell**: (a) At normal iron concentrations, the Fe-S clusters are assembled by the IscS–IscU complex and passed on to their acceptors (apo-proteins or transporters). (b) Any excess of iron as compared to the number of final acceptors will be rebalanced by slowing down the reaction to match the concentration of final acceptors and avoid unnecessary overproduction of Fe-S clusters. (c) ΔCyaY: there is no regulation. Fe-S clusters will be produced irrespectively of whether they can be transferred to an acceptor. Any iron excess will result in a surplus of Fe-S clusters, which, being highly unstable, will fall apart, generating Fenton reactions. Fe^{3+} will precipitate and form insoluble aggregates. (Adinolfi et al. 2009).*

On the other hand, CyaY is not simply an iron chaperone in prokaryote, it serves as an inhibitor specific for [2Fe-2S] cluster assemblage. Indeed, the function as iron donor is excluded since [2Fe-2S] cluster can be formed in absence of CyaY. The addition of CyaY reduces the rate of cluster formation. The direct interaction of CyaY-IscS is indispensable for the activity of frataxin. In addition, frataxin's inhibition depends on iron concentration, this suggests an iron sensors function of CyaY (Figure I.15) (Adinolfi et al. 2009).

Interestingly, it was found that a single amino acid substitution in the scaffold protein Isu1 effectively reverses many of defects in absence of frataxin. The methionine at 107 position in Isu1 is a highly conserved residue in eukaryotes but in prokaryote this position corresponds to an isoleucine. The mutation M107I on Isu1 restored several deficient functions in ΔYfh1, such as the improvement of iron homeostasis, ISPs activity, cytochrome and heme synthesis. (Yoon et al. 2014, Yoon et al. 2012).

In summary, the direct function of frataxins in [Fe-S] formation is well acknowledged. However, further studies are needed to establish the molecular mechanism of the process and to unify the function of eukaryotic frataxins.

2.3.3. Heme synthesis

Ferrochelatase is the terminal enzyme in the heme synthesis apparatus, which inserts iron into protoporphyrin IX. Frataxin is reported to bind directly to ferrochelatase (both human and yeast) with a sub-micromolar binding affinity (Bencze et al. 2007, He et al. 2004). Iron used in heme synthesis is suggested to be controlled by frataxin (Lesuisse et al. 2003, Yoon and Cowan 2004). In addition, the participation of frataxin in heme synthesis is independent of ISC synthesis since the overproduction of yeast frataxin impairs ISC assembly, but increases iron availability for heme synthesis (Seguin et al. 2009).

2.3.4. In response to oxidative stress

Frataxin-deficient yeast cells accumulate oxidized proteins in the mitochondria and cytosol (Bulteau et al. 2007). It is often assumed that an excess of ROS is generated in the case of the dysfunction of [Fe-S]-dependent enzymes in the respiration chain. This leads to iron accumulation and thereby induces Fenton reaction and generates a vicious circle of ROS production in deleted frataxin cells (Calabrese et al. 2005).

Conversely, the investigation of overproduction frataxin in various models supported its involvement in the defense against ROS/RNS. Overexpression of Yfh1 leads to lower levels of [Fe–S] cluster enzyme activity, including a decrease in the stability of aconitase (a [4Fe-4S] enzyme). However, smaller amounts of oxidized proteins and greater resistance to oxidative agents have been observed in yeast (Seguin et al. 2009). In *Drosophila*: a systemic increase in antioxidant capability, resistance to oxidative stress insults and longevity (Runko et al. 2008). In mammalian (Shoichet et al. 2002): over-expression of hFxn increases cellular antioxidant defenses. A study by Kim *et al.* interestingly demonstrated a frataxin dependent mechanism in neuroprotection from ROS in a Parkinson mouse model, which also suffers from oxidative stress (Kim et al. 2012).

2.4.   Functional interactions reported for frataxin

One classic manner to determine the functions of a biomolecule is the identification of interacting partners. Database bank SGD has listed 15 physical and 84 genetic interactions of Yfh1 protein (Figure I.16A). There are three proteins whose interaction with Yfh1 are determined by both physical and genetic interaction, they are Isu1, Sdh1 and Sdh2 (subunits of succinate dehydrogenase- the complex II of ETC).

The function of frataxin in ISC assembly is well documented. Frataxin interacts with single proteins in ISC assembly apparatus such as the cysteine desulfurase (Layer et al. 2006, Pandey et al. 2013) or the scaffold protein (Leidgens et al. 2010, Ramazzotti et al. 2004, Wang and Craig 2008, Yoon and Cowan 2003). It also binds the preformed tri-complex Nfs1-Isd11-Isu1 to form a tetra-complex (Gerber et al. 2003, Li H. et al. 2009, Ranatunga et al. 2016, Tsai and Barondeau 2010). In particular, Colin and his colleagues had synthesized *in vitro* [4Fe-4S] cluster by this tetra-complex in presence of inorganic iron and sulfur (Colin et al. 2013). No direct interaction between frataxin and ISC carriers proteins has been determined, nevertheless an identical phylogenetic distribution of the frataxin gene with *hscA/SSQ1* and *hscB/JAC1* (encode for the [Fe-S] cluster carriers) has been identified by phylogenetic studies (Huynen et al. 2001).
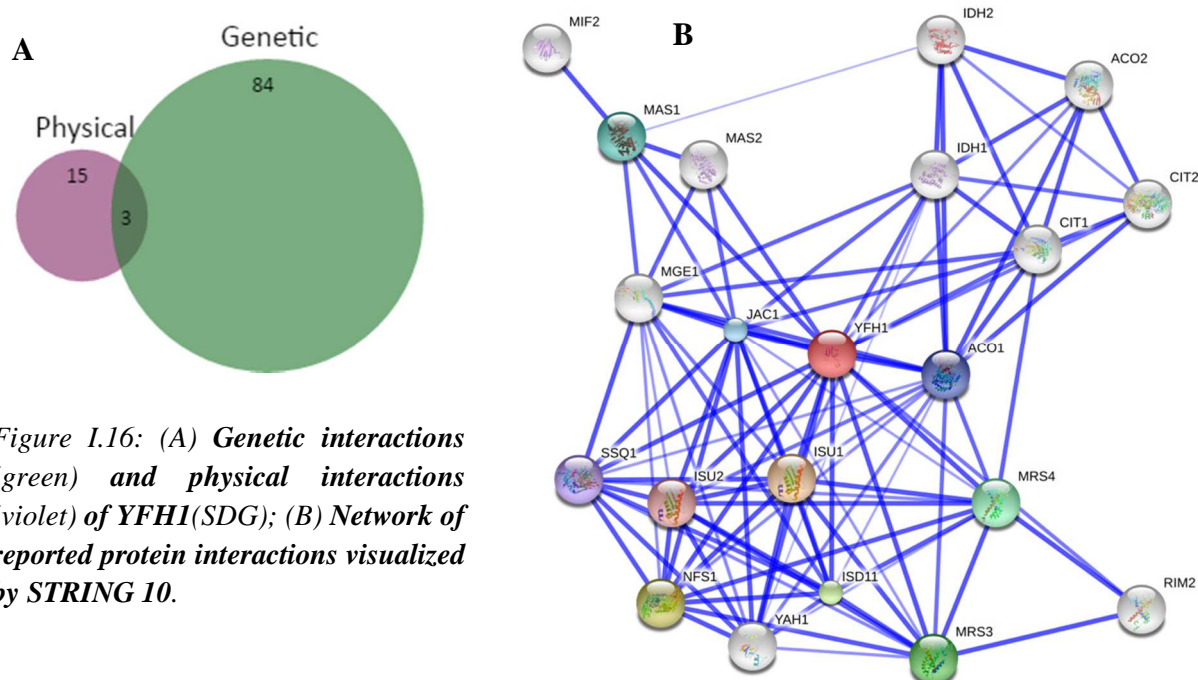

*Figure I.16: (A) **Genetic interactions (green) and physical interactions (violet) of YFH1**(SDG); (B) **Network of reported protein interactions visualized by STRING 10**.*

A specific interaction between frataxin and mitochondrial aconitase which allows the reinsertion of iron into the [3Fe-4S] cluster of enzyme was observed. It gives frataxin a role different from the assembly of protein iron-sulfur clusters (Bulteau et al. 2004). Testi's group showed the interaction of an extra-mitochondrial frataxin with cytosolic aconitase/iron regulatory protein-1, which is the oxidized form of cytosolic aconitase (Condo et al. 2006, Condo et al. 2010).

Frataxin of eukaryote cells has been showed to interact with ferrochelatase. The binding sites involve the highly conserved acidic patch of frataxin, which overlaps its iron-binding site (Bencze et al. 2007, He et al. 2004, Yoon and Cowan 2004).

A genetic interaction of Yfh1-SOD2 has been investigated by negative double mutant (Michael Costanzo et al. 2010). Yeast flavohemoglobin (Yhb1) was shown to interact with Yfh1 by yeast two hybrid systems and co-immunoprecipitation (Gonzalez-Cabo et al. 2005). SOD2 and Yhb1 are components of oxidative stress control systems.

Table I.6 summarizes the proteins partners whose interaction with Yfh1 was analyzed and suggested for frataxin's function.

Table I.6: Interaction partners and suggested functions for Yfh1 in each case

Proteins partners	Evidence	Suggested functions for Yfh1
Isu1 Mitochondrial [Fe-S] assembly scaffold protein	(+)(Michael Costanzo et al. 2010, Ramazzotti et al. 2004) (++)(Cook et al. 2010, Gerber et al. 2003, Leidgens et al. 2010, Li H. et al. 2009, Wang and Craig 2008) (+++)(Gerber et al. 2003)	Direct function in [Fe-S] cluster assembly: iron donor /enhance iron entry/conformational change to favor the S-S transfer.
Nfs1/Isd11 Nfs1: mitochondrial cysteine desulfurase; Isd11: the structural stabilizer of Nfs1	(+)(Michael Costanzo et al. 2010) (++)(Wang and Craig 2008) (+++)(Layer et al. 2006, Pandey et al. 2013)	Activator cystein desulfurase/ conformational changes to expose substrate binding site /enhance S-S transfer from Nfs1/Isd11 to Isu1.

Ternary complex Nfs1/Isd11/Isu1	(++) (+++)(Colin et al. 2013, Gerber et al. 2003, Manicki et al. 2014, Schmucker et al. 2011)	Regulator positive (eukaryotic) or negative (prokaryotic). Stabilize quaternary complex.
Yah1 - Ferredoxin of the mitochondrial matrix; electron donor for ISC and heme biosynthesis	(+) (Vilella et al. 2004)	Direct function in [Fe-S] cluster assembly.
Ssq1 and Jac1: function together in the dislocation of the Fe/S cluster from Isu1 and its insertion into apo-proteins	(+) gene co-occurrence with *hscA/SSQ1* and *hscB/JAC1*(Huynen et al. 2001)	Co-chaperone or in protecting the sulfhydryl groups of ISC apo-proteins. Or direct function in [Fe-S] cluster assembly.
Aco1-Aco2: [4Fe-4S] proteins required for the tricarboxylic acid (TCA) cycle and also independently required for mitochondrial genome maintenance.	(+++)(Bulteau et al. 2004) Citrate –dependent (++) (Condo et al, 2010)	Protection of the $[4Fe-4S]^{2+}$ cluster from disassembly; and facilitation of Fe(II) transfer to the $[3Fe-4S]^{1+}$ cluster of aconitase, allows the reactivation of the enzyme.
Sdh1/Sdh2 Succinate dehydrogenase complex subunits	(++) (Gonzalez-Cabo et al. 2005)	Direct role of frataxin in regulating the entry of electrons towards the electron transport chain, at least *via* complex II
Mrs3/Mrs4 - Iron carrier on inner membrane which are responsible for mitochondrial iron uptake	(+) (Zhang et al. 2005)	Iron-chaperone/Iron donor/ Iron efflux in mitochondria
Hem15 - Ferrochelatase - catalyzes the final step in heme biosynthesis	(++) (He et al. 2004, Yoon and Cowan 2004)	Iron donor for heme biosynthesis
SOD2 Mitochondrial manganese superoxide dismutase; protects cells	(+) (Irazusta et al. 2010, Michael Costanzo et al. 2010)	Role in the oxidative stress control

against oxygen toxicity		
Yhb1 - Flavohemoglobin involved in nitric oxide detoxification	(++) (Gonzalez-Cabo et al. 2005)	Role in nitrosative stress control

(+): genetic relation (negative mutant, gene co-occurrence)

(++): physical interaction (two hybrid, co-immunoprecipitation, affinity chromatography, co-structural, co-crystal…etc)

(+++): functional interaction (the interaction which affects the function of partner protein, the activity of reconstituted complex has been evaluated)

3. Objectives
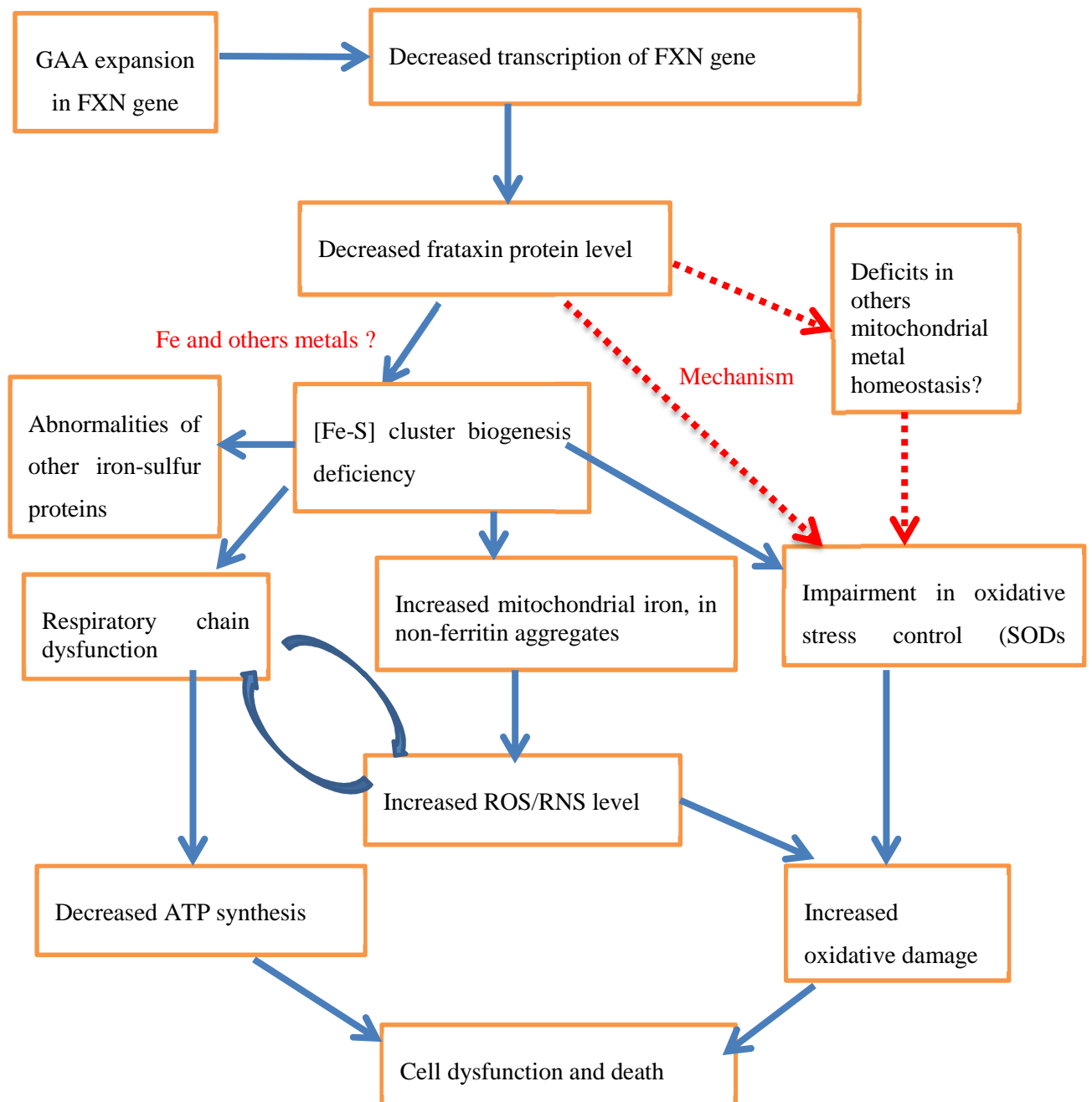
*Figure I.17: **The panorama of phenomena in FA.***

Figure I.17 summarizes the events which can occur in FA pathology. The expansion of (GAA) triplet in FXN gene induces the deficiency of frataxin in the mitochondria. The insufficient level of this protein leads to the abnormalities in [Fe-S] cluster biogenesis, which in turn impair the respiratory chain, induce the import of iron into the mitochondria and disturb the oxidative stress control. Recently, a time-resolved analysis demonstrated the order

of perturbation in murine FA model: the loss of ISC enzymes activity is the first event after inducing complete frataxin deficiency; this is followed by an elevated ROS production and then a late increase in iron content (Poburski et al. 2016). This result confirmed that the perturbation of [Fe-S] biogenesis is primary. Iron overload and oxidative stress are only secondary. However, oxidative stress can be observed without deficiency in iron-sulfur clusters (Tamarit et al. 2016). Indeed, in a yeast model, the authors have observed signs of oxidative stress long before iron-sulfur deficiency (Moreno-Cermeno et al. 2010). Different studies point out that oxidative stress is not secondary to the lack of ISC but can play a central role in FA.

The functions of frataxin are not known. Until recently, the most discussed assumption is the involvement in iron-sulfur cluster assembly and iron homeostasis. Few information is available for the role of frataxin in homeostasis of metals other than iron and about the mechanisms of frataxin's protection against the oxidative stress (red arrows).

In this work, we are interested in the involvement of frataxin in both metal metabolisms and oxidative stress. The results, which are presented in this thesis, are divided into three chapters.

For cell free studies, we dealt with yeast protein, Yfh1, as a model. Chapter I is devoted to the biosynthesis and characterization of yeast proteins we studied (frataxin and flavohemoglobin).

We then aimed to revisit the affinity and mechanism of frataxin – Fe binding. We investigated the interaction of frataxin with the physiological metals that play essential roles in the mitochondria, such as copper, zinc and manganese. The affinity of these metals for frataxin and the mechanism of their binding are described in Chapter III.

In Chapter IV, we characterize the molecular interaction of frataxin with the mitochondrial proteins involved in the antioxidant defense, such as superoxide dismutase in the intermembrane space CuZnSOD, that of the matrix MnSOD which scavenge the superoxide anion, and *Saccharomyces cerevisiae* flavohemoglobin, a protein which plays central roles in protection from nitrosative stress. Here, we, also, analyze how frataxin, in absence or presence of metal, may affect the enzymatic activity of these proteins.

REFERENCES

Abeti R, Uzun E, Renganathan I, Honda T, Pook MA, Giunti P. 2015. Targeting lipid peroxidation and mitochondrial imbalance in Friedreich's ataxia. Pharmacological Research 99: 344-350.

Abreu IA, Cabelli DE. 2010. Superoxide dismutases—a review of the metal-associated mechanistic variations. Biochimica et Biophysica Acta (BBA) - Proteins and Proteomics 1804: 263-274.

Acquaviva F, Castaldo I, Filla A, Giacchetti M, Marmolino D, Monticelli A, Pinelli M, Saccà F, Cocozza S. 2008. Recombinant Human Erythropoietin Increases Frataxin Protein Expression Without Increasing mRNA Expression. The Cerebellum 7: 360-365.

Adamec J, Rusnak F, Owen WG, Naylor S, Benson LM, Gacy AM, Isaya G. 2000. Iron dependent self-assembly of recombinant yeast frataxin-impliation for Friedreich's ataxia. Am. J. Hum. Genet. 67: 549-562.

Adinolfi S, Trifuoggi M, Politou AS, Martin S, Pastore A. 2002. A structural approach to understanding the iron-binding properties of phylogenetically different frataxins. Hum Mol Genet 11: 1865-1877.

Adinolfi S, Nair M, Politou A, Bayer E, Martin S, Temussi P, Pastore A. 2004. The factors governing the thermal stability of frataxin orthologues: how to increase a protein's stability. Biochemistry 43: 6511-6518.

Adinolfi S, Iannuzzi C, Prischi F, Pastore C, Iametti S, Martin SR, Bonomi F, Pastore A. 2009. Bacterial frataxin CyaY is the gatekeeper of iron-sulfur cluster formation catalyzed by IscS. Nat Struct Mol Biol 16: 390-396.

Al-Mahdawi S, et al. 2006. GAA repeat expansion mutation mouse models of Friedreich ataxia exhibit oxidative stress leading to progressive neuronal and cardiac pathology. Genomics 88: 580-590.

Aloria K, Schilke B, Andrew A, Craig EA. 2004. Iron-induced oligomerization of yeast frataxin homologue Yfh1 is dispensable in vivo. EMBO Rep 5: 1096-1101.

Anjomani Virmouni S, Al-Mahdawi S, Sandi C, Yasaei H, Giunti P, Slijepcevic P, Pook MA. 2015. Identification of telomere dysfunction in Friedreich ataxia. Mol Neurodegener 10: 22.

Anzovino A, Lane DJ, Huang J, Richardson DR. 2014. Fixing frataxin : 'ironing out' the metabolic defect in Friedreich's ataxia. British Journal of Pharmacology 171: 2174 - 2190.

Atkinson A, Winge DR. 2009. Metal acquisition and availability in the mitochondria. Chem. Rev. 109: 4708-4721.

Babcock M, Silva D, Oaks R, Davis-Kaplan S, Jiralerspong S, Montermini L, Pandolfo M, Kaplan J. 1997. Regulation of Mitochondrial Iron Accumulation by Yfh1p, a Putative Homolog of Frataxin. Science 276: 1709-1712.

Bencze KZ, Kondapalli KC, Cook JD, McMahon S, Millan-Pacheco C, Pastor N, Stemmler TL. 2006. The structure and function of frataxin. Crit Rev Biochem Mol Biol 41: 269-291.

Bencze KZ, Yoon T, Millan-Pacheco C, Bradley PB, Pastor N, Cowan JA, Stemmler TL. 2007. Human frataxin: iron and ferrochelatase binding surface. Chem Commun (Camb): 1798-1800.

Boddaert N, Le Quan Sang KH, Rötig A, Leroy-Willig A, Gallet S, Brunelle F, Sidi D, Thalabard J-C, Munnich A, Cabantchik ZI. 2007. Selective iron chelation in Friedreich ataxia: biologic and clinical implications. Blood 110: 401-408.

Bou-Abdallah F, Adinolfi S, Pastore A, Laue TM, Dennis Chasteen N. 2004. Iron binding and oxidation kinetics in frataxin CyaY of Escherichia coli. J Mol Biol 341: 605-615.

Bradley SA, Steinert JR. 2016. Nitric Oxide-Mediated Posttranslational Modifications: Impacts at the Synapse. Oxid Med Cell Longev 2016: 5681036.

Brazzolotto X, Gaillard J, Pantopoulos K, Hentze M, Moulis J. 1999. Human Cytoplasmic Aconitase (Iron Regulatory Protein 1) Is Converted into Its [3Fe-4S] Form by Hydrogen Peroxide in Vitro but Is Not Activated for Iron-responsive Element Binding. J Biol Chem 274(31): 21625-21630.

Bridwell-Rabb J, Winn AM, Barondeau DP. 2011. Structure-function analysis of Friedreich's ataxia mutants reveals determinants of frataxin binding and activation of the Fe-S assembly complex. Biochemistry 50: 7265-7274.

Bridwell-Rabb J, Fox NG, Tsai CL, Winn AM, Barondeau DP. 2014. Human frataxin activates Fe-S cluster biosynthesis by facilitating sulfur transfer chemistry. Biochemistry 53: 4904-4913.

Bulteau AL, O'Neill HA, Kennedy MC, Ikeda-Saito M, Isaya G, Szweda LI. 2004. Frataxin acts as an iron chaperone protein to modulate mitochondrial aconitase activity. Science 305: 242-245.

Bulteau AL, Dancis A, Gareil M, Montagne JJ, Camadro JM, Lesuisse E. 2007. Oxidative stress and protease dysfunction in the yeast model of Friedreich ataxia. Free Radic Biol Med 42: 1561-1570.

Bulteau AL, Planamente S, Jornea L, Dur A, Lesuisse E, Camadro JM, Auchere F. 2012. Changes in mitochondrial glutathione levels and protein thiol oxidation in yfh1 yeast cells and the lymphoblasts of patients with Friedreich's ataxia. Biochim Biophys Acta 1822: 212-225.

Calabrese V, Lodi R, Tonon C, D'Agata V, Sapienza M, Scapagnini G, Mangiameli A, Pennisi G, Stella AM, Butterfield DA. 2005. Oxidative stress, mitochondrial dysfunction and cellular stress response in Friedreich's ataxia. J Neurol Sci 233: 145-162.

Campuzano V, et al. 1996. Friedreich's Ataxia : Autosomal recessive disease caused by an intronic GAA triplet repeat expansion. Science 271: 1423 -1427.

Carletti B, et al. 2014. Frataxin silencing inactivates mitochondrial Complex I in NSC34 motoneuronal cells and alters glutathione homeostasis. Int J Mol Sci 15: 5789-5806.

Castro L, Demicheli V, Tórtora V, Radi R. 2011. Mitochondrial protein tyrosine nitration. Free Radical Research 45: 37-52.

Chen OS, Hemenway S, Kaplan J. 2002. Genetic analysis of iron citrate toxicity in yeast: Implications for mammalian iron homeostasis. PNAS 99: 16922-16927.

Colin F, Martelli A, Clemancey M, Latour JM, Gambarelli S, Zeppieri L, Birck C, Page A, Puccio H, Ollagnier de Choudens S. 2013. Mammalian frataxin controls sulfur production and iron entry during de novo Fe4S4 cluster assembly. J Am Chem Soc 135: 733-740.

Condo I, Ventura N, Malisan F, Tomassini B, Testi R. 2006. A pool of extramitochondrial frataxin that promotes cell survival. J Biol Chem 281: 16750-16756.

Condo I, Malisan F, Guccini I, Serio D, Rufini A, Testi R. 2010. Molecular control of the cytosolic aconitase/IRP1 switch by extramitochondrial frataxin. Hum Mol Genet 19: 1221-1229.

Cook JD, Kondapalli KC, Rawat S, Childs WC, Murugesan Y, Dancis A, Stemmler TL. 2010. Molecular details of the yeast frataxin-Isu1 interaction during mitochondrial Fe-S cluster assembly. Biochemistry 49: 8756-8765.

Cook JD, Bencze KZ, Jankovic AD, Crater AK, Courtney N. Busch, Bradley PB, Ann J. Stemmler, Mark R. Spaller, Stemmler* TL. 2006. Monomeric Yeast Frataxin Is an Iron-Binding Protein†. Biochem J 45: 7767-7777.

Copin J-C, Gasche Y, Chan PH. 2000. Overexpression of copper/zinc superoxide dismutase does not prevent neonatal lethality in mutant mice that lack manganese superoxide dismutase. Free Radical Biology and Medicine 28: 1571-1576.

Correia AR, Wang T, Craig EA, Gomes CM. 2010. Iron-binding activity in yeast frataxin entails a trade off with stability in the alpha1/beta1 acidic ridge region. Biochem J 426: 197-203.

Cossée M, Puccio H, Gansmuller A, Koutnikova H, Dierich A, LeMeur M, Fischbeck K, Dollé P, Koenig M. 2000. Inactivation of the Friedreich ataxia mouse gene leads to early embryonic lethality without iron accumulation. Hum Mol Genet 9: 1219-1226.

Cossée M, et al. 1999. Friedreich's ataxia: point mutations and clinical presentation of compound heterozygotes. Ann Neurol. 45: 200-206.

Culotta VC, Yang M, O'Halloran TV. 2006. Activation of superoxide dismutases: putting the metal to the pedal. Biochim Biophys Acta 1763: 747-758.

Dhe-Paganon S, Shigeta R, Chi YI, Ristow M, Shoelson SE. 2000. Crystal structure of human frataxin. J Biol Chem 275: 30753-30756.

Evans-Galea MV, Pebay A, Dottori M, Corben LA, Ong SH, Lockhart PJ, Delatycki MB. 2014. Cell and gene therapy for Friedreich ataxia: progress to date. Hum Gene Ther 25: 684-693.

Fang FC. 2004. Antimicrobial reactive oxygen and nitrogen species: concepts and controversies. Nat Rev Micro 2: 820-832.

Foury F. 1999. Low iron concentration and aconitase deficiency in a yeast frataxin homolog deficient strain. FEBS Letters 456: 281-284.

Foury F, Cazzalini O. 1997. Deletion of yfh1 of human genne associated with FRDA elicits iron accumulation in mitochondria. FEBS Letters 411: 373-377.

Foury F, Pastore A, Trincal M. 2007. Acidic residues of yeast frataxin have an essential role in Fe-S cluster assembly. EMBO Rep 8: 194-199.

Galea CA, et al. 2016. Compound heterozygous FXN mutations and clinical outcome in friedreich ataxia. Ann Neurol 79: 485-495.

Gardner PR. 1997. Superoxide-Driven Aconitase FE-S Center Cycling. Bioscience Reports 17: 33-42.

Gellera C, Castellotti B, Mariotti C, Mineri R, Seveso V, DiDonato S, Taroni F. 2007. Frataxin gene point mutations in Italian Friedreich ataxia patients. Neurogenetics 8: 289-299.

Gerber J, Muhlenhoff U, Lill R. 2003. An interaction between frataxin and Isu1/Nfs1 that is crucial for Fe/S cluster synthesis on Isu1. EMBO Rep 4: 906-911.

Gonzalez-Cabo P, Palau F. 2013. Mitochondrial pathophysiology in Friedreich's ataxia. J Neurochem 126 Suppl 1: 53-64.

Gonzalez-Cabo P, Vazquez-Manrique RP, Garcia-Gimeno MA, Sanz P, Palau F. 2005. Frataxin interacts functionally with mitochondrial electron transport chain proteins. Hum Mol Genet 14: 2091-2098.

Gottesfeld JM. 2007. Small molecules affecting transcription in Friedreich ataxia. Pharmacology & Therapeutics 116: 236-248.

Handy DE, Loscalzo J. 2012. Redox Regulation of Mitochondrial Function. Antioxidants & Redox Signaling 16: 1323-1367.

Haugen AC, et al. 2010. Altered gene expression and DNA damage in peripheral blood cells from Friedreich's ataxia patients: cellular model of pathology. PLoS Genet 6: e1000812.

Hayashi G, Cortopassi G. 2015. Oxidative stress in inherited mitochondrial diseases. Free Radic Biol Med 88: 10-17.

He Y, Alam SL, S.V. P, Zhang Y, Lesuisse E, Dancis A, Stemmler TL. 2004. Yeast Frataxin Solution Structure, Iron Binding, and Ferrochelatase Interaction. Biochemistry 43: 16254-16262.

Herrero E, Ros J, Belli G, Cabiscol E. 2008. Redox control and oxidative stress in yeast cells. Biochim Biophys Acta 1780: 1217-1235.

Huang ML, Beckera EB, Whitnall M, Rahmanto YS, Ponka P, Richardson DR. 2009. Elucidation of the mechanism of mitochondrial iron loading in Friedreich's ataxia by analysis of a mouse mutant. Pnas 106: 16381-16386.

Huynen MA, Snel B, Bork P, Gibson TJ. 2001. The phylogenetic distribution of frataxin indicates a role in iron-sulfur cluster protein assembly. 10 21: 2463-2468.

Indo HP, et al. 2015. A mitochondrial superoxide theory for oxidative stress diseases and aging. Journal of Clinical Biochemistry and Nutrition 56: 1-7.

Irazusta V, Obis E, Moreno-Cermeno A, Cabiscol E, Ros J, Tamarit J. 2010. Yeast frataxin mutants display decreased superoxide dismutase activity crucial to promote protein oxidative damage. Free Radic Biol Med 48: 411-420.

Karthikeyan G, Santos JH, Graziewicz MA, Copeland WC, Isaya G, Van Houten B, Resnick MA. 2003. Reduction in frataxin causes progressive accumulation of mitochondrial damage. Hum Mol Genet 12: 3331-3342.

Kim MJ, et al. 2012. Tat-Frataxin protects dopaminergic neuronal cells against MPTP-induced toxicity in a mouse model of Parkinson's disease. Biochimie 94: 2448-2456.

Knowles RG, Moncada S. 1994. Nitric oxide synthases in mammals. Biochemical Journal 298: 249-258.

Koeppen AH. 2011. Friedreich's ataxia: pathology, pathogenesis, and molecular genetics. J Neurol Sci 303: 1-12.

Koeppen AH, Mazurkiewicz JE. 2013. Friedreich Ataxia: Neurophatology revised. J Neuropathol Exp Neurol 72: 78-90.

Koeppen AH, Kuntzsch EC, Bjork ST, Ramirez RL, Mazurkiewicz JE, Feustel aPJ. 2013. Friedreich ataxia: metal dysmetabolism in dorsal root ganglia. Acta Neuropathologica Communications 1:26.

Koeppen AH, Michael SC, Knutson MD, Haile DJ, Qian J, Levi S, Santambrogio P, Garrick MD, Lamarche JB. 2007. The dentate nucleus in Friedreich's ataxia: the role of iron-responsive proteins. Acta Neuropathol 114: 163-173.

Koeppen AH, Morral JA, Davis AN, Qian J, Petrocine SV, Knutson MD, Gibson WM, Cusack MJ, Li D. 2009. The dorsal root ganglion in Friedreich's ataxia. Acta Neuropathol 118: 763-776.

Koeppen AH, Ramirez RL, Yu D, Collins SE, Qian J, Parsons PJ, Yang KX, Chen Z, Mazurkiewicz JE, Feustel PJ. 2012. Friedreich's ataxia causes redistribution of iron, copper, and zinc in the dentate nucleus. Cerebellum 11: 845-860.

Kondapalli KC, Kok NM, Dancis A, Stemmler TL. 2008. Drosophila Frataxin: An Iron Chaperone during Cellular Fe–S Cluster Bioassembly. Biochemistry 47: 6917-6927.

Lamarche J, Côté M, Lemieux B. 1980. The cardiomyopathy of Friedreich's ataxia morphological observations in 3 cases. Can J Neurol Sci. 7: 389-396.

Layer G, Ollagnier-de Choudens S, Sanakis Y, Fontecave M. 2006. Iron-sulfur cluster biosynthesis: characterization of Escherichia coli CYaY as an iron donor for the assembly of [2Fe-2S] clusters in the scaffold IscU. J Biol Chem 281: 16256-16263.

Lefevre S, Sliwa D, Rustin P, Camadro JM, Santos R. 2012. Oxidative stress induces mitochondrial fragmentation in frataxin-deficient cells. Biochem Biophys Res Commun 418: 336-341.

Leidgens S, De Smet S, Foury F. 2010. Frataxin interacts with Isu1 through a conserved tryptophan in its beta-sheet. Hum Mol Genet 19: 276-286.

Lesuisse E, Santos R, Matzanke BF, Knight SA, Camadro JM, Dancis A. 2003. Iron use for haeme synthesis is under control of the yeast frataxin homologue (Yfh1). Human Molecular Genetics 12: 879-889.

Levi S, Corsi B, Bosisio M, Invernizzi R, Volz A, Sanford D, Arosio P, Drysdale J. 2001. A human mitochondrial ferritin encoded by an intronless gene. J Biol Chem 276: 24437-24440.

Li DS, Ohshima K, Jiralerspong S, Bojanowski MW, Pandolfo M. 1999. Knock-out of the cyaY gene in Escherichia coli does not affect cellular iron content and sensitivity to oxidants. FEBS Letters 456: 13-16.

Li H, Gakh O, Smith DYt, Isaya G. 2009. Oligomeric yeast frataxin drives assembly of core machinery for mitochondrial iron-sulfur cluster synthesis. J Biol Chem 284: 21971-21980.

Li Y, et al. 1995. Dilated cardiomyopathy and neonatal lethality in mutant mice lacking manganese superoxide dismutase. Nat Genet 11: 376-381.

Lill R, et al. 2015. The role of mitochondria and the CIA machinery in the maturation of cytosolic and nuclear iron-sulfur proteins. Eur J Cell Biol 94: 280-291.

Lushchak VI. 2014. Free radicals, reactive oxygen species, oxidative stress and its classification. Chemico-Biological Interactions 224: 164-175.

Lutz T, Westermann B, Neupert W, Herrmann JM. 2001. The mitochondrial proteins Ssq1 and Jac1 are required for the assembly of iron sulfur clusters in mitochondria1. Journal of Molecular Biology 307: 815-825.

Maio N, Rouault TA. 2015. Iron-sulfur cluster biogenesis in mammalian cells: New insights into the molecular mechanisms of cluster delivery. Biochim Biophys Acta 1853: 1493-1512.

Manicki M, Majewska J, Ciesielski S, Schilke B, Blenska A, Kominek J, Marszalek J, Craig EA, Dutkiewicz R. 2014. Overlapping binding sites of the frataxin homologue assembly factor and the heat shock protein 70 transfer factor on the Isu iron-sulfur cluster scaffold protein. J Biol Chem 289: 30268-30278.

Marmolino D. 2011. Friedreich's ataxia: past, present and future. Brain Res Rev 67: 311-330.

Martelli A, Puccio H. 2014. Dysregulation of cellular iron metabolism in Friedreich ataxia: from primary iron-sulfur cluster deficit to mitochondrial iron accumulation. Front Pharmacol 5: 130.

McCormick SP, Moore MJ, Lindahl PA. 2015. Detection of Labile Low-Molecular-Mass Transition Metal Complexes in Mitochondria. Biochemistry 54: 3442-3453.

Meier T, Buyse G. 2009. Idebenone: An emerging therapy for Friedreich ataxia. Journal of Neurology 256: 25-30.

Michael Costanzo, 2* Anastasia Baryshnikova,1,2* Jeremy Bellay,3 Yungil Kim,3 Eric D. Spear,4, et al. 2010. The genetic lanscape of a cell. Science 327.

Moreno-Cermeno A, Obis E, Belli G, Cabiscol E, Ros J, Tamarit J. 2010. Frataxin depletion in yeast triggers up-regulation of iron transport systems before affecting iron-sulfur enzyme activities. J Biol Chem 285: 41653-41664.

Nachbauer W, Boesch S, Reindl M, Eigentler A, Hufler K, Poewe W, Loscher W, Wanschitz J. 2012. Skeletal Muscle Involvement in Friedreich Ataxia and Potential Effects of Recombinant Human Erythropoietin Administration on Muscle Regeneration and Neovascularization. J Neuropathol Exp Neurol 71: 708-715.

Nair M, Adinolfi S, Pastore C, Kelly G, Temussi P, Pastore A. 2004. Solution structure of the bacterial frataxin ortholog, CyaY: mapping the iron binding sites. Structure 12: 2037-2048.

Napoli E, Taroni F, Cortopassi GA. 2006. Frataxin, Iron–Sulfur Clusters, Heme, ROS, and Aging. Antioxid Rdeox Signal 8: 506-516.

Orengo CA, Thornton JM. 1993. Alpha plus beta folds revisited: some favoured motifs. Structure 1: 105-120.

Pandey A, Golla R, Yoon H, Dancis A, Pain D. 2012. Persulfide formation on mitochondrial cysteine desulfurase: enzyme activation by a eukaryote-specific interacting protein and Fe-S cluster synthesis. Biochem J 448: 171-187.

Pandey A, Gordon DM, Pain J, Stemmler TL, Dancis A, Pain D. 2013. Frataxin directly stimulates mitochondrial cysteine desulfurase by exposing substrate-binding sites, and a mutant Fe-S cluster scaffold protein with frataxin-bypassing ability acts similarly. J Biol Chem 288: 36773-36786.

Pandolfo M, Pastore A. 2009. The pathogenesis of Friedreich ataxia and the structure and function of frataxin. J Neurol 256 Suppl 1: 9-17.

Pandolfo M, Hausmann L. 2013. Deferiprone for the treatment of Friedreich's ataxia. J Neurochem 126 Suppl 1: 142-146.

Parent A, Elduque X, Cornu D, Belot L, Le Caer JP, Grandas A, Toledano MB, D'Autreaux B. 2015. Mammalian frataxin directly enhances sulfur transfer of NFS1 persulfide to both ISCU and free thiols. Nat Commun 6: 5686.

Park S, Gakh O, Mooney SM, Isaya G. 2002. The ferroxidase activity of yeast frataxin. J Biol Chem 277: 38589-38595.

Parkinson MH, Schulz JB, Giunti P. 2013. Co-enzyme Q10 and idebenone use in Friedreich's ataxia. J Neurochem 126 Suppl 1: 125-141.

Pastore A, Martin SR, Politou A, Kondapalli KC, Stemmler T, Temussi PA. 2007a. Unbiased cold denaturation: low- and high-temperature unfolding of yeast frataxin under physiological conditions. J Am Chem Soc 129: 5374-5375.

Pastore A, et al. 2003. Actin glutathionylation increases in fibroblasts of patients with Friedreich's ataxia: a potential role in the pathogenesis of the disease. J Biol Chem 278: 42588-42595.

Pastore C, Franzese M, Sica F, Temussi P, Pastore A. 2007b. Understanding the binding properties of an unusual metal-binding protein--a study of bacterial frataxin. FEBS J 274: 4199-4210.

Piemonte F, Pastore A, Tozzi G, Tagliacozzi D, Santorelli FC, R., Casali C, Damiano M, Federici G, Bertini E. 2001. Glutathione in blood of patients with FRDA. Eur J Clin Invest 31: 1007-1011.

Poburski D, Boerner JB, Koenig M, Ristow M, Thierbach R. 2016. Time-resolved functional analysis of acute impairment of frataxin expression in an inducible cell model of Friedreich ataxia. Biol Open 5: 654-661.

Ponka P. 1997. Tissue-Specific Regulation of Iron Metabolism and Heme Synthesis: Distinct Control Mechanisms in Erythroid Cells. Blood 89: 1-25.

Popovic M, Sanfelice D, Pastore C, Prischi F, Temussi PA, Pastore A. 2015. Selective observation of the disordered import signal of a globular protein by in-cell NMR: the example of frataxins. Protein Sci 24: 996-1003.

Puccio H, Simon D, Cossee M, Criqui-Filipe P, Tiziano F, Melki J, Hindelang C, Matyas R, Rustin P, Koenig M. 2001. Mouse models for Friedreich ataxia exhibit cardiomyopathy, sensory nerve defect and Fe-S enzyme deficiency followed by intramitochondrial iron deposits. Nat Genet 27: 181-186.

Radisky DC, Babcock MC, Kaplan J. 1999. The Yeast Frataxin Homologue Mediates Mitochondrial Iron Efflux: evidence for a mitochondral iron cycle Journal of Biological Chemistry 274: 4497-4499.

Ramazzotti A, Vanmansart V, Foury F. 2004. Mitochondrial functional interactions between frataxin and Isu1p, the iron–sulfur cluster scaffold protein, in Saccharomyces cerevisiae. FEBS Letters 557: 215-220.

Ranatunga W, Gakh O, Galeano BK, Smith DYt, Soderberg CA, Al-Karadaghi S, Thompson JR, Isaya G. 2016. Architecture of the Yeast Mitochondrial Iron-Sulfur Cluster Assembly Machinery: The Sub-Complex Formed by the Iron Donor, Yfh1, and the Scaffold, Isu1. J Biol Chem.

Richardson DR, Lane DJR, Becker EM, Huang ML-H, Whitnall M, Rahmanto YS, Sheftel AD, Ponka P. 2010. Mitochondrial iron trafficking and the integration of iron metabolism between the mitochondrion and cytosol. Proceedings of the National Academy of Sciences 107: 10775-10782.

Richardson TE, Kelly HN, Yu AE, Simpkins JW. 2013. Therapeutic strategies in Friedreich's Ataxia. Brain Research 1514: 91-97.

Ristow M, et al. 2003. Frataxin deficiency in pancreatic islets causes diabetes due to loss of β cell mass. J Clin Invest. 112: 527-534.

Rotig A, de Lonlay P, Chretien D, Foury F, Koenig M, Sidi D, Munnich A, Rustin P. 1997. Aconitase and mitochondrial iron-sulphur protein deficiency in Friedreich ataxia. Nat Genet 17: 215-217.

Runko AP, Griswold AJ, Min KT. 2008. Overexpression of frataxin in the mitochondria increases resistance to oxidative stress and extends lifespan in Drosophila. FEBS Lett 582: 715-719.

Rustin P, von Kleist-Retzow J-C, Chantrel-Groussard K, Sidi D, Munnich A, Rötig A. 1999. Effect of idebenone on cardiomyopathy in Friedreich's ataxia: a preliminary study. The Lancet 354: 477-479.

Sanfelice D, Puglisi R, Martin SR, Di Bari L, Pastore A, Temussi PA. 2014. Yeast frataxin is stabilized by low salt concentrations: cold denaturation disentangles ionic strength effects from specific interactions. PLoS One 9: e95801.

Santos R, Lefevre S, Sliwa D, Seguin A, Camadro JM, Lesuisse E. 2010. Friedreich Ataxia: Molecular Mechanisms, Redox Considerations, and Therapeutic Opportunities. Antioxid Redox Signal 13: 43.

Schmucker S, Martelli A, Colin F, Page A, Wattenhofer-Donze M, Reutenauer L, Puccio H. 2011. Mammalian frataxin: an essential function for cellular viability through an interaction with a preformed ISCU/NFS1/ISD11 iron-sulfur assembly complex. PLoS One 6: e16199.

Schulz JB, et al. 2000. Oxidative stress in patients with Friedreich ataxia. Neurology 55: 1719-1721.

Seguin A, Santos R, Pain D, Dancis A, Camadro JM, Lesuisse E. 2011. Co-precipitation of phosphate and iron limits mitochondrial phosphate availability in Saccharomyces cerevisiae lacking the yeast frataxin homologue (YFH1). J Biol Chem 286: 6071-6079.

Seguin A, Bayot A, Dancis A, Rogowska-Wrzesinska A, Auchere F, Camadro JM, Bulteau AL, Lesuisse E. 2009. Overexpression of the yeast frataxin homolog (Yfh1): contrasting effects on iron-sulfur cluster assembly, heme synthesis and resistance to oxidative stress. Mitochondrion 9: 130-138.

Seguin A, et al. 2010. Evidence that yeast frataxin is not an iron storage protein in vivo. Biochim Biophys Acta 1802: 531-538.

Seznec H, et al. 2005. Friedreich ataxia: the oxidative stress paradox. Hum Mol Genet 14: 463-474.

Shan Y, Napoli E, Cortopassi G. 2007. Mitochondrial frataxin interacts with ISD11 of the NFS1/ISCU complex and multiple mitochondrial chaperones. Hum Mol Genet 16: 929-941.

Shan Y, Schoenfeld RA, Hayashi G, Napoli E, Akiyama T, Iodi Carstens M, Carstens EE, Pook MA, Cortopassi GA. 2013. Frataxin deficiency leads to defects in expression of antioxidants and Nrf2 expression in dorsal root ganglia of the Friedreich's ataxia YG8R mouse model. Antioxid Redox Signal 19: 1481-1493.

Shoichet SA, Bäumer A, Stamenkovic D, Sauer H, Pfeiffer A, Kahn C, Müller-Wieland D, Richter C, Ristow M. 2002. Frataxin promotes antioxidant defense in a thiol-dependent manner resulting in diminished malignant transformation in vitro. Hum Mol Genet 11: 815-821.

Sparaco M, et al. 2009. Friedreich's ataxia: oxidative stress and cytoskeletal abnormalities. J Neurol Sci 287: 111-118.

Stadtman RE, Levine LR. 2003. Free radical-mediated oxidation of free amino acids and amino acid residues in proteins. Amino Acids 25: 207-218.

Stehling O, Wilbrecht C, Lill R. 2014. Mitochondrial iron-sulfur protein biogenesis and human disease. Biochimie 100: 61-77.

Stehling O, Elsasser HP, Bruckel B, Muhlenhoff U, Lill R. 2004. Iron-sulfur protein maturation in human cells: evidence for a function of frataxin. Hum Mol Genet 13: 3007-3015.

Sturm B, Stupphann D, Kaun C, Boesch S, Schranzhofer M, Wojta J, Goldenberg H, Scheiber-Mojdehkar B. 2005. Recombinant human erythropoietin: effects on frataxin expression in vitro. Eur J Clin Invest 35: 711-717.

Tamarit J, Obis È, Ros J. 2016. Oxidative stress and altered lipid metabolism in Friedreich ataxia. Free Radical Biology and Medicine.

Thierbach R, et al. 2005. Targeted disruption of hepatic frataxin expression causes impaired mitochondrial function, decreased life span and tumor growth in mice. Hum Mol Genet 14: 3857-3864.

Topal G, Brunet A, Walch L, Boucher JL, David-Dufilho M. 2006. Mitochondrial arginase II modulates nitric-oxide synthesis through nonfreely exchangeable L-arginine pools in human endothelial cells. J Pharmacol Exp Ther 318: 1368-1374.

Tsai CL, Barondeau DP. 2010. Human frataxin is an allosteric switch that activates the Fe-S cluster biosynthetic complex. Biochemistry 49: 9132-9139.

Vázquez-Manrique RP, González-Cabo P, Ros S, Aziz H, Baylis HA, Palau F. 2005. Reduction of Caenorhabditis elegans frataxin increases sensitivity to oxidative stress, reduces lifespan, and causes lethality in a mitochondrial complex II mutant. FASEB 20: 172-174.

Vest KE, Leary SC, Winge DR, Cobine PA. 2013. Copper import into the mitochondrial matrix in Saccharomyces cerevisiae is mediated by Pic2, a mitochondrial carrier family protein. J Biol Chem 288: 23884-23892.

Vest KE, Wang J, Gammon MG, Maynard MK, White OL, Cobine JA, Mahone WK, Cobine PA. 2016. Overlap of copper and iron uptake systems in mitochondria in Saccharomyces cerevisiae. Open Biol 6: 150223.

Vilanova B, Sanfelice D, Martorell G, Temussi PA, Pastore A. 2014. Trapping a salt-dependent unfolding intermediate of the marginally stable protein Yfh1. Frontiers in Molecular Biosciences 1.

Vilella F, Alves R, Rodriguez-Manzaneque MT, Belli G, Swaminathan S, Sunnerhagen P, Herrero E. 2004. Evolution and cellular function of monothiol glutaredoxins: involvement in iron-sulphur cluster assembly. Comp Funct Genomics 5: 328-341.

Wang T, Craig EA. 2008. Binding of yeast frataxin to the scaffold for Fe-S cluster biogenesis, Isu. J Biol Chem 283: 12674-12679.

Weidemann F, Stork S, Liu D, Hu K, Herrmann S, Ertl G, Niemann M. 2013. Cardiomyopathy of Friedreich ataxia. J Neurochem 126 Suppl 1: 88-93.

Whitnall M, Suryo Rahmanto Y, Sutak R, Xu X, Becker EM, Mikhael MR, Ponka P, Richardson DR. 2008. The MCK mouse heart model of Friedreich's ataxia: Alterations in iron-regulated proteins and cardiac hypertrophy are limited by iron chelation. Proc Natl Acad Sci U S A 105: 9757-9762.

Whitnall M, et al. 2012. Identification of nonferritin mitochondrial iron deposits in a mouse model of Friedreich ataxia. PNAS 109: 20590-20595.

Wong A, Yang J, Cavadini P, Gellera C, Lonnerdal B, Taroni F, Cortopassi G. 1999. The Friedreich's ataxia mutation confers cellular sensitivity to oxidant stress which is rescued by chelators of iron and calcium and inhibitors of apoptosis. Hum Mol Genet 8: 425-430.

Yoon H, Knight SA, Pandey A, Pain J, Zhang Y, Pain D, Dancis A. 2014. Frataxin-bypassing Isu1: characterization of the bypass activity in cells and mitochondria. Biochem J 459: 71-81.

Yoon H, Golla R, Lesuisse E, Pain J, Donald JE, Lyver ER, Pain D, Dancis A. 2012. Mutation in the Fe-S scaffold protein Isu bypasses frataxin deletion. Biochem J 441: 473-480.

Yoon T, Cowan JA. 2003. Iron-Sulfur Cluster Biosynthesis. Characterization of Frataxin as an Iron Donor for Assembly of [2Fe-2S] Clusters in ISU-Type Proteins. J. Am. Chem. Soc 125: 6078-6084.

—. 2004. Frataxin-mediated iron delivery to ferrochelatase in the final step of heme biosynthesis. J Biol Chem 279: 25943-25946.

Zhang Y, Lyver ER, Knight SA, Lesuisse E, Dancis A. 2005. Frataxin and mitochondrial carrier proteins, Mrs3p and Mrs4p, cooperate in providing iron for heme synthesis. J Biol Chem 280: 19794-19807.

CHAPTER II: PROTEIN PRODUCTION AND PURIFICATION

In order to investigate the involvement of frataxin in the metabolism of transition metals in mitochondria as well as in the defense against oxidative stress and nitrosative stress, we first synthesized and purified *S. cerevisiae* frataxin homologue (Yfh1) and *S. cerevisiae* flavohemoglobin (Yhb1), a protein which belongs to the hemoglobin family and plays key roles in the protection from nitrosative stress. We also determined the influence of Yfh1 on superoxide dismutases activities, these proteins are the gatekeepers of the defense against oxidative stress. The two superoxide dismutases have been used in their commercial form.

1. Yeast frataxin homologue 1 – Yfh1

1.1. Expression

In our study, the production of the protein was based on a pSBET vector, which contains downstream the coding sequence a T7 promoter. In case of yeast frataxin homolog (Yfh1), the plasmid pSBET-YFH1 is cloned into BL21(DE3) *E. coli* strain, which is compatible with the T7*lac* promoter system and deficient in the *lon* protease and *ompT* outer membrane protease (which can degrade proteins during purification). Indeed, the chromosome of this strain integrated a λDE3 lysogen which harbors a copy of the gene encoding the T7 RNA polymerase under the control of a *lac* promoter. The expression of the target protein by pSBET system is therefore controlled by the synthesis of the T7 RNA polymerase. Under repressive conditions (glucose containing media), T7 RNA polymerase is not produced, and transcription of the target gene is negligible. After induction of the *lac* regulon by isopropyl-β-D-thiogalactopyranoside (IPTG) or lactose, the T7 RNA polymerase is produced, and most of the cellular protein synthesis machinery becomes devoted for the target protein (Figure II.1).
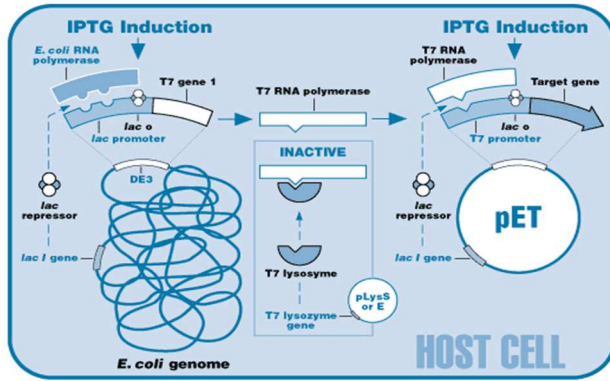
*Figure II.1: **Mechanism of protein production induced by IPTG in BL21(DE3) host strain by a T7lac vector.***

Using T7 systems, protein expression can be induced either with the chemical inducer IPTG or by modifying the carbon sources during *E. coli* growth (auto-induction medium). The advantage of using auto-induction medium is not only avoiding a step of manually adding chemical inducer, but also getting higher cells density and yields of target protein. In our study, the induction has been done in LBE5052 medium where glycerol 0.5 %, glucose 0.05 % and lactose 0.2 % have been used as sources of carbon (Studier 2005). The cells initiate growth by using glucose first. Then they use glycerol as a source of carbon, allowing efficient production of biomass. They finally use lactose, which is the physiological inducer of the *lac* operon. This allows (i) to relieve glucose repression on the *lac* promoter and (ii) to induce the expression of the gene cloned under the T7 promoter. The growth in LBE5052 allows higher culture densities and so on more target protein than in absent of lactose or LB medium (Figure II.2).
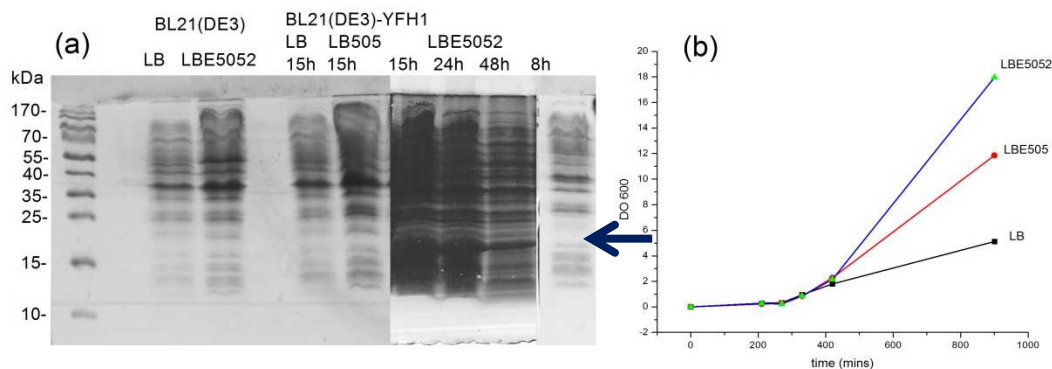

*Figure II.2: **Protein expression** (a) Crude extract from wild type or containing plasmid corresponding to BL21(DE3) or BL21(DE3)-YFH1. The intense protein band (shown by the blue arrow) migrates as a 15 kDa protein presented in auto-induction LBE5052 medium but not in LB505 and LB medium in the same incubation condition. (b) Growth under auto-induction medium LBE5052 give higher cells density than the others: LBE505 and LB.*

After 15 h of incubation at 37 °C under agitation at 200 rpm, cells were harvested by centrifugating at 4000 rpm for 15 min, and washed one time by milliQ water. The cell pellet was then disrupted physically by a French press "One-shot" system. Lysis buffer contains benzonase to avoid DNA contaminant. After being disrupted under a pressure of 7-8 kBar, cell lysate was mixed 1:1 (v/v) with the HEPES 50 mM, urea 6 M pH 7.0 buffer and kept at room temperature for 15 min. This mixture was centrifuged at 4000 rpm for 15 min at 4 °C to eliminate insoluble proteins. On 1D SDS PAGE, the supernatant from recombinant strain showed an intense protein band migrated as a 15 kDa protein, in contrary to the proteomic extract from wild type. This band corresponds probably to the target protein, Yfh1, which has molecular masse of 13800 Da.

1.2. Purification

After the centrifugation to eliminate the insoluble proteins, the supernatant was loaded onto an anion-exchange column of DEAE Sepharose Fast-flow (Sigma Aldrich). The target protein Yfh1 has theoretical pI value of 4.13. Hence, the DEAE column was previously equilibrated with buffer HEPES 50 mM pH 7.0, proteins were eluted by a linear gradient of NaCl from 0.1 M to 1 M. The fraction eluting at 0.4 M NaCl contained an intense protein band that migrated at 15 kDa and this band was visualized in Western blot analysis using anti-frataxin antibody (Figure II. 3a & 3b). However, these fractions contained nevertheless impurity, as shown in the gel SDS PAGE or Western blot. They were then sent to the next step of purification.
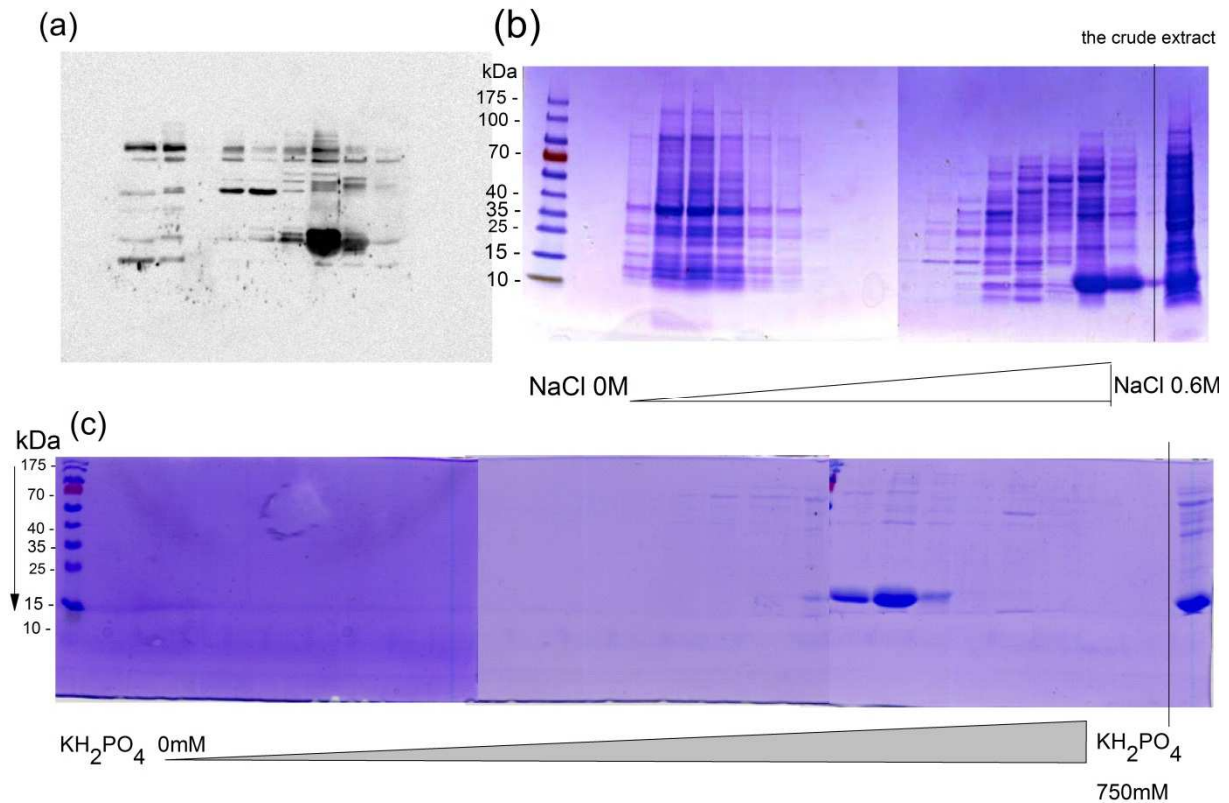
*Figure II.3: **Protein purification** (a) Western blot analysis of fractions eluting from DEAE column; (b) Electrophoresis gel colored by blue comassie 5% of the fractions eluting from DEAE anion-exchange chromatography column where Yfh1 was eluted at about 0.4 M of NaCl; (c) Electrophoresis gel of the fractions eluting from HAP chromatography where Yfh1 was eluted mainly at 350 mM of KH_2PO_4.*

These fractions were then pooled and submitted to the second step of anion exchange chromatography by a hydroxyapatite (HAP) column, which was previously equilibrated by HEPES 25 mM, pH 7.0 buffer. The elution was performed by a gradient of potassium phosphate from 50 mM to 750 mM. The fractions containing Yfh1 were found at 350 mM of KH_2PO_4 (Figure II.3c).

The fractions containing Yfh1 were pooled and concentrated, then injected into a column of size exclusion chromatography (Superdex^{TM}200 10/300 GL - GE Healthcare Lifescience). Proteins are eluted by HEPES 50 mM pH 7.0 buffer. Three peaks were detected: (i) the first elutes at 8.2 mL and contains impurity components (corresponding to the lanes 1D3 and 2D3 in SDS PAGE gel) (Figure II.4); (ii) the second is the highest and elutes at 14.7 mL. When being analyzed in gel SDS PAGE, the main component of these fractions migrates as a 15 kDa protein (see the 1F11 and 2F11 lanes in the SDS PAGE gel), which may correspond to the protein of interest; (iii) the third peak elutes before the major peak (12.7 mL), and

should probably contains oligomer forms of Yfh1 (blots 1F1 and 2E12), since in SDS PAGE gel, they also migrate as 15 kDa proteins (Figure II.4b).
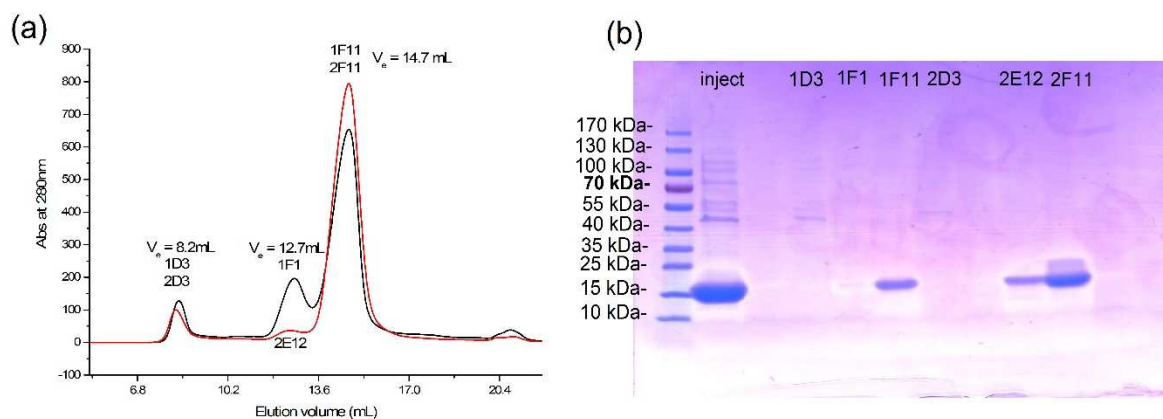

Figure II.4: **Yfh1 purification by Akta purifier system – size exclusion FPLC.** *(a) Mobile phase: HEPES 50 mM buffer, pH 7.0, injection and elution rate 0.5 mL/min. Detection by absorption at 280 nm. The chromatogram shows the highest peak eluted at 14.7 mL, which contains an important amount of Yfh1 (corresponding to the 1F11 and 2F11 lanes in the SDS PAGE gel) (b). The peak eluting at 8.2 mL contains impurity component (lanes 1D3 and 2D3) while the 12.7 mL peak contains oligomer forms of Yfh1 (lanes 1F1 and 2E12).*

1.3. Characterisation

These fractions (1F11 & 2F11) were pooled and the impurity checked by a frataxin more selective system of chromatography. In a size exclusion column Bio SEC-5 from Agilent (5 µm particle, 150Å, 7.8 mm × 300 mm), the fraction performed as highly pure sample, the component elutes at 7.85 mL, corresponding to a molecular weight of 25 kDa, which may correspond to the dimer form of Yfh1 (Figure II.5).
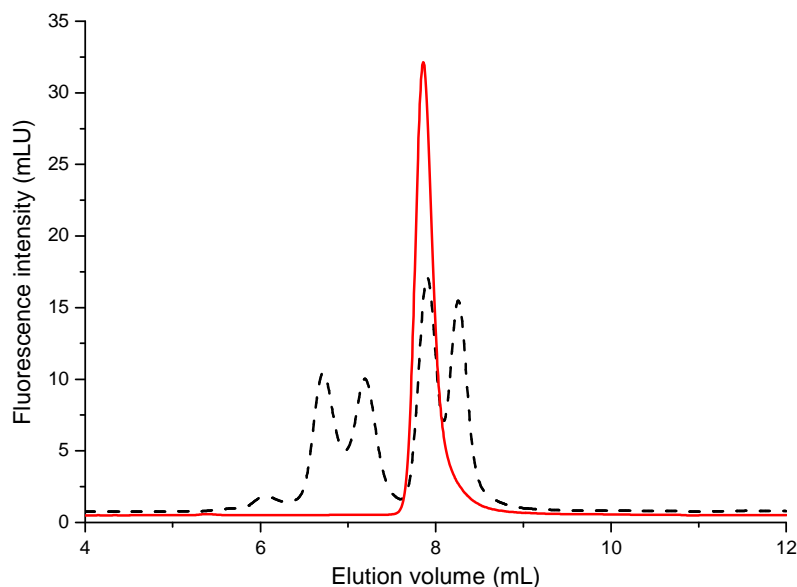
*Figure II.5: **Size-exclusion chromatography analysis of pure fraction** (Yfh1)$_2$ Ve = 7.85 mL). Mobile phase: KH$_2$PO$_4$ 50 mM buffer, pH 7.0, injection and elution rate 1 mL/min. Detection by emission spectroscopy λ_{exc} = 280 nm, λ_{em} = 340 nm. Overlaid black line is the chromatogram of calibration mixture containing: dimeric bovine albumin (132 kDa), monomeric bovine albumin (66 kDa), ovalbumin (45 kDa), carbonic anhydrase (29 kDa), lactalbumine (14.2 kDa).*

These fractions were analyzed by high-resolution electrospray ionization (ESI) mass spectrometry (Orbitrap Exactive EMR). The sample was briefly loaded in a micro-LC column; the elution was monitored by measuring the total ion current. The chromatogram showed a major peak at retention time of 6.51-6.63 min (Figure II.6a). The ions from this peak were analyzed and gave a full MS spectrum showing different charged states (Figure II.6b). The deconvolution spectra (Figure II.6c) showed a major peak of 27499.84 Da corresponding to the average mass of dimer yeast frataxin (theoretical value: 27500. 72 Da) with the precision of 0.003 %.
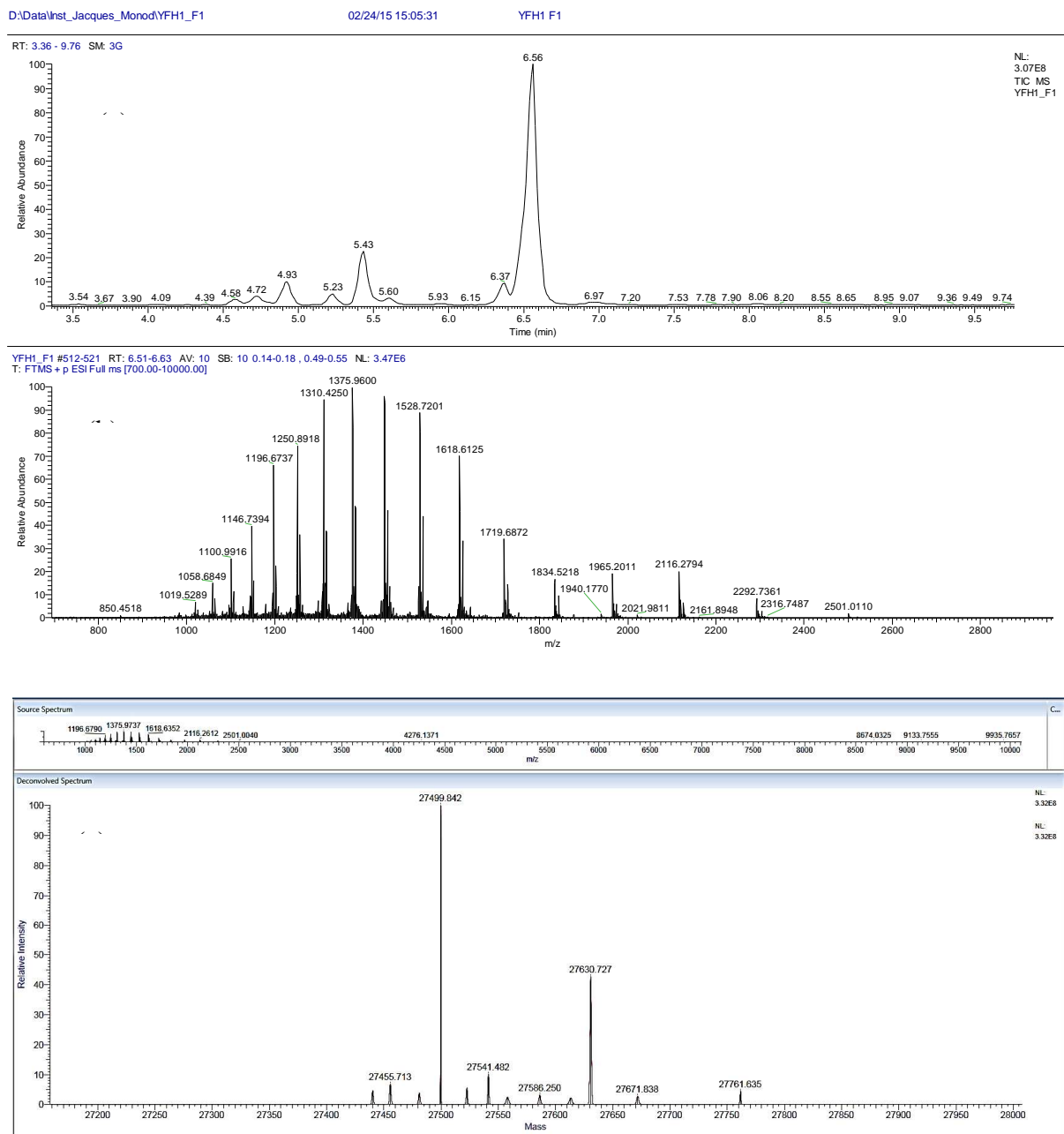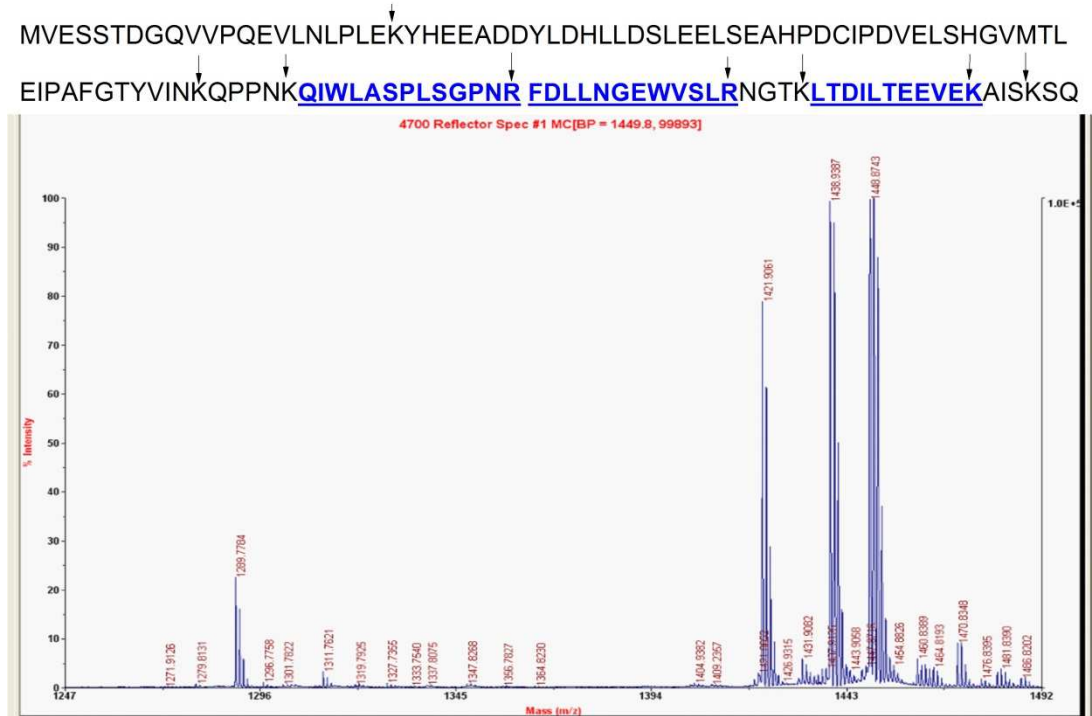
*Figure II.6: **MS spectra of pure fraction detected by the Exactive Plus EMR MS**: (a) Total ion current of flow eluted from micro-LC column (Proswift RP-4H 1x250mm). Elution by a gradient of acetonitrile 0.01 % formic acid from 10 – 80 % in 10 min, flow rate 0.2 mL/min, at 60 °C. The major peak with retention time (RT) is 6.51- 6.63 min was analyzed; (b) ESI full MS spectra with different charge states; (c) Deconvolution spectra confirms the dimer form of purified protein. Peak of 27499.842 Da corresponds to theoretical average mass the mature sequence of (Yfh1)$_2$ (27500.72 Da). The 27630.727 Da peak is probably the heterodimer of a full Yfh1 and a lost-methionine Yfh1.*

We used the peptide mass fingerprint analysis to confirm the expression of the right protein. Indeed, the 15 kDa band in 1D SDS PAGE gel was extracted by TFA 0.1 % and digested by trypsin. Figure II. 7a represents MS spectrum of digested peptides. The limited range of detectable masses for this experiment is 600-3000 Da. This cannot allow the identification of

high mass peptides (red in the sequence). MS/MS analysis by MALDI TOF TOF of each fragment allowed exploiting the sequence of each digested peptide (see material & methods) (Table II.7b). The blue peptides in the sequence correspond to the calculate peptides.

MVESSTDGQVVPQEVLNLPLEKYHEEADDYLDHLLDSLEELSEAHPDCIPDVELSHGVMTL

EIPAFGTYVINKQPPNK**QIWLASPLSGPNR** **FDLLNGEWVSLR**NGTK**LTDILTEEVEK**AISKSQ

(*) ▼: cut sites of Trypsin

(b) List of peptide information

Calculate mass	Observed mass	± Da	± ppm	Seq.	Peptide	Modification
1289.6835	1289.7599	0.0764	59	158-168	LTDILTEEVEK	
1438.7802	1421.9061	0.0336	23	129-141	QIWLASPLSGPNR	pyroglutamylation
1438.7802	1438.9204	0.1402	97	129-141	QIWLASPLSGPNR	
1448.7533	1448.8555	0.1022	71	142-153	FDLLNGEWVSLR	

*Figure II.7: **Peptide fingerprint analysis of cut band from 1D SDS PAGE gel.** (a) MS spectrum of digested peptide, the mass of peptides observed in the spectrum is conforming to expected sequences (blue). (b) Table listed the sequences, which are identified by MS/MS technique; data from MALDI TOF-TOF were exploited by Mascot.*

Consequently, after two steps of anion exchange chromatography and one step of size exclusion chromatography, we obtained $(Yfh1)_2$ purified as a dimer with the molecular weight of 27499.84 Da.

2. Yeast flavohemoglobin – Yhb1

The yeast flavohemoglobin, Yhb1, is a homologue of mammalian cytohemoglobin, which is implicated in responses to both the oxidative and nitrosative stress in *Saccharomyces cerevisiae.* In order to investigate the involvement of frataxin to anti-oxidative and nitrosative stress response, we investigated the molecular interaction between frataxin and Yhb1, and then the effect of frataxin on the enzymatic activity of Yhb1. We first optimized the biosynthesis of Yhb1 using DNA recombinant technique based on system pSBET vector and BL21 (DE3) competent cells. Yhb1 exists as a peptide of 399 residues and contains two cofactors: one flavin adenine dinucleotide (FAD) and one heme per peptide (Figure II.8) (Forrester and Foster 2012). These two cofactors play important roles in enzymatic activity of Yhb1. Therefore, it is essential for Yhb1 to be purified in assembly with the two cofactors FAD and heme.

*Figure II.8: **The three structural domains of Yhb1**: heme domain (green); FAD domain (yellow) and NADH binding domain (red). Visualization by Pymol of 4G1V (PDB) (El Hammi et al. 2012).*

2.1. Optimization of the expression

The sequence coding for Yhb1, was obtained by polymerase chain reaction (see Materials & methods). We introduced in the amplification primers the NdeI and BamHI restriction sites for easy cloning into the pUC18 vector. We verified the sequence of positive subclones, digested the cloning vector with Nde1 and BamH1 and cloned the fragment into the expression vector pSBET-2b. After ligation, the plasmids were transformed into a non-expression strain Top10 *E.coli* to amplify the plasmid. The competent cells Top 10 *E.coli* has the efficiency of 10^9 cfu/µg of plasmid DNA, it allows not only the highly effective transformation but also a stable replication of high copy number plasmids. Once being

amplified, the plasmid is extracted from the strain of Top10 and is cloned into the competent cells BL21(DE3) *E. coli* which allows the expression of protein.

Briefly, we compared protein expression in different types of media: LB medium and/or induction by addition of IPTG and auto-induction medium (LBE5052) in the same condition of induction as with Yfh1 (at 37 °C, 200 rpm stirring). Similar to the expression of Yfh1 by BL21(DE3), growth in auto-induction medium LBE5052 passed the exponential phase faster and allowed a higher OD600nm in stationary phase (Figure II. 9). However, it did not express higher amount of target protein (band at 44kDa in Figure II.10a).
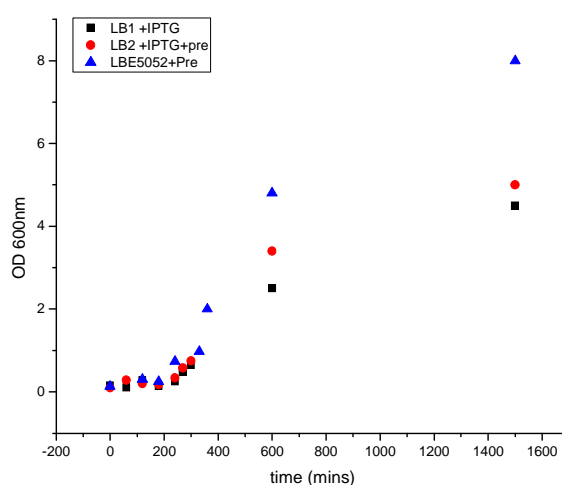

*Figure II.9: **Cells density of BL21DE3-YHB1 induced in different conditions**: LB induced by IPTG (black square); LB and precursors, induced by IPTG (red circle); auto-induction medium LBE5052 with the presence of precursors (blue triangle).*

The cells were harvested by a centrifugation step followed by milliQ water washing. After at least an overnight freezing at -80°C, the pellet was suspended in lysis buffer and lysed by a cycle of 5 min sonication or "One-shot" French press.

After lysing the cells, we centrifuged the extract to separate the soluble and the insoluble material. Indeed, we observed a red pellet in the insoluble part left by the auto-induction medium, which may correspond to the inclusion bodies because normally *E. coli* cells present in light green pellet. The lysis by sonication was more effective to liberate soluble protein from inclusion bodies. This phenomenon has also been reported by Parrilli *et al.* in case of bacterial flavohemoglobin expression (Parrilli et al. 2010). To reduce the formation of inclusion bodies, we decreased the incubation temperature to lower the induction rate.

In addition, we aimed to synthesize a holo-protein with both cofactors FAD and heme. Hence, the presence of precursors for the biosynthesis of these two cofactors in the induction media was also established. In physiological condition, riboflavin and δ-aminolevulinic acid (δ-ALA) are precursors for the biosynthesis of FAD and heme. In our studies, we compared the composition of the crude extracts from bacteria incubated in: (i) LB medium, inducted by IPTG; (ii) LB medium with the two supplementary precursors, inducted by IPTG; and (iii) auto-induction medium LBE5052 in presence of the two precursors. For each type of medium, we examined the incubation time in 8 h or 24 h.

After lysing the cells by sonication, the crude extracts were applied to SDS PAGE gels. These gels are stained by two methods:

- Classical method: blue Comassie 5% allows visualizing the proteomic compositions (Figure II.10a).
- Specific method for identifying hemoproteins: *o-dianisidine* (3,3′-dimethoxybenzidine) allows revealing the bands which contains hemoproteins (Figure II.10b). The holo-protein, would present as a green band in SDS-PAGE gel as in lane T, which contained catalase – a heme-protein.
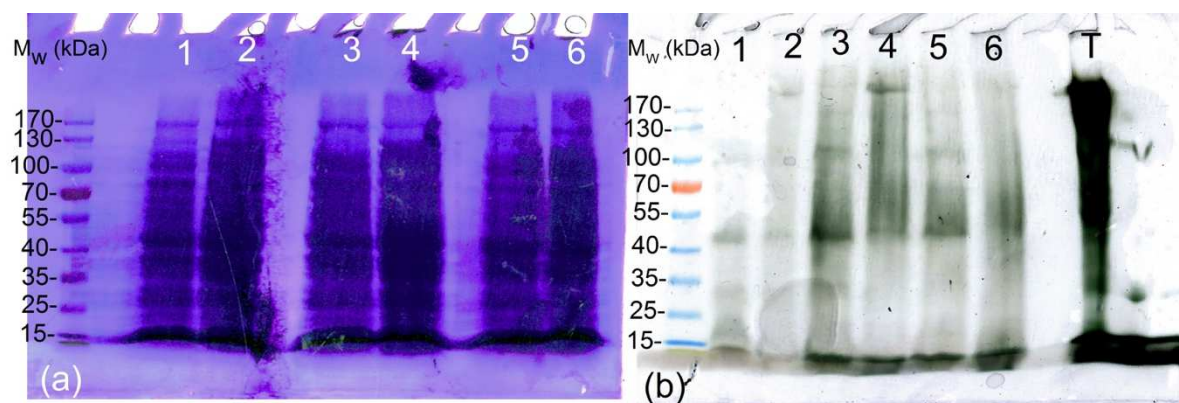

*Figure II.10: **Electrophoresis analysis of crude extract from BL21(DE3)-YHB1 induced in different conditions.** SDS PAGE gel stained by blue coomassie 5 % (a) or by o-dianisidine to identify hemoprotein (b). (1): LB + IPTG 8 h; (2): LB+ IPTG 24 h; (3): LB riboflavin and δ-ALA, 8 h; (4): LB riboflavin and δ-ALA 24 h; (5): LB5052 + riboflavin and δ-ALA 8 h;(6) LBE5052 + riboflavin and δ-ALA 24 h.*

Firstly, considering the blue Coomassie stain gel, the proteomic compositions of the different cultures are quite similar. In the *o-dianisidine* stained gel, in the crude extract from the medium LB without precursors, incubated in 8 h or 24 h (lanes 1 and 2), less intensive green bands were observed. That implies that only a little amount of holo-protein is expressed. On

the other hand, the green bands present at about 45 kDa are much more intense in lane 3 and lane 5, which correspond to the crude extracts of bacteria incubated for 8 h, in cultures with precursors (induction by IPTG – lane 3 or auto-induction medium – lane 5). The lanes 4 and 6 correspond to the crude extracts of cultures with precursors, which are incubated for 24 h at 37 °C. In lanes 4 and 6, other green bands are detected at molecular weight higher than 45 kDa, such as those observed in lanes 3 and 5. This probably means that Yhb1 is in the aggregated or oligomer form, and/or heme is inserted in bigger molecules.

In LB and LBE5052 media, we conclude that the presence of precursors favored the expression of holo-proteins. Moreover, the incubation should not exceed 24 h at 37 °C to avoid the aggregation of the overexpressed protein.

The presence of Yhb1 in the 8 h incubation sample suggests a high expression in the exponential phase of growth. To improve this expression, Terrific Broth medium (TB) can be a good choice for the recombinant strains of *E. coli*. Indeed, TB maintains an extended growth phase (El Hammi et al. 2012, Rosano and Ceccarelli 2014).

We compared this time the expressions of holo-Yhb1 in: (iv) LB medium, incubated at 25 °C for 20 h, inducted by IPTG; (v) TB medium, incubated at 25° C for 20 h and (vi) TB medium, incubated at 30 °C for 20 h. The precursors are presents in all media. We used the UV-visible spectrophotometry to evaluate the amount of soluble holo-proteins in the crude extracts (Figure II.11).
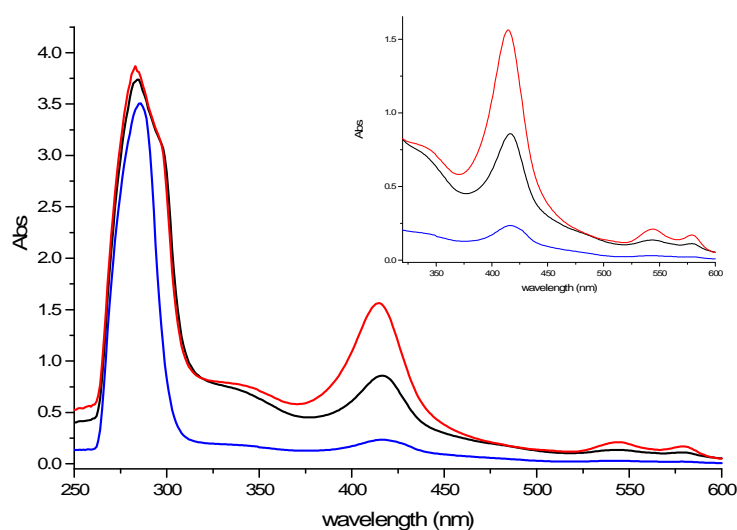

*Figure II.11: **UV-visible spectra of the crude extract** from BL21(DE3)-YHB1 grown in LB 25°C for 20h (blue), Terrific Broth at 25°C for 20h (red) and Terrific Broth at 30°C for 20h (black). Inset: The Soret band confirms the presence of soluble holo-Yhb1 in crude extract.*

Basically, heme presents a characteristic absorption band at about 410 nm (Soret band). The UV-visible spectrum of the proteomic extract from the bacteria incubated in LB medium (blue line) shows a lower absorption in the Soret band as compared to those in TB medium (red and black lines). This means that TB medium is more adopted for the expression of Yhb1, which is highly expressed during the exponential phase. On the other hand, when the temperature of incubation is changed (from 25 °C to 30 °C), the proteomic extract from the bacteria incubated at 25 °C (red line) has a higher absorption at 410 nm than that from 30 °C incubation (black line). That means better quantity of soluble holo-Yhb1 was expressed at 25 °C than at 30 °C (Figure II.11).

2.2. Purification

Yhb1 has the theoretical pI value of 5.86 (Expasy, https://www.expasy.org). The crude extract was loaded onto an anion-exchange column of DEAE-Sepharose (HiPrep DEAE FF 16/10) previously equilibrated with buffer A (KH_2PO_4 20 mM, pH 7.5). The elution was performed with 4 CV (column volume) of a linear gradient from 0 % to 100 % KCl 1 M. The absorption at 410 nm of the fractions containing proteins (20-60 % of KCl) was measured in 96 wells plaque by Spectra i3. Yhb1 was then identified and corresponded to the fractions eluted at 30-40 % of KCl 1 M (Figure II.12). The fractions that presented the higher absorptions at 410 nm were analyzed by SDS-PAGE, and were confirmed to contain Yhb1.
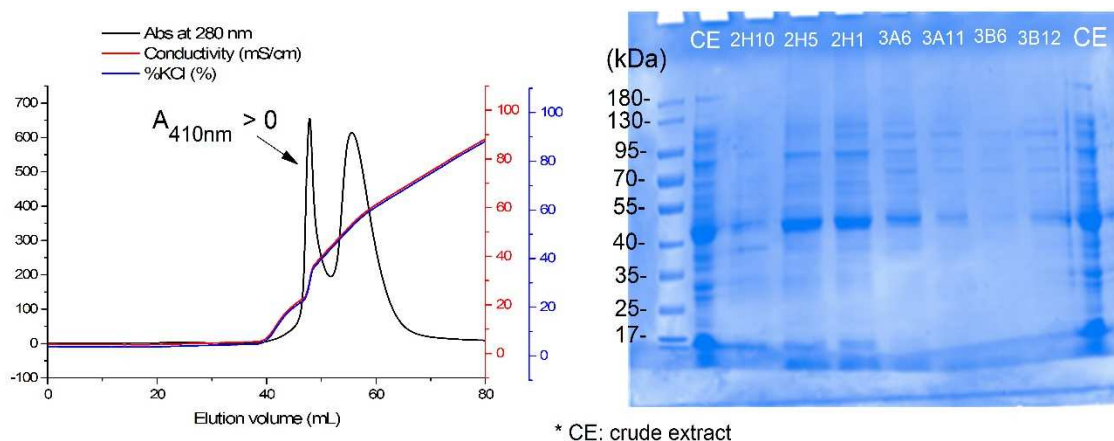

* CE: crude extract

*Figure II.12: **Yhb1 purification by anion exchange chromatography on a DEAE column** (HiPrep DEAE FF 16/10). Mobile phase: KH_2PO_4 20mM, pH 7.5. (a): chromatogram during the elution by a gradient of KCl 1M. "%KCl" corresponding to the KCl gradient obtained by the mix of a buffer A (KH_2PO_4 20mM, pH 7.5) and buffer B (KH_2PO_4 20mM, KCl 1M, pH 7.5). (b): SDS PAGE gel analysis of fractions which absorb at 410nm.*

The pool of the fractions containing Yhb1 was dialyzed overnight to remove salt and introduced into a second column of DEAE-Sepharose previously equilibrated with buffer A. Since in the "capture step", the target protein was eluted with 30-40 % KCl 1 M, in this second step, we planned to "polish" the elution to get a higher resolution by applying a linear gradient of salts from 25 % to 65 % KCl 1M. After sample injection, a washing step was carried out by two CV of equilibrium buffer with 25 % salts. Unexpectedly, Yhb1 was eluted in this washing step. This is confirmed by the absorption at 410 nm and by SDS-PAGE experiment (Figure II.13). Even though, a part of contaminant proteins was held in the column and eluted later. This early elution is probably due to a change in conformation and/or loss of cofactors, which can modify the exposed charge of protein.
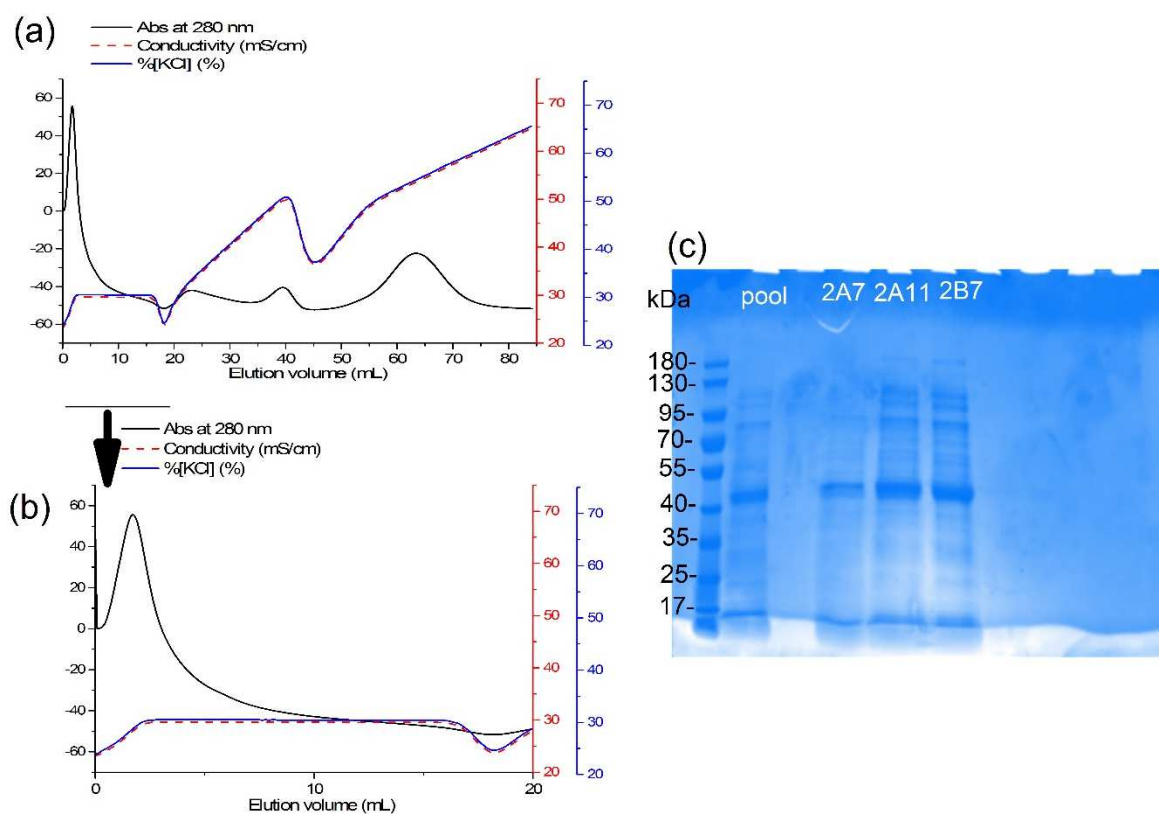

*Figure II.13: **The second step of purification by DEAE column.** (a): chromatogram during the elution by a gradient of KCl. "%KCl" corresponding to the KCl gradient obtained by the mix of a buffer A (KH$_2$PO$_4$ 20mM, pH 7.5) and buffer B (KH$_2$PO$_4$ 20mM, KCl 1M, pH 7.5). (b) zoom-in of washing step. (c) Electrophoresis analysis of washing fractions which absorb at 410nm.*

These Yhb1 fractions were pooled, concentrated and introduced into a size exclusion column of Superdex 200/300 previously equilibrated with buffer C (Tris/HCl 20 mM, KCl 10 mM, pH 7.5). Yhb1 was eluted at 13.1 ml, relevant to the theoretical molar weight of 44 636 Da. (Figure II.14a&b).
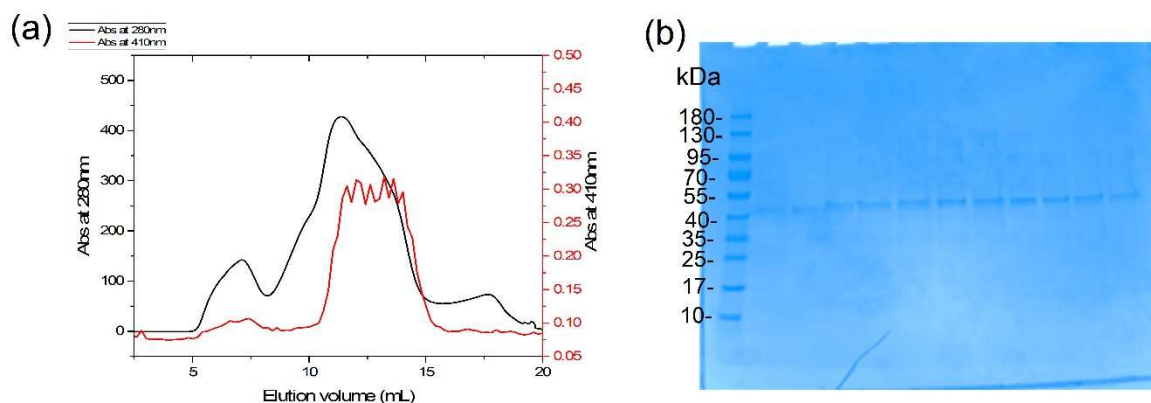
*Figure II.14: **Yhb1 purification by size exclusion chromatography.** (a): chromatogram (black line: absorption at 280 nm; red line: absorption at 410 nm) obtained during the purification by size-exclusion chromatography. (b): Electrophoresis analysis of the fractions eluted at 13.1 mL and absorb at 410 nm.*

2.3. Characterization

As for frataxin, we loaded the previous protein in size exclusion column Bio SEC-5 from Agilent (5 µm particle, 150Å, 7.8 mm × 300 mm). A part of Yhb1 formed rapidly the dimer of protein, which elutes at 6.9 mL, after being dialyzed against BisTris 50 mM, KCl 150 mM, pH = 7.0 buffer (Figure II.15). The detection at 410 nm showed that this dimer is heme free, whereas the fraction at 7.25 mL corresponds to the Yhb1 monomer associated with heme. Further experiments are nevertheless required to optimize the condition that can avoid this self-oligomerization.
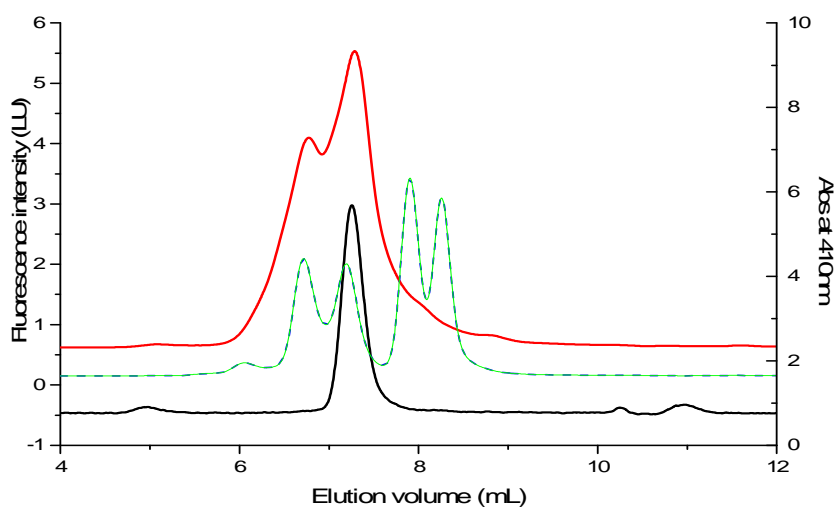

*Figure II.15: **Size exclusion chromatography analysis of pure fraction after the dialysis against BisTris 50 mM, KCl 150 mM, pH 7.0 buffer** (Yhb1: Ve = 7.25 mL). Mobile phase: KH$_2$PO$_4$ 50 mM*

buffer, pH 7.0, injection and elution rate 1 mL/min. Detection by emission spectroscopy λ_{ex} = 280 nm, λ_{em} = 340nm (red line) and absorption at 410nm (black line). Green line is the calibration curve containing: dimeric bovine albumin (132 kDa), monomeric bovine albumin (66 kDa), ovalbumin (45 kDa), carbonic anhydrase (29 kDa), lactalbumine (14.2 kDa).

The peptide was extracted from a cut band from 1D SDS PAGE electrophoresis gel by TFA 0.1%, then digested by Trypsin and analyzed by ESI Orbitrap MS/MS. An example of identification peptide fragment by *Proteome Discoverer 1.4* is given below (Figure II.16b & c). The table II.1 lists the expected mass obtained by MS/MS analysis of fragment VGAQPNALATTVLAAAK, which locates at position 49-66 on the Yhb1 peptide sequence, corresponding to the α5 helix. The b and y ions represent the most common fragment ions by imparting energy in collision cell and successively splitting of peptide link. If the charge is retained on the N terminal fragment, the ion is classed as *b*. If the charge is retained on the C terminal, the ion type is either *y* (Figure II.16a). The red or blue numbers correspond to the experimentally detected mass. Figure II.16 presents the MS/MS spectra and the highlighted texts show detected residues.

Table II.1: List of expected mass obtained by MS/MS analysis the fragmentation of VGAQPNALATTVLAAAK peptide.

| #1	b⁺	b²⁺	Seq.	y⁺	y²⁺	y³⁺	#2
1	100.07570	50.54149	V				17
2	157.09717	79.05222	G	1496.84320	748.92524	499.61925	16
3	228.13429	114.57078	A	1439.82173	720.41450	480.61209	15
4	356.19287	178.60007	Q	1368.78461	684.89594	456.93305	14
5	453.24564	227.12646	P	1240.72603	620.86665	414.24686	13
6	567.28857	284.14792	N	1143.67326	572.34027	381.89594	12
7	638.32569	319.66648	A	1029.63033	515.31880	343.88163	11
8	751.40976	376.20852	L	958.59321	479.80024	320.20259	10
9	822.44688	411.72708	A	845.50914	423.25821	282.50790	9
10	923.49456	462.25092	T	774.47202	387.73965	258.82886	8
11	1024.54224	512.77476	T	673.42434	337.21581	225.14630	7
12	1123.61066	562.30897	V	572.37666	286.69197	191.46374	6
13	1236.69473	618.85100	L	473.30824	237.15776	158.44093	5
14	1307.73185	654.36956	A	360.22417	180.61572	120.74624	4
15	1378.76897	689.88812	A	289.18705	145.09716	97.06720	3
16	1449.80609	725.40668	A	218.14993	109.57860	73.38816	2
17			K	147.11281	74.06004	49.70912	1

(a)

(b)

(c)
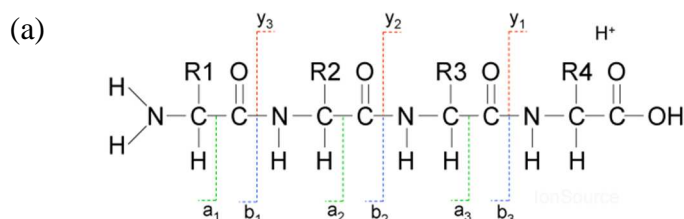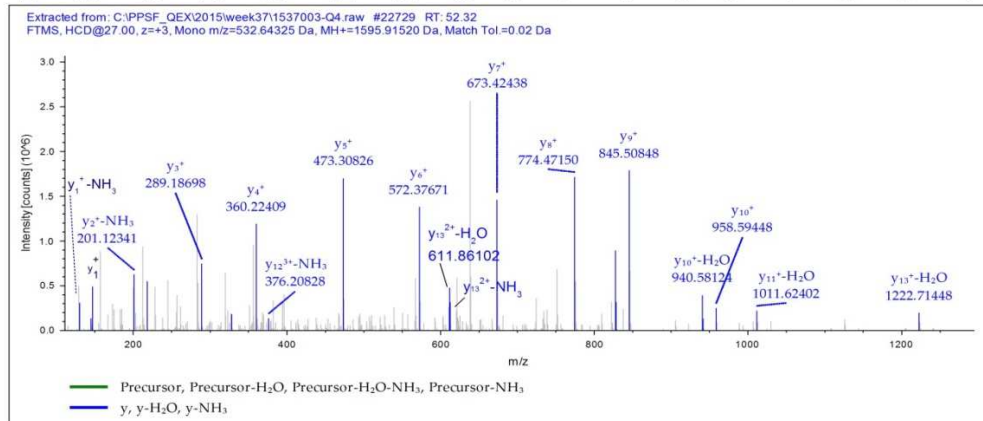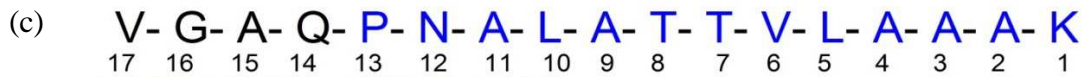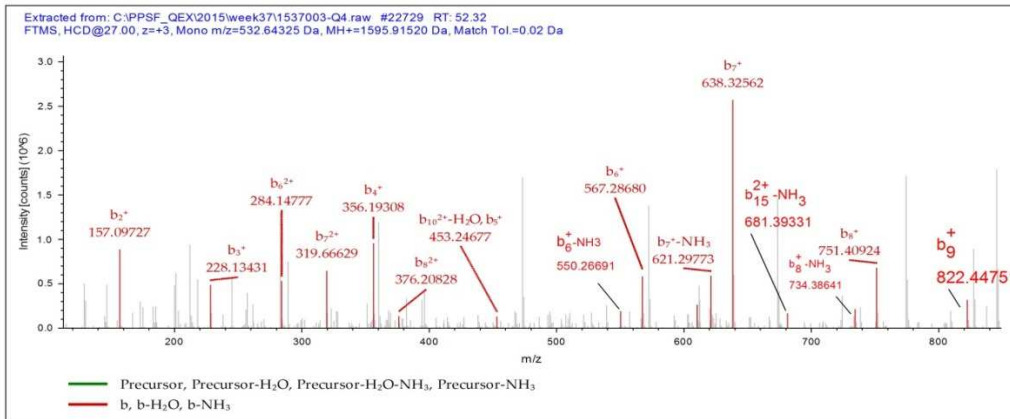
*Figure II.16: **Mass spectroscopy analysis of fractions containing Yhb1.** (a) The most common fragments observed by imparting energy in collision cell of a mass spectrometer. The a and b ions are prefix/N-terminal ions, the y-ions are suffix/C-terminal ions. (b) and c) MS analysis of VGAQPNALATTVLAAAK. (b) b-ions identification, (c) y-ions identification. Peptide charge: +3. Monoisotopic mass (m/z): 532.64325 Da (+1.19 mmu/+2.24 ppm), MH+: 1595.91520 Da, retention time: 52.32 min. Identified with Mascot (v1.30). Ion score: 81. Experimental value: $2.7E^{-008}$. Ions matched by search engine: 13/180. Fragment match tolerance used for search: 0.02 Da. Fragments used for search: a; a-H_2O; a-NH_3; b; b-H_2O; b-NH_3; y; y-H_2O; y-NH_3.*

In this way, 60-80 % residues of Yhb1 peptides have been identified, (Figure II.17), we then assumed that the right peptide has been expressed and purified.
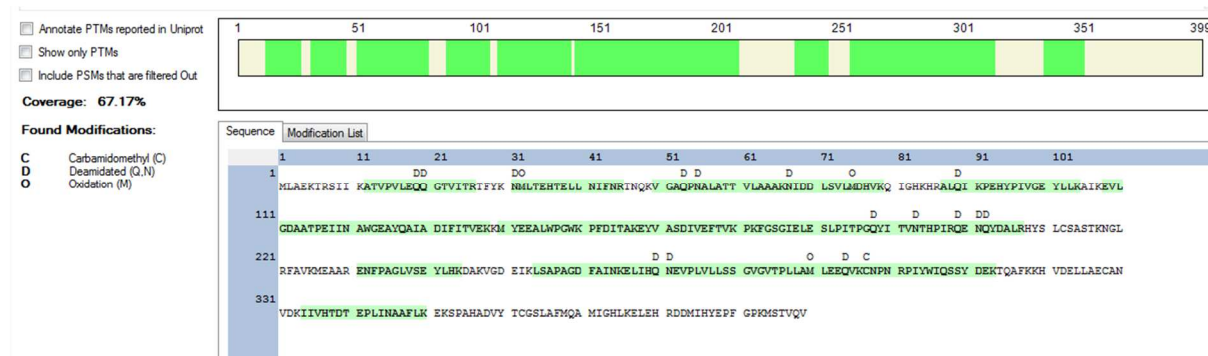
*Figure II.17: **The residues identified by MS analysis fit to 67% of Yhb1 sequences.***

2.4.   Verification of the presence of the two cofactors

The pure fraction of Yhb1 was dialyzed against buffer BisTris 50 mM, KCl 150 mM pH 7.0 at 4 °C and protected from light during 24 h before being scanned for UV-visible spectra. We observed the characteristic absorption bands at 275 nm, 412 nm, 484 nm, 545 nm, 580 nm and 640 nm (insert (d) Figure II.18). The absorption band usually found for protein at 280 nm is for Yhb1 at 275 nm, probably due to the fact that Yhb1 contains 14 Tyr and only 4 Trp. *Candida* flavohemoglobin was also reported to present an absorption maximum at 275 nm (Kobayashi et al. 2002). The Soret band at 412 nm is similar to that previously reported by other groups (El Hammi et al. 2012, Gardner et al. 2000). The Soret maximum at 412 nm and the broad shoulders at 543 nm and 580 nm show that the heme group in Yhb1 was purified in the reduced [Fe^{2+}-O_2] form. In the oxidized state ($Fe^{2+} \rightarrow Fe^{3+}$), this band shifts to 406 nm.

FAD absorbs at 348 nm and 450 nm, but in the presence of heme, the absorption bands of FAD can be overlaid by heme absorption bands. We extracted FAD by boiling Yhb1 in a solution of 7% TCA during 5 min, followed by a 12 000 rpm centrifugation to remove all precipitated proteins. The spectra of supernatant absorbs at 450 nm (inset (b) Figure II.18) which confirms the presence of cofactor FAD.
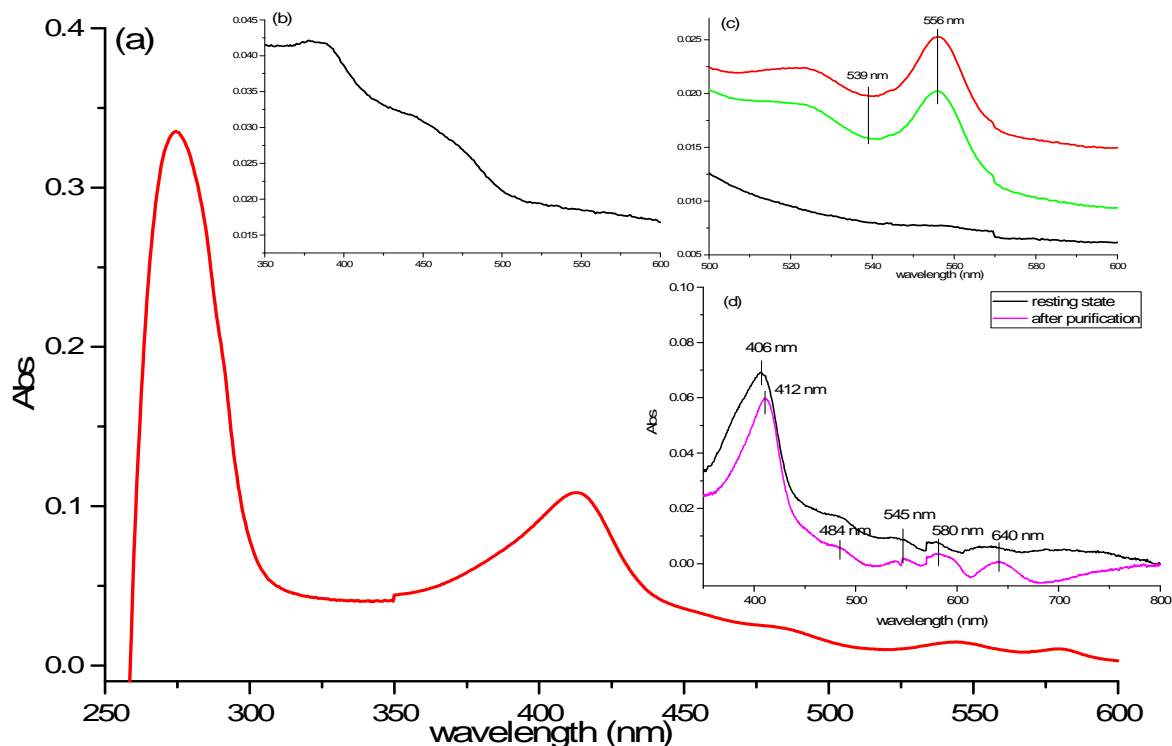
*Figure II.18: **UV-visible analysis of Yhb1.** (a) Absorption spectrum of Yhb1 pure fraction. (b): FAD absorption spectrum of the extract after precipitating peptide; (c): absorption band of Yhb1 in presence of pyridine (black); absorption band of Yhb1 in presence of pyridine and DTT (red); absorption band of Yhb1 in presence of pyridine and DTT and FeKCN in excess (green); (d): Soret bands of freshly purified fraction (violet) and the same fraction in oxidized state (black).*

The dosage of peptide and two cofactors have performed to verify the state of the purified protein. FAD content was measured based on the absorption at 450 nm (ε = 11,300 M^{-1} cm^{-1}) of extract after protein precipitation as explained above (Aliverti et al. 1999). Heme was quantified by the pyridine haemochrome method (inset (c) figure II.18, see Material & methods).

Table II.2: Dosage of peptide and two cofactors of Yhb1 in the pure fractions.

Peptide		Cofactors	
Abs at λ = 275 nm	Bradford assay	[FAD]	[Heme]
0.334 (7.74 µM)	0.56 mg/mL (12.55 µM)	5.3 µM	1.2 µM

Considering the dosage results, the Bradford assay allows determining the amount of peptide. The Bradford essay showed 0.56 mg/mL of peptide in the pure fraction which corresponds to a concentration of 12.55 µM (M_w = 44636 Da). On the other hand, based on the number of the aromatic amino acid present in Yhb1, the theoretical value of absorption coefficient was estimated is ε = 43100 M^{-1} cm^{-1} at 275 nm. At this wavelength, we measured and absorption of 0.334, which leads to a concentration of 7.74µM, which differs from the 12.55 µM determined by Bradford above. The difference of 38 % is probably the result of the partial aggregation that occurs during the storage (as being shown in figure II.15). The dosage of two cofactors showed that the pure fraction was covered about 70 % by FAD cofactor (0.7 mol FAD / 1 mol peptide) and only 15 % of heme (0.15 mol heme / 1 mol peptide).

3. Discussion

In this chapter, we report the biosynthesis of two proteins Yfh1 and Yhb1. The optimized conditions for the expression of these proteins were determined. The T7-based vector pSBET cloned in BL21 (DE3) *E.coli* strain was utilized to express target proteins. The recombinant protein expression is induced without the addition of IPTG using an auto-induction medium. This method of growth and induction relies on the medium components that are differentially metabolized to promote high-density growth and automatic induction of protein expression from *lac*-based promoters.

The phenomenon of unintended induction has been described by Grossman *et al.* (Grossman et al. 1998) as the induction of the target protein upon approach to bacterial saturation, independent of inducer, which can stress the host cells. Too high level of induction can kill the cells that carry a multi-copy plasmid with a T7 promoter even if the target protein is innocuous. It was demonstrated previously that only a trace of lactose present as impurity component can lead to unintended induction (Studier 2005). The use of auto-induction was showed to reduce the unintended induction. In the auto-induction LBE5052 medium, a mixture of carbon sources includes glycerol 0.5 %, glucose 0.05 % and 0.2 % of lactose is applied. Glucose prevents the uptake and utilization of lactose and allows the growth to high density. Glycerol supports the growth as well as glucose and does not prevent the uptake and induction by lactose. The medium LBE5052 performs high cell density first and shifts to the induction of target protein at saturation phase when lactose starts being consumed. When this medium is used in case of Yfh1 expression, we observed that Yfh1 is not produced during the exponential phase (8 h) but later (15 h) as expected. In contrary, although the same condition of culture formulation, temperature and agitation rate have been applied in expression of Yhb1, the protein was expressed majorly during the exponential phase and oligomerized or aggregated in the inclusion bodies in the saturation phase. The use of Terrific Broth medium and the incubation at 25 ºC increased the yield of soluble Yhb1. Interestingly, the composition of TB medium does not include lactose nor glucose, glycerol 0.4% is the only carbohydrate source. The inducer IPTG was not added, even though Yhb1 is well expressed.

In our study, we aimed to investigate the interaction of Yfh1 with metals and others proteins involved in the anti-oxidative/nitrosative stress. Yhb1 is known as an important protein in detoxification of NO in yeast. The two proteins are expressed in the mature form without poly

his-tag, which can avoid the unexpected binding phenomenon. However, the purification demands several steps and can lead to some secondary effects.

Preliminary attempts to produce recombinant Yfh1 using a classical pET21b expression vector failed, mostly because the IPTG mediated induction of the protein production was poorly efficient, and the protein was purified together with major chaperones from *E. coli* (DnaJ, IbpA) identified by peptide mass fingerprints from SDS-PAGE separated proteins (works of others colleagues in group). We therefore cloned the open reading frame of the mature Yfh1 into the pSBET-b expression vector that carries the ArgU gene, allowing efficient production of eukaryote proteins in *E. coli*. The auto-induction medium together with the two-steps purification strategy taking advantage of the low pI (4.13) of the protein, allowed us to produce up to 10 mg purified protein / g cell paste. After the purification, Yfh1 has been found in dimer form as being confirmed by MS and size-exclusion chromatography. Even if frataxin from a psychrophilic bacterium has shown to be mainly in monomeric form, a fraction has been found to be dimeric at high concentration (Noguera et al. 2015). In addition, *in vitro*, Yfh1 was susceptible to homo-oligomerization without iron 2 weeks after its isolation (Cook et al. 2006). To our knowledge, in the absence of metal this oligomerization has not been observed *in vivo*.

In the case of Yhb1 production, Yhb1 is expressed in holo-protein in the presence of two precursors in culture. However, after purification, only 70% of the peptides are covered by FAD cofactor and 15% by heme in the pure fraction. The deficiency of the cofactors after several steps of chromatography has been reported previously by other groups (Sasaki et al. 2004, Takaya et al. 1997). The cofactors would partially dissociate from the Yhb1 during the purification process. In our case, the lost of cofactor seems concern to heme more than FAD. Indeed, the eukaryotic flavin binding proteins were reported to be produced as holo-protein efficiently by DNA recombinant in *E. coli* (Martínez-Martínez et al. 2006, Volonte et al. 2010). On the other hand, over-expression of heme binding proteins in *E. coli* often results in sub-optimal heme incorporation (Sudhamsu et al. 2010, Varnado and Goodwin 2004). The rate of protein synthesis is much too high when compare to that of heme biosynthesis. This explains the vast quantity of peptide folding without the insertion of heme during the induction. The problems can be resolved by: (i) matching the rate of heme synthesis and protein expression by increasing the concentration of δ-ALA in the range of mM – the precursors of heme biosynthesis (Kery et al. 1995, Summerford et al. 1995); (ii) adding hemin

into the bacterial culture together with the expression of outer membrane bound heme receptors (Varnado C. L. and Goodwin 2004); (iii) co-expression of the factors which support heme insertion during protein folding (Graves et al. 2008, Wu et al. 1996). Interestingly, it has been shown that the co-expression with ferrochelatase along with the addition of a small amount of δ –ALA (60 μM) is sufficient to produce fully incorporated heme protein. The presence of ferrochelatase increases the rate of heme biosynthesis and avoids the incorporation of free protoporphyrin IX into the peptide (Sudhamsu et al. 2010). In our study, δ –ALA was present in medium at concentration of 0.75 -1 mM. Perspectively, the solutions of co-expression with a heme-chaperone, which increases the heme insertion and stabilizes the heme- Yhb1 peptide binding, can be considered for a better production of holo-Yhb1.

REFERENCES

Aliverti A, Curti B, Vanoni MA. 1999. Identifying and quantitating FAD and FMN in simple and in iron-sulfur containing flavoproteins. Methods in Molecular Biology, vol. 131: Flavoprotein protocols.

Cook JD, Bencze KZ, Jankovic AD, Crater AK, Courtney N. Busch, Bradley PB, Ann J. Stemmler, Mark R. Spaller, Stemmler* TL. 2006. Monomeric Yeast Frataxin Is an Iron-Binding Protein†. Biochem J 45: 7767-7777.

El Hammi E, Warkentin E, Demmer U, Marzouki NM, Ermler U, Baciou L. 2012. Active site analysis of yeast flavohemoglobin based on its structure with a small ligand or econazole. FEBS J 279: 4565-4575.

Forrester MT, Foster MW. 2012. Protection from nitrosative stress: a central role for microbial flavohemoglobin. Free Radic Biol Med 52: 1620-1633.

Gardner PR, Gardner AM, Martin LA, Dou Y, Li T, Olson JS, Zhu H, Riggs AF. 2000. Nitric-oxide dioxygenase activity and function of flavohemoglobins. sensitivity to nitric oxide and carbon monoxide inhibition. J Biol Chem 275: 31581-31587.

Graves PE, Henderson DP, Horstman MJ, Solomon BJ, Olson JS. 2008. Enhancing stability and expression of recombinant human hemoglobin in E. coli: Progress in the development of a recombinant HBOC source. Biochim Biophys Acta 1784: 1471-1479.

Grossman TH, Kawasaki ES, Punreddy SR, Osburne MS. 1998. Spontaneous cAMP-dependent derepression of gene expression in stationary phase plays a role in recombinant expression instability. Gene 209: 95-103.

Kery V, Elleder D, Kraus JP. 1995. δ-Aminolevulinate Increases Heme Saturation and Yield of Human Cystathionine β-Synthase Expressed in Escherichia coli. Archives of Biochemistry and Biophysics 316: 24-29.

Kobayashi G, Nakamura T, Ohmachi H, Matsuoka A, Ochiai T, Shikama K. 2002. Yeast flavohemoglobin from Candida norvegensis. Its structural, spectral, and stability properties. J Biol Chem 277: 42540-42548.

Martínez-Martínez I, Navarro-Fernandez J, Lozada-Ramírez J, García-Carmona F, Sanchez-Ferrer A. 2006. Maximization of Production of His-Tagged Glycine Oxidase and Its M261 Mutant Proteins. Biotechnol Prog 22: 647-652.

Noguera ME, Roman EA, Rigal JB, Cousido-Siah A, Mitschler A, Podjarny A, Santos J. 2015. Structural characterization of metal binding to a cold-adapted frataxin. J Biol Inorg Chem 20: 653-664.

Parrilli E, Giuliani M, Marino G, Tutino ML. 2010. Influence of production process design on inclusion bodies protein: the case of an Antarctic flavohemoglobin. Microb Cell Fact 9: 19.

Rosano GL, Ceccarelli EA. 2014. Recombinant protein expression in Escherichia coli: advances and challenges. Front Microbiol 5: 172.

Sasaki Y, Takaya N, Nakamura A, Shoun H. 2004. Isolation of flavohemoglobin from the Actinomycete Streptomyces antibioticus. Grown without external nitric oxide stress. Biosci. Biotechnol. Biochem 68: 1106-1112.

Studier FW. 2005. Protein production by auto-induction in high-density shaking cultures. Protein Expression and Purification 41: 207-234.

Sudhamsu J, Kabir M, Airola MV, Patel BA, Yeh SR, Rousseau DL, Crane BR. 2010. Co-expression of ferrochelatase allows for complete heme incorporation into recombinant proteins produced in E. coli. Protein Expr Purif 73: 78-82.

Summerford CM, Pardanani A, Betts AH, Poteete AR, Colotti G, Royer WE. 1995. Bacterial Expression Of Scapharca Dimeric Hemoglobin: A Simple Model System For Investigating Protein Cooperativity. Protein Engineering 8: 593-599.

Takaya N, Suzuki S, Matsuo M, Shoun H. 1997. Purification and characterization of a flavohemoglobin from the denitrifying fungusFusarium oxysporum. FEBS Letters 414: 545-548.

Varnado CL, Goodwin DC. 2004. System for the expression of recombinant hemoproteins in Escherichia coli. Protein Expr Purif 35: 76-83.

Volonte F, Pollegioni L, Molla G, Frattini L, Marinelli F, Piubelli L. 2010. Production of recombinant cholesterol oxidase containing covalently bound FAD in E. coli. BMC Biotechnology 10.

Wu C, Zhang J, Abu-Soud H, Ghosh DK, Stuehr DJ. 1996. High-level expression of mouse inducible nitric oxide synthase in E. coli requires coexpression with calmodulin. Biochem Biophys Res Commun 222(2): 439-444.

CHAPTER III: MECHANISM OF METAL-FRATAXIN INTERACTIONS

1. Introduction

Although the involvement of frataxin in Friedreich's ataxia is well documented, the precise function of the protein remains a matter of debate. One of the hypotheses is the involvement of frataxin in iron metabolism. It has been shown in *Saccharomyces cerevisiae* and other model organisms that frataxin can serve as iron binding chaperone which is involved in Fe-S clusters biosynthesis. It facilitates heme biosynthesis, and protects the cell against oxidative damage (Bayot et al. 2011).

Frataxin homologs have a unique "α-β sandwich" structure with a large number of highly conserved negative residues (Asp, Glu) which are located between the first helix and the edge of the β1-sheet. This semi-conserved acidic ridge generates a negatively charged surface which covers roughly a quarter of frataxin's total accessible surface (Dhe-Paganon et al. 2000). In yeast mutants, mutations of acidic residues in this region show no defect in the biosynthesis of the Fe-S clusters (Aloria et al. 2004, Gakh et al. 2006). However, a change in the electrostatic properties of the acidic ridge impairs Fe-S clusters assembly, weakens the interaction between yeast frataxin (Yfh1) and scaffold protein in Fe-S cluster assembly (Isu1), and increases oxidative damage (Correia et al. 2010, Foury et al. 2007). In addition, mutations in bacterial frataxin lead to the loss of Fe^{2+} binding indicating that this region has a high affinity for this cation(Nair et al. 2004, Pastore et al. 2007). Therefore, this region appears to be important for the physiological role of frataxin (Huang et al. 2008).

Previous works have shown that frataxins from human, yeast and *Escherichia coli* bind Fe^{2+} and Fe^{3+} with comparable affinity. HFxn binds six or seven iron ions with $K_d \sim$ 12–55 μM (Yoon T. and Cowan 2003), CyaY bind two ferrous iron with $K_d \sim 4$ μM (Bou-Abdallah et al. 2004); frataxin from *Drosphila* Dfh binds one ferrous iron $K_d \sim 6$ μM (Kondapalli et al. 2008) and monomeric Yfh1 binds two ferrous irons $K_d \sim 2.5$ μM (Cook et al. 2006). The dissociation constants of these iron-frataxin complexes are in the micromolar range. This probably means that iron reacts with frataxin with low selectivity and specificity. Moreover, mutations of the acidic residues on helix α1 or/and β1 sheet decrease the affinity of yeast

frataxin for iron without abolishing the interaction (Foury et al. 2007). Several studies with bacterial frataxin using NMR and X-ray crystalllography showed that these proteins may interact with metals, such as Co^{2+}, Eu^{3+}, Mn^{2+}, Zn^{2+} (Nair et al. 2004, Noguera et al. 2015, Pastore et al. 2007).

Mitochondria require transition metals for many physiological functions. Iron, copper, manganese and zinc participate in multiple roles in protein structures and functions (catalysis, electron transfer, ligand binding) (Atkinson and Winge 2009, Pierrel et al. 2007). These metals complex low-molecular-mass ligands form the labile metal pools in the cell, and recent studies using liquid chromatography coupled with plasma mass spectrometer estimated that they constitute 20-40 % of total mitochondrial Mn, Fe, Zn and Cu ions (McDonald-McGinn et al. 2013).

In this chapter, we investigate in cell-free assay interactions of mitochondrial metals (Fe, Cu, Mn, and Zn) with yeast frataxin. Emission spectroscopy is used to investigate the affinity of frataxin for each metal. We then revisit the complexation of Fe^{2+} and Fe^{3+} by yeast frataxin by means of microcalorimetry and size exclusion chromatography and demonstrate that frataxin interacts with Cu^+, Cu^{2+} and Mn^{2+} with higher affinities than iron. We establish for the first time the mechanisms of these iron- and copper-frataxin interactions. These investigations are based on the use of chemical relaxations (Bernasconi 1976, Eigen and DeMaeyer 1963).

2. Results

The frataxin we obtain is a dimer, consisted of the association of two identical frataxin subunits (chapter II). We assumed that frataxin dimer $(Yfh1)_2$ has identical metal-binding sites for each subunit. Therefore, our kinetic and thermodynamic analysis deal with each subunit separately. Except with Fe(III), Cu(II) and Zn(II), all the experiments were performed under anaerobic conditions in a glove box under argon to avoid any oxidation and reaction with oxygen to generate superoxide anions.

2.1. Iron (II) binding

2.1.1. Thermodynamics of iron(II) uptake

The Fe^{2+} donor to $(Yfh1)_2$ used in our experiment is ferrous ammonium sulfate in the absence or presence of reduced glutathione. Spectrophotometric detection was used in all thermodynamic and kinetic runs. The kinetic processes related to Fe^{2+} uptake by $(Yfh1)_2$ were acquired by fluorescence emission.
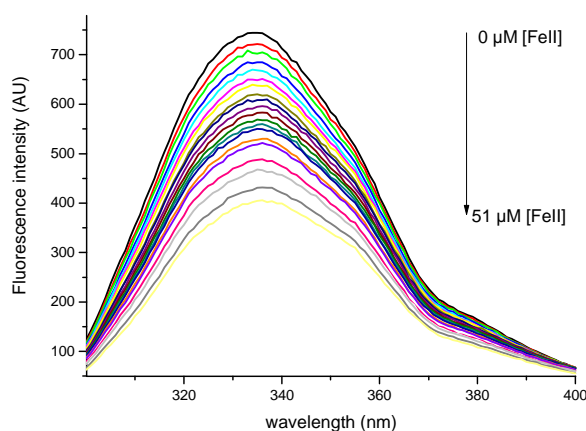
*Figure III.1: **Emission spectra** ($\lambda_{ex} = 280$ nm) **of (Yfh1)₂** (0.9 μM) **at different concentrations of Fe²⁺** (0 μM to 51 μM), in 50 mM Bis-Tris, 150 mM KCl pH 7.0.*

Under anaerobic conditions, adding Fe^{2+} to a solution of $(Yfh1)_2$ leads to a decrease in the fluorescence emission accompanied by a 2 nm red-shift (from 334 to 336 nm) (Figure III.1). Since a monomer of Yfh1 can form two complexes with one or two Fe^{2+} (Cook et al. 2006), we assumed that each subunit interacts with one or two Fe^{2+}. A SPECFIT analysis shows that two Fe^{2+} complexes are produced sequentially with Yfh1 (equations III. 1 and III. 2).

$$Yfh1 + Fe^{2+} \rightleftharpoons (Yfh1)Fe^{II} \qquad (III.1)$$

$$(Yfh1)Fe^{II} + Fe^{2+} \rightleftharpoons (Yfh1)Fe^{II}_2 \qquad (III.2)$$

With $K_{d1}^{FeII} = \frac{[Fe^{2+}][Yfh1]}{[(Yfh1)Fe^{II}]}$; $K_{d2}^{FeII} = \frac{[Fe^{2+}][(Yfh1)Fe^{II}]}{[(Yfh1)Fe^{II}_2]}$;

K_{d1}^{FeII} and K_{d2}^{FeII} values are measured in presence or in absence of GSH. They seem independent of GSH concentration (Table III.1). The average values are: $-\log K_{d1}^{FeII} = 6.3 \pm 0.4$ and $-\log K_{d2}^{FeII} = 4.7 \pm 0.3$.

Table III.1: Dissociation constants of (Yfh1)₂Feᴵᴵ₂ and (Yfh1)₂Feᴵᴵ₄ complexes determined by spectrophotometric titration, at pH 7.0 and at 25 °C in the absence or presence of GSH.

[GSH] (mM)	-log (K_{d1}^{FeII})	-log (K_{d2}^{FeII})
0	6.6 ± 0.2	4.8 ± 0.3
2.5	5.8 ± 0.1	4.5 ± 0.2
5	6.9 ± 0.6	4.7 ± 0.6
10	6.0 ± 0.2	4.8 ± 0.2

2.1.2. Kinetics of Iron(II) uptake

When a solution of (Yfh1)₂ is rapidly mixed with a solution of Fe^{2+} at pH 7.0, three kinetic processes are observed (Figure III.2). The first occurs as an exponential increase in the fluorescence in the 200 ms range (Figure III.2A). The second appears as an exponential decrease in fluorescence occurring in about 5 seconds (Figure III.2B). These two processes are followed by a third exponential decrease in emission in the 500 s range (Figure III.2C). The experimental reciprocal relaxation times related to the first two processes depend on Fe^{2+} concentration, whereas the last process seems independent of all our experimental parameters.
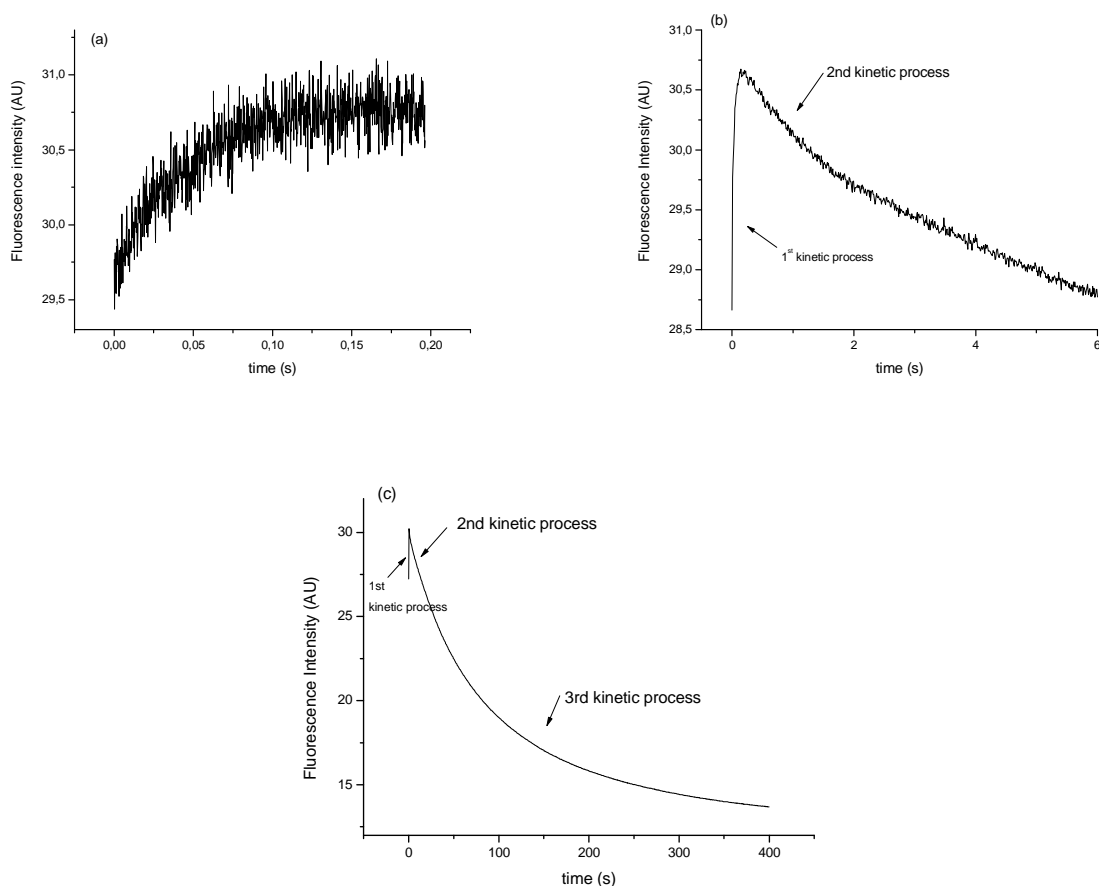
*Figure III.2: **Fluorescence intensity variation with time after a fast mixing of a (Yfh1)$_2$ solution (0.5 μM) with a Fe^{2+} solution** (250 μM) at pH 7.0, 25.0 °C and ionic strength μ = 0.2 (50 mM Bis-Tris, 150 mM KCl).*

a) *First kinetic process:*

The reciprocal relaxation times associated with the fast process of Figure III.2A depend on Fe^{2+} concentration in a continuous but non-linear fashion (Figure III.3).
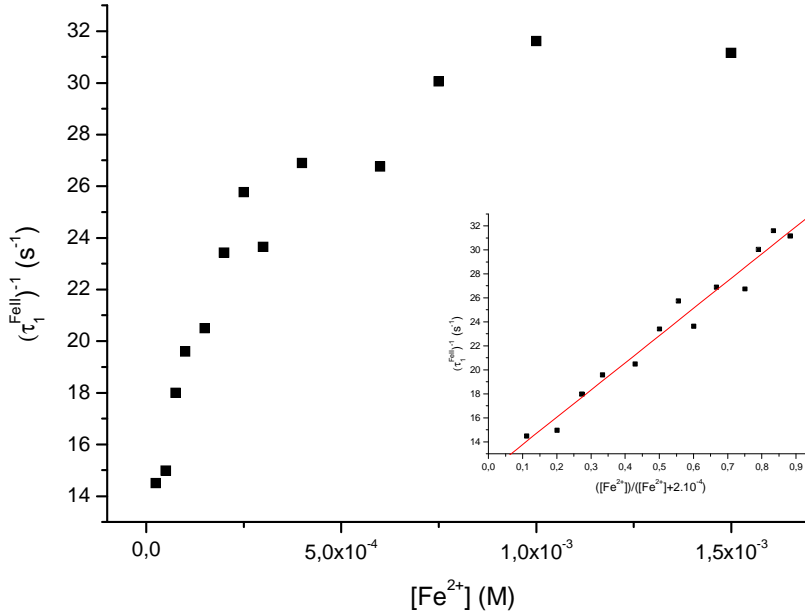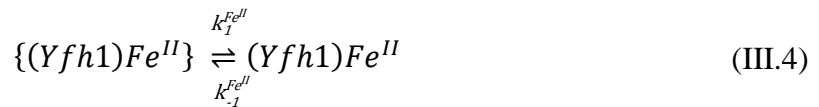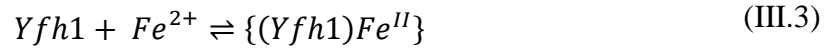
Figure III.3: ***Plot of*** $(\boldsymbol{\tau_1^{FeII}})^{-1}$ ***against*** ***[Fe^{2+}]*** *at pH 7.0 and T= 25°C. Inset: Plot of* $(\tau_1^{FeII})^{-1}$ *against [Fe^{2+}]/([Fe^{2+}] +K_1^{FeII}) with K_1^{FeII} = 200 μM; slope, 22.7 ± 1.2 s^{-1}; intercept, 11.5 ± 0.7 s^{-1}; r = 0.98418.*

As recently described for metal uptake by ceruloplasmin (Eid et al. 2014), we ascribe this phenomenon to the fast uptake of a first Fe^{2+} by a frataxin subunit Yfh1, followed by a rate-limiting monomolecular reaction (equations III.3-4).

$$Yfh1 + Fe^{2+} \rightleftharpoons \{(Yfh1)Fe^{II}\} \tag{III.3}$$

$$\{(Yfh1)Fe^{II}\} \underset{k_{-1}^{Fe^{II}}}{\overset{k_1^{Fe^{II}}}{\rightleftharpoons}} (Yfh1)Fe^{II} \tag{III.4}$$

With the dissociation constant: $K_1^{Fe^{II}} = \frac{[Yfh1]\,[Fe^{2+}]}{[\{(Yfh1)Fe^{II}\}]}$ and $\left(K_1^{Fe^{II}}\right)' = \frac{[(Yfh1)Fe^{II}]}{[\{(Yfh1)Fe^{II}\}]} = \frac{k_1^{Fe^{II}}}{k_{-1}^{Fe^{II}}}$

The rate equation of equation III.4 is expressed as equation III.5:

$$\frac{d\Delta[(Yfh1)Fe^{II}]}{dt} = k_1^{Fe^{II}}\Delta[\{(Yfh1)Fe^{II}\}] - k_{-1}^{Fe^{II}}\Delta[(Yfh1)Fe^{II}] \tag{III.5}$$

Masse conservation:

$$\Delta[\{(Yfh1)Fe^{II}\}] + \Delta[(Yfh1)Fe^{II}] + \Delta Yfh1 = 0 \tag{III.6}$$

$$\Delta[Yfh1] = \frac{K_1^{Fe^{II}}}{[Fe^{2+}]}\Delta[\{(Yfh1)Fe^{II}\}] \tag{III.7}$$

$$\Rightarrow \qquad \Delta[\{(Yfh1)Fe^{II}\}] = -\left(\frac{[Fe^{2+}]}{K_1^{Fe^{II}} + [Fe^{2+}]}\right)\Delta[(Yfh1)Fe^{II}] \tag{III.8}$$

Apply equation III.8 to equation III.5, we have:

$$\frac{d\Delta[(Yfh1)Fe^{II}]}{dt} = -(k_1^{Fe^{II}}\frac{[Fe^{2+}]}{K_1^{Fe^{II}} + [Fe^{2+}]} + k_{-1}^{Fe^{II}})\Delta[(Yfh1)Fe^{II}] \tag{III.9}$$

The reciprocal relaxation time equation associated with equation III.4 can be expressed as equation III.10:

$$(\tau_1^{Fe^{II}})^{-1} = k_1^{Fe^{II}}\frac{[Fe^{2+}]}{K_1^{Fe^{II}} + [Fe^{2+}]} + k_{-1}^{Fe^{II}} \tag{III.10}$$

Varying K_1^{FeII} from 10 to 1000 µM with a ΔK_1^{FeII} step of 10 µM shows that the best linear regression of $(\tau_1^{FeII})^{-1}$ against $[Fe^{2+}]/(K_1^{FeII} + [Fe^{2+}])$ is obtained for $K_1^{FeII} = 200 \pm 10$ µM (Inset Figure III.3). From the slope and intercept, $k_1^{FeII} = 23 \pm 1$ s⁻¹, $k_{-1}^{FeII} = 11.5 \pm 0.7$ s⁻¹ and $(K_1^{FeII})' = 2.0 \pm 0.1$ are determined.

b) *Second kinetic process:*

The experimental reciprocal relaxation times associated with this second process depend on $[Fe^{2+}]$.
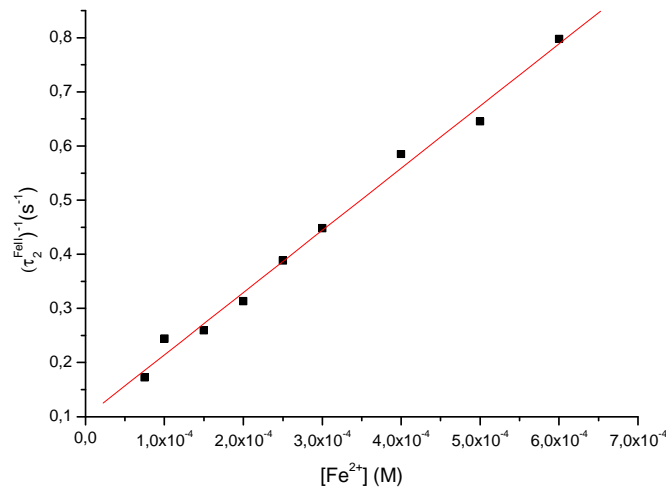
*Figure III.4: **Plot of** $(\tau_2^{FeII})^{-1}$ **against [Fe²⁺]** at pH 7.0 and T= 25°C; slope, $(1.15 \pm 0.04) \times 10^3$ s⁻¹ M⁻¹; intercept, $(9.9 \pm 1.3) \times 10^{-2}$ s⁻¹; r = 0.98947.*

This phenomenon is assumed to be the uptake of a second Fe^{2+} (equation III.11).

$$(Yfh1)Fe^{II} + Fe^{2+} \underset{k_{-2}^{Fe^{II}}}{\overset{k_2^{Fe^{II}}}{\rightleftharpoons}} (Yfh1)Fe_2^{II} \qquad (III.11)$$
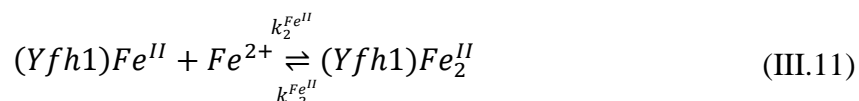
The reciprocal relaxation time equation associated with equation III.11 can be expressed as equation III.12:

$$(\tau_2^{Fe^{II}})^{-1} = k_2^{Fe^{II}}([(Yfh1)Fe^{II}] + [Fe^{2+}]) + k_{-2}^{Fe^{II}} \qquad (III.12)$$

Since, under our experimental conditions, $[Fe^{2+}] \gg [(Yfh1)Fe^{II}]$, equation III.12 simplifies into equation III.13:

$$(\tau_2^{Fe^{II}})^{-1} = k_2^{Fe^{II}}[Fe^{2+}] + k_{-2}^{Fe^{II}} \qquad (III.13)$$

A very good linear least-squares regression of the experimental $(\tau_2^{Fe^{II}})^{-1}$ against $[Fe^{2+}]$ (Figure III.4). From the slopes and intercepts of the best lines, $k_2^{FeII} = (1.15 \pm 0.04) \times 10^3$ M^{-1} s^{-1}, $k_{-2}^{FeII} = (9.9 \pm 1.3) \times 10^{-2}$ s^{-1} and $K_2^{FeII} = k_2^{FeII}/k_{-2}^{FeII} = (1.2 \pm 0.2) \times 10^4$ M^{-1} values are determined.

c) *Third kinetic process:*

The last kinetic process lasts 500s and seems independent of Fe^{2+} concentrations.

$(\tau_3^{FeII})^{-1} = (8 \pm 1) \times 10^{-3}$ s^{-1}

2.2. Iron(III) binding

2.2.1. Thermodynamics

The Iron(III) binding to $(Yfh1)_2$ was investigated in Bis-Tris 50 mM, KCl 150 mM, pH 7.0 by emission spectrophotometry, microcalorimetry, size exclusion chromatography and stopped flow. The addition Fe(III) to a solution of $(Yfh1)_2$ leads to changes in emission spectra (Figure III.5).
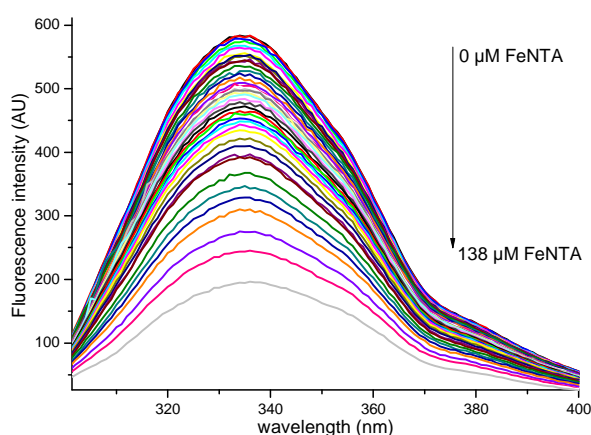
*Figure III.5: **Emission spectra** (λ_{ex} = 280 nm) **of (Yfh1)₂** (0.9 μM) **at different concentrations of FeNTA** (0 μM to 138 μM), in Bis-Tris 50 mM, KCl 150 mM pH 7.0.*

Furthermore, a typical thermogram obtained upon the addition of FeNTA to a solution of $(Yfh1)_2$ at 25 °C is shown in Figure III.6. This titration implies that the binding of Fe^{3+} to $(Yfh1)_2$ is an exothermic process (ΔH = -32 ± 4 kJ.mol^{-1}). The data were curve-fitted using a model of one set of independent binding sites. The fitting yields 9 ± 1 equivalent Fe(III) bound to $(Yfh1)_2$ and K_a = 4.0 x 10^4 M^{-1}.
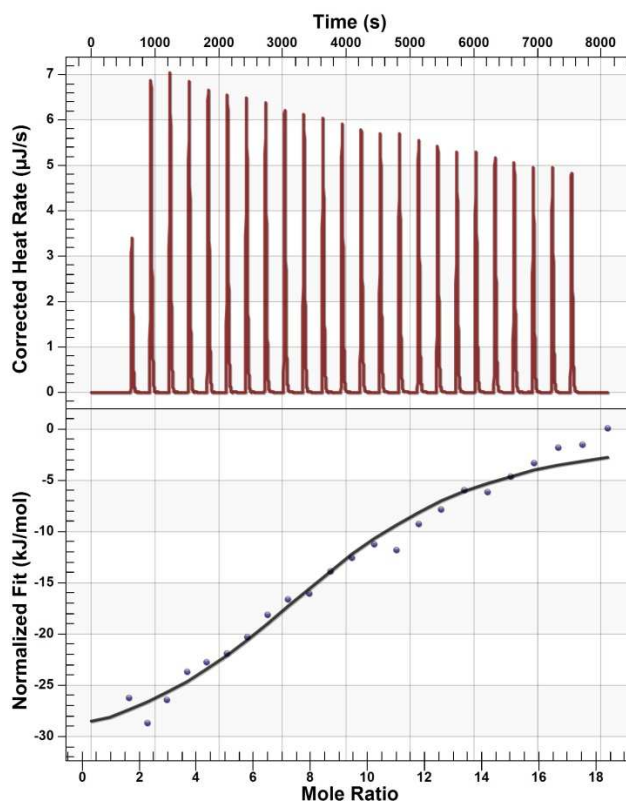
*Figure III.6: **Raw ITC** (top) **and binding isotherm data** (bottom) **for FeNTA to yeast frataxin**. The red line in the bottom graph shows the simulated fit to the binding isotherm data. Data were collected*

at 25 °C, pH 7.0, ionic strength μ = 0.2 (50 mM Bis-Tris, 150 mM KCl).

The solution was afterward injected in a size exclusion chromatography to determine the oligomeric state of frataxin in the presence of Fe^{3+} (Gakh et al. 2002). With FeNTA, the absorption and emission chromatogram of the elution profile showed two peaks, one of $(Yfh1)_2$ and another peak at ~ 60 ± 5 kDa, leading to the conclusion, that in presence of Fe^{3+}, $(Yfh1)_2$ forms a stable four-subunit complex (equation III.14, Figure III.7). Furthermore, no complexes of higher molecular weight were observed.

$$2(yfh1)_2 Fe_9^{III} \rightleftharpoons 2(yfh1)_4 Fe_{18}^{III} \qquad \text{(III.14)}$$
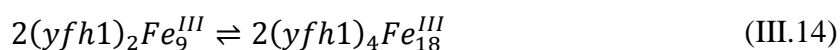
With $K_{dim} = \dfrac{[(Yfh1)_4 Fe_{18}^{III}]}{[(Yfh1)_2 Fe_9^{III}]^2}$
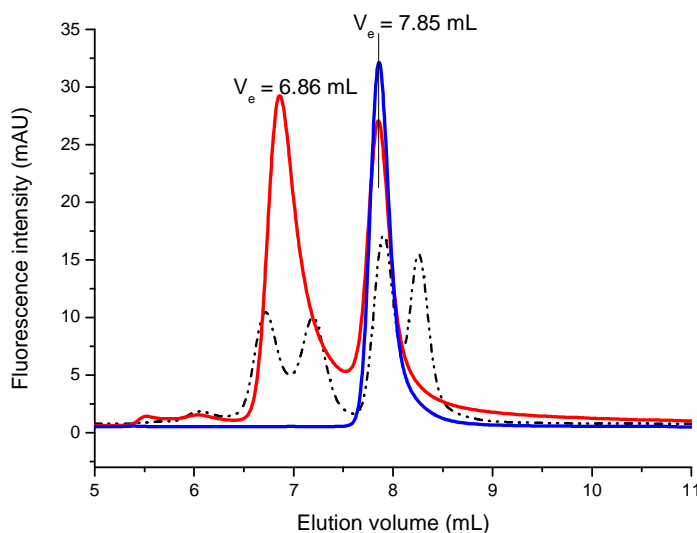
Figure III.7: **Chromatograms of (Yfh1)₂** *(V_e = 7.85 mL)* **in absence** *(blue)* **and presence** *(red)* **of FeNTA.** *Mobile phase: 50 mM KH_2PO_4 buffer, pH 7.0, injection and elution rate 1 mL/min. Detection by emission spectroscopy (top) λ_{ex} = 280 nm, λ_{em} = 340 nm. Overlaid dash line is the chromatogram of calibration mixture containing: dimeric bovine albumin (132 kDa), monomeric bovine albumin (66 kDa), ovalbumin (45 kDa), carbonic anhydrase (29 kDa), lactalbumine (14.2 kDa).*

Using microcalorimetry, the dissociation constant of the complex formed in presence of FeNTA is determined. Typically, the complex (2.75 µM) was injected under stirring in the calorimeter cell (166 µL) initially containing the buffer, with a typical injection sequence of 25×2 µl at 5 min intervals. Dilution of the complex in Bis-Tris buffer, pH 7.0, at 25 °C gave a series of endothermic heat pulses (Figure III.8). This is consistent with the dissociation of protein oligomers modeled as dimers, with a dimerization constant K_{dim} of 2.89 x 10^5 M^{-1} and a dissociation enthalpy (ΔH) of 4730 kJ.mol^{-1}.
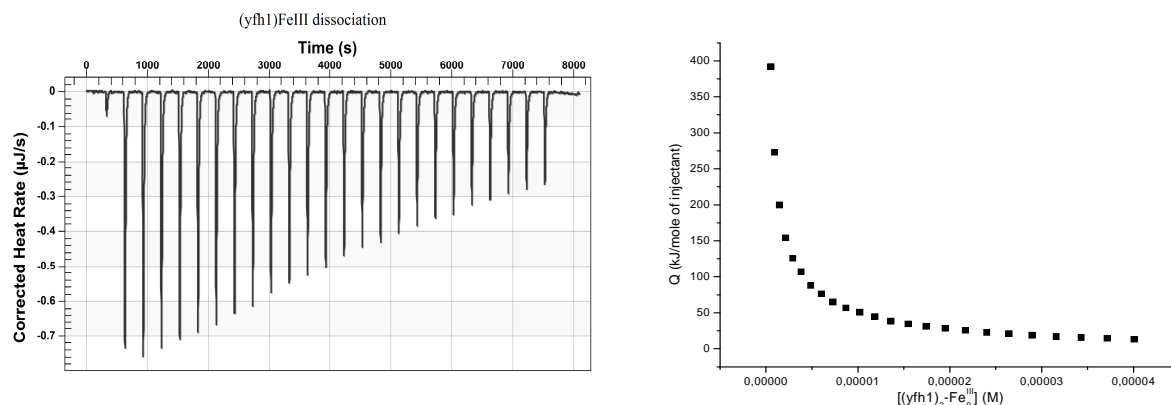
*Figure III.8: **Raw ITC** (left) **and dissociation isotherm data** (right) **for (Yfh1)₄Feᴵᴵᴵₗⱼₜto (Yfh1)₂Feᴵᴵᴵ₉.*** *Data were collected at 25 ℃, pH 7.0, ionic strength µ = 0.2 (50 mM Bis-Tris, 150 mM KCl).*

2.2.2. Kinetics of Iron(III) uptake

When a solution of FeNTA is rapidly mixed with a solution of $(Yfh1)_2$ in Bis-Tris buffer, pH 7.0, three kinetic phenomena are observed (Figure III.9). The first is a monoexponential increase in fluorescence in the 500 ms range (Figure III.9a). It is followed by a second process which occurs in 50 s as another monoexponential increase in emission (Figure III.9b). The third kinetic process manifests as a decrease in fluorescence and lasts about 1000 s (Figure III.9c).
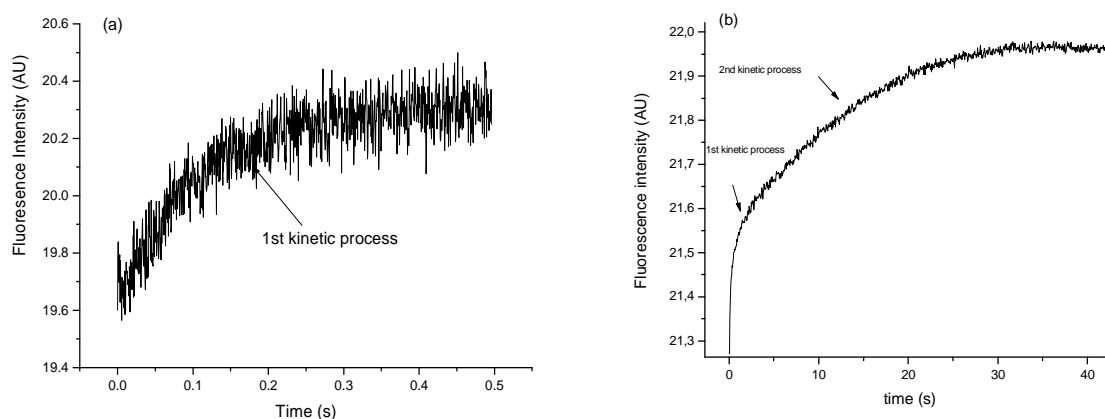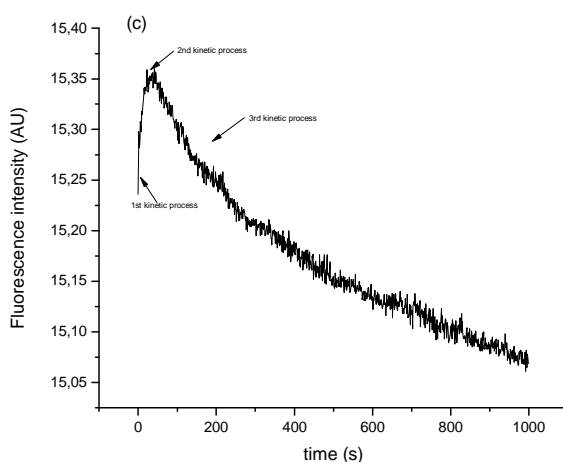
*Figure III.9: **Fluorescence intensity variation with time after a fast mixing of an (Yfh1)₂ solution** (1 μM) **with a FeNTA solution** (75 μM) at pH 7.0, 25.0 °C and ionic strength μ=0.2 (50 mM Bis-Tris, 150 mM KCl).*

a) First kinetic process:

The reciprocal relaxation time associated with this first phenomenon depends on Fe^{3+} concentration (Figure III.10).
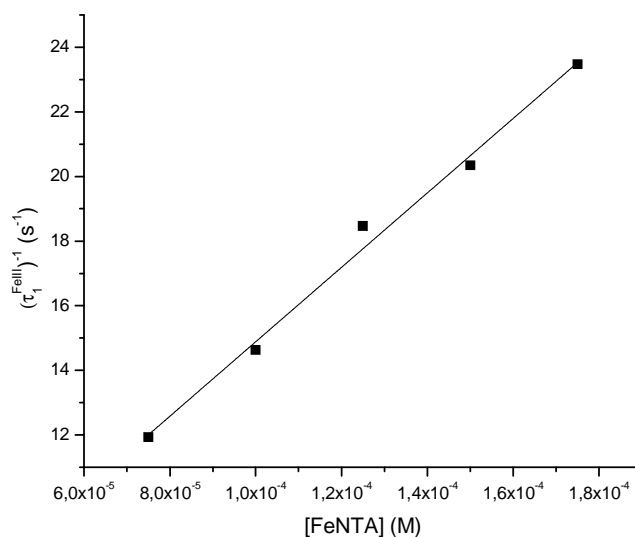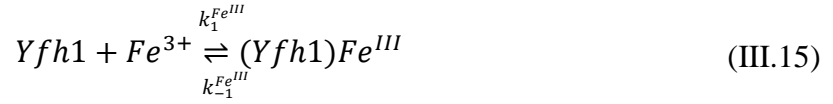

*Figure III.10: **Plot of** $(\tau_1^{FeIII})^{-1}$ **against [FeNTA]** at pH 7.0 with [(Yfh1)₂] = 1 μM and 75 μM ≤ [FeNTA] ≤ 175 μM; slope of (11.5 ± 0.6) x 10⁴ M⁻¹ s⁻¹; intercept, 3.4 ± 0.7 s⁻¹; r = 0.99606.*

We ascribe it to the uptake of one Fe^{3+} (equation III.15).

$$Yfh1 + Fe^{3+} \underset{k_{-1}^{Fe^{III}}}{\overset{k_{1}^{Fe^{III}}}{\rightleftharpoons}} (Yfh1)Fe^{III} \qquad \text{(III.15)}$$

With $K_1^{FeIII} = \dfrac{[(Yfh1)Fe^{III}]}{[Yfh1][Fe^{III}]}$

Under our experimental conditions ($[Fe^{3+}]>>[Yfh1]$), the reciprocal relaxation time equation associated with equation III.15 is expressed as equation III.16:

$$(\tau_1^{Fe^{III}})^{-1} = k_1^{Fe^{III}}[Fe^{3+}] + k_{-1}^{Fe^{III}} \qquad \text{(III.16)}$$

A good linear regression of the experimental reciprocal relaxation times against $[Fe^{3+}]$ is obtained (Figure III.10). From the slope and intercept of the best line, $k_1^{FeIII} = (11.5 \pm 0.5) \times 10^4$ M^{-1} s^{-1}, $k_1^{FeIII} = 3.4 \pm 0.7$ s^{-1} and $K_1^{FeIII} = k_1^{FeIII}/k_{-1}^{FeIII} = (3.4 \pm 0.8) \times 10^4$ values are determined. The K_1^{FeIII} value is, within the limits of uncertainty, identical to that determined by microcalorimetry for one iron.

b) *Second and third kinetic processes:*

The second and third processes are independent of iron and frataxin concentrations. They are, therefore, assumed to be monomolecular reactions such as a change in the conformation of the protein-metal complex.

$(\tau_2^{FeIII})^{-1} = (64 \pm 5) \times 10^{-3} s^{-1}$

$(\tau_3^{FeIII})^{-1} = (3.3 \pm 0.2) \times 10^{-3} s^{-1}$

2.3. Copper(II) binding

2.3.1. Thermodynamics of copper(II) uptake

The thermodynamic constants of Copper(II)-frataxin interactions were determined by emission spectroscopy and microcalorimetry.

Size exclusion chromatography experiments show that, unlike with Fe^{3+}, $(Yfh1)_2$ does not oligomerize in the presence of Cu^{2+} (Figure III.11).
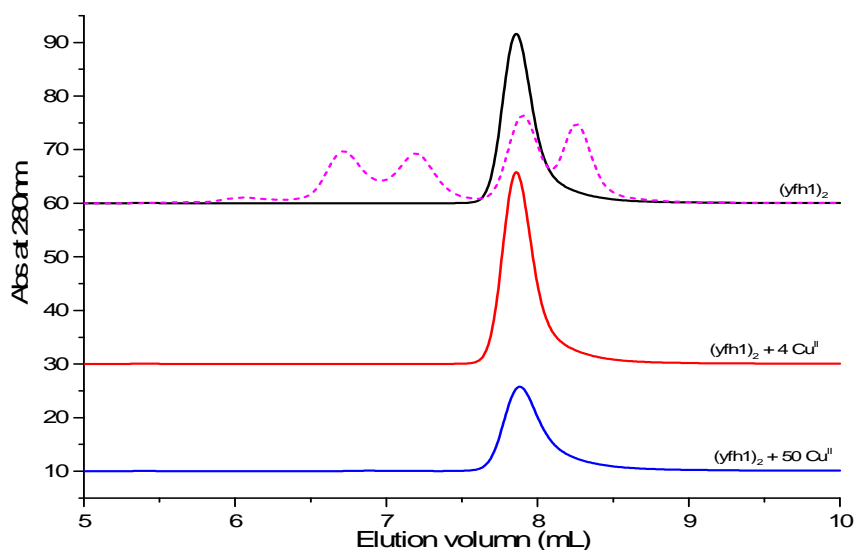
*Figure III.11: **Chromatograms of (Yfh1)₂** (V_e = 7.85 mL) **in absence** (black) **and presence of Cu^{II} at 4:1** (red) **or 50:1** (blue) **ratio**. Mobile phase: 50 mM KH$_2$PO$_4$ buffer, pH 7.0, injection and elution rate 1 mL/min. Detection by absorption at 280 nm. Overlaid dash line is the chromatogram of calibration mixture containing: dimeric bovine albumin (132 kDa), monomeric bovine albumin (66 kDa), ovalbumin (45 kDa), carbonic anhydrase (29 kDa), lactalbumine (14.2 kDa).*

The addition of Cu^{2+} to a solution of (Yfh1)₂ leads to a 3 nm red-shift (from 334 to 337 nm) and to a decrease in the fluorescence emission (Figure III.12).
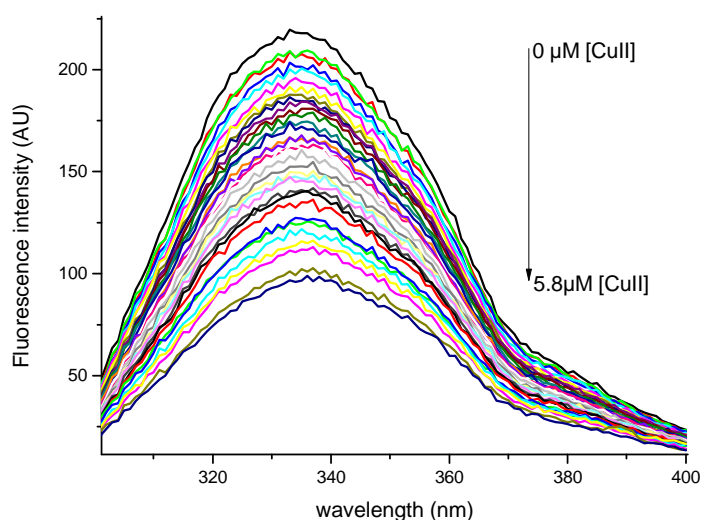

*Figure III.12: **Emission spectra** (λ_{ex}=280 nm) **of (Yfh1)₂ (0.12 µM) at different concentration of Cu^{2+}** (0 µM to 5.8 µM) at pH 7.0, ionic strength µ = 0.2 (50 mM Bis-Tris, 150 mM KCl).*

SPECFIT analysis shows two Cu^{2+} complexes form sequentially with (Yfh1)₂ which allows the measurement of two affinity constants for each subunit (equations III.17 & 18).

$$Yfh1 + Cu^{2+} \rightleftharpoons (Yfh1)Cu^{II} \qquad \text{(III.17)}$$

$$(Yfh1)Cu^{II} + Cu^{2+} \rightleftharpoons (Yfh1)Cu_2^{II} \qquad \text{(III.18)}$$

With $K_{d1}^{CuII} = \frac{[Yfh1][Cu^{2+}]}{[(Yfh1)Cu^{II}]}$; $K_{d2}^{CuII} = \frac{[(Yfh1)Cu^{II}][Cu^{2+}]}{[(Yfh1)Cu_2^{II}]}$;

The values of those constants are independent of pH in the 6.5-7.5 pH range. The average values are: $-\log K_{d1}^{CuII} = 6.9 \pm 0.5$ and $-\log K_{d2}^{CuII} = 5.5 \pm 0.6$.

Using microcalorimetry, the affinity constant of $(Yfh1)_2$ for Cu^{2+} was determined. Typically, a Cu^{2+} solution (600 µM) was injected under stirring in the calorimeter cell (166 µL) initially containing the $(Yfh1)_2$ solution (120 µM), with a typical injection sequence of 25×2 µl at 5 min intervals. Analysis of raw signal gave thermodynamics parameters of reaction between $(Yfh1)_2$ and Cu^{2+} (Figure III.13).

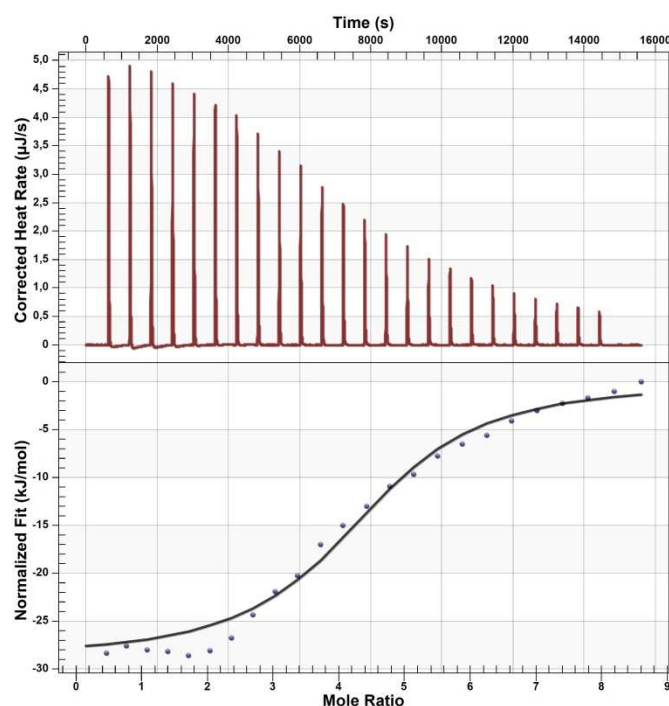*Figure III.13: **Raw ITC (top) and binding isotherm data** (bottom) **for Cu²⁺ to (Yfh1)₂**. The black lines in bottom graphs show the simulated fit to the binding isotherm data. Data were collected at 25 °C, pH 7.0, ionic strength µ = 0.2 (50 mM Bis Tris, 150 mM KCl).*

The binding of Cu^{2+} to $(Yfh1)_2$ is an exothermic process, as shown in the ITC experiment, $\Delta H_1 = -(28.2 \pm 0.5)$ kJ mol^{-1} & $\Delta H_2 = -(30 \pm 4)$ kJ mol^{-1}. The data were curve-fitted using a model of multiple independent binding sites. The fitting yields 2.2 ± 0.5 & 2.4 ± 0.3

equivalent Cu^{2+} bound to $(Yfh1)_2$ and $K_1 = (2.0 \pm 0.5) \times 10^7$ ($\log K_1 = 7.3$) and $K_2 = (3.4 \pm 0.8) \times 10^4$ ($\log K_2 = 4.5$), which are within the limits of uncertainty identical to those found spectrophotometrically.

2.3.2. Kinetics of Copper(II) uptake

When a solution of $(Yfh1)_2$ is mixed with a solution of Cu^{2+} in Bis-Tris buffer, three kinetic processes are observed (Figure III.14). The first is fast and occurs in the 50 ms range as exponential decrease of the fluorescence to yield a first kinetic product (Figure III.14A). The latter yields a second kinetic product in a process, which manifests by a monoexponential increase in emission occurring in the 200 s range (Figure III.14B). These two processes are followed by a slow kinetic phenomenon which lasts about 2000 s (Figure III.14C).
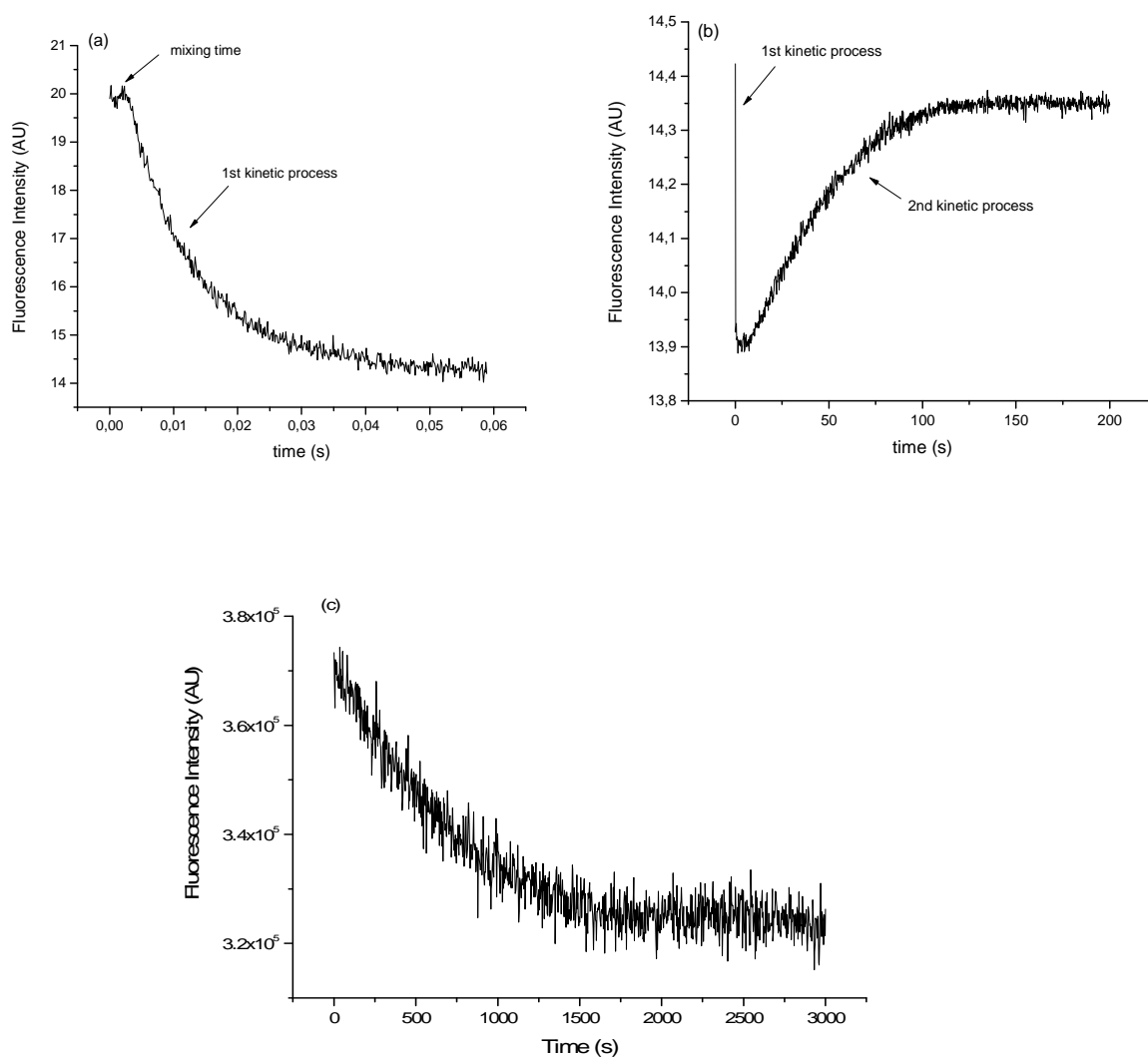

*Figure III.14: **Fluorescence intensity variation with time after a fast mixing of a (Yfh1)₂ solution** (0.5 μM) **with a solution of** (a) and (b) 25 μM **CuSO₄** at pH 7.3, (c) 200μM CuSO₄ at pH 7.0, 25.0 °C and ionic strength μ = 0.2 (50 mM Bis-Tris, 150 mM KCl).*

a) First kinetic process:

The reciprocal relaxation times associated to this first phenomenon depend on Cu^{2+} concentration, pH, but are independent of [Yfh1].
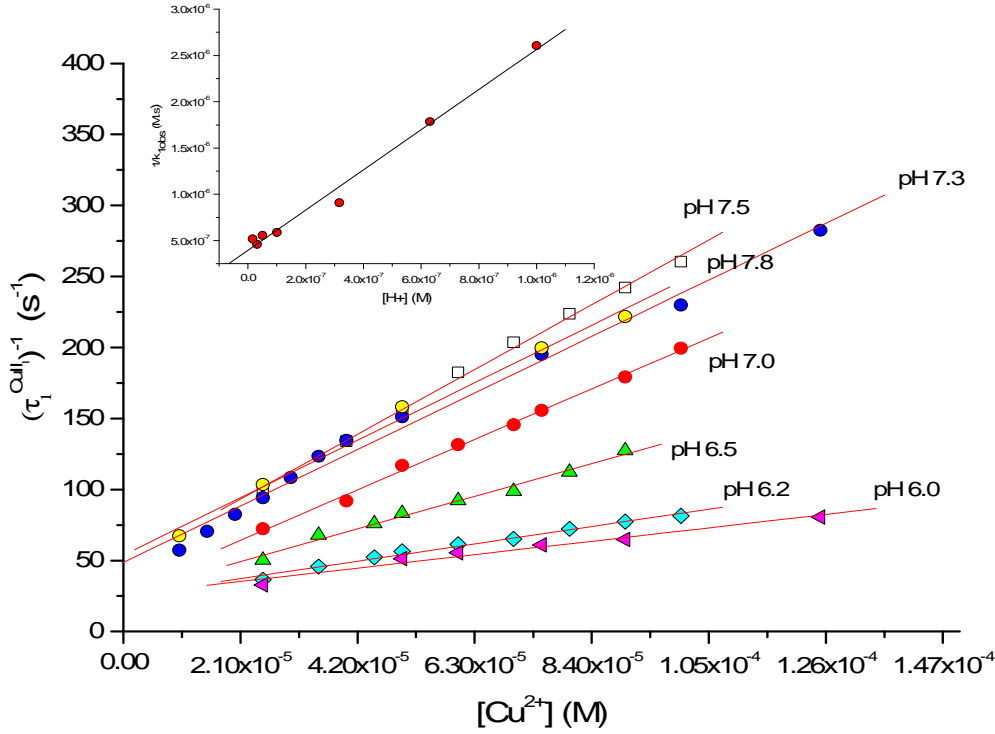

*Figure III.15: **Plot of** $(\tau_1^{CuII})^{-1}$ **against [Cu^{2+}]** at seven fixed pH values with [(Yfh1)₂] = 0.5 μM; 25 μM ≤ [Cu^{2+}] ≤ 125 μM. Inset: Plot of $1/k_{1obs}$ against [H^+]; intercept, (3.95 ± 0.4)×10⁻⁷M.s; slope, 2.17 ± 0.1 s; r = 0.9947.*

Under our experimental conditions ([Yfh1] <<[Cu^{2+}]) and at a fixed pH, there is a linear relationship between the experimental relaxation time $(\tau_1^{Cu^{II}})^{-1}$ and Cu^{2+} concentration (Figure III.15).

This can be expressed by equation III.19:

$$(\tau_1^{Cu^{II}})^{-1} = k_{1obs}^{Cu^{II}}[Cu^{2+}] + k_{-1obs}^{Cu^{II}} \qquad \text{(III.19)}$$

We ascribe this first step to the uptake of one Cu^{2+} by Yfh1 subunit (equation III.20).

From the slopes and intercepts of the best linear regression of τ^{-1} against [Cu^{2+}] performed at each of the seven fixed pHs (6.0, 6.2, 6.5, 7.0, 7.3, 7.5 and 7.8), k_{1obs} and k_{-1obs} are determined (Table III.2) at each pH value. k_{-1obs} appear to be independent of pH, whereas k_{1obs} increase with pH.

A plot of $1/k_{1obs}$ against $[H^+]^n$ shows a linear relationship for n = 1 (Inset Figure III.15) . This leads us to assume that the Cu^{2+} uptake by Yfh1 involves a single proton transfer.

Table III.2: Apparent rate constants $k_{1obs}^{Cu^{II}}$ and $k_{-1obs}^{Cu^{II}}$ after fast mixing of Cu^{II} and $(Yfh1)_2$ by stopped-flow.

pH	$k_{1obs}^{Cu^{II}}$ (s^{-1})	$k_{-1obs}^{Cu^{II}}$ (M^{-1}.s^{-1})
6.0	25.8 ± 3.1	(4.5 ± 0.4) x 10^5
6.2	27.1 ± 1.1	(5.6 ±0.1) x 10^6
6.5	26.0 ± 3.0	(1.1 ± 0.1) x 10^6
7.0	28.7 ± 2.8	(1.6 ± 0.1) x 10^6
7.3	34.4 ± 3.9	(1.8 ± 0.1) x 10^6
7.5	47.6 ± 3.6	(2.2 ± 0.1) x 10^6
7.8	52.7 ± 4.3	(1.9 ± 0.1) x 10^6

For this kinetics process, we suggest four possible mechanisms. Mechanisms I and II involve the protonation or deprotonation of the complex (Yfh1Cu^{2+}), while mechanisms III and IV deal with the protonation/deprotonation of Yfh1.

(i)   Mechanism I:
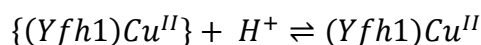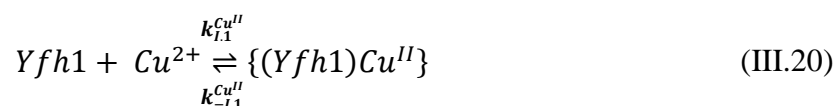
$$Yfh1 + Cu^{2+} \underset{k_{-I.1}^{Cu^{II}}}{\overset{k_{I.1}^{Cu^{II}}}{\rightleftharpoons}} \{(Yfh1)Cu^{II}\} \tag{III.20}$$

$$\{(Yfh1)Cu^{II}\} + H^+ \rightleftharpoons (Yfh1)Cu^{II}$$

With $K_{I.1}^{Cu^{II}} = \frac{[Yfh1][Cu^{2+}]}{\{(Yfh1)Cu^{II}\}}$ and $K_a^{(yfh1)Cu^{II}} = \frac{[\{(Yfh1)Cu^{II}\}]\times[H^+]}{[(Yfh1)Cu^{II}]}$

The reciprocal relaxation time associated with eq III. 20 can be expressed as equation III. 21:

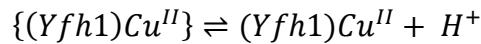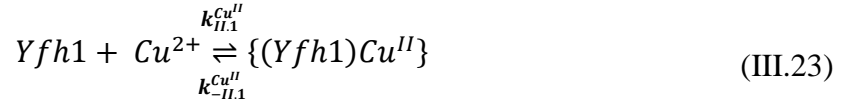$$\tau_{I.1}^{Cu^{II}} = k_{I.1}^{Cu^{II}} \times \left(1 + \frac{[H^+]}{K_a^{(Yfh1)Cu^{II}}}\right)[Cu^{2+}] + k_{-I.1}^{Cu^{II}} \tag{III.21}$$

Or:

$$k_{I.1obs}^{Cu^{II}} = k_{I.1}^{Cu^{II}} + \frac{k_{I.1}^{Cu^{II}}}{K_a^{(Yfh1)Cu^{II}}} [H^+] \tag{III.22}$$

Equation III.22 shows a linear relation between $k_{I.1obs}^{Cu^{II}}$ and [H$^+$] concentration, which is not compatible with the experimental observation (inset of figure III.15).

(ii)   <u>Mechanism II:</u>

$$Yfh1 + Cu^{2+} \underset{k_{-II.1}^{Cu^{II}}}{\overset{k_{II.1}^{Cu^{II}}}{\rightleftharpoons}} \{(Yfh1)Cu^{II}\} \tag{III.23}$$

$$\{(Yfh1)Cu^{II}\} \rightleftharpoons (Yfh1)Cu^{II} + H^+$$

With $K_{I.1}^{Cu^{II}} = \frac{[Yfh1][Cu^{2+}]}{\{(Yfh1)Cu^{II}\}}$ and $K_a^{\{(Yfh1)Cu^{II}\}} = \frac{[(Yfh1)Cu^{II}] \times [H^+]}{[\{(Yfh1)Cu^{II}\}]}$

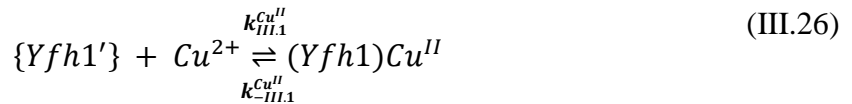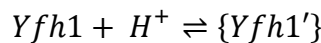The reciprocal relaxation time associated with equation III.23 can be expressed as equation III.24:

$$\tau_{II.1}^{Cu^{II}} = k_{II.1}^{Cu^{II}} \times \left(1 + \frac{K_a^{\{(Yfh1)Cu^{II}\}}}{[H^+]}\right)[Cu^{2+}] + k_{-II.1}^{Cu^{II}} \tag{III.24}$$

And:

$$k_{II.1obs}^{Cu^{II}} = k_{II.1}^{Cu^{II}} + k_{II.1}^{Cu^{II}} . K_a^{\{(Yfh1)Cu^{II}\}} \frac{1}{[H^+]} \tag{III.25}$$

Equation III.25 shows a linear relation between $k_{I.1obs}^{Cu^{II}}$ and [H$^+$]$^{-1}$, which is not compatible with the experimental observation (inset of figure III.15).

(iii)   <u>Mechanism III:</u>

$$Yfh1 + H^+ \rightleftharpoons \{Yfh1'\}$$

$$\{Yfh1'\} + Cu^{2+} \underset{k_{-III.1}^{Cu^{II}}}{\overset{k_{III.1}^{Cu^{II}}}{\rightleftharpoons}} (Yfh1)Cu^{II} \tag{III.26}$$

With $K_a^{(yfh1)} = \frac{[Yfh1] \times [H^+]}{[\{Yfh1\}']}$ and $K_d^{Cu^{II}} = \frac{[\{Yfh1'\}][Cu^{2+}]}{[(Yfh1)Cu^{II}]}$

The reciprocal relaxation time associated with equation III.26 can be expressed as equation III.27:

$$\tau_{III.1}^{Cu^{II}} = k_{III.1}^{Cu^{II}} \times \left(\frac{K_a^{(Yfh1)}}{[H^+]} + 1\right)^{-1} [Cu^{2+}] + k_{-III.1}^{Cu^{II}} \tag{III.27}$$
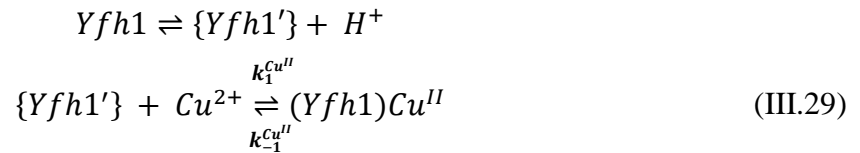
Or

$$k_{1obs}^{Cu^{II}} = k_{III.1}^{Cu^{II}} \times \left(\frac{K_a^{(yfh1)}}{[H^+]} + 1 \right)^{-1}$$

$$\frac{1}{k_{1obs}^{Cu^{II}}} = \frac{1}{k_{III.1}^{Cu^{II}}} + \frac{K_a^{(yfh1)}}{k_{III.1}^{Cu^{II}}} \times \frac{1}{[H^+]} \tag{III.28}$$

Equation III.28 shows a linear relation between $(k_{I.1obs}^{Cu^{II}})^{-1}$ and $[H^+]^{-1}$, which is not compatible with the experimental observation (inset of figure III.15).

(iv) Mechanism IV:

$$Yfh1 \rightleftharpoons \{Yfh1'\} + H^+$$

$$\{Yfh1'\} + Cu^{2+} \underset{k_{-1}^{Cu^{II}}}{\overset{k_1^{Cu^{II}}}{\rightleftharpoons}} (Yfh1)Cu^{II} \tag{III.29}$$

With $K_a^{(yfh1)} = \frac{[\{Yfh1'\}] \times [H^+]}{[Yfh1]}$ and $K_d^{Cu^{II}} = \frac{[\{Yfh1'\}][Cu^{II}]}{[(Yfh1)Cu^{II}]}$

The rate equation associated with equation III.29 is expressed as equation III.30:

$$\frac{d\Delta[(Yfh1)Cu^{II}]}{dt} = k_1^{Cu^{II}}\Delta[\{Yfh1'\}][Cu^{2+}] - k_{-1}^{Cu^{II}}\Delta[(Yfh1)Cu^{II}] \tag{III.30}$$

Masse conservation:

$$\Delta[Yfh1] + \Delta[\{Yfh1'\}] + \Delta[(Yfh1)Cu^{II}] = 0 \tag{III.31}$$

As $K_a^{(Yfh1)} = \frac{[\{Yfh1'\}] \times [H^+]}{[Yfh1]}$, we have: $\Delta[Yfh1] = \Delta[\{Yfh1'\}]\frac{[H^+]}{K_a^{(Yfh1)}}$. Equation III.31 becomes:

$$\Delta[\{Yfh1'\}] \left(1 + \frac{[H^+]}{K_a^{(Yfh1)}} \right) = -\Delta[(Yfh1)Cu^{II}] \tag{III.32}$$

The replacement of equation III.32 into equation III.30 leads to equation III.33:

$$\frac{d\Delta[Yfh1Cu]}{dt} = -\left(k_1^{Cu^{II}}(1 + \frac{[H^+]}{K_a^{(Yfh1)}})^{-1}[Cu^{2+}] + k_{-1}^{Cu^{II}} \right)\Delta[(Yfh1)Cu^{II}] \tag{III.33}$$

The reciprocal relaxation time associated with equation III.29 can be expressed as equation III.34:

$$(\tau_1^{Cu^{II}})^{-1} = k_1^{Cu^{II}} \times \left(1 + \frac{[H^+]}{K_a^{(Yfh1)}}\right)[Cu^{2+}] + k_{-1}^{Cu^{II}} \qquad (III.34)$$

With:
$$k_{1obs} = k_1^{Cu^{II}}\left(1 + \frac{[H^+]}{K_a^{(Yfh1)}}\right)^{-1} \qquad (III.35)$$

Or:
$$\frac{1}{k_{1obs}^{Cu^{II}}} = \frac{1}{k_1^{Cu^{II}}} + \frac{1}{k_1^{Cu^{II}}.K_a^{(Yfh1)}}[H^+] \qquad (III.36)$$

Equation III.36 expresses a linear relationship between $(k_{1obs}^{Cu^{II}})^{-1}$ and [H$^+$] (inset of figure III. 15).

Furthermore, Yfh1 emission spectra depend on pH as shown in Figure III.16. SPECFIT analysis of these spectra allowed the determination of the protodissociation constant, pK_a = 6.7 ± 0.1.
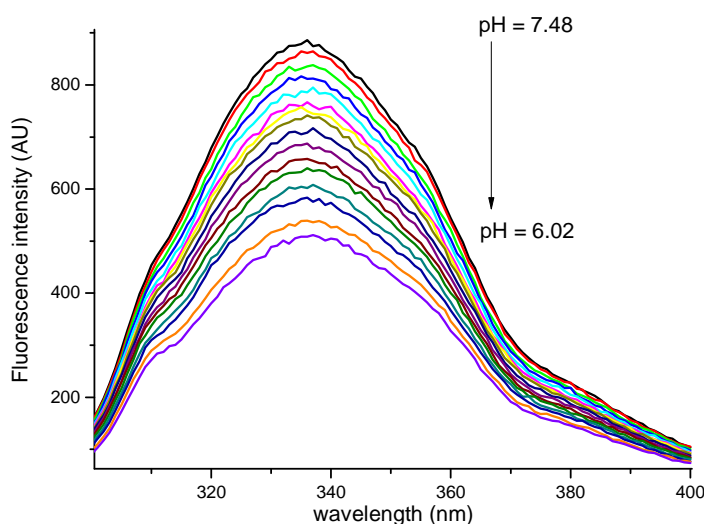

*Figure III.16: **Emission spectra** (λ_{ex} = 280 nm) **of (Yfh1)₂ (0.12 μM) at different pH values** and μ = 0.2 (Bis-Tris 50 mM, KCl 150 mM) at 25 °C.*

From the slope and intercept of the best line of the inset of Figure III.15, $k_1^{Cu^{II}}$ = (2.5 ± 0.2) x 10^6 M^{-1} s^{-1}, K_a = (1.8 ± 0.3) x 10^{-7} M values are determined. The latter is, within the limits of uncertainty, identical to the one determined by fluorescence titration (Figure III.16).

With K_a known, a linear regression of all experimental data at different pH and [Cu^{2+}] values against equation III.34 is obtained (Figure III.17). $k_1^{Cu^{II}}$ = (2.7± 0.1) x 10^6 M^{-1} s^{-1} was confirmed within the experimental uncertainty, and $k_{-1}^{Cu^{II}}$ = 30.4 ± 2.1 s^{-1} is determined from

the intercept of the best regression line of Figure III.17. This allows the measurement of $K_1^{CuII} = k_1^{CuII} / k_{-1}^{CuII} = 8.9 \times 10^4$ M^{-1}.

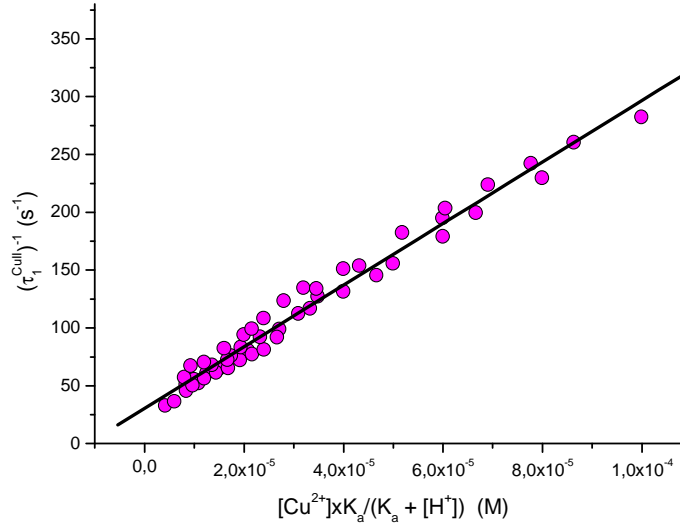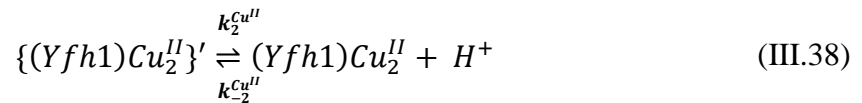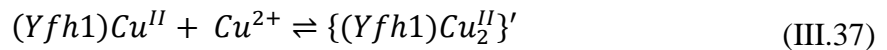*Figure III.17:* **Plot of** $(\tau_1^{CuII})^{-1}$ **against [Cu^{2+}]x K$_a$/(K$_a$+[H$^+$]);** *intercept of 30.4 $\pm$ 2.1 s^{-1}; slope (2.7 $\pm$ 0.05) x 10^6 M^{-1}.s^{-1}; r = 0.98934.*

b) Second kinetic process:

The reciprocal relaxation times related to the second phenomenon (Figure III.14b) depend on Cu^{2+} concentration and pH. We therefore, assumed that the uptake of a second Cu^{2+} is followed by structural conformation change that rate-limits a proton transfer (equation III.37-38):

$$(Yfh1)Cu^{II} + Cu^{2+} \rightleftharpoons \{(Yfh1)Cu_2^{II}\}' \tag{III.37}$$

$$\{(Yfh1)Cu_2^{II}\}' \underset{k_{-2}^{CuII}}{\overset{k_2^{CuII}}{\rightleftharpoons}} (Yfh1)Cu_2^{II} + H^+ \tag{III.38}$$

With: $K_{d1} = \frac{[Yfh1][Cu^{2+}]}{[(Yfh1)Cu^{II}]}$; $K_{d2} = \frac{[(Yfh1)Cu^{II}][Cu^{2+}]}{[(Yfh1)Cu_2^{II}]}$ and $K_{a2} = \frac{[\{(Yfh1)Cu_2^{II}\}'][H^+]}{[(Yfh1)Cu_2^{II}]}$

$$\Delta[(Yfh1)] = K_{d1} \frac{\Delta[(Yfh1)Cu^{II}]}{[Cu^{2+}]} = K_{d1}K_{d2} \frac{\Delta[(Yfh1)Cu_2^{II}]}{[Cu^{2+}]^2} \tag{III.39}$$

$$\Delta[(Yfh1)Cu^{II}] = K_{d2}\frac{\Delta[(Yfh1)Cu_2^{II}]}{[Cu^{2+}]} \tag{III.40}$$

The rate equation associated with equation III.38 is expressed as equation III.41:

$$\frac{d\Delta[\{(Yfh1)Cu_2^{II}\}']}{dt} = k_2^{Cu^{II}}\Delta[(Yfh1)Cu_2^{II}] - k_{-2}^{Cu^{II}}[H^+]\Delta[\{(Yfh1)Cu_2^{II}\}'] \tag{III.41}$$

The conservation mass allows us to write:

$$\Delta[(Yfh1)] + \Delta[(Yfh1)Cu^{II}] + \Delta[(Yfh1)Cu_2^{II}] + \Delta[\{(Yfh1)Cu_2^{II}\}'] = 0 \tag{III.42}$$

which leads to equation III.43:

$$K_{d1}K_{d2}\frac{\Delta[(Yfh1)Cu_2^{II}]}{[Cu^{2+}]^2} + K_{d2}\frac{\Delta[(Yfh1)Cu_2^{II}]}{[Cu^{2+}]} + \Delta[(Yfh1)Cu_2^{II}]$$
$$= -\Delta[\{(Yfh1)Cu_2^{II}\}'] \tag{III.43}$$

$$\Delta[\{(Yfh1)Cu_2^{II}\}'] = -\left(1 + \frac{K_{d2}}{[Cu^{2+}]} + \frac{K_{d1}K_{d2}}{[Cu^{2+}]^2}\right).\Delta[(Yfh1)Cu_2^{II}] \tag{III.44}$$

From equation III.44 and equation III.41, we obtained equation III.45:

$$\frac{d\Delta[\{(Yfh1)Cu_2^{II}\}']}{dt} = -\left[k_2^{Cu^{II}}\left(1 + \frac{K_{d2}}{[Cu^{2+}]} + \frac{K_{d1}K_{d2}}{[Cu^{2+}]^2}\right)^{-1} + k_{-2}^{Cu^{II}}[H^+]\right]\Delta[\{(Yfh1)Cu_2^{II}\}'] \tag{III.45}$$

The reciprocal relaxation time associated with equation III.38 is expressed as equation III.46

$$\tau_2^{Cu^{II}} = k_2^{Cu^{II}}\left(1 + \frac{K_{d2}}{[Cu^{2+}]} + \frac{K_{d1}K_{d2}}{[Cu^{2+}]^2}\right)^{-1} + k_{-2}^{Cu^{II}}[H^+] \tag{III.46}$$

$$\frac{\tau_2^{Cu^{II}}}{[H^+]} = k_2^{Cu^{II}}\frac{[Cu^{2+}]^2}{[H^+].([Cu^{2+}]^2 + K_{d2}[Cu^{2+}] + K_{d1}K_{d2})} + k_{-2}^{Cu^{II}} \tag{III.47}$$

With $K_{d1}^{Cu^{II}} = 1/K_1 = 5 \times 10^{-8}$ M^{-1}, and $K_{d2}^{Cu^{II}} = 2.94 \times 10^{-5}$ M^{-1}, determined earlier by ITC, the plot of the experimental data related to equation III.47 is linear (Figure III.18). From the slope of the best line, we determine $k_{-2}^{Cu^{II}} = 0.141 \pm 0.004$ M^{-1} s^{-1}.
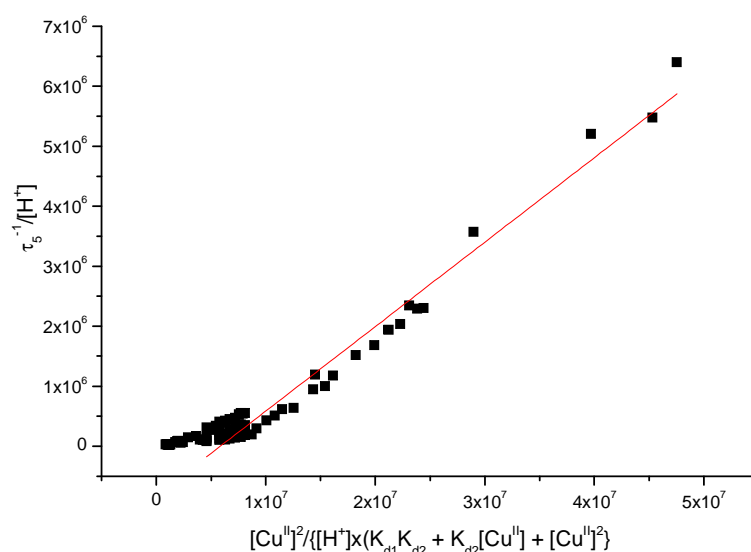
*Figure III.18: **Plot of $\tau_5^{-1}/[H^+]$ against $[Cu^{2+}]^2/\{[H^+]x(K_{d1}xK_{d2} + K_{d2}x[Cu^{2+}] + [Cu^{2+}]^2)\}$**; intercept of (-4.8 $\pm$ 0.8) x 10^5 s^{-1}, slope 0.114 $\pm$ 0.003 $M^{-1}.s^{-1}$; r = 0.97003.*

c) *Third kinetic process:*

The third kinetic process (Figure III.14c) seems to be independent of our experimental parameters. It is therefore assumed to be a molecular reaction, such as a conformational change, $(\tau_3^{CuII})^{-1} = (1.2 \pm 0.3) \times 10^{-3} s^{-1}$.

2.4. Copper(I) binding

2.4.1. Thermodynamics of copper(I) uptake

The Cu^+ donor to $(Yfh1)_2$ used in our experiment is the $Cu^I(GSH)_2$ complex. The synthesis of this complex and titration of Cu(I) were previously described (Ciriolo et al. 1990, Hanna et al. 1988).

The binding of $(Yfh1)_2$ with $Cu(GSH)_2$ was first investigated by size exclusion chromatography (Figure III.19a). When one equivalent of $Cu(GSH)_2$ is mixed with one equivalent of $(Yfh1)_2$ the chromatogram does not show any peaks corresponding to $Cu(GSH)_2$ or GSH. This indicates that the reaction between $(Yfh1)_2$ and $Cu(GSH)_2$ is not a Cu(I) exchange. Indeed, such an exchange should release GSH in the medium. We, therefore, assume that we are dealing with an interaction between $Cu(GSH)_2$ and the protein. On the other hand, when one to ten equivalents of GSH are mixed with one equivalent of $(Yfh1)_2$, we

do not observe any significant change in the elution peak of GSH (Figure III.19b). This result suggests that there is no specific interaction between (Yfh1)$_2$ and reduced glutathion.
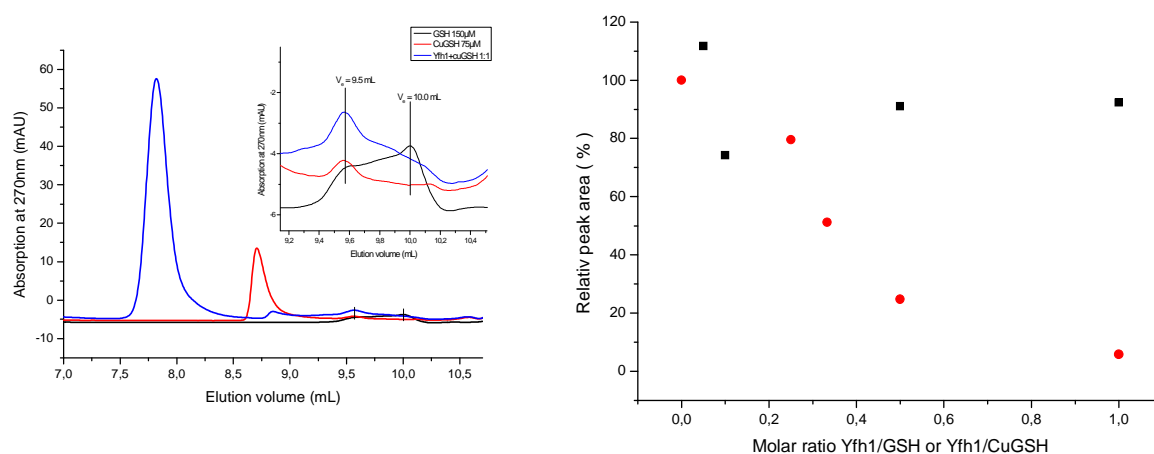

Figure III.19: (a) **Chromatograms of Cu(GSH)$_2$ 75 µM in the absence** *(red),* **or in the presence of (Yfh1)$_2$ 75 µM** *(blue);* **GSH 150 µM** *(black). Inset: zoom-in elution volume corresponding to GSSG/GSH at pH 7.0. Mobile phase: 50 mM KH$_2$PO$_4$ buffer, pH 7.0, elution rate 1 mL/min. Detection by UV-visible absorbance at λ = 270 nm. (b) Relative area under curve of GSH peaks (black square) and Cu(GSH)$_2$ peaks (red circle) in function of molar ratio between Yfh1/GSH or Yfh1/Cu(GSH)$_2$.*

Furthermore, under anaerobic conditions, at pH 7.0, the addition of Cu(GSH)$_2$ to a solution of (Yfh1)$_2$ leads to a decrease in the fluorescence emission accompanied by a 2 nm red-shift (from 334 to 336 nm) (Figure III.20). When the fluorescence intensity is plotted against the ratio of [Cu(GSH)$_2$]/[Yfh1] (Inset of Figure III.20), two linear sections are observed. The firest line occurs for $0 \leq$ [Cu(GSH)$_2$]/[(Yfh1)$_2$] ≤ 2, whereas the second occurs above the ratio of 2 metals per (Yfh1)$_2$ with, however, a lower slope.
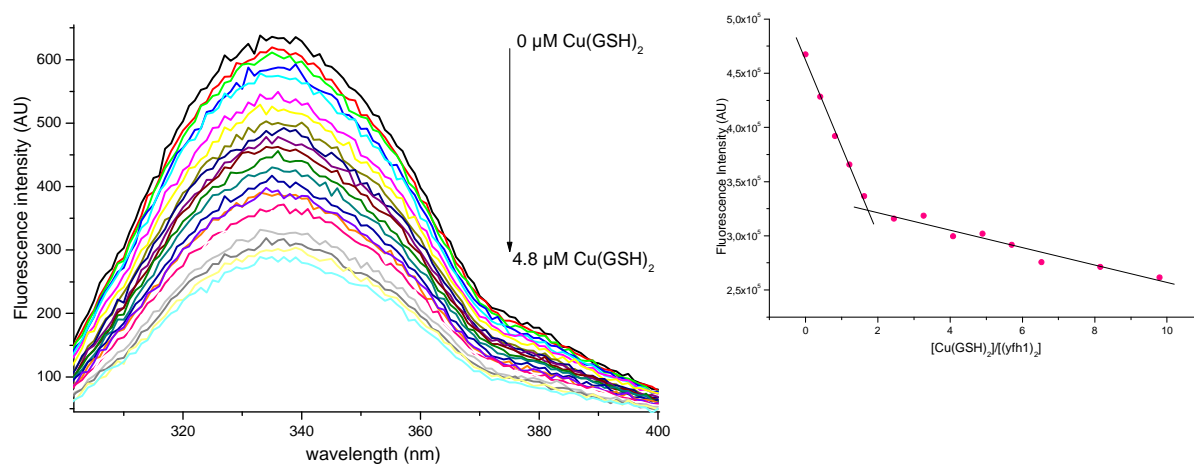

Figure III.20: (a) **Emission spectra** *(λ$_{ex}$ = 280 nm)* **of (Yfh1)$_2$ (0.24 µM) at different concentration of Cu(GSH)$_2$ (0 µM to 4.8 µM), at pH 7.0, ionic strength µ = 0.2 (50 mM Bis-Tris, 150 mM KCl); (b) Intensity fluorescence of (Yfh1)$_2$ at λ$_{em}$ = 334 nm in function of molar ratio [Cu(GSH)$_2$]/[(Yfh1)$_2$].*

This implies the formation of one complex with stoichiometry of 2 Cu(GSH)$_2$ per (Yfh1)$_2$ (equation III.48). SPECFIT analysis allows the determination of the dissociation constant of the Cu$^+$-Yfh1 subunit complex (equation III.49), -log K_d^{CuI} = 7.5 ± 0.5. The same experiments were repeated in the presence of 1.5 mM GSH, and at different pHs (6.5 < pH < 7.8). The dissociation constants were identical to that measured at pH 7.0.

$$Yfh1 + \text{Cu(GSH)}_2 \rightleftharpoons (Yfh1)\text{Cu(GSH)}_2 \qquad \text{(III.48)}$$

With $K_d^{CuI} = \dfrac{[\text{Cu(GSH)}_2][Yfh1]}{[(Yfh1)\text{Cu(GSH)}_2]}$ (III.49)

2.4.2. Kinetics of Copper(I) uptake

When a solution of (Yfh1)$_2$ is mixed with a solution of Cu(GSH)$_2$ in Bis-Tris buffer, three kinetic processes are observed (Figure III.21). The first appears as a monoexponential increase in the fluorescence intensity occuring in the 500 ms range (Figure III.21a). The second kinetic process occurs in the 20 s range as a monoexponential increase in the emission (Figure III.21b). Finally, the last process is a slow kinetic phenomenon which lasts about 3000 s (Figure III. 21c).
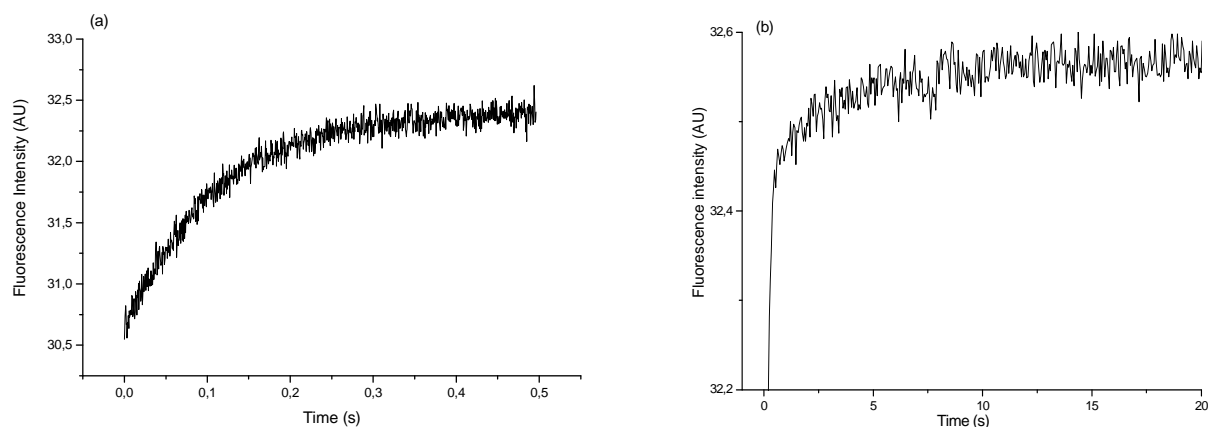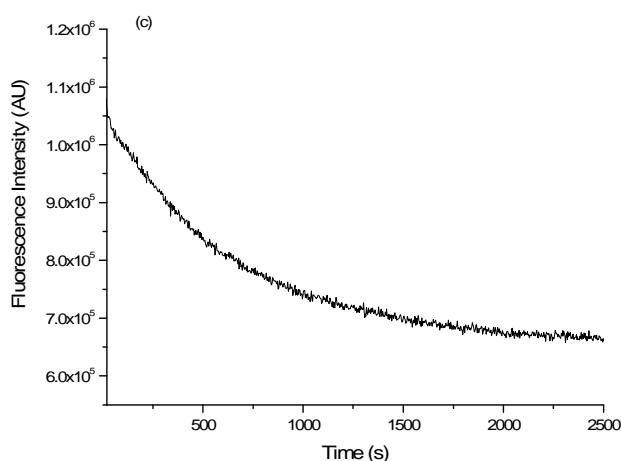
*Figure III.21: **Fluorescence intensity variation with time after a fast mixing of a (Yfh1)₂ solution (1 μM) with a solution of 20 μM Cu(GSH)₂** at pH 7.0, at pH 7.0, 25.0 °C and ionic strength μ = 0.2 (50 mM Bis-Tris, 150 mM KCl).*

a) First kinetic process:

The experimental reciprocal relaxation times related to the first process (Figure III.21a) depend on Cu(GSH)$_2$ concentration. They grow linearly with the Cu$^+$ concentration to reach a plateau above [Cu(GSH)$_2$] ≥ 75 μM (Figure III.22).

*Figure III.22: **Plot of $(\tau_1^{Cu^I})^{-1}$ against [Cu(GSH)₂] at pH 7.0 and T= 25•C**. Inset: Plot of $(\tau_1^{Cu^I})^{-1}$ against [Cu(GSH)₂]/([Cu(GSH)₂] + $K_1^{Cu^I}$ with $K_1^{Cu^I}$ = 35 μM; slope, 10.8 ± 0.8 s⁻¹; intercept, 5.8 ± 0.5 s⁻¹; r = 0.98418.*

As for Fe^{2+}, we assumed that this phenomenon is the uptake of a first $Cu(GSH)_2$ followed by a monomolecular reaction (equation III.50-51).

$$(Yfh1) + Cu^+ \rightleftharpoons \{(Yfh1)Cu^I\} \qquad \text{(III.50)}$$

$$\{(Yfh1)Cu^I\} \underset{k_{-1}^{CuI}}{\overset{k_1^{CuI}}{\rightleftharpoons}} (Yfh1)Cu^I \qquad \text{(III.51)}$$
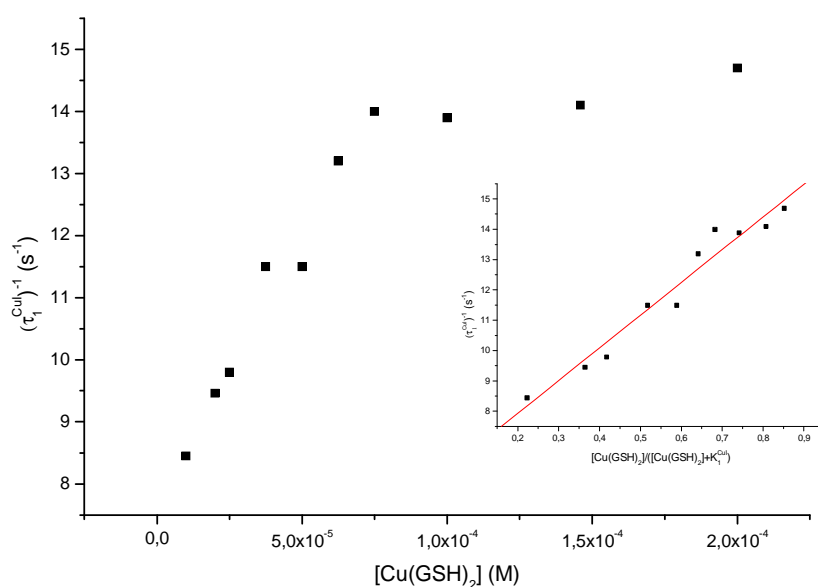
With an overall dissociation constant $K_1^{CuI} = \frac{[(Yfh1)Cu^I]}{[Yfh1][Cu^+]}$ and $(K_1^{CuI})' = \frac{[(Yfh1)Cu^I]}{[\{(Yfh1)Cu^I\}]} = \frac{k_1^{CuI}}{k_{-1}^{CuI}}$.

The reciprocal relaxation time equation associated with equation III. 51 can be expressed as equation III. 52:

$$(\tau_1^{CuI})^{-1} = \frac{k_1^{CuI}[Cu^+]}{[Cu^+] + K_1^{CuI}} + k_{-1}^{CuI} \qquad \text{(III.52)}$$

Varying K_1^{CuI} from 1 to 100 μM with a ΔK_1^{CuI} step of 5 μM shows that the best linear regression of $(\tau_1^{CuI})^{-1}$ against $[Cu^+]/(K_1^{CuI} + [Cu^+])$ is obtained for $K_1^{CuI} = 35 \pm 5$ μM (Inset Figure III.22). From the slope and intercept, $k_1^{CuI} = 10.8 \pm 0.8$ s^{-1}, $k_{-1}^{CuI} = 5.8 \pm 0.5$ s^{-1} and $(K_1^{CuI})' = 1.9 \pm 0.3$ are determined.

b) Second and third kinetic processes

These 2nd and 3rd processes (Figure III.21b & c) are independent of $Cu(GSH)_2$ concentrations. They are, therefore, assumed to be monomolecular reactions, which may imply changes in conformation.

$(\tau_2^{CuI})^{-1} = (2.8 \pm 0.3)$ x 10^{-1} s^{-1} and $(\tau_3^{CuI})^{-1} = (1.6 \pm 0.7)$ x 10^{-3} s^{-1}.

2.5. Manganese (II) and zinc (II) binding

As the others metals, the addition of Mn(II) or Zn(II) to a solution of $(Yfh1)_2$ leads to the decrease of fluorescence emission intensity.

Manganese
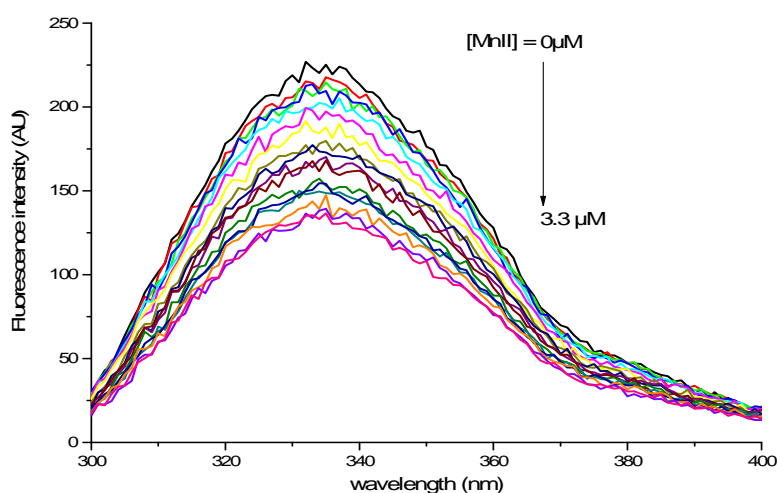
Figure III.23: **Emission spectra** *(λ_{ex}=280 nm) of (Yfh1)₂ (0.12 μM) at different concentration of* **Mn²⁺** *(0 μM to 3.3 μM) at pH 7.0, ionic strength μ = 0.2 (50 mM Bis-Tris, 150 mM KCl).*

SPECFIT analysis shows that two Mn^{2+} complexes form sequentially with $(Yfh1)_2$ which allows the measurement of two affinity constants for each subunit (equations III.53 and 54).

$$(Yfh1)_2 + Mn^{2+} \rightleftharpoons (Yfh1)_2Mn^{II} \tag{III.53}$$

$$(Yfh1)_2Mn^{II} + Mn^{2+} \rightleftharpoons (Yfh1)_2Mn^{II}_2 \tag{III.54}$$
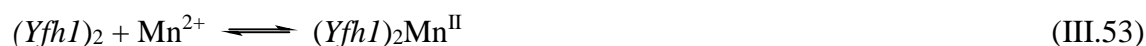
With $-logK_{d1}^{Mn^{II}} = 7.4 \pm 0.1$ and $-logK_{d2}^{Mn^{II}} = 6.4 \pm 0.2$

Zinc

SPECFIT analysis shows that two Zn^{2+} complexes form sequentially with $(Yfh1)_2$ which allows the measurement of two affinity constants for each subunit $-logK_{d1}^{Zn^{II}} = 5.8 \pm 0.2$ and $-logK_{d2}^{Mn^{II}} = 6.1 \pm 0.1$ (equation III.55 & 56).

$$(Yfh1)_2 + Zn^{2+} \rightleftharpoons (Yfh1)_2Zn^{II} \tag{III.55}$$

$$(Yfh1)_2Zn^{II} + Zn^{2+} \rightleftharpoons (Yfh1)_2Zn^{II}_2 \tag{III.56}$$
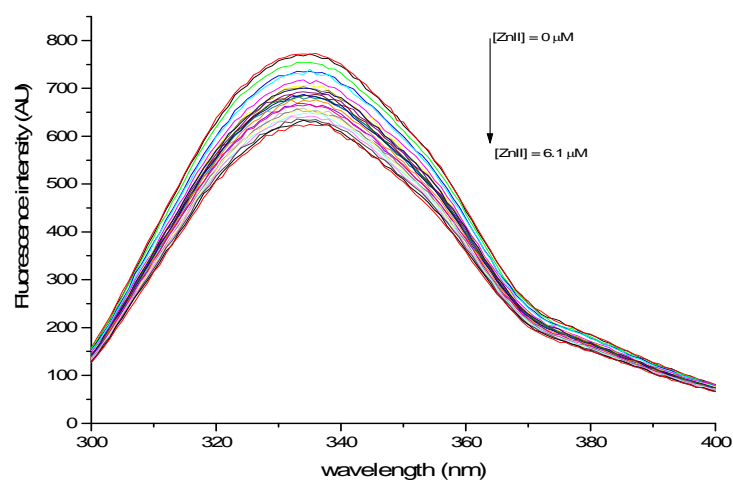
Figure III.24: **Emission spectra** *(λ_{ex}=280 nm)* **of (Yfh1)$_2$** *(0.12 μM)* **at different concentration of Zn^{2+}** *(0 μM to 6.1 μM) at pH 6.5, ionic strength μ = 0.2 (50 mM Bis-Tris, 150 mM KCl pH 6.8).*

3. Discussion

3.1. Metal-Yfh1 interaction

In this chapter, we investigated the uptake by yeast frataxin (Yfh1)$_2$ of some of the important metals involved in the metabolism and present in mitochondria, such as Fe^{II}/Fe^{III}; Cu^{I}/Cu^{II}; Mn^{II} and Zn^{II}. Yfh1 binds these metals forming complexes with dissociation constants in the micromolar range (Table III.3). In the presence of Fe(III), (Yfh1)$_2$ forms an oligomer, with a dissociation constant of 1.8 µM, whereas it does not with Cu(I) or Cu(II) (Figure III.7 &11). By ITC, we showed that (Yfh1)$_2$ interacts with 8 to 10 Fe(III), this metal-binding induces the formation of a four subunits complex. No other oligomeric form was observed under our experimental conditions, whereas Isaya's group detected a trimer and a 24-mer at high Fe(II) concentration, and after iron oxidation (Adamec et al. 2000, Soderberg et al. 2013). The physiological function of this oligomer is unclear, nevertheless, it was assumed to be an iron donor to Fe-S cluster biosynthesis or to play a role in iron storage (Vaubel and Isaya 2013).

Frataxin has an acidic ridge that covers almost a quarter of its surface. This area seems essential for its physiological function. On Yfh1, the exposed acidic residues are localized on the α1 helix and the β1 strand, and are semi-conserved between the different species (D78, D86, E89, E90, and D101 – Figure III.25). The aim of this work was to investigate the eventual specificity iron- binding to frataxin. We have studied the thermodynamics and kinetics of the interactions of yeast frataxin with Fe(II), Fe(III), Cu(I) and Cu(II) by fast kinetic technics, microcalorimetry, emission spectrophotometry and size exclusion chromatography. The bioavailable metal pools in mitochondria mainly contain iron, zinc, copper and manganese (Atkinson and Winge 2009, McCormick et al. 2015). These metals are weakly complexed by low molecular ligands. In yeast mitochondria, they are at the concentration of ~ 90 µM for Fe complex, ~ 16 µM for the dominant copper species, ~ 2 µM for Mn and ~ 110 µM for Zn (McCormick et al. 2015). On the other hand, in mitochondria the number of yeast frataxin units was estimated to vary from 200 to 1500, which implies concentrations in the µM range (0.4 to 60 µM) (Seguin et al. 2009).
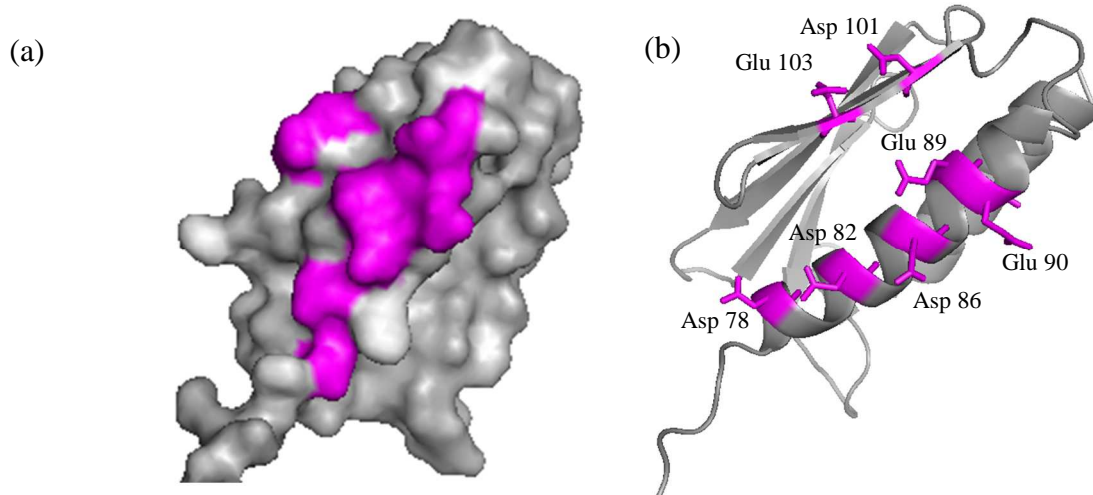
*Figure III.25: **The iron-binding residues** (rose) **with numbering refers to Yfh1 are indicated on secondary structural** (Cook et al. 2006, Foury et al. 2007). Yfh1 structure presents as (a) space-filled (b) ribbon.*

We confirmed by fluorescence that yeast frataxin binds Fe(II), with dissociation constants values of 2.5×10^{-7} M for the (*Yfh1*)Fe^{II} complex and 1.6×10^{-5} M for the second complex (*Yfh1*)Fe$^{II}_2$. The average dissociation constant for one iron reported for one subunit of frataxin is 2 µM, which is close to the Kd values previously found for Yfh1 by Cook et al. (3 and 2 µM) and for CyaY by Bou-Abdallah et al. (~ 4µM) (Bou-Abdallah et al. 2004, Cook et al. 2006). In this work, we investigated the role of frataxin in copper homeostasis and focused on the Cu-Yfh1 interaction. Indeed, Seguin et al. showed that the copper added in the growth medium was more toxic for ΔYfh1 cells than for wild type cells (Seguin et al. 2010). We showed here that (Yfh1)$_2$ interacts with Cu(II) and Cu(I), with higher affinities than Fe(II) (Table III.3).

Table III.3: Comparison of dissociation constants of metal-Yfh1 complexes determined by spectrophotometry, at pH 7.0 and at 25 °C

Metals	-logK$_{d1}$	-logK$_{d2}$
Fe^{II}	6.6 ± 0.2	4.8 ± 0.3
Cu^{II}	6.9 ± 0.3	5.5 ± 0.3
Cu^{I}	7.5 ± 0.3	-
Mn^{II}	7.4 ± 0.1	6.4 ± 0.2
Zn^{II}	5.8 ± 0.2	6.1 ± 0.1

The formation of complexes between Cu(II) and $(Yfh1)_2$, are shown to be enthalpically privileged ($\Delta H < 0$, Figure 12). This negative value of the enthalpy indicates coordination bonds and/or electrostatic interactions between Cu(II) and residues of the protein. As for Fe(II), Yfh1 presents two independent binding sites for Cu(II). The affinity constants in the first complex ($Yfh1$)M and in the second one ($Yfh1$)M_2 are higher for Cu(II) than for Fe(II). But the highest affinity found is for the complex formed between $Yfh1$ subunit and one $Cu(GSH)_2$ ($\sim 10^{7.5}$ M^{-1}). Copper is essential for respiratory, metabolic and stress response enzymes. Redox cycling between Cu(II) and Cu(I) oxidation states is a fundamental requirement for single electron transfer reactions in copper-containing proteins. In mitochondria, the two main copper enzymes are cytochrome c oxidase, the last electron acceptor in the respiratory chain, and superoxide dismutase 1, a copper-zinc enzyme involved in oxidative stress. In a Fenton-like reaction, Cu(I) generates reactive oxygen species which can damage cell components. To avoid radical formation, copper transfer occurs *via* a direct protein-protein interaction between copper enzymes and copper chaperones (Robinson and Winge 2010, Rosenzweig and O'Halloran 2000). These proteins present similar $\alpha-\beta$ sandwich structures that are also observed in frataxin. On the other hand, frataxin does not possess the conserved CXXC motif involved in Cu(I) binding in the copper chaperones. Nevertheless, in addition to the negatively charged residues of Yfh1 there are four histidine (H74, H83, H95 and H106), and a cysteine (C98) (Figure III.27) which are well-known to be Cu(II) and Cu(I) ligands, respectively, and which may improve the chelation to frataxin.
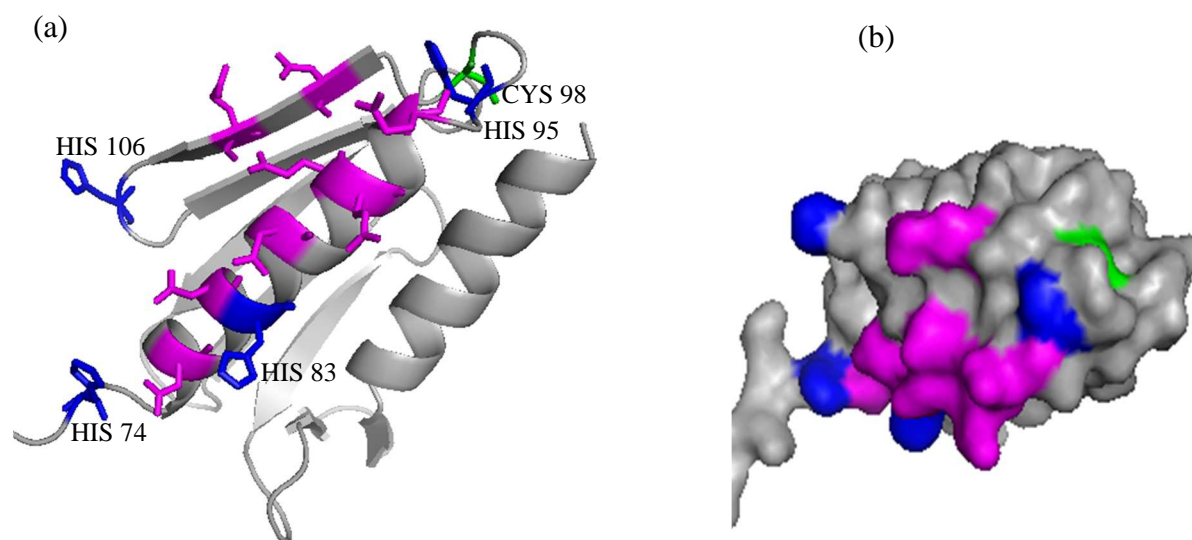

*Figure III.26: **In addition to iron-binding residues (rose), four histidines (blue) and a cysteine (green) are also found near of (α1/β1) interface.** The residues are indicated with numbering refers to Yfh1. Yfh1 structure presents as (a) ribbon (c) space-filled.*

3.2. Role of glutathion

Cu(I) used in our experiment is the $Cu^I(GSH)_2$ complex. Reduced glutathione is the most abundant non-protein thiol-molecules in cells. It contributes to thiol redox-control and plays a role in iron metabolism in cytoplasm and mitochondria (Gostimskaya and Grant 2016, Kumar et al. 2011, Toledano et al. 2013). The intracellular concentration of GSH varies from 2 to 10 mM and may form a stable complex with labile Cu(I) (Osterberg et al. 1979). We show by size exclusion chromatography that $(Yfh1)_2$ interacts with the entire $Cu^I(GSH)_2$ complex, but not with GSH alone (Figure III.19 a & b). Furthermore, the presence of GSH in the medium has no effect on the dissociation constant values for both Cu(I) and Fe(II)-frataxin complexes (Table III.1). In cytoplasm, Fe(II)-GSH is the dominant component of the iron labile pool and provides iron to mitochondrion for heme and iron-sulfur cluster maturation (Hider and Kong 2011). In addition, in depleted Yfh1 cells, iron accumulates in mitochondria, leading to an increased GSH flux or a decrease in glutathione export (Bulteau et al. 2012). Glutathione can coordinate and stabilize $[Fe_2S_2]$ iron-sufur centers (Qi et al. 2012). However, in glutaredoxin, GSH ligands are unstable and can be exchanged with free GSH, which inhibits Fe-S cluster transfer to ferredoxin (Wang et al. 2012). Frataxin is involved in Fe-S cluster (ISC) biosynthesis, it interacts with the Fe-S cluster machinery composed by the cysteine desulfurase Nfs1, its activator Isd11 and scaffold protein Isu1. Nevertheless, the role of Yfh1 in the Fe-S cluster biosynthesis is still unclear. As frataxin is an iron-binding protein and as it interacts with Isu1, it was first thought to provide iron to the Fe-S cluster (Stemmler et al. 2010). Yoon *et al.* showed that a single mutation (M107I) in Isu1 improves the Fe-S cluster enzymatic activities in Yfh1-depleted cells, implying that frataxin plays a minor role as an iron donor (Yoon H. et al. 2015, Yoon H. et al. 2012). Recently, frataxin was suggested to be an allosteric effector of the ISC complex: the bacterial ortholog frataxin CyaY strengthens the interaction between desulfurase and scaffold proteins in bacteria (Prischi et al. 2010); Yfh1 stimulates binding of cysteine to Nfs1, by inducing exposure of substrate-binding site and enhances the Nfs1 activity (Pandey et al. 2013, Yoon H. et al. 2014) (Figure III.28). Moreover, human frataxin increases the rate of persulfide formation on human scaffold protein (IscU) and of sulfur transfer from Nfs1 persulfide to IscU or to small thiols such as cysteine or glutathione (Parent et al. 2015) (Figure III.29).
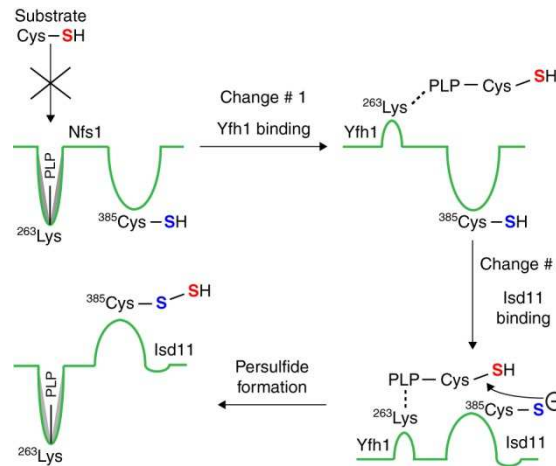
*Figure III.28: **Model for two-tier regulation of persulfide formation by Nfs1**. The enzyme Nfs1 is shown by a green line. The Lys263 residue of the Nfs1 substrate-binding site forms a Schiff base with the cofactor pyridoxal phosphate. Nfs1 by itself inefficiently binds the substrate cysteine (Cys-SH, sulfur indicated in red). Frataxin/Yfh1 interacts with Nfs1, inducing a conformational change in the enzyme (Change #1) and exposing new sites with Lys263-PLP, now able to efficiently bind the substrate cysteine. Isd11 then interacts with Nfs1 with substrate cysteine already bound, inducing a second conformational change (Change #2), and bringing the substrate cysteine (red sulfur) into proximity to the Cys385 (sulfur indicated in blue) in the peptide backbone of the Nfs1 active site loop. A nucleophilic attack by the thiolate anion of the active site Cys385 extracts the –SH group of the substrate, forming a covalent persulfide (Nfs1-S-SH)(Pandey et al. 2013).*
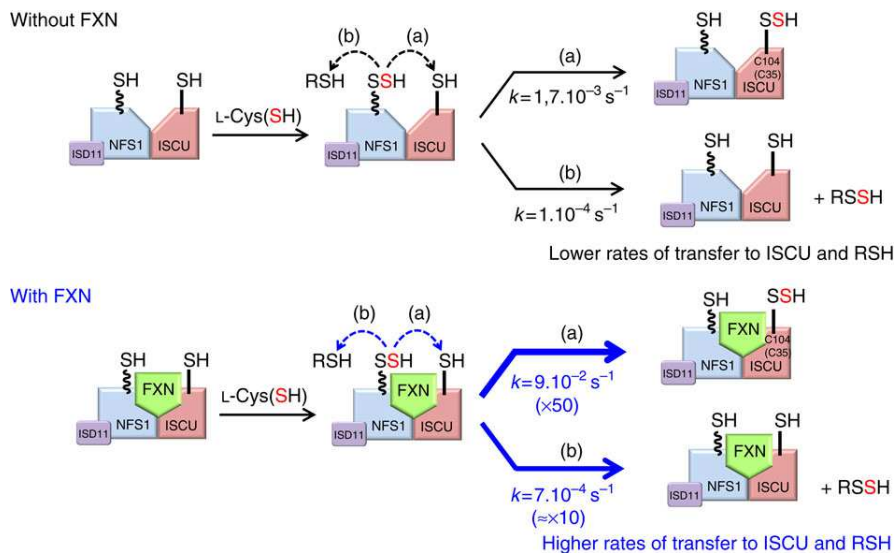

*Figure III.29: **In the presence of frataxin, the rates of two reactions are enhanced** (a) sulfur transfer to ISCU and (b) sulfur transfer to free thiol-containing molecules (RSH) such as L-cysteine and GSH. The rate constants are indicated (Parent et al. 2015).*

Yeast frataxin presents a high affinity for Cu(GSH)$_2$, whereas it cannot bind GSH. The role of this Yfh1-(Cu(GSH)$_2$) complex is unknown, we can nevertheless, emphasize several proposals: (i) copper may help the approach of GSH to the ISC complex *via* frataxin; (ii) CuI-Yfh1 can increase the rate of persulfide formation or increase the interaction between the proteins of the ISC machinery. To confirm these hypotheses some additional experiments are required.

3.3.   Kinetic of metal-uptake by yeast frataxin

We report in this chapter the mechanisms of metal-uptake by yeast frataxin (Table III.4). For all the studied metals, we observe at least three kinetics steps. The first phenomena correspond to the uptake of a first cation and are fast, they occur in 50 to 500 ms. For Fe(II) and Cu(I), the experimental reciprocal relaxation times related to these first kinetic steps increase with metal concentration to reach a plateau (Figure III.3 & III. 22). As already described, this implies a fast uptake of a cation followed by a monomolecular reaction, such as a conformational change (Table III.4) (Eid et al. 2014, Pilotelle-Bunner et al. 2009, Thompson et al. 2011). The equilibrium constants related to these changes in conformation are identical for both metals. These first steps are followed by two other kinetics steps. For Fe(II), the second step corresponds to the uptake of a second iron and the third to a change of the conformation which may stabilize the iron-Yfh1 complex. As (Yfh1)$_2$ can complex only one Cu(GSH)$_2$, the second and third kinetic phenomena correspond to monomolecular reactions. On the other hand, a first Cu(II) is uptaken by a deprotonated form of Yfh1. The pKa value of this acid-base reaction is 6.7 ± 0.1 (Table III.5), which may imply the deprotonation of a histidine residue. Indeed, at the acidic surface, there are three histidines (H74, H83 and H95) which may be involved in Cu(II) interaction.

This work revisited the formation of complexes between iron and frataxin and determined the mechanism these interactions. In addition, we investigated the copper-frataxin interaction and, confirmed that frataxin does not specifically bind iron. The best affinity constant found is for Cu(GSH)$_2$. Nevertheless, the role of the (Yfh1)-Cu(GSH)$_2$ complex is unknown and further experiments should be performed to determine its involvement in the Fe-S cluster biosynthesis or in the protection against oxidative stress.

Table III.4: Metal uptake by Yfh1

Reaction	Direct rate constant	Reverse rate constant	Equilibrium constant
FeII uptake $Yfh1 + Fe^{2+} \rightleftharpoons \{(Yfh1)Fe^{II}\}$ (3) $\{(Yfh1)Fe^{II}\} \rightleftharpoons (Yfh1)$ (4) $(Yfh1)Fe^{II} + Fe^{2+} \rightleftharpoons (Yfh1)Fe^{II}{}_2$ (5)	 23 ± 1 s^{-1} (1.15 ± 0.04) x 10^3 M^{-1} s^{-1}	 11.5 ± 0.7 s^{-1} (9.9 ± 1.3) x 10^{-2} s^{-1}	200 ± 10 µM 2.0 ± 0.1 86 ± 5 µM
FeIII uptake $Yfh1 + Fe^{3+} \rightleftharpoons (Yfh1)Fe^{III}$ (9)	 (11.5 ± 0.5) x 10^4 M^{-1} s^{-1}	 3.4 ± 0.7 s^{-1}	 3.4 x 10^4
CuII uptake $Yfh1 \rightleftharpoons (Yfh1)' + H$ (14) $(Yfh1)' + Cu^{2+} \rightleftharpoons (Yfh1)Cu^{II}$ (15) $(Yfh1)Cu^{II} + Cu^{2+} \rightleftharpoons ((Yfh1)Cu^{II}{}_2)'$ (17) $((Yfh1)Cu^{II}{}_2)' \rightleftharpoons (Yfh1)Cu^{II}{}_2 + H^+$ (18)	 (2.7 ± 0.1) x 10^6 M^{-1} s^{-1}	 30.4 ± 2.1 s^{-1} 0.114 ± 0.003 M^{-1} s^{-1}	 (1.8 ± 0.3) x 10^{-7} 8.9 x 10^4 M^{-1}
Cu(GSH)₂ uptake $Yfh1 + Cu^+ \rightleftharpoons \{(Yfh1)Cu^I\}$ (22) $\{(Yfh1)Cu^I\} \rightleftharpoons (Yfh1)Cu^I$ (23)	 10.8 ± 0.8 s^{-1}	 5.8 ± 0.5 s^{-1}	 35 ± 5 µM 1.9 ± 0.3

REFERENCES

Adamec J, Rusnak F, Owen WG, Naylor S, Benson LM, Gacy AM, Isaya G. 2000. Iron dependent self-assembly of recombinant yeast frataxin-impliation for Friedreich's ataxia. Am. J. Hum. Genet. 67: 549-562.

Aloria K, Schilke B, Andrew A, Craig EA. 2004. Iron-induced oligomerization of yeast frataxin homologue Yfh1 is dispensable in vivo. EMBO Rep 5: 1096-1101.

Atkinson A, Winge DR. 2009. Metal acquisition and availability in the mitochondria. Chem Rev 109: 4708-4721.

Bayot A, Santos R, Camadro JM, Rustin P. 2011. Friedreich's ataxia: the vicious circle hypothesis revisited. BMC Med 9: 112.

Bernasconi CF. 1976. Relaxation kinetics. New-York: Academic Press.

Bou-Abdallah F, Adinolfi S, Pastore A, Laue TM, Dennis Chasteen N. 2004. Iron binding and oxidation kinetics in frataxin CyaY of Escherichia coli. J Mol Biol 341: 605-615.

Bulteau AL, Planamente S, Jornea L, Dur A, Lesuisse E, Camadro JM, Auchere F. 2012. Changes in mitochondrial glutathione levels and protein thiol oxidation in yfh1 yeast cells and the lymphoblasts of patients with Friedreich's ataxia. Biochim Biophys Acta 1822: 212-225.

Ciriolo MR, Sette M, Paci M, Rotilio G. 1990. A study of the intracellular effects of glutathione by 1H-spin echo NMR of intact human erythrocytes. Biochem Int 20: 397-403.

Cook JD, Bencze KZ, Jankovic AD, Crater AK, Courtney N. Busch, Bradley PB, Ann J. Stemmler, Mark R. Spaller, Stemmler* TL. 2006. Monomeric Yeast Frataxin Is an Iron-Binding Protein†. Biochem J 45: 7767-7777.

Correia AR, Wang T, Craig EA, Gomes CM. 2010. Iron-binding activity in yeast frataxin entails a trade off with stability in the alpha1/beta1 acidic ridge region. Biochem J 426: 197-203.

Dhe-Paganon S, Shigeta R, Chi YI, Ristow M, Shoelson SE. 2000. Crystal structure of human frataxin. J Biol Chem 275: 30753-30756.

Eid C, Hemadi M, Ha-Duong NT, El Hage Chahine JM. 2014. Iron uptake and transfer from ceruloplasmin to transferrin. Biochim Biophys Acta 1840: 1771-1781.

Eigen M, DeMaeyer L. 1963. Relaxation methods. Pages 895-1029 in Friess SL, Lewis ES, Weissberger A, eds. Techniques of organic chemistry - Investigation of rates and mechanism of reactions, part II, vol. 8. New York: Wiley Intersciences.

Foury F, Pastore A, Trincal M. 2007. Acidic residues of yeast frataxin have an essential role in Fe-S cluster assembly. EMBO Rep 8: 194-199.

Gakh O, Adamec J, Gacy AM, Twesten RD, Owen WG, Isaya G. 2002. Physical evidence that yeast frataxin is an iron storage protein. Biochemistry 41: 6798-6804.

Gakh O, Park S, Liu G, Macomber L, Imlay JA, Ferreira GC, Isaya G. 2006. Mitochondrial iron detoxification is a primary function of frataxin that limits oxidative damage and preserves cell longevity. Hum Mol Genet 15: 467-479.

Gostimskaya I, Grant CM. 2016. Yeast mitochondrial glutathione is an essential antioxidant with mitochondrial thioredoxin providing a back-up system. Free Radic Biol Med 94: 55-65.

Hanna PM, Tamilarasan R, McMillin DR. 1988. Cu(I) analysis of blue copper proteins. Biochem J 256: 1001-1004.

Hider RC, Kong XL. 2011. Glutathione: a key component of the cytoplasmic labile iron pool. Biometals 24: 1179-1187.

Huang J, Dizin E, Cowan JA. 2008. Mapping iron binding sites on human frataxin: implications for cluster assembly on the ISU Fe-S cluster scaffold protein. J Biol Inorg Chem 13: 825-836.

Kondapalli KC, Kok NM, Dancis A, Stemmler TL. 2008. Drosophila Frataxin: An Iron Chaperone during Cellular Fe–S Cluster Bioassembly. Biochemistry 47: 6917-6927.

Kumar C, Igbaria A, D'Autreaux B, Planson AG, Junot C, Godat E, Bachhawat AK, Delaunay-Moisan A, Toledano MB. 2011. Glutathione revisited: a vital function in iron metabolism and ancillary role in thiol-redox control. EMBO J 30: 2044-2056.

McCormick SP, Moore MJ, Lindahl PA. 2015. Detection of Labile Low-Molecular-Mass Transition Metal Complexes in Mitochondria. Biochemistry 54: 3442-3453.

McDonald-McGinn DM, et al. 2013. Hemizygous mutations in SNAP29 unmask autosomal recessive conditions and contribute to atypical findings in patients with 22q11.2DS. J Med Genet 50: 80-90.

Nair M, Adinolfi S, Pastore C, Kelly G, Temussi P, Pastore A. 2004. Solution structure of the bacterial frataxin ortholog, CyaY: mapping the iron binding sites. Structure 12: 2037-2048.

Noguera ME, Roman EA, Rigal JB, Cousido-Siah A, Mitschler A, Podjarny A, Santos J. 2015. Structural characterization of metal binding to a cold-adapted frataxin. J Biol Inorg Chem 20: 653-664.

Osterberg R, Ligaarden R, Persson D. 1979. Copper(I) complexes of penicillamine and glutathione. J Inorg Biochem 10: 341-355.

Pandey A, Gordon DM, Pain J, Stemmler TL, Dancis A, Pain D. 2013. Frataxin directly stimulates mitochondrial cysteine desulfurase by exposing substrate-binding sites, and a mutant Fe-S cluster scaffold protein with frataxin-bypassing ability acts similarly. J Biol Chem 288: 36773-36786.

Parent A, Elduque X, Cornu D, Belot L, Le Caer JP, Grandas A, Toledano MB, D'Autreaux B. 2015. Mammalian frataxin directly enhances sulfur transfer of NFS1 persulfide to both ISCU and free thiols. Nat Commun 6: 5686.

Pastore C, Franzese M, Sica F, Temussi P, Pastore A. 2007. Understanding the binding properties of an unusual metal-binding protein--a study of bacterial frataxin. FEBS J 274: 4199-4210.

Pierrel F, Cobine PA, Winge DR. 2007. Metal Ion availability in mitochondria. Biometals 20: 675-682.

Pilotelle-Bunner A, Cornelius F, Sebban P, Kuchel PW, Clarke RJ. 2009. Mechanism of Mg2+ binding in the Na+,K+-ATPase. Biophys J 96: 3753-3761.

Prischi F, Konarev PV, Iannuzzi C, Pastore C, Adinolfi S, Martin SR, Svergun DI, Pastore A. 2010. Structural bases for the interaction of frataxin with the central components of iron-sulphur cluster assembly. Nat Commun 1: 95.

Qi W, Li J, Chain CY, Pasquevich GA, Pasquevich AF, Cowan JA. 2012. Glutathione complexed Fe-S centers. J Am Chem Soc 134: 10745-10748.

Robinson NJ, Winge DR. 2010. Copper metallochaperones. Annu Rev Biochem 79: 537-562.

Rosenzweig AC, O'Halloran TV. 2000. Structure and chemistry of the copper chaperone proteins. Curr Opin Chem Biol 4: 140-147.

Seguin A, Bayot A, Dancis A, Rogowska-Wrzesinska A, Auchere F, Camadro JM, Bulteau AL, Lesuisse E. 2009. Overexpression of the yeast frataxin homolog (Yfh1): contrasting effects on iron-sulfur cluster assembly, heme synthesis and resistance to oxidative stress. Mitochondrion 9: 130-138.

Seguin A, et al. 2010. Evidence that yeast frataxin is not an iron storage protein in vivo. Biochim Biophys Acta 1802: 531-538.

Soderberg CA, Rajan S, Shkumatov AV, Gakh O, Schaefer S, Ahlgren EC, Svergun DI, Isaya G, Al-Karadaghi S. 2013. The molecular basis of iron-induced oligomerization of frataxin and the role of the ferroxidation reaction in oligomerization. J Biol Chem 288: 8156-8167.

Stemmler TL, Lesuisse E, Pain D, Dancis A. 2010. Frataxin and mitochondrial FeS cluster biogenesis. J Biol Chem 285: 26737-26743.

Thompson LC, Goswami S, Ginsberg DS, Day DE, Verhamme IM, Peterson CB. 2011. Metals affect the structure and activity of human plasminogen activator inhibitor-1. I. Modulation of stability and protease inhibition. Protein Sci 20: 353-365.

Toledano MB, Delaunay-Moisan A, Outten CE, Igbaria A. 2013. Functions and cellular compartmentation of the thioredoxin and glutathione pathways in yeast. Antioxid Redox Signal 18: 1699-1711.

Vaubel RA, Isaya G. 2013. Iron-sulfur cluster synthesis, iron homeostasis and oxidative stress in Friedreich ataxia. Mol Cell Neurosci 55: 50-61.

Wang L, Ouyang B, Li Y, Feng Y, Jacquot JP, Rouhier N, Xia B. 2012. Glutathione regulates the transfer of iron-sulfur cluster from monothiol and dithiol glutaredoxins to apo ferredoxin. Protein Cell 3: 714-721.

Yoon H, Knight SA, Pandey A, Pain J, Zhang Y, Pain D, Dancis A. 2014. Frataxin-bypassing Isu1: characterization of the bypass activity in cells and mitochondria. Biochem J 459: 71-81.

Yoon H, Knight SA, Pandey A, Pain J, Turkarslan S, Pain D, Dancis A. 2015. Turning Saccharomyces cerevisiae into a Frataxin-Independent Organism. PLoS Genet 11: e1005135.
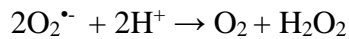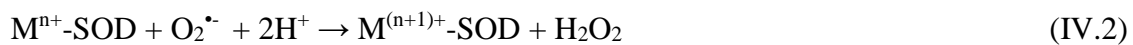
Yoon H, Golla R, Lesuisse E, Pain J, Donald JE, Lyver ER, Pain D, Dancis A. 2012. Mutation in the Fe-S scaffold protein Isu bypasses frataxin deletion. Biochem J 441: 473-480.

Yoon T, Cowan JA. 2003. iron-sulfur cluster biosynthesis. Characterization of frataxin as an iron donor for assembly of [2Fe-2S] clusters in ISU-type proteins. J. Am. Chem. Soc 125: 6078 - 6084.

CHAPTER IV: INTERACTIONS OF FRATAXIN WITH PROTEINS INVOLVED IN ANTI OXIDATIVE STRESS AND EFFECTS OF FRATAXIN ON THEIR ACTIVITY

1. Introduction

In mitochondria, 1-2 % of the molecular oxygen is converted to superoxide anion by the uptake of an electron leaking from the oxidative phosphorylation (OXPHOS). Complex I, III and possibly succinate dehydrogenase (SDH) are each considered to be key sites of superoxide anion $O_2^{\bullet-}$ formation (Figure IV.1A). This free radical is highly reactive with transition metal which are found in the cofactors of multiple mitochondrial proteins. In the dysregulating state of $O_2^{\bullet-}$, metalloproteins such as [Fe-S] proteins are among the damage targets. Superoxide dismutase (SODs) scavenge $O_2^{\bullet-}$ by disproportioning it into O_2 and H_2O_2 (equations IV.1 &2).

$$M^{(n+1)+}\text{-SOD} + O_2^{\bullet-} \rightarrow M^{n+}\text{-SOD} + O_2 \qquad\qquad (IV.1)$$

$$M^{n+}\text{-SOD} + O_2^{\bullet-} + 2H^+ \rightarrow M^{(n+1)+}\text{-SOD} + H_2O_2 \qquad\qquad (IV.2)$$

$$2O_2^{\bullet-} + 2H^+ \rightarrow O_2 + H_2O_2$$

(*) M= Cu, Mn, Fe, Ni
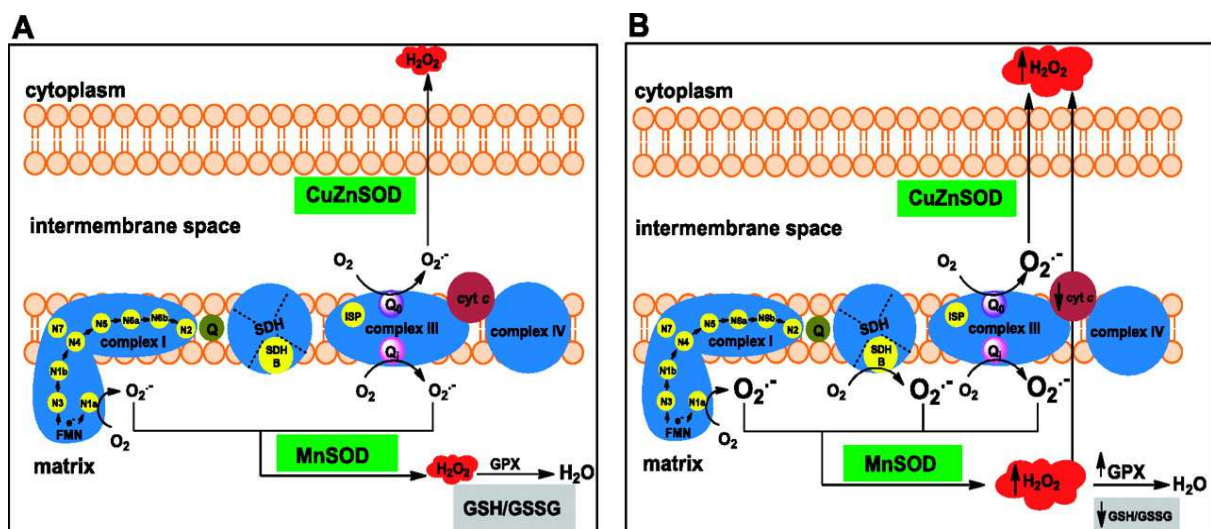
*Figure IV.1: **Schematic representation showing mitochondrial $O_2^{\bullet-}$ production in normal and in FA cells.** A) Physiological $O_2^{\bullet-}$ production is thought to occur at respiratory complexes I and III in the mitochondrial matrix and in the intermembrane space. Most matrix-generated H_2O_2 is broken down by the GSH-dependent enzyme systems, although a minor fraction may enter the cytoplasm from the mitochondrial intermembrane space due to the presence of CuZnSOD (yellow circles in complexes I,*

III, and SDH show enzymes containing Fe-S clusters). B) In FA cells, Fe-S complexes are thought to be defective, and $O_2^{\bullet-}$ production may be increased significantly both at complex I and complex III and probably at the SDH. The altered GSH redox status in FA cells may result in increased levels of H_2O_2, which can diffuse into the cytoplasm of the cell (Armstrong et al. 2010)

The importance of oxidative stress in FA was underestimated for a while by the fact that frataxin plays an explicit role in Fe-S cluster assembly. Its deficit is associated with the reduced activity of complexes I, III and SDH, thereby the increase of ROS/RNS production (Figure IV.1B). Indeed, a nearly double overproduction of mitochondrial superoxide anion was observed in FA lymphoblast (Napoli et al. 2006), and in depleted frataxin yeast (Kim et al. 2009), NO overproduction was also observed in Yfh1 deletion model (Martin et al. 2009). We already summarized the evidences of oxidative stress signs in FA model in chapter I (see 1.2.2.2). The oxidized proteins accumulation, DNA and lipids damages by ROS found in FA models are at first regarded as the secondary effects of frataxin deficiency, after Fe-S cluster deficit and mitochondrial iron accumulation. However, independent reports do not support this hypothesis. A time-resolved functional analysis on mammalian model revealed that a full depletion of frataxin induced a massive increase in ROS production before iron accumulation. Tamarit's studies reported that oxidative stress can be observed without deficiency in iron-sulfur clusters (Tamarit et al. 2016). Indeed, in a yeast model, the authors have observed signs of oxidative stress long before iron-sulfur deficiency (Moreno-Cermeno et al. 2010). Moreover, the over-expression of frataxin in different models from yeast to mammalian leads to the reduction of Fe-S enzymes activity but increases cellular antioxidant defenses (Seguin et al. 2009), (Runko et al. 2008),(Shoichet et al. 2002).

Proteomics analysis of Δ*Yfh1* revealed that these cells displayed the induction of proteins that are involved in antioxidant defense, including MnSOD (SOD2) and CuZnSOD (SOD1). However, their activities are reduced. The cytosolic SOD1 was reported to be damaged by oxidative stress while SOD2 is inactivated because of the dysregulation of iron metabolism within mitochondria (Irazusta et al. 2006) (Irazusta et al. 2010) (Yang et al. 2006). Another study reported that normal SOD2 up-regulation failed to occur in FA fibroblast exposed to iron (Jiralerspong et al. 2001). Nevertheless, using a SOD2 mimetic (MnTBAP) and SOD1 overexpression on the murine FA cardiomyopathy does not extend significantly life span (Seznec et al. 2005). In the point of view of the authors the dismutation of $O_2^{\bullet-}$ by SODs is not supposed to be favored in FA disease because it generates hydrogen peroxide. This reactive

specie together with the over-accumulation of non-ferritin iron in mitochondria emphasizes the oxidative stress *via* Fenton reaction.

In this work, to investigate the participation of Yfh1 in the protection against oxidative stress, we analyzed the functional relationship between Yfh1 and the proteins which play essential roles in regulation of the reactive species in mitochondria: superoxide dismutases SOD1, SOD2 which defense against oxidative stress, and Yhb1- the yeast flavohemoglobin – a protein responsible for protection from nitrosative stress.

1.1.   CuZn-superoxide dismutase (SOD1)

Copper and zinc dependent superoxide dismutase (SOD1) is generally acknowledged as a cytosolic enzyme, a minor fraction (less than 5 %) of total SOD1 localizes in the mitochondrial intermembrane space (IMS). In human, SOD1 is encoded by the *SOD1* gene which resides on chromosome 21q22. The encoded product is a 17 kDa peptide that must undergo a range of post-translational modifications including the formation of intramolecular disulfide bonds, the binding of Zn and Cu metal ion (metallation) and a dimerization step. Despite the lack of a N-terminal mitochondrial targeting sequence, a small amount of unfolded SOD1 might enter mitochondria after the translation *via* transporter of outer mitochondrial membrane (OMM).

Eukaryotic SOD1 is highly conserved in quaternary structure composed by two identical subunits. Each subunit folds into a ''Greek-key'' barrel with eight antiparallel β-strands (Figure IV.2). Intra-subunit disulfide bonds localize nearby the dimer interface that stabilize both the subunit fold and the dimer stability. Cu and Zn sites are positioned outside the barrel. The copper ion, bound to histidine residues H46, H48, H63, and H120, is at the center of the catalysis reaction. Zinc, coordinated to H63, H71, H80, and D83, does not participate in catalytic process, but plays a structural role for the active site of the enzyme. H63 is the bridge of the two metals. Electrostatic loop (blue helix) guides and accelerates the substrate $O_2^{\bullet-}$ entry into the active site (Tafuri et al. 2015), and steric strains selectively prevent the access of bigger anions than superoxyde, such as phosphate.
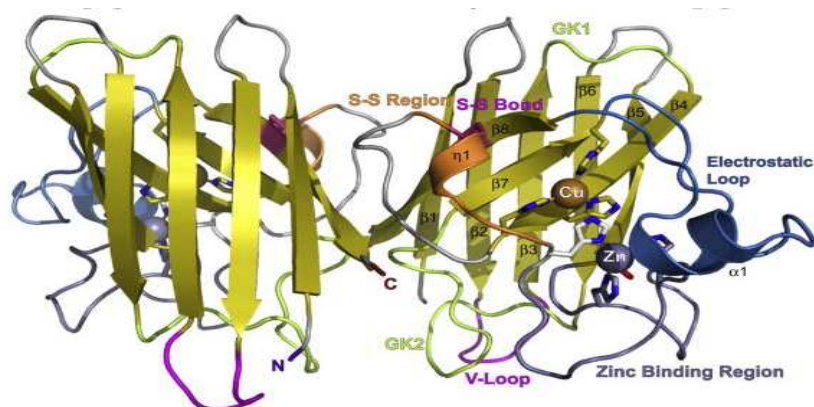
*Figure IV.2: **Human SOD1 structure with β-barrel folding** (Perry et al. 2010).*

Importantly, only unfolded SOD1 is imported into IMS. In IMS, SOD1 is trapped by copper chaperone for SOD1 (CCS1) to kick-off the folding process with the disulfide bridge formation by a transient CCS1-SOD1 intermolecular disulfide link; also, during the two molecules docking, copper is transferred from CCS1 to SOD1. Whether copper transfer and S-S formation are concurrent or sequential is not known, both of CCS1 and SOD1 are imported into IMS as apo-proteins. The copper source for SOD1 metallation is likely from mitochondrial copper pool. The mechanism and components proteins involved in copper trafficking across mitochondrial membrane as well as transfer from matrix to IMS are still open questions (Kawamata and Manfredi 2010).

SOD1 works through a so-called "ping pong" mechanism (Figure IV.3, equations IV.3 & 4) in which the first reacting superoxide reduces the cofactor Cu^+ at the active site, depositing an electron and leaving as molecular oxygen. The second reacting superoxide then accepts an electron from the reduced Cu^+ to become hydrogen peroxide (HOOH) and leaving the Cu^{2+} and ready to accept another electron, thus completing the cycle.
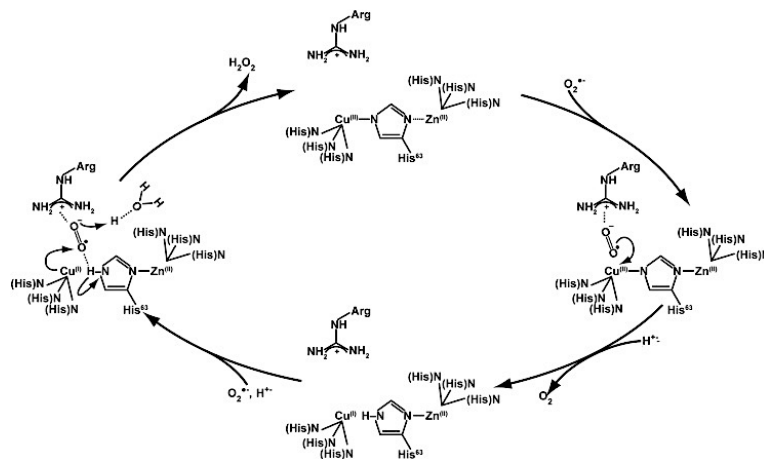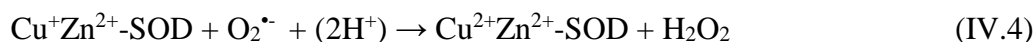

*Figure IV.3: **Catalytic cycle of SOD1** (Abreu and Cabelli , Hitchler and Domann 2014)*

Catalytic cycle reactions:

$$Cu^{2+}Zn^{2+}SOD + O_2^{\bullet-} \rightarrow Cu^{+}Zn^{2+}\text{-}SOD + O_2 \qquad (IV.3)$$

$$Cu^{+}Zn^{2+}\text{-}SOD + O_2^{\bullet-} + (2H^+) \rightarrow Cu^{2+}Zn^{2+}\text{-}SOD + H_2O_2 \qquad (IV.4)$$

1.2. Manganese superoxide dismutase (SOD2)

Superoxide dismutation in mitochondria is catalyzed by SOD2. In prokaryote and chloroplasts, there is also FeSOD which is classified in the same family with SOD2 as they are closely related with regard to three-dimensional structure and amino acid sequence (Bafana et al. 2011). SOD2 is homodimeric or tetrameric enzyme that contains one metal atom per subunit. It is encoded by *SOD2* gene located on the 6th chromosome. Complete knockout of *SOD2* gene expression causes early death in mouse (Li et al. 1995) and *Drosophila* models (Duttaroy et al. 2003). Among human, yeast and *E. coli*, SOD2 is a highly conserved protein with 40 % sequence homology (Candas and Li 2014). Each monomer is translated as a 223 amino acids peptide containing a mitochondrial targeting sequence. Once being within mitochondrial matrix, the targeting sequence is clipped off, leaving a 22 kDa monomer, which later incorporates a Mn^{3+} ion. Metal activation of SOD2 occurs in the mitochondria and only with newly synthesized peptide (Culotta et al. 2006). The metal chaperone for SOD2 – manganese incorporation is still unknown. Proper manganese loading into SOD2 depends on several proteins, such as: Smf2 – an essential transporter to the delivery of Mn to the mitochondrial matrix, and Mtm1 – a member of the mitochondrial carrier family of transporters (Whittaker 2010) (Reddi et al. 2009).

SOD2 subunit contains a C-terminal α/β domain with five α-helix and three antiparallel β-strands, and a N-terminal domain which mediates the multimerization. The active site of SOD2 is located between these two domains. Mn is coordinated in a strained trigonal bipyramidal geometry by four amino acid side chains (H26, H74, D159 and H163), the fifth ligand is a water molecule (Figure IV.4). The superoxide reaches the active site through a funnel that uses electrostatics for guidance and has a narrow entrance to the active site, limiting access to only small ions. H30 and Y34 are gatekeepers of this funnel, specifically block access to the metal ion (Perry et al. 2010).
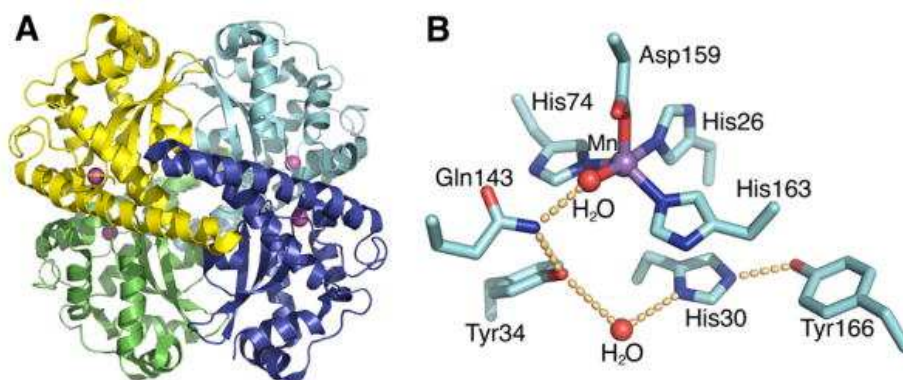
*Figure IV.4: (A) **Human MnSOD crystal structure**. (B) **Active site of human MnSOD** (Perry et al. 2010).*

Like other SODs, SOD2's superoxide dismutation mechanism involves cycling between oxidized (Mn^{3+}) and reduced (Mn^{2+}) metal. The overall proposed mechanism is described as reaction IV.5 & IV.6. (Figure IV.5) (Hsu et al. 1996).
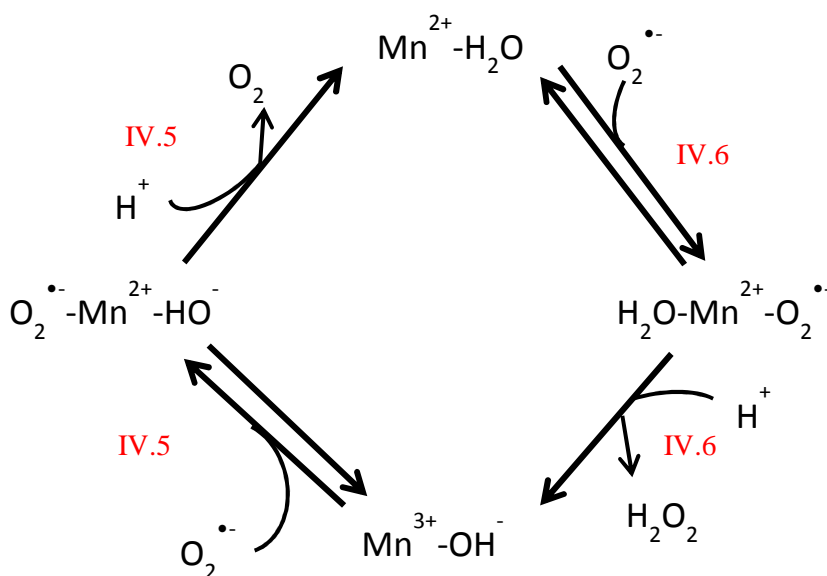
*Figure IV.5: **Catalytic cycle of SOD2** (Hsu et al. 1996).*

Catalytic cycle reactions:

$$Mn^{3+}\text{-}SOD(OH^-) + O_2^{\bullet-} + H^+ \rightarrow Mn^{2+}\text{-}SOD\,(H_2O) + O_2 \qquad\qquad (IV.5)$$

$$Mn^{2+}\text{-}SOD(H_2O) + O_2^{\bullet-} + H^+ \rightarrow Mn^{3+}\text{-}SOD(OH^-) + H_2O_2 \qquad\qquad (IV.6)$$

Actually, the altered expression or mutations of SOD2 have dramatic effects on cellular iron handling (Ibrahim et al. 2013). On the other hand, the disruption of iron metabolism also leads to perturbation on SOD2 activity. It is noteworthy that mitochondrial iron can associate with SOD2 and irreversibly inactivate it. Indeed, the binding constant of apo-SOD2 for Mn(II) is surprisingly low $K_{Mn(II)} = 3.2 \times 10^8$ M^{-1}, only 10 fold higher than that of Fe(II) (4×10^7 M^{-1}) (Mizuno et al. 2004). Iron inactivation of SOD2 has been observed in *mtm1* deletion and some mutants with defective in mitochondrial ISC synthesis such as *ssq1, grx5*. All these mutants present with iron accumulation in the mitochondria. A study of Culotta's group reported that Yfh1 contributed to iron inactivation of yeast SOD2 (Sod2) since in Δ*yfh1*, the overaccumulation of iron does not lead to the reduction in Sod2 activity. Moreover, Δ*mtm1* leads to iron misincorporation in Sod2 while double mutant Δ*yfh1*Δ*mtm1* does not (Yang et al. 2006). Similarly, the author also reported that total loss of Isu1 in yeast in the background of Δ*mtm1* or *Δgrx5* could disrupt the trafficking of iron toward Sod2 (Naranuntarat et al. 2009). Thus, they proposed the existence of a pool of mitochondrial iron which can compete with manganese for binding to SOD2 in manganese starvation or iron dysregulation (Figure IV.6), where Yfh1 and Isu1 are responsible for the inactivation of SOD2 by "SOD2-reactive" iron in the condition of iron accumulation but not in manganese starvation. However, the mechanism is still unclear (Yang et al. 2006) (Naranuntarat et al. 2009).
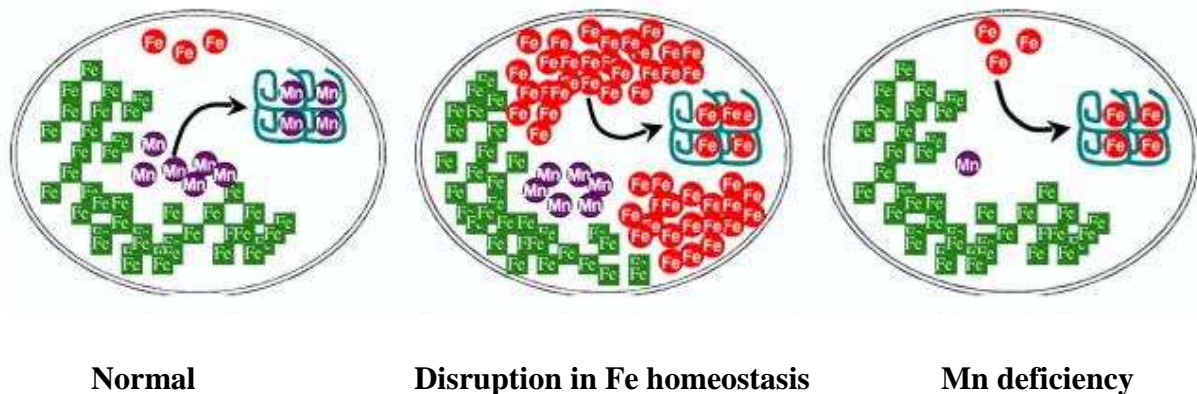

Normal   **Disruption in Fe homeostasis**   **Mn deficiency**

*Figure IV.6: **Illustration of the effects of Mn/Fe homeostasis on SOD2 metalation**. Under normal condition, even if iron is in excess over total mitochondrial manganese, this iron is actually unavailable for SOD2 (green boxes). There is always a small amount of "SOD2-reactive" iron (red circles), which cannot compete with manganese (violet circles). Otherwise, when iron homeostasis is disrupted, "SOD2-reactive" iron amount can be substantially increased, and now compete well with Mn for binding to SOD2. Also, under the manganese deficiency condition, a small level of "SOD2-reactive" iron gain access to the active guide of SOD2 (Culotta et al. 2006).*

1.3.   Yhb1- *S.cerevisiae* flavohemoglobin

Nitric-oxide (NO) is a product of numerous environmental and biological reactions. NO is known to function in normal physiology and cellular signaling. However, as a free radical, it also drives some toxicities and serves as a precursor for a range of RNS such as N_2O_3, $NO_2^{\bullet-}$, and $ONOO^-$. These RNS overproduction leads to the molecular modifications and disrupt cellular functions, the phenomenon is the so-called nitrosative stress. Hence, NO production in mammals is tightly regulated. Nitric-oxide dioxygenases (NOD), which have been recently added to the family of free radical and peroxide scavenging enzymes, convert efficiently NO and O_2 to nitrate and play an important role in the defense against nitrosative stress. Most NODs are hemoglobins (Hbs), and most Hbs have the capacity to function as NODs. Belonging to the hemoglobin's family, flavohemoglobin is a conserved protein in bacteria, yeast and filamentous fungi but not in archaea, plants and animals. It plays the central role in scavenging NO (Gardner 2012).

Flavohemoglobins are composed of three domains: the globin domain carrying heme *b*, the flavoprotein ferredoxin reductase domain built up of a flavin adenine dinucleotide (FAD), and a NADH binding domain (Figure IV.7A). The globin domain folding of Yhb1 is similar to that of human hemoglobin except helix D, which is a loop in Yhb1 (Frey and Kallio 2003).
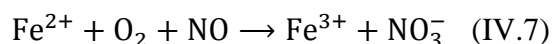

$$Fe^{2+} + O_2 + NO \longrightarrow Fe^{3+} + NO_3^- \quad (IV.7)$$

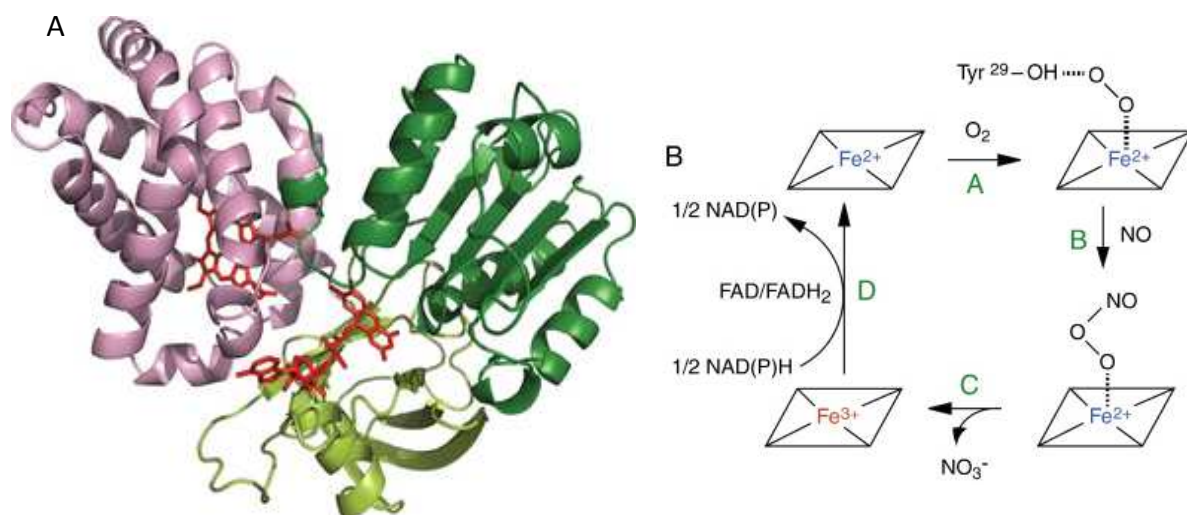*Figure IV.7:* (A) ***Overall fold of S. cerevisiae flavohemoglobin*** *(Yhb1). The two domains are the globin (pink), the flavoprotein ferredoxin reductase domain with two sub-domains: flavin binding (light green) and NADH binding (green). The cofactors heme and FAD are indicated in red (El Hammi et al. 2012).* (B) ***Illustration of NO dioxygenation catalyzed by hemoglobin*** *(Forrester and Foster 2012).*

The dioxygenation of NO by hemoproteins is based on the reaction between NO and ferrous-oxygen (Fe^{2+}-O_2) of heme to yield NO_3^- and Fe^{3+} (Figure IV.7B and equation IV. 7). In mammalian, ferric hemoglobin needs to undergo a turnover step by cellular reductants or ferric-globin reductases. In contrast, microbial flavohemoglobin uses the reducing power of cellular NAD(P)H to drive the regeneration of the ferrous heme (step D, Figure IV.7B) by *flavoprotein ferredoxin reductase* domain (Forrester and Foster 2012).

Indeed, null mutant yeast lacking the frataxin gene *Δyfh1* produces higher NO quantities than wild-type cells (Martin et al. 2009). It has been shown by yeast two-hybrid system and co-immunoprecipitation that Yfh1 interacts with Yhb1(Gonzalez-Cabo et al. 2005). The same authors also suggested a direct role of frataxin in regulating the entry of electrons toward succinate dehydrogenase – the complex II of the mitochondrial electron transport chain by stabilizing its quaternary structure that allows an efficient electron transfer. Yhb1 is indeed a special protein that carries out internally the electron transfer process. Hence, we investigated the interaction between Yfh1 and Yhb1 to know whether Yfh1 participates in NO detoxification.

2. Results

2.1. CuZnSOD (SOD1)

2.1.1. Yfh1-SOD1 molecular interaction

SOD1 does not contain tryptophan, then does not fluoresce for the excitation wavelength at 280 nm whereas Yfh1 does. The addition of one molar equivalent of Yfh1 into a SOD1 solution leads to an increase of fluorescence intensity. This experimental spectrum is different from the theoretical sum of each protein spectral contribution, which indicates the existence of molecular interaction between two proteins Yfh1 and SOD1 (Figure IV.8A).
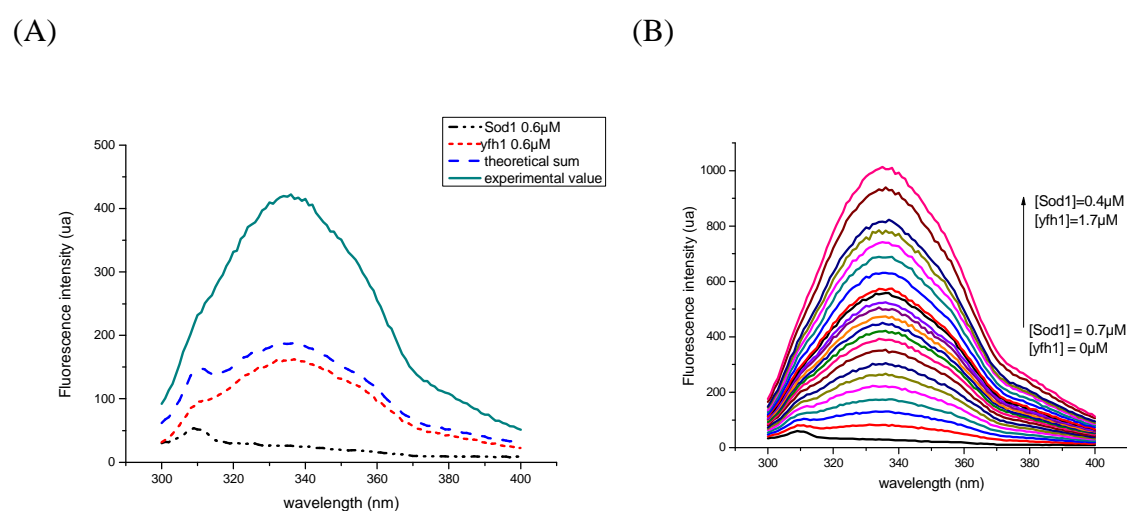
(A)   (B)

Figure IV.8: (A) **Emission fluorescence spectra of SOD1** *0.64μM (black dash-dot);* **Yfh1** *0.64μM (red dot);* **theoretical sum of the emission contribution of SOD1** *0.64μM* **and Yfh1** *0.64μM (blue dash);* **experimental spectrum of mixture SOD1** *0.64μM* **and Yfh1** *0.64μM (green solid). (B)* **Fluorescence spectra of SOD1** *0.4 μM* $\leq c1 \leq 0.7$ *μM* **in presence of Yfh1** *c2 (0 $\leq c2 \leq 2.18μM$), λ_{ex} = 280nm; μ=0.2, pH 7.00, at 25°C.*

The emission spectra of SOD1 in the presence of increased amount of Yfh1 are shown at the Figure IV.8B. The titration curve of a SOD1 solution (0.4 μM $\leq c1 \leq 0.7$ μM) by a solution of Yfh1 is different from the theoretical sum of the emission contribution of each species presenting in the solution (Figure IV.9). We assume that there is an interaction between these two proteins in this range of concentration. The binding phenomenon can be expressed by equation IV. 8.

$$\text{SOD1} \quad + \quad \text{Yfh1} \quad \rightleftharpoons \quad \text{Yfh1-SOD1} \qquad (IV.8)$$

Initial: c1   c2

Final: c1-c3   c2-c3   c3

With:

$$K_{d\,obs} = \frac{[Yfh1][SOD1]}{[Yfh1-SOD1]} = \frac{(c1-c3).(c2-c3)}{c3} \qquad (IV.9)$$

$$\frac{K_{d\,obs}}{(c2-c3)} = \frac{(c1-c3)}{c3} \qquad (IV.10)$$

$$K_{d\,obs} \times \frac{1}{(c2-c3)} + 1 = \frac{c1}{c3} \qquad (IV.11)$$

where c1 and c2 are the analytical concentrations of SOD1 and Yfh1, respectively. The concentrations of the two proteins are in the micromolar range ($0.4\ \mu M \leq c1 \leq 0.7\ \mu M$ and $0 \leq c2 \leq 2.18\ \mu M$). In this range of concentration, the fluorescence emission (F) is proportional to the protein concentration F = f . c, where f (f1, f2) is the experimental factors that associate, at a fixed wavelength, the fluorescence intensity with protein concentration.
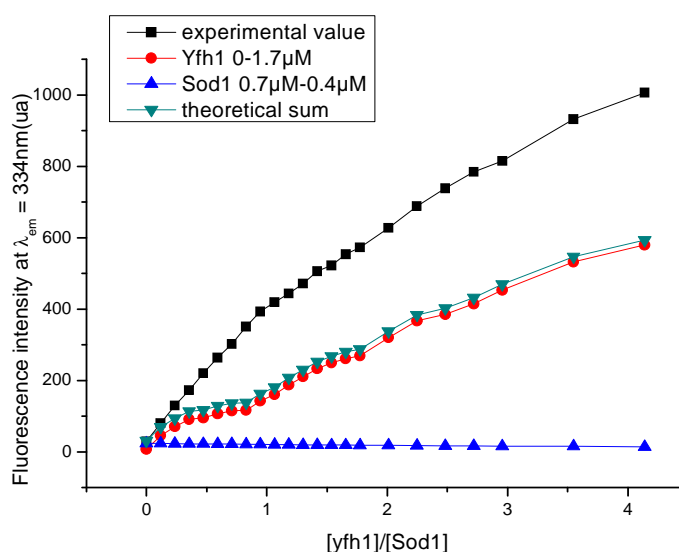

Figure IV.9: **Variation of fluorescence emission with molar ratio Yfh1/SOD1 of a frataxin solution in presence or absence of SOD1**, *after subtraction of the emission contribution of buffer. c_1 SOD1 (blue triangle) and c_2 Yfh1 (red circle), c_2 in presence of c_1 (black square), theoretical sum of fluorescence contribution of c_1 and c_2 (green upside down triangle) at λ_{ex} = 280 nm and λ_{em} = 334 nm μ = 0.2, pH 7.00, at 25°C ($0 \leq c_1 \leq 1.7\ \mu M$; $0.4\ \mu M \leq c_2 \leq 0.7 \mu M$).*

If Yfh1-SOD1 is formed according to the equation IV.8, the fluorescence intensity is consist of three individual components: SOD1, Yfh1 and Yfh1-SOD1 (equation IV.12).

131

$$Fi \; = \; f1 \times (c1 - c3) + f2 \times (c2 - c3) + f3 \times c3 \qquad (IV.12)$$

Or: $$Fi - f1 \times c1 + f2 \times c2 - c3 \times (f1 + f2 - f3) = 0 \qquad (IV.13)$$

Where $f3$ is the experimental factor that links the fluorescence intensity of complex Yfh1-SOD1 to its concentration, $c3$. $c3$ can be calculated from equation IV.13.

The slope of the best-fit line of the plot of $c1/c3$ against $1/(c2-c3)$ is equal to $1/K_{obs}$ and the intercept is 1 (Figure IV.10). The same method is used to study the other protein-protein interactions, such as SOD1 or Yhb1 with Yfh1, in the absence or presence of metals.
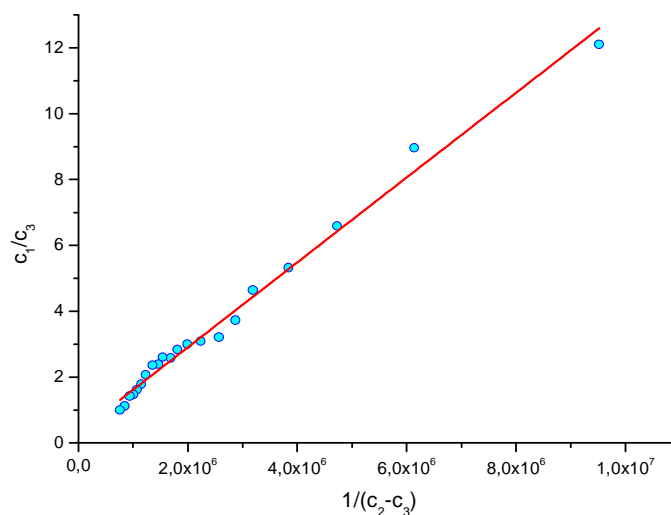

*Figure IV.10: **Plot of c_1/c_3 vs. $1/(c_2$-$c_3)$** where $0 \leq c_2 \leq 1.7\ \mu M$; $0.4\ \mu M \leq c_1 \leq 0.7 \mu M$, at μ=0.2, pH 7.00, 25°C. Intercept, (0.33±0.1); Slope, $(1.29 \pm 0.03)10^{-6}$ M, and r = 0.98874.*

As shown in Chapter III, Yfh1 binds mitochondrial metals without any specificity. Hence, we are also interested in the role of metal in molecular interaction between Yfh1 and SOD1. Yfh1's affinity for $Cu^I(GSH)_2$ is higher than that of the others studied metals. Copper is also the cofactor that participates to the catalytic cycle of SOD1. Then, Yfh1 was loaded with $Cu^I(GSH)_2$ and Cu^{II} and these complexes were used to titrate a solution of SOD1.

Indeed, when Yfh1- $Cu^I(GSH)_2$ ($0 \leq c_2' \leq 1.6\ \mu M$) was added to a solution of SOD1 (0.4 $\mu M \leq c_1' \leq 0.7\ \mu M$), within the experimental uncertainties, the titration curve was superimposable with the theoretical sum of the emission contribution (Figure IV.11a), which implies no complex formation. We assumed that $Cu^I(GSH)_2$ abolishes the protein - protein interaction. On the other hand, when Yfh1-Cu^{II}_2 was added to SOD1 solution, the titration curve on figure IV.11b allowed us to determine the dissociation constant of the {SOD1-

(Yfh1-Cu^{II}_2)} complex, which corresponds to the slope of the regression line on figure IV. 12. K_d{SOD1-(Yfh1-Cu^{II}_2)} = 0.93 ±0.04 µM is close to the K_d(SOD1-Yfh1) value found for SOD1-Yfh1 complex (1.29 ± 0.03 µM). The similar dissociation constants imply that the presence of Cu^{II} does not change the affinity of Yfh1 for SOD1. Table IV.1 resumes the K_d values obtained for SOD1-Yfh1 interaction.
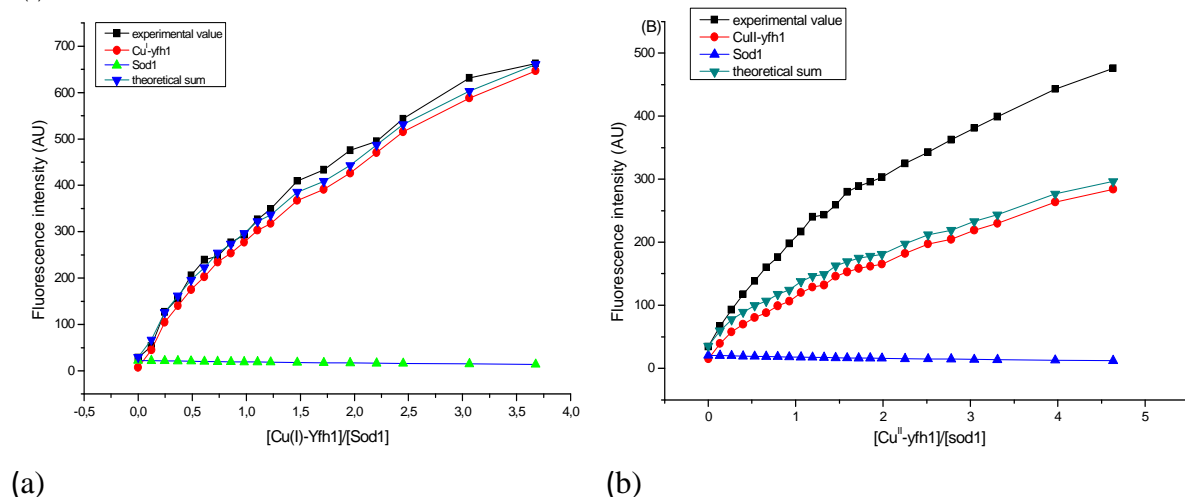

(a) (b)

Figure IV.11: **Variation of fluorescence emission with molar ratio holo-Yfh1/SOD1 of a frataxin solution in presence or absence of SOD1** *after subtraction of the emission contribution of buffer. (A): c_1' SOD1 (green triangle), c_2' Cu^I-Yfh1 (red circle), c_1' in presence of c_2' (black square), theoretical sum of fluorescence contribution of c_1' and c_2' (blue upside down triangle) (0.4 µM≤ c_1' ≤ 0.7µM; 0 ≤ c_2' ≤ 1.6 µM). (B): c_1" SOD1 (blue triangle); c_2" Yfh1-Cu^{II}_2 (red circle) and, c_1" in presence of c_2" (black square), theoretical sum of fluorescence contribution of c_1" and c_2" (green upside down triangle) (0.4 µM≤ c_1" ≤ 0.7µM; 0 ≤ c_2" ≤ 1.6 µM) at λ_{ex} = 280 nm and λ_{em} = 334 nm µ = 0.2, pH 7.00, at 25°C.*
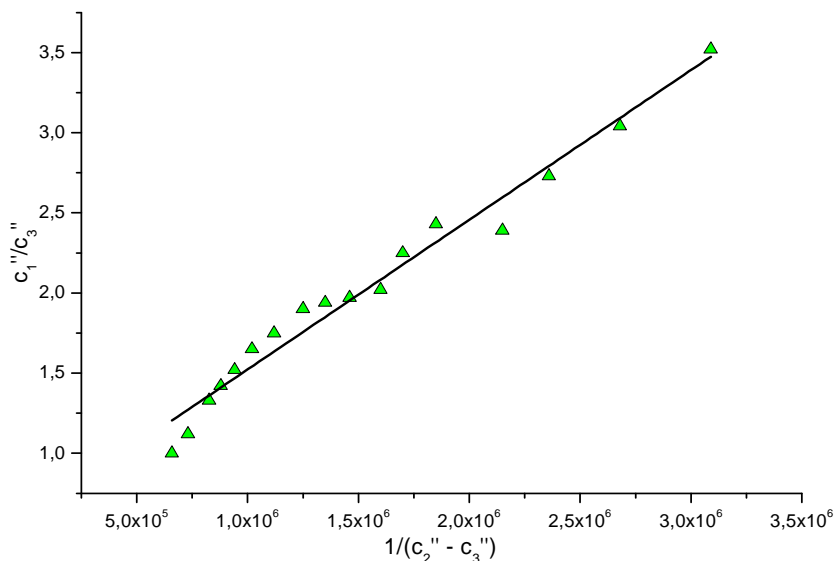
*Figure IV.12: **Plot of c_1''/ c_3'' vs. 1/ (c_2''-c_3'')** where $0 \leq c_2$'' ≤ 1.7 µM; 0.4 µM$\leq c_1$'' ≤ 0.7µM, at µ=0.2, pH 7.00, 25°C. Intercept, (0.59±0.1), slope, (0.93 ± 0.04)10^{-6} (M), and r = 0.97137.*

Table IV.1: Dissociation constants of Yfh1-SOD1 complexes at pH 7.00

	SOD1 + apo-Yfh1	**SOD1 + Yfh1-Cu$^{II}_2$**	**SOD1 + Yfh1-Cu^I(GSH)$_2$**
K_{obs} (µM)	1.29 ± 0.03	0.93 ± 0.04	No interaction

2.1.2. Enzymatic activity of SOD1 in presence of Yfh1

The SODs activity was evaluated by a commercial assay kit (see Materials and methods).

*Figure IV.13: **Superoxide dismutase activity assay**. (A) UV-visible absorption spectra of WST-1 (black) and WST-1 formazan (blue); (B) Variation of A_{450nm} with time without SOD1 (black) or in presence of SOD1 (red).*

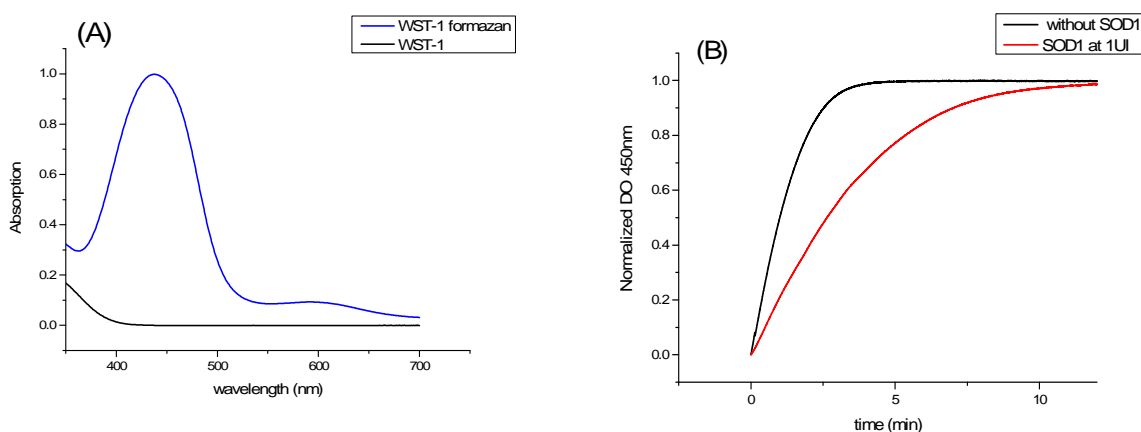Superoxide anion was generated by xanthine oxidase (XO), which will oxidize WST-1 to WST-1 formazan. WST-1 does not absorb at 450 nm while the oxidized product does (Figure IV.13A). The reaction was initialized by adding XO and the initial rate of WST oxidation was measured at 450 nm. The rate value in absence of SOD1 (v_o) was considered as the reference of total activity of XO. The SOD1 was then added into the reaction mixture which reduced the initial rate of the WST oxidation reaction (v_i) (Figure IV.13B). The activity of SOD1 was evaluated as the percentage of inhibition XO activity (equation IV.14).

$$\%inhibition = \frac{(v_o - v_i) \times 100}{v_o} \quad (\%) \tag{IV.14}$$

To see how Yfh1 affects SOD1 activity, we added Yfh1-SOD1 complex into the reaction mixture. The molar ratio of Yfh1 and SOD1 was increased from one to ten. We observed that SOD1's activity increases with the Yfh1/SOD1 ratio to attain its maximum for 5 equivalents of Yfh1 (Figure IV.14).
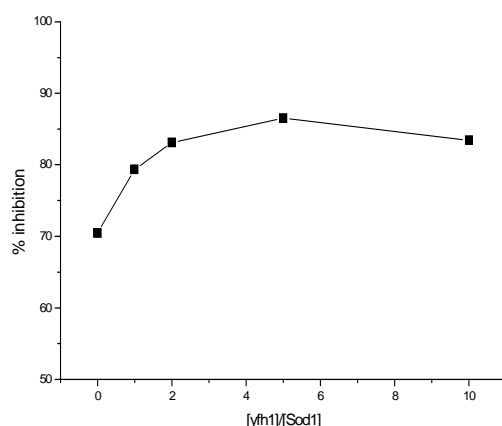
*Figure IV.14: **Variation of SOD1 activity in presence of Yfh1 from 1 to 10 equivalents.***

We defined the IC50 concentration, which corresponds to the concentration of SOD1 that inhibits 50 % of the total activity of XO (Figure IV.15b). To evaluate the influence of apo- or metal loaded-Yfh1 on the enzymatic activity of SOD1, we measured the IC50 in the presence of different protein-protein complexes: Yfh1-SOD1, iron or copper loaded frataxin complexed to SOD1 (SOD1-Yfh1-Fe^{II}_2, SOD1-Yfh1-Cu^{II}_2). (Figure IV. 15c).

The complex (Yfh1-SOD1) has a better activity than SOD1 as the IC50 decreases ~5 fold. As previously described (Table IV.1), the presence of Cu^{II} does not change the affinity of Yfh1-SOD1 complex, however it improves significantly the effect of Yfh1 on SOD1 activity as

{SOD1-(Yfh1-Cu$^{II}_2$)} has the IC50 ~ 20 times lower than that of (Yfh1-SOD1) (column FCuS1 in Figure IV.15c).

Moreover, when Fe^{II} is added to the reaction mixture, the IC50 decreases compared to that of SOD1 itself (column Fe-S1 and column S1). When Fe^{II} is loaded previously into Yfh1, we do not observe any additive effect compared to apo-Yfh1 (column FFe-S1 and column F-S1). The IC50 of {SOD1-(Yfh1-Fe$^{II}_2$)} is similar to that of (Yfh1-SOD1) (Figure IV.15c).
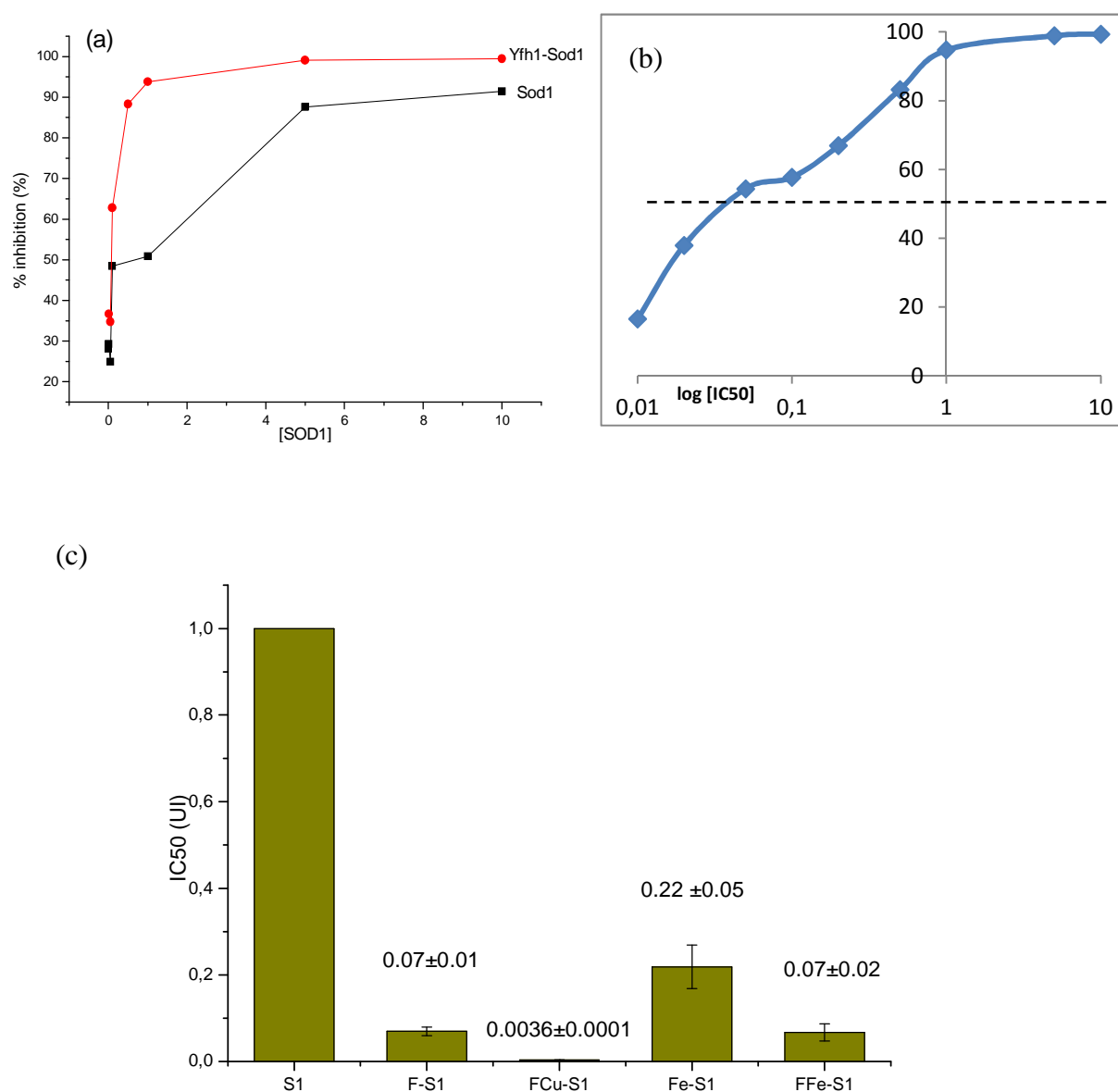
*Figure IV.15: **Characterization of SOD1 activity in presence of Yfh1.** (a): % inhibition of WST-1 formazan formation rate catalyzed by XO in presence of SOD1 (black) or apoYfh1-SOD1 (red). (b): Determination of IC50 value for Yfh1-SOD1 complex. (c) IC50 of SOD1 in different conditions: S1:SOD1; F-S1: SOD1 activity in presence of Yfh1; FCu-S1: SOD1 in presence of Yfh1-Cu$^{II}_2$, Fe-S1: SOD1 in presence of Fe^{2+}, FFe-S1: SOD1 in presence of Yfh1-Fe$^{II}_2$.*

2.2. MnSOD (SOD2)

2.2.1. Yfh1- SOD2 interaction

The addition of Yfh1 to a SOD2 solution leads to an increase of fluorescence emission accompanied by a 3 nm red shift (from 332 nm to 335 nm). As for Yfh1-SOD1, the theoretical sum of these emission contributions is different from the experimental value. This confirms the formation of at least one complex between the two molecules Yfh1-SOD2 (Figure IV.16).

Figure IV.16: (A) ***Emission fluorescence spectra of SOD2*** *0.8 μM (pink short dash);* ***Yfh1*** *0.8 μM (black dash);* ***theoretical sum of the emission contribution of Yfh1*** *0.8 μM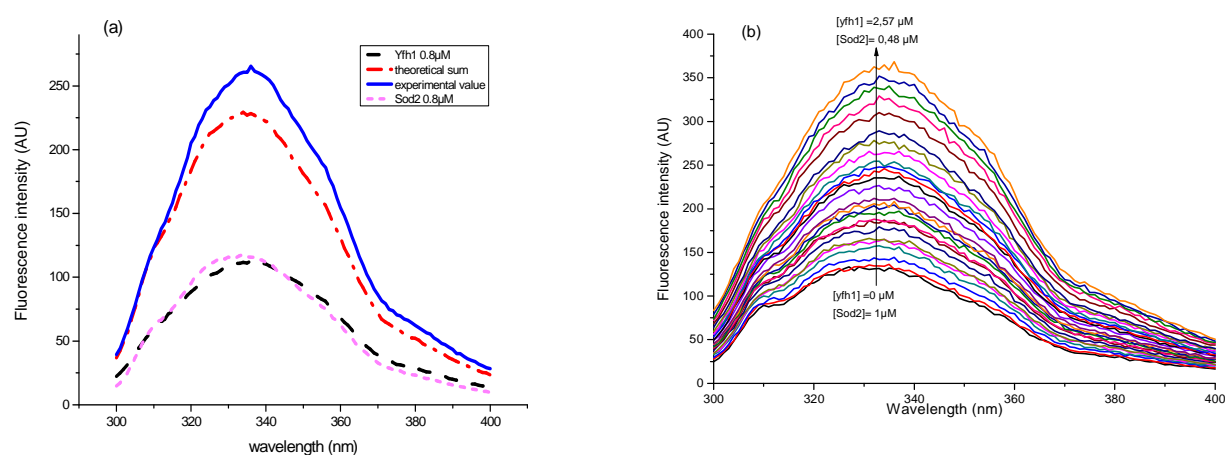* ***and SOD2*** *0.8 μM (red dash-dot);* ***experimental spectrum of mixture SOD2*** *0.8 μM +* ***Yfh1*** *0.8 μM (blue solid); λ_{ex} = 280 nm; μ = 0.2, pH 7.00, at 25 °C. (B)* ***Fluorescence spectra of SOD2*** *c3 (0.6 μM≤ c3 ≤ 1 μM)* ***in presence of apo-Yfh1*** *c4 (0 ≤ c4 ≤ 1.7 μM), λ_{ex} = 280 nm; μ = 0.2, pH 7.00, at 25°C.*

A SPECFIT analysis shows that two complexes can be formed with stoichiometry of Yfh1/SOD2 of 1/1 and 2/1 (equation IV.15&16).

$$Yfh1 + SOD2 \longleftrightarrow Yfh1 - SOD2 \qquad (IV.15)$$

$$2Yfh1 + SOD2 \longrightarrow (Yfh1)_2 - SOD2 \qquad (IV.16)$$
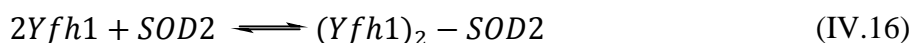
With $K_{d1}^{FS2} = \frac{[Yfh1]\times[SOD2]}{[Yfh1-SOD2]}$ and $K_{d2}^{FS2} = \frac{[Yfh1-SOD2]\times[SOD2]}{[(Yfh1)_2-SOD2]}$

Yfh1 forms two complexes with Mn^{2+} with $K_{d1}^{Yfh1-Mn}$ = 7.4 ± 0.1 μM and $K_{d2}^{Yfh1-2Mn}$ = 6.4 ± 0.2 μM (see chapter III). The effects of Mn^{II} on the affinity of Yfh1 for SOD2 were then investigated. Yfh1 was incubated with two equivalents of Mn^{II} to form Yfh1-Mn^{II}_2 before

titrating SOD2. We also observed two proteins complex {(Yfh1-Mn$_2$)-SOD2} and {(Yfh1-Mn$_2$)$_2$-SOD2} (equations IV.17 & 18). Interestingly, the presence of Mn^{II} favors the formation of these two complexes (Table IV.2).

$$(Yfh1 - Mn_2) + SOD2 \rightleftharpoons \{(Yfh1Mn_2) - SOD2\} \qquad (IV.17)$$

$$2(Yfh1 - Mn_2) + SOD2 \rightleftharpoons \{(Yfh1Mn_2)_2 - SOD2\} \qquad (IV.18)$$
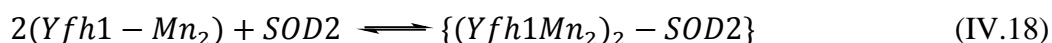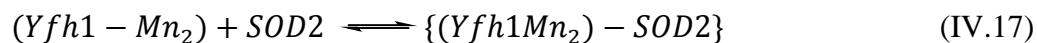
With $K_{d1}^{FMnS2} = \frac{[Yfh1-Mn_2][SOD2]}{[Yfh1Mn_2-SOD2]}$ and $K_{d2}^{FMnS2} = \frac{[Yfh1Mn_2-SOD2][SOD2]}{[(Yfh1Mn_2)_2-SOD2]}$

(*) FMnS2 = Yfh1Mn$_2$-SOD2

Table IV.2: Dissociation constants of complexes between Yfh1 or Yfh1-Mn$_2$ and SOD2 at pH 7.00

K$_d$ (µM)	Yfh1 vs. SOD2	Yfh1-Mn$_2$ vs. SOD2
K$_{d1}$	1.05 ± 0.05	0.11 ± 0.01
K$_{d2}$	6.6 ± 0.1	0.39 ± 0.01

2.2.2. Enzymatic activity of SOD2

Briefly, the activity of SOD2 was measured in the absence or presence of Yfh1. When the concentration of SOD2 was kept constant while increasing that of Yfh1, no significant change in the SOD2 activity was observed (Figure IV.17).
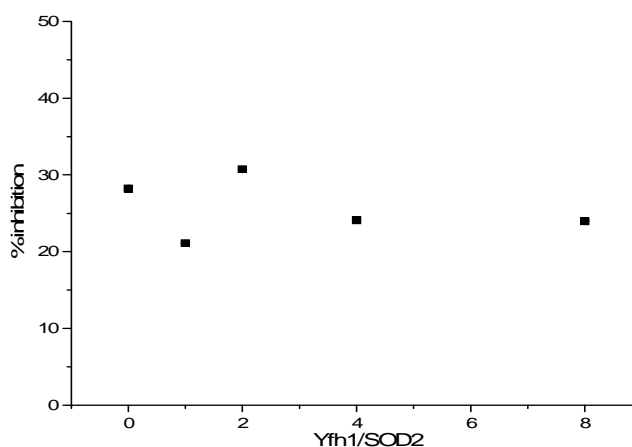

*Figure IV.17: **Variation of SOD2 activity in presence of Yfh1 from 1 to 8 equivalents***

The IC50 of SOD2 and its complexes with apo-Yfh1, Yfh1-Mn$^{II}_2$ and Yfh1-Fe$^{II}_2$ were also determined (Figure IV.18). The addition of free Mn^{II} inhibits the activity of SOD2 (column Mn-S2, figure IV.18) while free Fe^{II} decreases the IC50 of SOD2 (column Fe-S2) similar to the phenomenon observed when the activity of SOD1 was tested. However, when these metals are complexed to Yfh1, their influences on SOD2 activity are suppressed, we obtained within the experimental uncertainty IC50 values within the same range as for free SOD2 or {(apo-Yfh1)-SOD2} (columns S2, F-S2, MnF-S2 and FeF-S2, figure IV.18). Yfh1, in presence or absence of metals, does not change significantly the IC50 of SOD2.
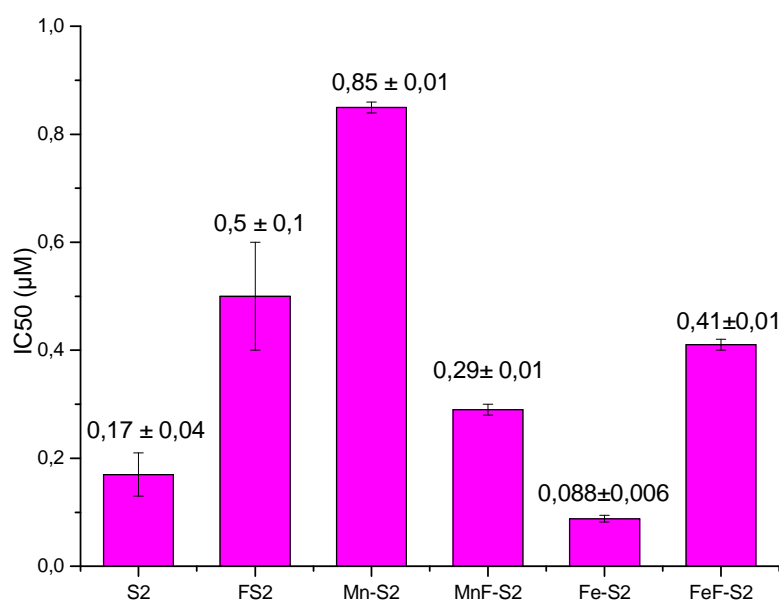
*Figure IV.18: **IC50 of SOD2 and the complexes**: S2: SOD2; FS2: Yfh1-SOD2, Mn-S2: SOD2 in presence of 2 equivalents of MnII, MnF-S2: {(Yfh1-Mn$^{II}_2$)-SOD2}, Fe-S2: SOD2 in presence of 2 equivalents of Fe^{II} and FeF-S2: {(Yfh1-Fe$^{II}_2$)-SOD2}.*

2.3. Yhb1

2.3.1. Yfh1-Yhb1 interaction

UV-Visible absorption

The differential spectrum of a mixture Yfh1-Yhb1 (1:1), which was obtained by subtracting the absorbance spectrum of Yfh1, presents a decrease in absorption at 275 nm and 411 nm. Moreover, two blue shifts appeared: from 580 nm to 577 nm and from 640 nm to 636 nm (Figure IV.19). We then assumed that Yfh1 and Yhb1 form a protein-protein complex.
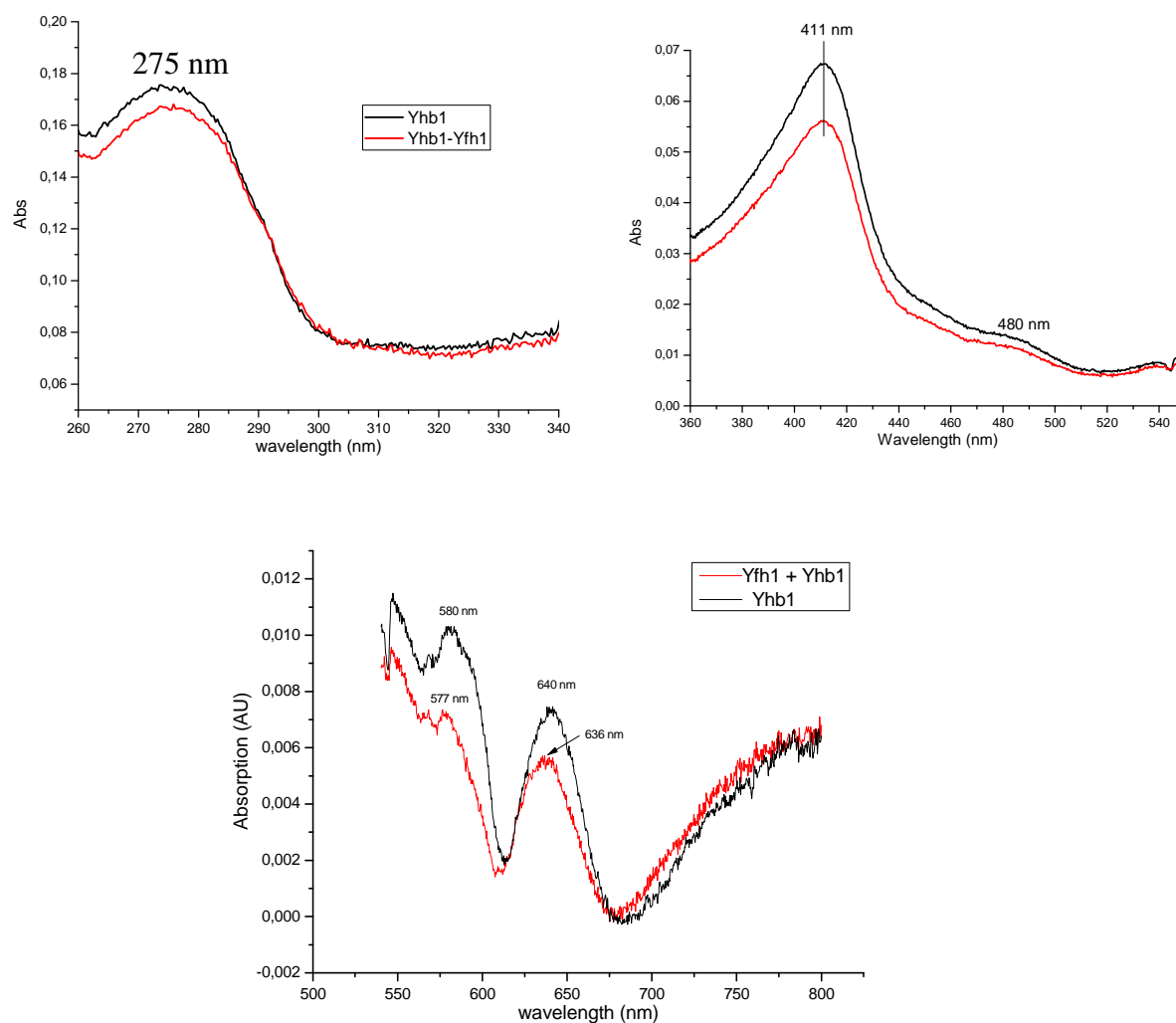
*Figure IV.19: **Absorption spectrum of Yhb1** (black line) **and differential spectrum of Yhb1-Yfh1 mixture at 1:1 equivalent after sustracting the absorbance of Yfh1** (red line).*

Fluorescence emission spectroscopy

The dissociation constant of Yfh1-Yhb1 was determined by fluorescence spectroscopy. The addition of an apo- Yfh1 solution or Yfh1 loaded with metals, such as $Yfh1\text{-}Fe^{II}{}_2$, $Yfh1\text{-}Cu^{II}{}_2$, $Yfh1\text{-}Cu(GSH)_2$ to a solution of Yhb1 leads to an increase of fluorescence emission (Figure IV.20 &21).
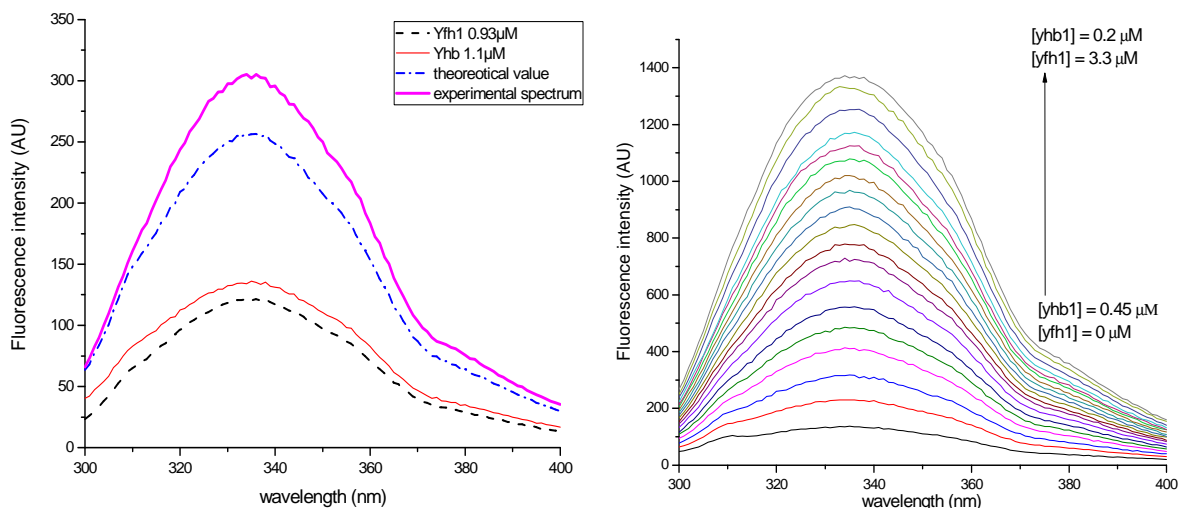
Figure IV.20: (A) **Emission fluorescence spectra of Yhb1 1 μM** *(black dash);* **Yfh1** *0.9 μM (red thin solid);* **theoretical sum of the emission contribution of Yhb1** *1 μM* **and Yfh1** *0.9 μM (blue dash-dot);* **experimental spectrum of mixture Yhb1 1 μM and Yfh1 0.9 μM** *(pink solid);* λ_{ex} = 280 nm; μ = 0.2, pH 7.00, at 25°C. (B) **Fluorescence spectra of Yhb1** c_5 *(0.2 μM≤ c_5 ≤ 0.45 μM)* **in presence of apo-Yfh1** c_6 *(0 ≤ c_6 ≤ 3.3 μM),* λ_{ex} = 280 nm; μ = 0.2, pH 7.00, at 25°C.
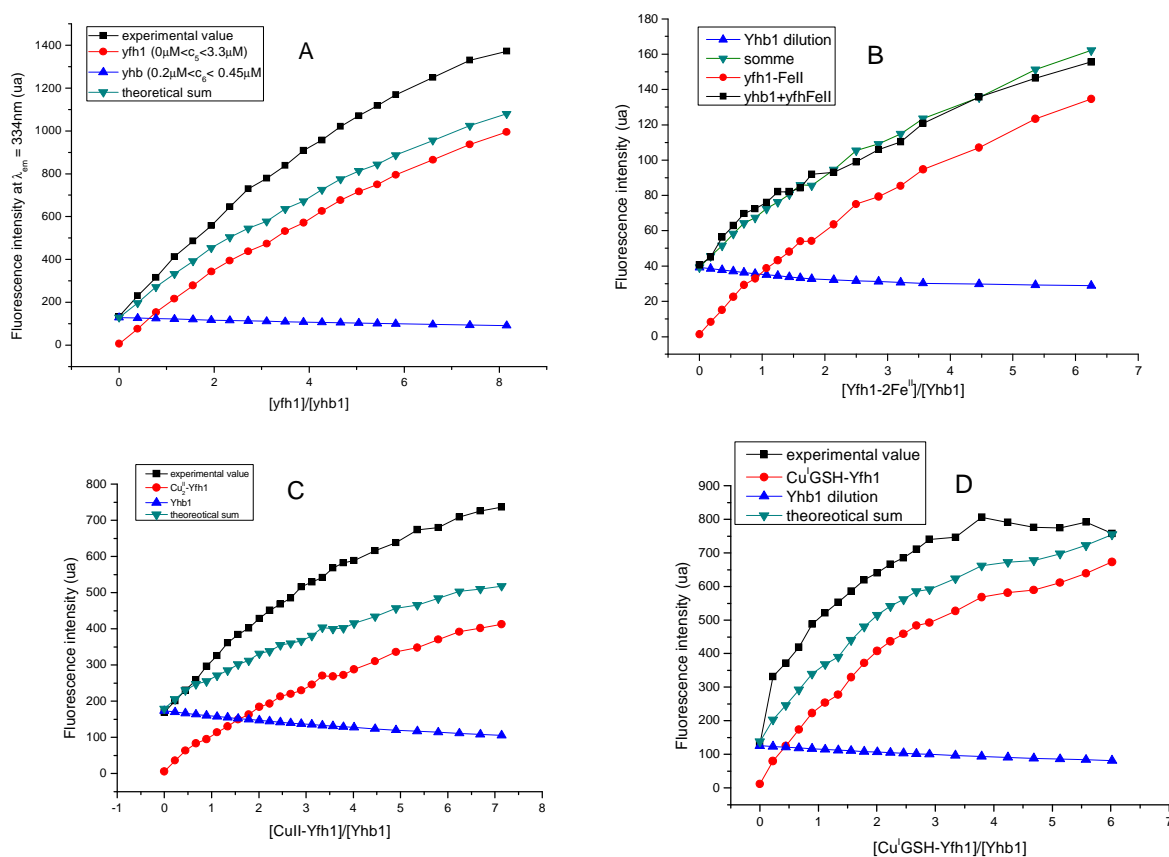
Figure IV.21: **The variation of fluorescence emission with molar ratio Yfh1/Yhb1 of a frataxin solution in presence or absence of Yhb1** *after subtraction of the emission contribution of buffer.* c_{yfh1}

Yfh1 (red circle) and c_{yhb1} Yhb1 (blue triangle); c_{yfh1} in presence of c_{yhb1} (square); theoretical sum of fluorescence contribution of c_{yfh1} and c_{yhb1} (upside down green triangle) at λ_{ex} = 280 nm and a λ_{em} = 334 nm, μ = 0.2, pH 7.00, at 25°C (0 ≤ c_{yfh1} ≤ 3.3 µM; 0.2 µM≤ c_{yhb1} ≤0.45 µM). Yfh1 corresponds to: (a) apo-Yfh1, (b) Yfh1-Fe$^{II}_2$, (c) Yfh1-Cu$^{II}_2$, (d) Yfh1-Cu^{I}(GSH)$_2$

The reaction between Yfh1, apo- or holo-protein, is expressed as equation IV.19:

$$Yfh1 + Yhb1 \rightleftharpoons \{Yfh1 - Yhb1\} \qquad \text{(IV.19)}$$
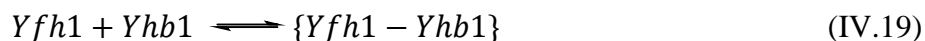
With $K_d^{FH} = \dfrac{[Yfh1].[Yhb1]}{[Yfh1-Yhb1]}$

We used the same method as before for Yfh1-SOD1 to determine the dissociation constants of Yfh1-Yhb1 complex. The K_d was determined from titration experiments by the use of equation IV.20.

$$K_{d\ obs}^{FH} \times \frac{1}{([Yhb1] - [Yfh1 - Yhb1])} + 1 = \frac{[Yfh1]}{[Yfh1 - Yhb1]} \qquad \text{(IV.20)}$$
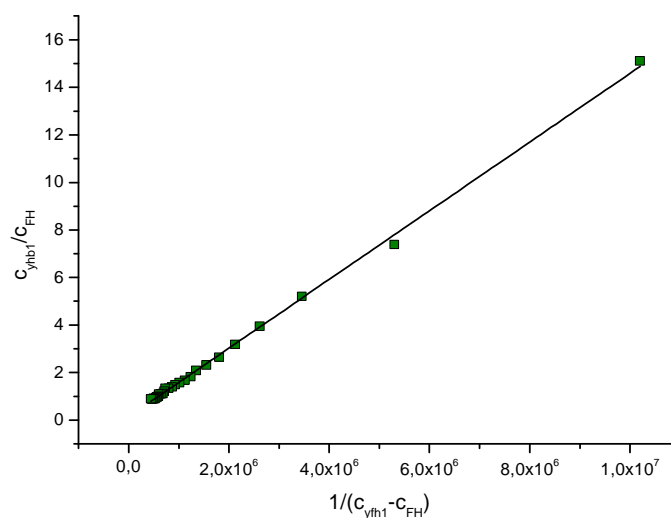
*Figure IV.22: **Plot of $c_{yhb1}/c_{yfh1-yhb1}$ vs $1/(c_{yfh1}-c_{yfh1-yhb1})$** where 0 ≤ c_{yfh1} ≤ 1.7 µM; 0.2 µM≤ c_{yhb1} ≤ 0.4µM, at μ = 0.2, pH 7.00, 25°C. Intercept (0.14 ± 0.03), slope (1.4 ± 0.01) x 10^{-6}M, and r = 0.99853.*

The titration curves of Yhb1 by Yfh1 point out a molecular interaction between Yhb1 and Yfh1 (Figure IV.21a), Yfh1-Cu$^{II}_2$ (Figure IV.21c) and Yfh1-Cu^{I}(GSH)$_2$ (Figure IV.21d). The dissociation constants of the complexes of Yhb1 with apo/holo-Yfh1were determined as for

Yfh1-SOD1 from the slope of the regression linear (Figure IV. 22). We found that apo/holo-Yfh1 and Yhb1 form a complex with 1/1 stoichiometry. The K_d values are resumed in table IV.3. Indeed, the dissociation constant of complex Yfh1-Yhb1 is in the micromolar range. When Yfh1 was loaded with $Cu^I(GSH)_2$ or Cu^{II}, the affinity for Yhb1 did not change. However, no interaction was observed between Yhb1 and $Yfh1-Fe^{II}_2$ with the superimposable titration curves between the theoretical and experimental sums of the emission contribution of the two species (Figure IV. 21b). Thus, Fe^{II} loaded in Yfh1 abolishes the interaction.

Table IV.3: Dissociation constants of complexes between apo-Yfh1 or holo-Yfh1 and Yhb1

	Yhb1-Yfh1	**(Yfh1-Fe^{II}$_2$)**	**{Yhb1-Cu^{II}$_2$(Yfh1)}**	**{Yhb1-Cu^{I}(Yfh1)}**
K_d^{FH} (µM)	1.4 ± 0.1	No interaction	1.5 ± 0.1	1.5 ± 0.1

2.3.2. Enzymatic activity:

The proposed enzymatic cycle of Yhb1 is described in figure IV.7b that includes two main steps: NO dioxygenation, which is carried out on globin domain, and NADH oxidation carrying out on flavin domain. As shown in chapter II, the Yhb1 was obtained with 70 % of peptide covered by FAD but only 15 % covered by heme. We therefore only dealt with the NADH oxidase activity.

NADH oxidase activity

The NADH oxydase activity of Yhb1 was evaluated indirectly by the reduction of cytochrome c oxidase ($cytcFe^{3+}$, equation IV.21) The product ($cytcFe^{2+}$) has a typical absorption band at 550 nm (Figure IV.23) with molar extinction coefficient of $\varepsilon_{550} = 21.1$ $mM^{-1}.cm^{-1}$. (Van Gelder and Slater 1962).

$$NADH + cytcFe^{3+} \rightleftharpoons NAD^+ + H^+ + cytcFe^{2+} \qquad (IV.21)$$
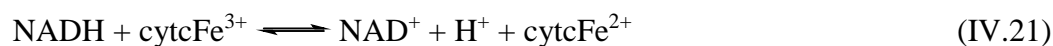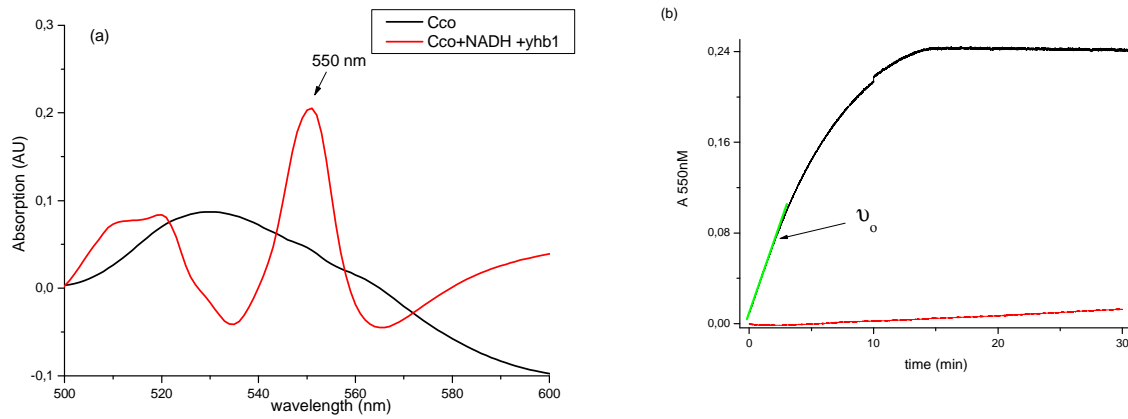
*Figure IV.23: (a) **Absorbance spectrum of cytochrome c before** (black) **and after** (red) **the reduction by NADH and Yhb1**. (b) **Variation of absorbance at 550 nm with time**.*

The initial rate of cytochrome c reduction is proportional to the initial rate of NADH oxidation. The Michaelis Menten model shows how the initial rate of oxidative reaction (υ_o) depends on initial concentration of substrate [NADH] (equation IV.22). The initial rates of NADH oxidase activity was measured at different concentrations of NADH. We determined *Vmax* and *Km* and *kcat* of Yhb1 in presence or absence of Yfh1 (equations IV.23&24). The influence of metals was also evaluated. These enzymatic constants of Yhb1, Yhb1-Yfh1 complexe, and {Yhb1-(Yfh1-Cu^I(GSH)$_2$)} are resumed in the table IV.4

$$\upsilon_o = \frac{V_{max}[NADH]}{K_m + [NADH]} \qquad (IV.22)$$

Or:
$$\frac{1}{\upsilon_o} = \frac{K_m}{V_{max}} \cdot \frac{1}{[NADH]} + \frac{1}{V_{max}} \qquad (IV.23)$$

$$k_{cat} = \frac{V_{max}}{K_m} \qquad (IV.24)$$

144
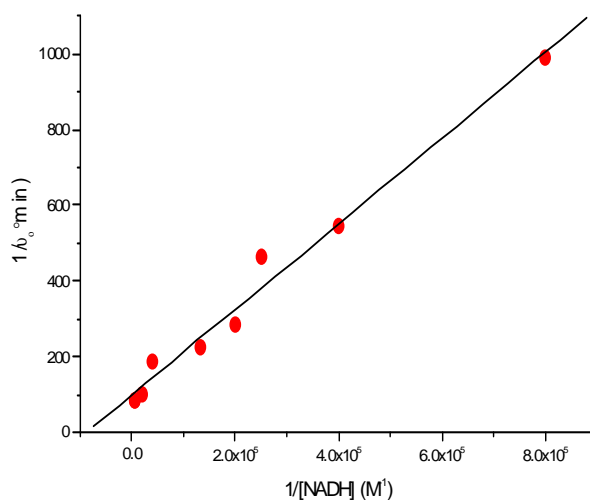
*Figure IV.23: **Lineweaver-Burk plot**. Plot of reciprocal v_o against the reciprocal substrate concentration [NADH] (red blots), regression line (black): slope, $(1.13 \pm 0.06).10^{-3}$ $(M.min^{-1})$; intercept, (99.8 ± 18.6) min, r = 0.99086.*

Tables IV.4: Vm and Km of Yhb1 in presence of apo or holo-Yfh1

	Km (µM)	V_{max} (s⁻¹)	kcat (M⁻¹.s⁻¹)
Yhb1	11.3 ± 0.8	$(5.02 \pm 0.02) \times 10^{-3}$	444 ± 25
Yhb-Yfh1	12.6 ± 0.3	$(4.43 \pm 0.06) \times 10^{-3}$	351 ± 14
{Yhb1-(Yfh1-Cu^I(GSH)$_2$)}	9.4 ± 0.5	$(4.52 \pm 0.05) \times 10^{-3}$	480 ± 33

The presence of Yfh1 does not change significantly the catalytic constants of the NADH oxidase activity of Yhb1.

3. Discussion

3.1. Protein-protein interaction

In this chapter, we reported for the first time the molecular interaction between yeast frataxin and the gatekeepers in antioxidant defense: SOD1, SOD2 and flavohemoglobin. The flavohemoglobin is from yeast, whereas, the two SODs used are both mammalian proteins. Nevertheless, these proteins are well conserved during the evolution. The structures of mammalian SOD1 and SOD2 are similar to yeast SODs, with 52 and 41 % of identity, respectively (Candas and Li 2014) (Figure IV.24).
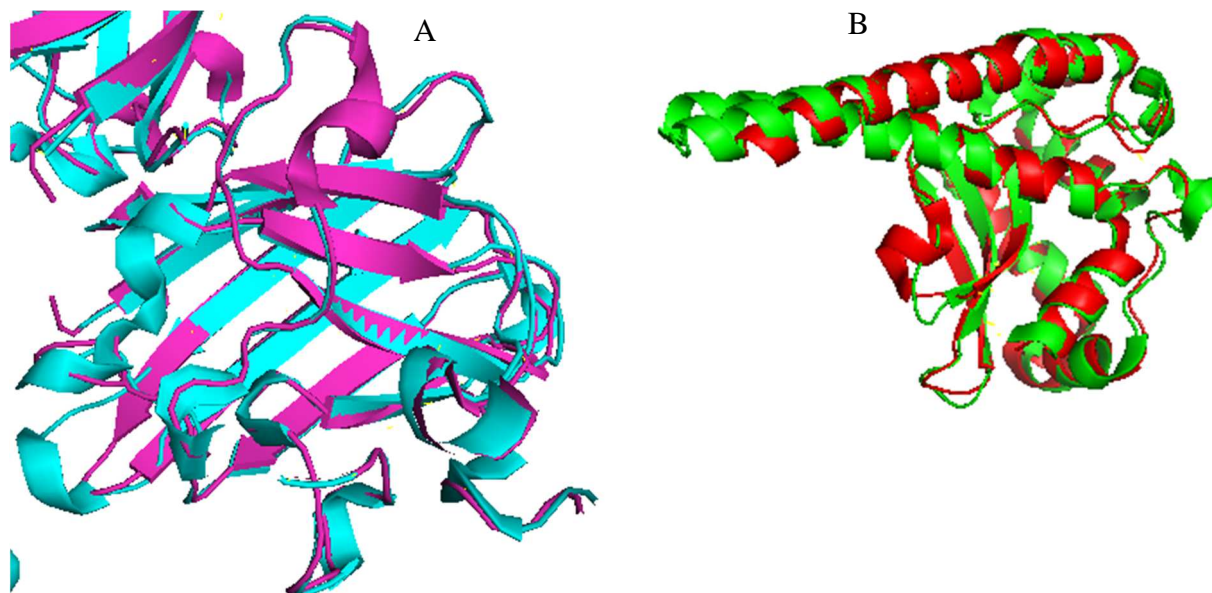
*Figure IV.24: **Structure visualization of the subunits of** (a) **bovine SOD1** (pink - PDB code:2E9P) **overlayed with yeast SOD1** (turquoise- PDB code: 1SDY), (b) **human SOD2** (red – PDB code: 1PM9) **overlayed with yeast SOD2** (green – PDB code 3LSU). Visualisation by Pymol.*

The K_d values of the complexes between Yfh1 and these proteins are in the micro-molar range. Do these interactions occur in the cells? Let us first consider the compartments where these proteins are present. In fact, the subcellular localization of frataxin is subject to controversy. In the majority of reports about FA, eukaryotic frataxin had been considered as a protein exclusively confined to the mitochondrial matrix (Campuzano et al. 1997). It is encoded by nucleus DNA and its mRNAs is translated on cytoplasmically-free ribosomes (Saint-Georges et al. 2008). Human frataxin is synthesized as a precursor polypeptide (210 amino acids), directed to the mitochondrial matrix where it is cleaved by the mitochondrial processing peptidase to the mature form *via* a processing intermediate. The mitochondrial

targeting sequence includes the amino acids (aa) from 1 to 40. The mature form sequence was reported to include residues from 81 - 210 aa (52 - 172 aa for Yfh1). The other isoforms of human frataxin (56-210 hFxn or 78-210 hFxn) also localize in the mitochondria (Schmucker et al. 2008). Follow the proteomics analysis database, the non-mature form of both Yfh1 and hFxn are seldom detected (GPM database http://gpmdb.thegpm.org). Nevertheless, several studies observed a pool of extra-mitochondrial frataxin in several human cell lines (Acquaviva et al. 2005) (Condo et al. 2006, Condo et al. 2010). They also showed that both mitochondrial and extramitochondrial isoforms are identical hFxn (81-210 aa) and suggested that after the maturation inside the mitochondrial, a part of mature hFxn is exported back to the cytoplasm (Condo et al. 2010).

SOD1 is mainly found in the cytosol at 4000-120 000 molecules per cell (Kulak et al. 2014). Only 5 % of total SOD1 localizes in the mitochondrial intermembrane space, corresponding to a concentration of 0.01-0.6 µM. Consequently, a complex between Yfh1 and SOD1, which dissociates with $K_d = 1.29 \pm 0.03$ µM, would rarely be formed in the mitochondrion *in vivo.*

On the other hand, the SOD key-player in the mitochondrial matrix is SOD2 with concentrations varying from 0.8 µM to 1.2 mM (Kulak et al. 2014). In cell free assay, we showed that two complexes are formed between Yfh1 and SOD2 with 1/1 or 2/1 stoichiometry with K_d in range of micromolar $K_{d1} = 1.05 \pm 0.05$ µM and $K_{d2} = 6.6 \pm 0.1$ µM. Accordingly, the two complexes Yfh1-SOD2, 2Yfh1-SOD2 can occur *in vivo.* Furthermore, a previous research by synthetic genetic array technique showed a negative genetic interaction between SOD2 and Yfh1, which may involve a functional relationship (Michael Costanzo et al. 2010). Our results underline, for the first time, the existence of a molecular interaction between Yfh1-SOD2.

Likewise, Yhb1-Yfh1 binding was predicted by yeast two hybrid systems and co-immunoprecipitation analyses (Gonzalez-Cabo et al. 2005). Yhb1 is located in both cytosol and mitochondria. It is found at 20-43 000 molecules per cell, which corresponds to concentrations of 1 nM to 20 µM (Kulak et al. 2014). Being in the same compartment with Yfh1, with a Kd of 1.4 ± 0.1 µM, the interaction of Yfh1 and Yhb1 is therefore feasible *in vivo*. This suggests a physiological role for the Yhb1 -Yfh1 complex. Nevertheless, Yhb1 is not a candidate for the pathogenesis of FA because it is not conserved in non-plant multicellular organisms. However, it is noteworthy that Yhb1 contains a flavoprotein ferredoxin reductase domain and a globin domain, whose structures are conserved in

mammalian. Interestingly, the perturbation in the Soret band observed when Yhb1 is mixed with Yfh1 (Figure IV.17) supports the interaction between Yfh1 and the globin-domain of Yhb1. Moreover, this domain folding of Yhb1 is similar to that of human hemoglobin (Frey and Kallio 2003), which is well accepted to be responsible for NO detoxification (Gardner 2012).

Table IV.5: Dissociation constants of complexes between Yfh1 and SOD1, SOD2 or Yhb1.
(nd:not determined)

	CuZnSOD	MnSOD	Yhb1
Apo-Yfh1	1.29 ± 0.03 μM	$K_{d1} = 1.05 \pm 0.05$ μM $K_{d2} = 6.6 \pm 0.1$ μM	1.4 ± 0.1 μM
Fe^{II}_2- Yfh1	nd	nd	No interaction
Cu^{II}_2-Yfh1	0.93 ± 0.04 μM	nd	1.5 ± 0.1 μM
Cu^{I}-Yfh1	No interaction	nd	1.5 ± 0.1 μM
Mn^{II}_2-Yfh1	nd	$K_{d1} = 0.11 \pm 0.01$ μM $K_{d2} = 0.39 \pm 0.01$ μM	nd

The interaction of frataxin with proteins in ISC assembly machinery and heme- biosynthesis are well characterized with K_d values resumed in table IV. 6. The dissociation constants between Yfh1 and ferrochelatase (Hem15) were determined by surface plasmon resonance in the absence and presence of iron. The presence of this metal improves affinity of Yfh1 for Hem15 by one order of magnitude (without Fe: $K_d = 17 – 40$ nM – with Fe: $K_d = 0.17$ nM) (Lesuisse et al. 2003) (Yoon and Cowan 2004) (Mielcarek et al. 2015). Moreover, frataxin from *E.coli* (CyaY) interacts with IscS – homologue of cysteine desulfurase with K_d value of 18.5 ± 2.4 μM. However, no interaction was observed between CyaY and IscU- ISC scaffold protein (Prischi et al. 2010), whereas, yeast and drosophile frataxin have been reported to bind Isu1 in an iron-dependent fashion with dissociation constants in the micromolar range (Cook et al. 2010), (Kondapalli et al. 2008). The affinity constants of Yfh1 for the anti-oxydant proteins determined in this study are within the same order of magnitude as the ISC components. It may suggest that Yfh1 is a multi-functions protein, which can "switch" from one form to another under alterations in the physiological environment.

Table IV.6: Dissociation constants of complexes between Yfh1 and ISC components or Hem15.

Proteins	K_d	Reference
CyaY-IscS CyaY-IscU (*E. coli*)	18.5 ± 2.4 µM - Independent of iron No interaction	(Prischi et al. 2010)
Yfh1-Isu1 (*S. cereviseae*) Dfh-Isu1 (*Drosophile*)	(1:1) 166 ± 112 nM -Iron dependent (1:2) 5 ± 3 µM 0.21 µM	(Cook et al. 2010) (Kondapalli et al. 2008)
Yfh1-Hem15	17 - 40nM (determined by SPR technique) *B.subtilis* : 0.17 nM (in presence of iron)	(Lesuisse et al. 2003) (Yoon and Cowan 2004) (Mielcarek et al. 2015)

We also dealt here with the influences of metals. In Chapter III, we showed that the affinity of Yfh1 for metals is unspecific since Yfh1 binds the majority of mitochondrial metals (Fe^{II}/Fe^{III}, Cu^I/Cu^{II}, Mn^{II}, Zn^{II}) with dissociation constants in the micromolar range. SOD1, SOD2 or Yhb1 are all metalloproteins and each of which contains a specific metal. For each experiment, the corresponding metal is complexed to Yfh1 and the affinity of the metal-loaded Yfh1 for the protein is investigated. In the case of SOD1, adding Cu^{II} does not change the affinity of Yfh1 for SOD1, while $Cu^I(GSH)_2$ abolishes the binding. Ferrous iron also abolishes the binding between Yhb1 and Yfh1, whereas both Cu^{II} and Cu^I do not change the K_d value. Furthermore, in the presence of Mn, the Yfh1-SOD2 complex is stronger. All these results suggest several hypotheses: (i) metal binding sites on Yfh1 should be different. Indeed, in Chapter III, we suggested that Yfh1 binds Cu^{II} and Cu^I via at least one of the four histidines (H74, H83, H95 and H106), and a cysteine (C98), respectively (see chapter III, figure III.27), whereas iron binding sites are D78, D86, E89, E90, and D101. (ii) $Cu^I(GSH)_2$ prevents the interaction of Yfh1- SOD1 because of its size. As the affinity of Yfh1 for Yhb1 remains unchanged in the presence of Cu^I, we suggest that the binding interface of Yfh1 with SOD1 is different from that of Yfh1 and Ybh1. (iii) Metal-binding probably changes Yfh1 conformation, which may increase or decrease the interactions with other proteins by allosteric effect. We therefore conclude that these metals participate differently to Yfh1 functions.
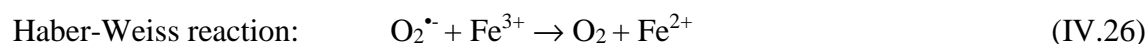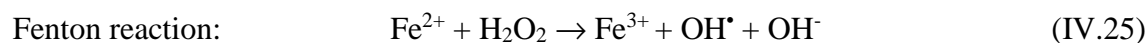
3.2.   Enzymatic activity

In the second part, we studied the influence of Yfh1 on the enzymatic activity of SODs and Yhb1, in the presence or absence of metal.

Interestingly, Yfh1 improves the activity of SOD1 (Figure IV. 13&14). Indeed, SOD1 exposes externally an electrostatic loop which guides and accelerates the substrate $O_2^{\bullet-}$ into the active site (Tafuri et al. 2015). This α helix is highly selective for the molecular size of substrate (Figure IV. 2). We suggest that the binding to Yfh1 alters the environment of this "entrance" in a manner that favors the dismutase reaction catalyzed by SOD1. Previously, Condò and coworkers showed that the expression of an extramitochondrial frataxin pool directly suppresses apoptosis and protects FA patients' lymphoblasts from stress-induced cell death (Condo et al. 2006). This is compatible with our finding that cytosolic SOD activity is enhanced by Yfh1.

Yfh1-Cu^{II}_2 complex enhances the activity of SOD1 when compared to that of metal-free frataxin (Figure IV.15). This effect was also observed in *Δyfh1* cells, indeed, copper supplement restores the activity of SOD1 (Irazusta et al. 2010). In any case, Yfh1-Fe^{II}_2 does not modify the SOD1 activity compared to apo-Yfh1. This can imply that Fe and Cu bind Yfh1 on different sites.

Furthermore, Fe^{II} decreases the IC50 of SOD1 in the absence of Yfh1. This effect can be due to the Fenton reaction between Fe^{II} and H_2O_2 generated from the dismutation catalyzed by SOD1 (equation IV.25). The Fenton reaction removes H_2O_2 and the balance $O_2^{\bullet-} + 2H^+ \rightarrow O_2 + H_2O_2$ shifts to favor the consumption of $O_2^{\bullet-}$. In addition, the Haber-Weiss reaction can also play a role, because Fe^{3+} is formed by Fenton reaction (equation IV.26). Both of oxidation states can increase the dismutation of superoxide anion and decrease the IC50 of SOD1.

Fenton reaction: $$Fe^{2+} + H_2O_2 \rightarrow Fe^{3+} + OH^{\bullet} + OH^-$$ (IV.25)

Haber-Weiss reaction: $$O_2^{\bullet-} + Fe^{3+} \rightarrow O_2 + Fe^{2+}$$ (IV.26)

That is probably why Fe^{II} decreases the IC50 of SOD1 (Figure IV.15). In addition, Fe_2-Yfh1 does not change the IC50 value of SOD1 as compared to apo-Yfh1. That implies that the action of iron in Fenton or Haber reactions is prevented.

In case of the mitochondrial SOD, the impact of Yfh1 on SOD2 activity is not as significant as on SOD1. Our result is in accordance with that of Culotta's group, which indicated that in Yfh1 deleted cells, the SOD2 activity is unchanged (Yang et al. 2006). Nevertheless, Yfh1's effects on reactive metals are not negligible. We notice that free Fe^{2+} decreases the IC50 of SOD2 by 50 %, probably because of the Fenton reaction, as mentioned for SOD1. On the other hand, when SOD2 is mixed with Mn^{II}, the effect of SOD2 on WST-formazan formation rate decreases. However, when these metals are added to Yfh1, the IC50 values are similar to those for metal-free frataxin. The interaction of these metals with Yfh1 avoids the effects of metals on superoxide dismutation. We suggest that Yfh1 behaves as a regulator and/or protector when the metabolism of mitochondrial metals is disrupted.

Concerning to Yhb1 enzymatic activity, the evaluation of NADH oxidase by our purified Yhb1 gave Km = 11.3 ± 0.8 µM. The Michealis Menten constant is in the micromolar range similar to that found in the literature (Km = 28 µM (Gardner et al. 2000); 3.2 µM (Bonamore and Boffi 2008). The insignificant influence of Yfh1 on NADH oxidase activity of Yhb1 is in accordance with the hypothesis that Yfh1 probably binds Yhb1 on the globin domain. Unfortunately, we cannot evaluate NO dioxygenase activity of Yhb1 with only 15 % of protein covered by heme (as shown in chapter II).
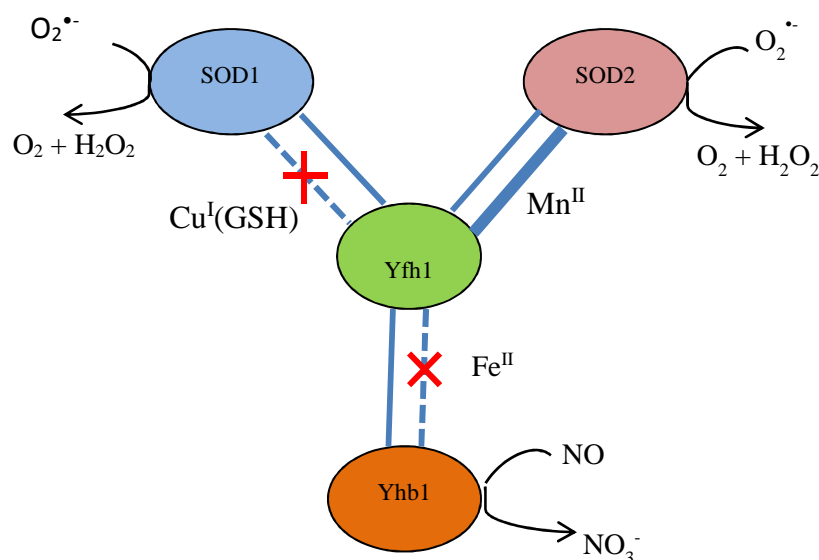
Figure IV.25: ***Evidences for the participation of Yfh1 on antioxidant defense. Influence of metals.***

In this chapter, we reported by cell-free assays that Yfh1 interacts with SOD2, Yhb1 and SOD1, three mitochondrial proteins which participate in the anti-oxidant defense (Figure IV.25). Surprisingly, Yfh1 has no significant effect on SOD2 activity. On the other hand, the

effect of Yfh1 on SOD1 activity is the most substantial, it enhances the dismutation of the superoxide anion by SOD1. Our data confirm the remarkable participation of Yfh1 to cellular anti-oxidative stress. That can explain why the deficiency of frataxin increases the sensitivity to oxidant agents, not only by the impairment in ISC or heme biogenesis. Moreover, our results tend to imply that frataxin play the role of a "regulator" in metal homeostasis. Indeed, the presence of mitochondrial metals influences the protein-protein interactions and the effect of Yfh1 on enzymatic activities.

REFERENCES

Abreu IA, Cabelli DE. 2010. Superoxide dismutases-a review of the metal-associated mechanistic variations. Biochim Biophys Acta 1804: 263-274.

Acquaviva F, Biase ID, Nezi L, Ruggiero G, Tatangelo F, Pisano C, Monticelli A, Garbi C, Acquaviva AM, Cocozza S. 2005. Extra-mitochondrial localisation of frataxin and its association with IscU1 during enterocyte-like differentiation of the human colon adenocarcinoma cell line Caco-2. The journal of cell science 118: 3917-3924.

Armstrong JS, Khdour O, Hecht SM. 2010. Does oxidative stress contribute to the pathology of Friedreich's ataxia? A radical question. FASEB J 24: 2152-2163.

Bafana A, Dutt S, Kumar S, Ahuja PS. 2011. Superoxide dismutase: an industrial perspective. Critical Reviews in Biotechnology 31: 65-76.

Bonamore A, Boffi A. 2008. Flavohemoglobin: structure and reactivity. IUBMB Life 60: 19-28.

Campuzano V, et al. 1997. Frataxin is reduced in Friedreich ataxia patients and is associated with mitochondrial membranes. Hum Mol Genet 6: 1771-1780.

Candas D, Li JJ. 2014. MnSOD in oxidative stress response-potential regulation via mitochondrial protein influx. Antioxid Redox Signal 20: 1599-1617.

Condo I, Ventura N, Malisan F, Tomassini B, Testi R. 2006. A pool of extramitochondrial frataxin that promotes cell survival. J Biol Chem 281: 16750-16756.

Condo I, Malisan F, Guccini I, Serio D, Rufini A, Testi R. 2010. Molecular control of the cytosolic aconitase/IRP1 switch by extramitochondrial frataxin. Hum Mol Genet 19: 1221-1229.

Cook JD, Kondapalli KC, Rawat S, Childs WC, Murugesan Y, Dancis A, Stemmler TL. 2010. Molecular details of the yeast frataxin-Isu1 interaction during mitochondrial Fe-S cluster assembly. Biochemistry 49: 8756-8765.

Culotta VC, Yang M, O'Halloran TV. 2006. Activation of superoxide dismutases: putting the metal to the pedal. Biochim Biophys Acta 1763: 747-758.

Duttaroy A, Paul A, Kundu M, Belton A. 2003. A Sod2 null mutation confers severely reduced adult life span in Drosophila. Genetics 165: 2295-2299.

El Hammi E, Warkentin E, Demmer U, Marzouki NM, Ermler U, Baciou L. 2012. Active site analysis of yeast flavohemoglobin based on its structure with a small ligand or econazole. FEBS J 279: 4565-4575.

Forrester MT, Foster MW. 2012. Protection from nitrosative stress: a central role for microbial flavohemoglobin. Free Radic Biol Med 52: 1620-1633.

Frey AD, Kallio PT. 2003. Bacterial hemoglobins and flavohemoglobins: versatile proteins and their impact on microbiology and biotechnology. FEMS Microbiology Reviews 27: 525-545.

Gardner PR. 2012. Hemoglobin: a nitric-oxide dioxygenase. Scientifica (Cairo) 2012: 683729.

Gardner PR, Gardner AM, Martin LA, Dou Y, Li T, Olson JS, Zhu H, Riggs AF. 2000. Nitric-oxide dioxygenase activity and function of flavohemoglobins. sensitivity to nitric oxide and carbon monoxide inhibition. J Biol Chem 275: 31581-31587.

Gonzalez-Cabo P, Vazquez-Manrique RP, Garcia-Gimeno MA, Sanz P, Palau F. 2005. Frataxin interacts functionally with mitochondrial electron transport chain proteins. Hum Mol Genet 14: 2091-2098.

Hitchler MJ, Domann FE. 2014. Regulation of CuZnSOD and its redox signaling potential: implications for amyotrophic lateral sclerosis. Antioxid Redox Signal 20: 1590-1598.

Hsu J-L, Hsieh Y, Tu C, O'Connor D, Nick HS, Silverman DN. 1996. Catalytic Properties of Human Manganese Superoxide Dismutase. Journal of Biological Chemistry 271: 17687-17691.

Ibrahim WH, Habib HM, Kamal H, St Clair DK, Chow CK. 2013. Mitochondrial superoxide mediates labile iron level: evidence from Mn-SOD-transgenic mice and heterozygous knockout mice and isolated rat liver mitochondria. Free Radic Biol Med 65: 143-149.

Irazusta V, Cabiscol E, Reverter-Branchat G, Ros J, Tamarit J. 2006. Manganese is the link between frataxin and iron-sulfur deficiency in the yeast model of Friedreich ataxia. J Biol Chem 281: 12227-12232.

Irazusta V, Obis E, Moreno-Cermeno A, Cabiscol E, Ros J, Tamarit J. 2010. Yeast frataxin mutants display decreased superoxide dismutase activity crucial to promote protein oxidative damage. Free Radic Biol Med 48: 411-420.

Jiralerspong S, Ge B, Hudson TJ, Pandolfo M. 2001. Manganese superoxide dismutase induction by iron is impaired in friedreich ataxia cells. FEBS Lett 509: 101-105.

Kawamata H, Manfredi G. 2010. Import, Maturation, and Function of SOD1 and Its Copper Chaperone CCS in the Mitochondrial Intermembrane Space. Antioxidants & Redox Signaling 13: 1375-1384.

Kim JH, Sedlak M, Gao Q, Riley CP, Regnier FE, Adamec J. 2009. Oxidative stress studies in yeast with a frataxin mutant : a proteomics perspective. J Proteome Res. 9: 730-736.

Kondapalli KC, Kok NM, Dancis A, Stemmler TL. 2008. Drosophila Frataxin: An Iron Chaperone during Cellular Fe–S Cluster Bioassembly. Biochemistry 47: 6917-6927.

Kulak NA, Pichler G, Paron I, Nagaraj N, Mann M. 2014. Minimal, encapsulated proteomic-sample processing applied to copy-number estimation in eukaryotic cells. Nat Meth 11: 319-324.

Lesuisse E, Santos R, Matzanke BF, Knight SA, Camadro JM, Dancis A. 2003. Iron use for haeme synthesis is under control of the yeast frataxin homologue (Yfh1). Human Molecular Genetics 12: 879-889.

Li Y, et al. 1995. Dilated cardiomyopathy and neonatal lethality in mutant mice lacking manganese superoxide dismutase. Nat Genet 11: 376-381.

Martin M, Colman MJ, Gomez-Casati DF, Lamattina L, Zabaleta EJ. 2009. Nitric oxide accumulation is required to protect against iron-mediated oxidative stress in frataxin-deficient Arabidopsis plants. FEBS Lett 583: 542-548.

Michael Costanzo, 2* Anastasia Baryshnikova,1,2* Jeremy Bellay,3 Yungil Kim,3 Eric D. Spear,4, et al. 2010. The genetic lanscape of a cell. Science 327.

Mielcarek A, Blauenburg B, Miethke M, Marahiel MA. 2015. Molecular Insights into Frataxin-Mediated Iron Supply for Heme Biosynthesis in <italic>Bacillus subtilis</italic>. PLoS ONE 10: e0122538.

Mizuno K, Whittaker MM, Bachinger HP, Whittaker JW. 2004. Calorimetric studies on the tight binding metal interactions of Escherichia coli manganese superoxide dismutase. J Biol Chem 279: 27339-27344.

Moreno-Cermeno A, Obis E, Belli G, Cabiscol E, Ros J, Tamarit J. 2010. Frataxin depletion in yeast triggers up-regulation of iron transport systems before affecting iron-sulfur enzyme activities. J Biol Chem 285: 41653-41664.

Napoli E, Taroni F, Cortopassi GA. 2006. Frataxin, Iron–Sulfur Clusters, Heme, ROS, and Aging. Antioxid Rdeox Signal 8: 506-516.

Naranuntarat A, Jensen LT, Pazicni S, Penner-Hahn JE, Culotta VC. 2009. The interaction of mitochondrial iron with manganese superoxide dismutase. J Biol Chem 284: 22633-22640.

Perry JJP, Shin DS, Getzoff ED, Tainer JA. 2010. The structural biochemistry of the superoxide dismutases. Biochimica et biophysica acta 1804: 245-262.

Poburski D, Boerner JB, Koenig M, Ristow M, Thierbach R. 2016. Time-resolved functional analysis of acute impairment of frataxin expression in an inducible cell model of Friedreich ataxia. Biol Open 5: 654-661.

Prischi F, Konarev PV, Iannuzzi C, Pastore C, Adinolfi S, Martin SR, Svergun DI, Pastore A. 2010. Structural bases for the interaction of frataxin with the central components of iron-sulphur cluster assembly. Nat Commun 1: 95.

Reddi AR, Jensen LT, Culotta VC. 2009. Manganese Homeostasis in Saccharomyces cerevisiae. Chemical Reviews 109: 4722-4732.

Runko AP, Griswold AJ, Min KT. 2008. Overexpression of frataxin in the mitochondria increases resistance to oxidative stress and extends lifespan in Drosophila. FEBS Lett 582: 715-719.

Saint-Georges Y, Garcia M, Delaveau T, Jourdren L, Le Crom S, Lemoine S, Tanty V, Devaux F, Jacq C. 2008. Yeast mitochondrial biogenesis: a role for the PUF RNA-binding protein Puf3p in mRNA localization. PLoS One 3: e2293.

Schmucker S, Argentini M, Carelle-Calmels N, Martelli A, Puccio H. 2008. The in vivo mitochondrial two-step maturation of human frataxin. Hum Mol Genet 17: 3521-3531.

Seguin A, Bayot A, Dancis A, Rogowska-Wrzesinska A, Auchere F, Camadro JM, Bulteau AL, Lesuisse E. 2009. Overexpression of the yeast frataxin homolog (Yfh1): contrasting effects on iron-sulfur cluster assembly, heme synthesis and resistance to oxidative stress. Mitochondrion 9: 130-138.

Seznec H, et al. 2005. Friedreich ataxia: the oxidative stress paradox. Hum Mol Genet 14: 463-474.

Shoichet SA, Bäumer A, Stamenkovic D, Sauer H, Pfeiffer A, Kahn C, Müller-Wieland D, Richter C, Ristow M. 2002. Frataxin promotes antioxidant defense in a thiol-dependent manner resulting in diminished malignant transformation in vitro. Hum Mol Genet 11: 815-821.

Tafuri F, Ronchi D, Magri F, Comi GP, Corti S. 2015. SOD1 misplacing and mitochondrial dysfunction in amyotrophic lateral sclerosis pathogenesis. Frontiers in Cellular Neuroscience 9: 336.

Tamarit J, Obis È, Ros J. 2016. Oxidative stress and altered lipid metabolism in Friedreich ataxia. Free Radical Biology and Medicine.

Van Gelder BF, Slater EC. 1962. The extinction coefficient of cytochrome c. Biochimica et Biophysica Acta 58: 593-595.

Whittaker JW. 2010. Metal uptake by manganese superoxide dismutase. Biochim Biophys Acta 1804: 298-307.

Yang M, Cobine PA, Molik S, Naranuntarat A, Lill R, Winge DR, Culotta VC. 2006. The effects of mitochondrial iron homeostasis on cofactor specificity of superoxide dismutase 2. The EMBO Journal 25: 1775-1783.

Yoon T, Cowan JA. 2004. Frataxin-mediated iron delivery to ferrochelatase in the final step of heme biosynthesis. J Biol Chem 279: 25943-25946.

CONCLUSIONS AND PERSPECTIVES

The question of what a protein does inside a living cell is not simple to answer. Beside the *in cellulo* assays, there are other methods to investigate the functions of an isolated protein, such as studying its structure, its sequence, and since most proteins act in concert with other proteins, the information about its interactions with others proteins and/or ligands is useful. In the present work, the role of frataxin (yeast homologue – Yfh1) – a protein with unknown functions –is studied by exploring its interactions with mitochondrial metals and the proteins involved in anti-oxidative stress. The thermodynamics and kinetics methods were used to characterize these binding phenomena.

Frataxin is a highly conserved protein from bacterial to human. In eukaryotes, it is located in mitochondria. Its deficiency leads to several physiological perturbations, such as dysregulation of iron homeostasis, inefficiency in iron-sulfur cluster assembly and hypersensitivity to oxidant agents. In human, the insufficiency of frataxin is responsible of Friedreich's ataxia. The discovery of the gene encoding for frataxin in the nineties broadened the research about its functions by different models among which the yeast. The research about the involvement of frataxin in ISC machinery is the most "eye catching" and has been widely investigated. However, the participation of frataxin in anti-oxidant defense remains a problem of debate. Here, we explored the frataxin's functions dealing with the anti-oxidant systems.

In the first part of this work, two yeast proteins- Yfh1 and Yhb1- were synthesized by DNA recombinant techniques and purified by anion exchange and size exclusion chromatography. For the purpose of biophysical studies, both of them were obtained in mature form without polyhis-tag. Yfh1 was isolated in its dimer form. Yhb1 was expressed as a holo-protein with 70 % peptide covered by FAD cofactor and 15 % by heme cofactor.

In the second part, the interactions of Yfh1 with mitochondrial transition metals were investigated by thermodynamic and kinetic measurements. We reported briefly the affinity of Yfh1 for most of the mitochondrial metals: Fe^{2+}/Fe^{3+}, Cu^{2+}/Cu^{+}, Mn^{2+} and Zn^{2+}. Our results indicated that **Yfh1 forms complexes with all these metals** with affinities in the micromolar range (0.03 to 1.6 µM). This proved that Yfh1 binds mitochondrial metals without any specificity. Yfh1 has a better affinity for $Cu^{I}(GSH)_2$ ($logK_d = 7.5 \pm 0.3$) and Mn^{2+}($logK_{d1} = 7.4 \pm 0.1$; $logK_{d2} = 6.4 \pm 0.2$) and a surprisingly low affinity for iron.

The role of GSH is also discussed. Indeed, we did not observe any direct interaction between Yfh1 and GSH in the absence of metals. However, Yfh1 binds the entire $Cu^I(GSH)_2$ molecule. Furthermore, GSH has no effect on the affinity of Yfh1 for Fe^{II}. Dealing with the suggestion that frataxin is a modulator that enhances the formation and transfer of persulfide from cysteine desulfurase to ISC scaffold (Parent et al. 2015), we emphasized several proposals for the role of $Cu^I(GSH)_2$: (i) copper may help the approach of GSH to the ISC complex *via* frataxin; (ii) CuI-Yfh1 can increase the rate of persulfide formation or increase the interaction between the proteins of the ISC machinery.

We also presented the mechanism of metals uptake by Yfh1 in chapter III. The uptake of the first metal occurs in the hundred ms range and involves a conformational change (case of Fe^{II} and $Cu^I(GSH)_2$). A slow conformational change was always observed in the final step of the uptake leading to the thermodynamic product. The first Cu(II) is uptaken by a deprotonated form of Yfh1. The pKa of this acid-base reaction is 6.7 ± 0.1, which may imply the deprotonation of a histidine residue. We suggest that the binding site of Yfh1-Cu(II) includes one of four exposing histidines on the negatively charged interface of Yfh1 (H74, H83, H95 and H106). Referring to the binding sites of Yfh1 with Fe, which are well studied, it might be concluded that Yfh1 binds copper and iron on different sites. We, therefore, propose **a relationship between frataxin and copper metabolism**. Indeed, copper dysregulation is observed in DN of FA patients, where iron overload does not occur. In this organ, the net amount of Fe, Cu or Zn does not increase or decrease significantly but the distributions of these metals are altered. The Cu and Zn rich regions broaden and overlap extensively with Fe-rich region. The atrophy of DN of FA correlates with Cu and Zn redistribution rather than with Fe dysregulation only (Koeppen et al. 2007).

In the third part (chapter IV), we reported **the molecular interactions between Yfh1 and the enzymes involved in antioxidant defense SOD1, SOD2 and Yhb1**. Based on the finding in Chapter III, which indicates that Yfh1 binds Cu and Mn with better affinity than iron, mitochondrial proteins containing Cu and Mn are selected for this study. SOD1 and SOD2 are the gatekeepers of antioxidant defense, which contains Cu and Mn in their catalytic centers, respectively. On the other hand, Yhb1 is the protein responsible for the NO detoxification in yeast. Yhb1, which contains a heme domain similar to hemoglobin in human, is the scaffold for NO-deoxygenation. Yfh1 forms at least a complex with these proteins with affinities in the micromolar range ($K_d \sim 1.3 - 1.5$ µM). The effects of metal on the affinities of Yfh1 for these

proteins were also studied. The different effects observed suggest a "switch" function for Yfh1 when the metal metabolism is altered.

The enzymatic activities of SOD1 and SOD2 in the presence of apo-Yfh1 and metal-loaded Yfh1 were characterized. Mn^{2+} and Fe^{2+}, which can carry out Fenton-like reaction, affect the superoxide dismutation catalyzed by the two enzymes. However, these effects are abolished when the metals are complexed toYfh1. We suggest that Yfh1 also plays the role of a "regulator" for metal homeostasis. Our results underline the hypothesis that Yfh1 is a multifunctional protein which **participates in antioxidant mechanisms**. Thus, frataxin deficiency increases the sensitivity to oxidant agents not only by the impairment in ISC or heme biogenesis but also probably by its interference with the dismutation of superoxide anion catalyzed by SODs.

In perspectives, the expression and purification protocol need to be optimized to get a higher coverage of heme for Yhb1. It should be interesting to study the structure of the complexes between Yfh1 and metals. The binding sites would reveal the functions of copper when complexed to Yfh1. The studies can also be followed by the determination of the mechanism of SOD1 activity enhancement by Yfh1. Further, the impact of frataxin on nitric oxide detoxification by flavohemoglobin or another member of the hemoglobin family is a promising approach for studying of the frataxin physiological functions. In the near future, the interaction of frataxin with other components of cellular antioxidant system can be helpful for a better understanding of the highly controversial role of the protein. Since the frataxin-lacking cells are highly sensitive for H_2O_2, it will also be interesting to investigate the interactions of frataxin with the proteins responsible for H_2O_2 detoxification, such as glutathione peroxidases, peroxiredoxins and catalase.

CHAPTER V: MATERIALS AND METHODS

1. Materials

1.1. Chemical materials

- The Bis Tris (Amresco) concentration in neutral buffers was 50 mM. Final pHs were continuously controlled and adjusted to between 6.6 and 8.6 with micro-quantities of concentrated HCl or NaOH. All final ionic strengths were adjusted to 0.2 M with KCl (Sigma-Aldrich). pH values were measured with a Jenco pH-meter equipped with a "Metrohm" combined calomel/glass mini-electrode.

- **Fe^{II}:** Crystalline ferrous ammonium sulfate hexahydrate, $Fe(NH_4)_2SO_4.6H_2O$ (Fluka), was used as the ferrous iron source and was dissolved at 10 mM in a 0.2 M deoxygenated KCl solution. Solutions were stocked under argon.

- **$Fe^{III}NTA$** (iron nitrilotriacetic acid complex) solutions were prepared as previously described (El Hage Chahine and Fain 1994).

- **$CuSO_4$, $ZnSO_4$, $MnCl_2$** (Prolabo) were dissolved in 50 mM Bistris, 150 mM KCl buffer.

- **$Cu(GSH)_2$** was prepared under argon atmosphere as previously described (Ciriolo et al. 1990). CuCl powder (Aldrich) was weighted and introduced into a dry vial. Reduced glutathione (GSH, Sigma-Aldrich) were dissolved in deoxygenated 50 mM Bis Tris, 150 mM KCl buffer. The complex was prepared by adding a volume of GSH solution to the vial containing an appropriate amount of CuCl powder. The final Cu:GSH molar ratio is 1:2. $Cu(GSH)_2$ concentration was measured before each experiments using (2,2')-biquinoline ((2,2')-BBQ, Fluka) which form selectively a complexe with Cu^+, $\varepsilon_{545} = 6370$ M^{-1} cm^{-1} (Hanna et al. 1988). (2,2')-BBQ was dissolved in acetic acid at 0.5 mg/mL.

1.2. Biological materials

The competent cells BL 21(DE3) or Top10 *E. coli* are purchased from Invitrogen. The cells are conserved in -80 °C was 50 µL sample eppendorf tube.

Bovine CuZnSOD was purchased from Sigma Aldrich and diluted in enzyme dilution buffer including in SOD activity assay kit. Recombinant human MnSOD was purchased from Bioscience Innovation- Interchim and diluted in Bis Tris buffer (pH 7.0). The SOD initial solution was aliquoted and conserved in -20 °C until being used. The SODs were used without further purification.

2. Protein production

2.1. Plasmid

The mature full-length yeast frataxin homolog coding sequence YFH1 (51-174) was amplified from genomic DNA by PCR, cloned into a pUC19 vector and the nucleotide sequence verified by Sanger sequencing. The Nde1-BamH1 fragment with the coding sequence from the initiation methionine to a stop codon was subcloned into a pSBET-2b bacterial vector expression (Schenk et al. 1995).

The coding region of flavohemoglobin YHB1 was polymerase chain reaction-amplified from vectors pYADE4 (Buisson. N and Labbe-Bois 1997) using forward (5'-CGC<u>CATATG</u> CTAGCCGAAAAAACCCG) and reverse (5'-CGC<u>GGATCC</u>TAAACTTGCACGGTTGAC ATC) primers containing sequences for NdeI and BamHI restriction sites (underlined). The resulting DNA fragment was inserted into the polylinker of pSBET-2b (Figure V.1). Then, the plasmid psBET2b-YHB1 was formed by a step of ligation with digested vector pSBET-2b overnight at room temperature.
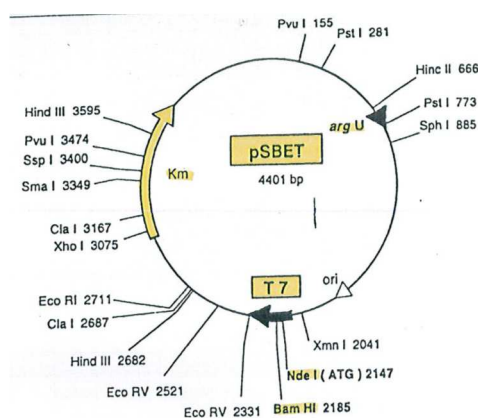

*Figure V.1: **Plasmid pSBET-2b.***

2.2. Transformation into competent cells

Transformation is a process in which exogenous genetic material is introduced into competent bacterial cells. The competent cells were thawed rapidly on ice (less than 5 min). Then 3-5 µL plasmid solution was added to 25 µL of cells. This mixture is kept on ice for 30 mins before incubation of 30 s on 42 °C, and then it is turned to the ice for 5 min. After this thermal sock, 150 µL of S.O.C medium (purchased with the competent cells) was added to the transformed cells. The cells were then incubated at 37°C under an agitation of 200 rpm during 1 h. The transformation cells were selected by plating on LB-plates (LB medium with 50 µg/mL kanamycin) and incubating overnight at 37°C. The LB-plates are inspected for growth of colonies the next day.

2.3. Protein expression

- _Starter culture:_ a single colony of plasmid-containing cells from selection LB-plates was suspended in 3 mL of LB medium with 50 µg/mL kanamycin. This suspension was incubated at 37 °C, under 200 rpm stirring for 10-15 h.

- _Expression culture:_ the starter culture was inoculated into the expression culture at 1/1000 (v/v) dilutions. The expression culture is one of the media presenting in table V.1 with 50 µg/mL kanamycin.

Table V.1: Ingredients of expression cultures for 1L.

	Luria-Bertani (LB)	Terrific Broth (TB)	Auto-induction medium	
			LBE 505	LBE 5052
Yeast extract	5 g	24 g	1 g	1 g
Tryptone	10 g	12 g	0.5 g	0.5 g
NaCl	10 g			
Glycerol		8 mL	0.5 g	0.5 g
Glucose			0.05 g	0.05 g
Lactose				0.2 g
K_2HPO_4		9.4 g	0.4 g	0.4 g
KH_2PO_4		2.2 g	0.4 g	0.4 g
Metals			≤ 0.01 g	≤ 0.01 g

With LB medium, the induction was initialized by adding isopropyl β-D-1-thiogalactopyranoside (IPTG) at 0.4 mM when the OD 600 nm reaches 0.8 – 1.

2.4. Crude extracts preparation

After incubation time, cells were harvested by centrifugating at 4000 rpm for 15 min following by a milliQ water washing. The pellets were stocked at -80 °C for at least one night before lysing. Cells were then lysed by a cycle of French press or sonication. 1 g of wet pellet was suspended in 7 mL of lysis buffer (50 mM Tris-HCl, 1 mM $MgCl_2$, pH 8.0). Benzonase (Sigma) was added to avoid DNA contaminant (0.5 µL per gram of wet pellet). The suspension was then treated by the pressure of 7000 to 8000 psi in a French press system. In sonication protocol, the suspension was kept in ice and treated by 5 cycles of sonication (a pulse of 10 s per cycle, 30 s pause between two cycles). Cell lysate was collected in a flask that is kept on ice. The cell debris was removed by ultracentrifugation 18 000 rpm at 4°C for 30 min (Beckman).

In the case of the Yfh1 crude extract, the cell lysate was mixed 1/1 (v/v) with the HEPES 50 mM, urea 6 M pH 7.0 buffer (corresponding to the equilibrium buffer of the first chromatography column) and kept at room temperature for 15 min. This mixture was centrifuged at 4000 rpm for 15 min at 4 °C to eliminate insoluble materials.

2.5. Purification

2.5.1. Anion exchange chromatography

a) DEAE Sepharose Fast-flow chromatography

A column of DEAE Sepharose Fast-flow (Sigma Aldrich) was previously equilibrated by 5 CV (column volume) of HEPES 50 mM, pH 7, then by 5 CV of HEPES 50 mM, urea 6 M pH 7.0. After the injection with the rate of 1 mL/min, the column was washed by 2 CV of HEPES 50 mM, urea 6 M pH 7.0. Then, the proteins were eluted at a flow rate of 2 mL/min by a gradient of KCl solution 0.1 M, 0.2 M, 0.4 M, 0.6 M and 1 M, respectively. The fractions containing frataxin were determined by SDS PAGE electrophoresis gel. The pool of these fractions are dialyzed against HEPES 25 mM pH 7.0 and submitted to a step of hydroxyapatite anion-exchanged chromatography.

b) *Hydroxyapatite chromatography*

A column of hydroxyapatite (Bio-Grad Labs.) was previously equilibrated by 5 CV of HEPES 25 mM, pH 7.0. The fraction containing frataxin was injected into this column (1 mL/min). The column was washed by 2 CV of the equilibrium buffer. Then, proteins were eluted by a gradient of KH_2PO_4 from 25 mM to 500 mM. Electrophoresis gel SDS PAGE was used to determine the fractions that contain frataxin.

2.5.2. Size-exclusion chromatography

In a system FPLC (Äkta purifier - GE Healthcare Lifescience), the column of Superdex^{TM}200 10/300 GL (GE Healthcare Lifescience) was previously equilibrated by buffer HEPES 50 mM, then sample was injected at the rate of 0.5 mL/min. The elution was carried on at flow rate of 0.5 mL/min. The means of detection was the absorption at 280 nm.

2.5.3. Concentration and dialysis

The pure fractions containing the target protein were pooled and concentrated by VIVASPIN 10000 MWCO (GE Healthcare Lifescience). The proteins were dialyzed against Bis Tris 50mM, KCl 150 mM buffer three time during at least 24 h at 4 °C before all physicochemical studies.

2.6. Protein identification by electrophoresis

Samples from different purification steps were analyzed by sodium dodecyl sulfate (SDS) polyacrylamide gel electrophoresis (SDS-PAGE). SDS is an anionic detergent that binds to proteins, causing it to linearize and to become negatively charged. The charge of the protein becomes proportional to the mass, and proteins are separated by mass on the gel by an electric field. The polyacrylamide gels with 10-15% acrylamide were used in their commercial form (Bio-Rad).

Table V.2: Stock solutions for SDS PAGE assay.

Laemmli 4x	2-Mercaptoethanol, 0.4%
	Bromophenol blue, 0.002%
	Glycerol, 40%
	SDS (electrophoresis-grade), 8%
	Tris-HCl, 250 mM (pH 6.8)
Running buffer	0.3 % Tris base
	1.5 % g of glycine
	0.1 % of SDS
	pH 8.3

Before the migration, protein samples were mixed with Laemmli 4x (1/4 v/v) and boiled for 3 min (Table V.2). This treatment with reducing agent (2-mercaptoethanol) disrupts intramolecular and intermolecular disulfide bonds of the proteins. That allows the protein to achieve complete protein unfolding and to maintain proteins in their fully reduced states. The samples were then loaded separately to the wells of SDS-PAGE gel. Typically, the migration was run briefly for 15 min at 80 V and shift to 150 V during 45 min with the running buffer. 5 µL of Pre-stained protein standards (Invitrogen) ladder was used. After the electrophoresis migration, the gel was stained by either Coomassie Blue method or Heme-stain method.

2.6.1. Coomassie stain

Table V.3: Stock solutions for coomassie stain method.

Coomassie	0.1 % Brilliant Blue R250
	10 % Acetic acide
	45 % Ethanol
Fixing solution	10 % Acetic acide
	45 % Ethanol
Destaining solution	25 % Ethanol
Gel stock solution	1 % Acetic acid

The gel was incubated with Commasie solution for at least 2 h on an orbital shaker (50-70 rpm). After the coloration, the fixing solution was replaced and shakes for 30 s. Then, the gel

was destained by the destaining solution few times until the well appearance of the protein bands (Table V.3).

2.6.2. Heme- stain

Heme containing proteins (hemoproteins) can be specifically visualized on SDS-PAGE gel by a reaction with benzidine derivatives based on their peroxidase activity. Indeed, hemoglobin in the presence of H_2O_2 oxidizes the amine groups of 3,3′-dimethoxybenzidine (Figure V.2), the product has dark green color (Broyles et al. 1979).
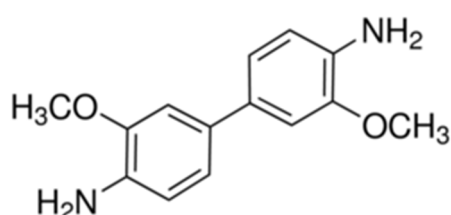

*Figure V.2: **o-dianisidine (3,3'-Dimethoxybenzidine).***

Table V.4: Stock solutions for heme-stain method.

A1	0.0625 M Tris pH 6.8
	2 % SDS
	10 % glycerol
	0.01 % Bromophenol
A2	12.5 % Trichloroacetic acid (TCA)
A3	0.2 g de *o-dianisidine* (3,3′-Dimethoxybenzidine) dissolving in 20 mL of glacial acetic acid.
A4	Tricitrate sodium buffer pH 4.4
A5	30 % H_2O_2
Stain solution	10 mL A3 + 10 mL A4 + 80 mL H_2O+ 400 µL A5 (A5 was added immediately before use)

Briefly, 5 µL of A1 was mixed with 45 µL protein solution. The mixture was kept 10 min at room temperature. This 50 µL sample was applied to SDS-PAGE 10% acrylic acid gel. After a typical electrophoresis migration, the gel was incubated with 100 mL of A2 for 30 min on

an orbital shaker. TCA was then removed by two washing steps by milliQ water. The gel was finally stained by 100 mL of stain solution. The dark green band is visible after 15 min (Table V.4).

2.7. Western blot

For Western blot analysis, proteins were separated by SDS-PAGE and then electrophoretically transferred onto nitrocellulose membrane (Protran BA85, GE Healthcare Life Sciences). After protein transfer, the membranes were treated with the blocking buffer (milk proteins) followed by incubation with an anti-frataxin antibody. We used an anti-rabbit horseradish peroxidase-conjugated secondary antibody (Sigma Aldrich) and an enhanced chemiluminescent reagent (West Pico and Femto, Thermo Scientific) for detection of immunoreactive material.

2.8. Mass spectroscopy (MS)

The identifications of isolated proteins were based on bottom-up approach. In this approach, proteins of interest are digested with trypsin, and the resulting "tryptic peptides" are analyzed by electrospray ionization (ESI) or matrix-assisted laser desorption/ionization (MALDI). The main steps are presented in Figure V.3.
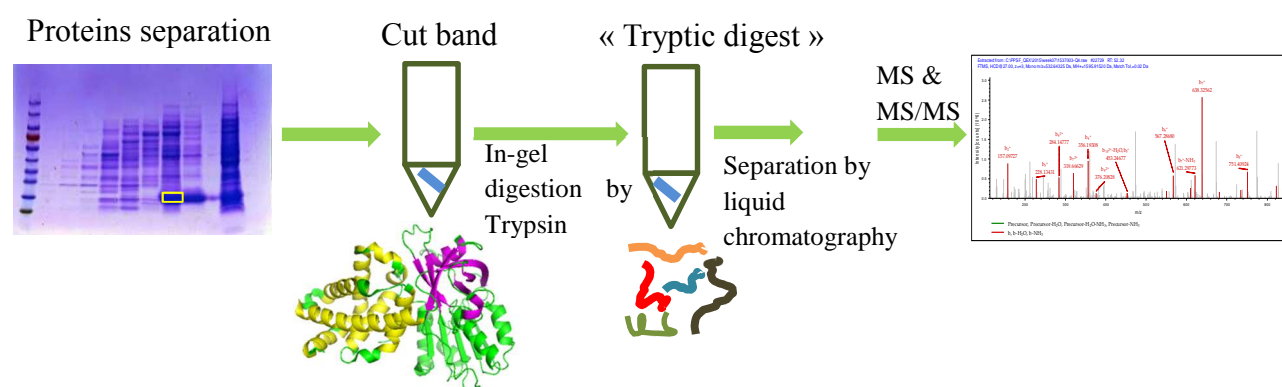

*Figure V.3: **The steps of bottom-up approach in MS analysis.***

2.8.1. In-gel digestion by Trypsin:

Table V.5: Stock solutions for the Trypsin digestion protein from SDS-PAGE gels

B1	Acetonitrile (ACN) 50 % in NH_4HCO_3 50 mM
B2	10^{-3} g/L Trypsin in NH_4HCO_3 25 mM
B3	Dithiothreitol 10mM in water
B4	Iodoacetamide 55mM in water
B5	0.01 % Trifluoroacetic acid (TFA) in ACN 50 %

SDS-PAGE band was cut by a scapel blade and put in a microcentrifuge tube (Table V.5).

- Washing step: The excised band was washed by two incubation cycles in 100 µl of B1 solution for 15 min/950 rpm at room temperature. The gel piece was dehydrated by stirring with 10 min/950 rpm in 100 µL of ACN 100 %. Then, ACN was removed and the gel piece was dried at 37 °C for 10 min.

- Reduction/Alkylation: B3 was added to cover completely the gel piece. Protein reduction was performed by soaking 45 min in B3 at 56 °C in an air thermostat. The band was chilled down to room temperature. B3 was replaced by B4 and the protein alkylation was carried out by incubation in B4 for 45 min at room temperature in the darkness. B4 was removed and 100 µL of miliQ water was added. Incubation for 10 min allowed washing the gel piece. Later, it was dehydrated for the second time by 100 µL of ACN 100 %.

- Digestion: At 4 °C, B2 was added enough to cover and saturate the dried gel piece (20 µL typically). The digestion was effected by the overnight incubation at 37 °C.

- Extraction: After the digestion, the supernatant was transferred to another tube. 20 µL of B5 was added. The 15 min incubation under 950 rpm agitation allowed the second extraction. The two solutions are finally combined and sample is immediately dried with Speed-Vac. The samples are now ready for ESI MS analysis or being desalted by Zip-Tip procedures.

2.8.2. Zip-tip procedures:

Samples for MALDI need to be desalted and concentrated using Zip-Tip$_{c18}$ pipette tip.

Table V.6: Stock solutions for Zip-tip procedures

Wetting solution	acetonitrile 100%
Equilibration and wash solutions	0.1% TFA in water
Elution solution	0.1% TFA in water containing 70% CAN

20 µL pipette was utilized for all aspirate/dispense cycles. The Zip-Tip$_{c18}$ pipette tip was wet first by wetting solution. Equilibration was then achieved by two aspirate/dispense cycles of the equilibration solution. Peptides were bound with 15 slow aspirate/dispense cycles of the sample solution. The tip was rinsed with two aspirate/dispense cycles of the wash solution. Peptides were recovered with an aspiration of 15 µL of elution solution. Samples are now ready for MALDI TOF-TOF analysis (Table V.6).

2.8.3. MALDI TOF TOF analysis

Tryptic peptides were spotted on a MALDI plate. The matrix (α-cyano-4-hydroxycinanamic acid in 50 % ACN, 0.01 % TFA) was mixed to tryptic peptides solution directly on the plate with ratio of 1/1 (v/v). Mass spectra were acquired on a MALDI TOF/TOF ABI 4800+ (Applied Biosystems/MDS Sciex) (Figure V.4).
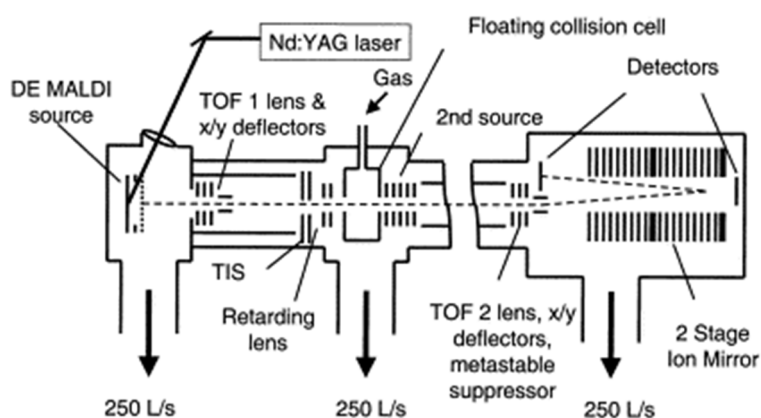

*Figure V.4: **Schematic representation of MALDI TOF-TOF instrument** (Yergey et al. 2002)*

2.8.4. ESI analysis

ESI mass spectra were acquired on an Orbitrap Fusion Tribrid coupled to a Nano-LC Proxeon 1000 equipped with an easy spray ion source (Thermo Scientific, San Jose, CA) (Figure V.5).
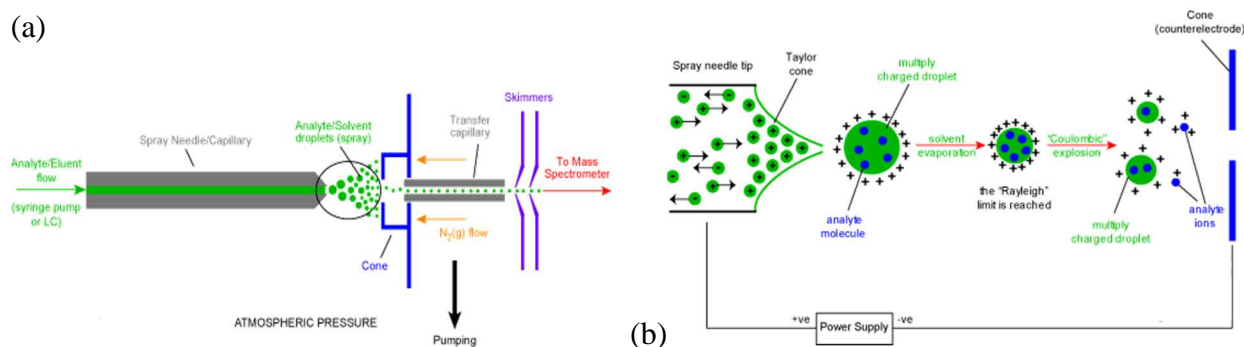
(a)

(b)

*Figure V.5: **Schematic representation of (a) ESI interface; (b) mechanism of ion formation.***

2.9. HPLC-Size exclusion chromatography

The HPLC system (1260 Infinity, Agilent) consists of a quaternary pump, absorption and emission detectors. It was used to determine the oligomeric state of frataxin in the presence and absence of metals and to study the interaction between Cu(GSH)$_2$ and frataxin, and finally the state of flavohemoglobin.

Protein samples were prepared in Bis Tris 50 mM, KCl 20 mM, pH 7.0 and loaded (20 µL) in a size exclusion column (Bio SEC-5, 5 µm particle, 150 Å, 7.8 mm × 300 mm) from Agilent. The column was previously calibrated with dimeric bovine albumin (132 kDa), monomeric bovine albumin (66 kDa), ovalbumin (45 kDa), carbonic anhydrase (29 kDa), lactalbumine (14.2 kDa). The mobile phase consisted of KH$_2$PO$_4$ 50 mM buffer, pH 7.0. The flow rate of the HPLC system was set at 1.0 mL/min. The elution was monitored by absorption at 280 nm, and emission at 340 nm (λ_{ex} = 280 nm). For the characterisation of flavohemoglobin, the elution was monitored by absorption at 410 nm and emission at 340 nm (λ_{ex} = 280 nm).

2.10. Dosage

2.10.1. Protein concentration

Yfh1 concentration was determined through UV-visible spectroscopy by measuring absorbance at 280 nm with extinction coefficients of 20 000 M^{-1}.cm^{-1}. Absorption measurements were performed at 25°C on a Cary 4000 spectrophotometer equipped with a Peltier thermostated cell-carrier.

Protein concentration was measured by Bradford protein assay (Biorad). The standard linear curve was based on a range of human serum albumin (HSA) concentration varying from 0 to 100 µg/mL.

2.10.2. Heme quantification

Heme content was determined by pyridine hemochromagen method (Barr and Guo 2015). This method is based on the changes in the hemoglobin absorbance spectrum upon reduction of heme iron to Fe(II) (Figure V.6). In the first step, 250 µL sample of flavohemoglobin was mixed with 250 µL of 4.4 M pyridine/0.2 M NaOH. The spectrum of this mixture, which corresponds to the oxidized state of heme iron, was obtained by measuring the absorption between 500- 600 nm. DTT was added in excess, the sample was scanned again for absorption between 500-600 nm. In presence of DTT, the spectrum corresponds to the reduced state of heme iron. In this step, the sample turns into reddish color. The scan was repeated until the absorbance peak does not increase. The scan with the highest peak is that of the reduced spectrum. The concentration of heme was calculated based on the absorption band at 557 nm of reduced state by the Beer Lambert relation with an extinction coefficients of 34 700 $M^{-1}.cm^{-1}$ (Paul et al. 1953).
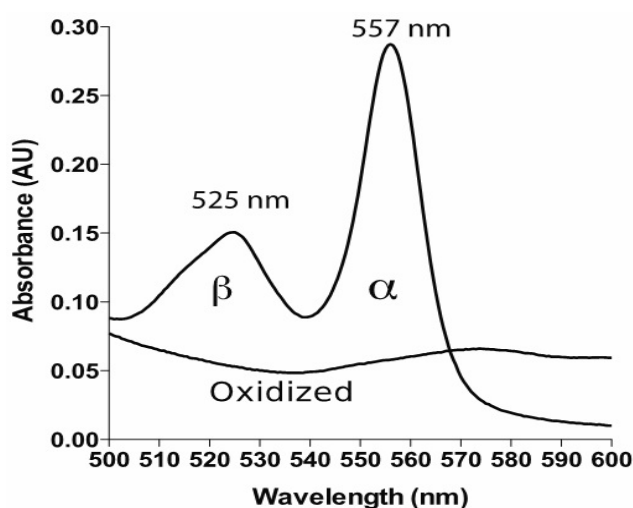

Figure V.6: **Example spectrum of reduced and oxidized pyridine hemochromagen** *(heme b).*

2.10.3. FAD quantification

Protein was mixed with one equivalent of A2 (12.5 % TCA) and boiled for 3-5 min. The solution was then centrifuged at 12 000 rpm to remove precipitated proteins. The absorption of the supernatant was measured at 450 nm. Concentration of FAD was estimated with and absorption coefficient of 11 300 $M^{-1}.cm^{-1}$ (Gardner 2008)

3.   Thermodynamic study

3.1. Spectrofluorimetric measurements

Fluorimetric measurements were performed at 25˚C on an Aminco-Bowman series 2 luminescence spectrometer equipped with external thermostated water-bath circulation. The excitation wavelength was set at 280 nm and the emission spectra were measured between 300 and 400 nm.

The light path length was 1 cm and the monochromator slit openings were 4 nm for both excitation and emission. The spectra used for the determination of equilibrium constants were recorded at the final equilibrated state of the species involved. The titrations were carried out in the 1000 µL cuvette. For the anaerobic experiments, especially designed cuvettes were used and manipulated in a glove box before being transferred to the spectrometers.

Dissociation constants of metal-frataxin complexes were determined from spectrofluorimetric data sets collected at multiple wavelengths using the multivariate data analysis program SPECFIT 32 (Binstead et al. 2003).

3.2.Isothermal titration calorimetric

ITC measurements were performed to determine the binding affinity and stoichiometry of Yfh1 and metals (Figure V.7).
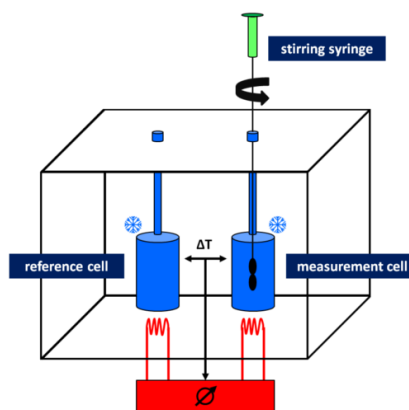
*Figure V.7: **Isothermal titration calorimetric illustration***

The experiments were carried out on a TA Instruments low-volume Nano ITC with gold cells and an active cell volume of 166 µL. The anaerobic experiments were performed by keeping the ITC machine in the glove box. All ITC titrations were performed at 25 °C and a stirring rate of 250 rpm using a titrating syringe volume of 50 µL. Typically, after an initial 1 µL injection, an automated sequence of 24 injections, each of 2 µL metal titrant into the sample cell containing Yfh1, spaced at 5 min intervals. The data were collected automatically and analyzed using the NanoAnalyze software from TA Instruments and a mathematical model involving one class of independent multiple binding sites.

4.   Kinetic study

4.1. Stopped flow technique

Stopped-flow experiments were performed on a Hi-Tech Scientific SF61DX2 stopped-flow spectrofluorimeter equipped with a Xe/Hg light source and a thermostated bath held at 25°C. Solutions of frataxin were mixed with a metal solution in buffered aqueous solutions (Bis Tris 50 mM, KCl 150 mM) (Figure V.8). For the anaerobic experiments, all solutions were prepared in a glove box under a positive atmosphere of pure argon gas. The stopped-flow apparatus and mixing syringes were kept under pure argon in a specially designed glove box.

For the stopped-flow experiments, the excitation wavelength was set at 295 nm, which is one of the emission peaks of the Xe/Hg light source, and detection was set at $\lambda_{em} \geq 300$ nm. All stopped-flow generated kinetic curves were 10-times signal averaged.
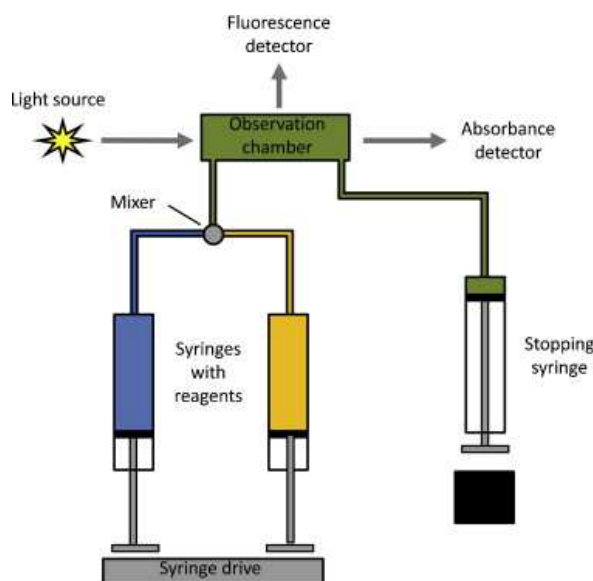
*Figure V.8: **Stopped flow system illustration** (Zheng et al. 2015)*

4.2. Relaxation chemistry

Consider a chemical equilibrium such as the common system:

$$A + B \underset{k_{-1}}{\overset{k_1}{\rightleftharpoons}} C \tag{V.1}$$

The rate equation of equation V.1 is expressed as equation V.2

$$-\frac{d[A]}{dt} = -\frac{d[B]}{dt} = \frac{d[C]}{dt} = k_1[A][B] - k_{-1}[C] \tag{V.2}$$

At equilibrium:

$$-\frac{d[A]}{dt} = -\frac{d[B]}{dt} = \frac{d[C]}{dt} = 0 \tag{V.3}$$

Thus, the equilibrium constant K_1 can be calculated from equation V.4:

$$K_1 = \frac{[A][B]}{[C]} = \frac{k_{-1}}{k_1} = constant \tag{V.4}$$

A chemical equilibrium is a dynamic affair. A reacts continuously with B to form C but at the same time an equal number of molecules of C decompose to regenerate A and B. The equilibrium state of this and any other chemical system not only depends on the chemical identity of the species involved but is determined by a set of external parameters such as the

temperature, pressure, solvent, stoichiometric concentrations, etc. When this equilibrium state is perturbed for instance by the addition of more reactants, dilution, a change of pH, or a change in temperature, pressure, etc., the system adjusts itself to the changed set of external parameters.

In the case of system equation V.1, if for instance we modify the concentration of reactants A or B, or K_1 (which depends on several variable parameters such as temperature or pressure) and if the perturbation is faster than system response, the system is instantly out of equilibrium state. The concentration of reactant (A, B or C) will change to be adaptable with the new equilibrium imposed by the perturbation (Figure V.9). A model of relaxation associated with chemical reaction is obtained. (Bernasconi, CF. 1976)
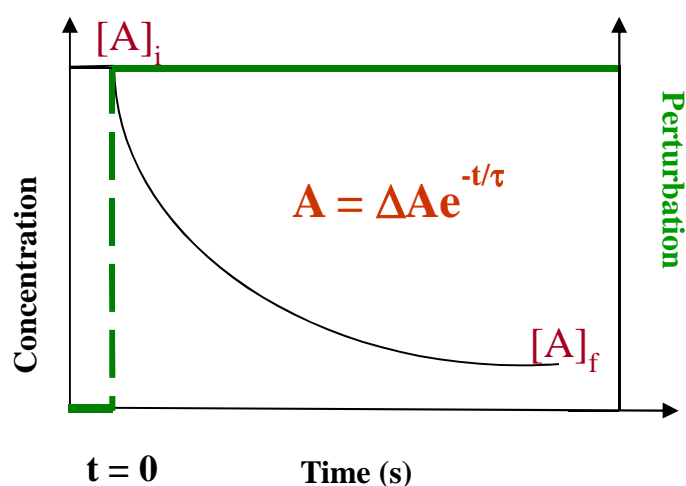

Figure V.9: **The perturbation must be excessively rapid when compared to system response.**

Since in a relaxation experiment the system relaxes from an initial equilibrium state to a final equilibrium state, we introduce the following symbols:

$$c_A^i, \ c_B^i, \ c_C^i \qquad \text{Equilibrium concentration at initial state}$$

$$c_A^f, \ c_B^f, \ c_C^f \qquad \text{Equilibrium concentration at final state}$$

The concentration of reactants can be expressed in terms of their new equilibrium values and their deviations occurring during chemical relaxation as below:

$$c_A^i = c_A^f + \Delta c_A$$
$$c_B^i = c_B^f + \Delta c_B \qquad\qquad (\text{V.5})$$
$$c_C^i = c_C^f + \Delta c_C$$

According to the principle of mass conservation (or mass balance), we have:

$$\Delta c_A + \Delta c_C = 0 \tag{V.6}$$
$$\Delta c_B + \Delta c_C = 0$$

Or
$$\Delta c_A = \Delta c_B = -\Delta c_C = x$$

Hence equation V.5 becomes:

$$c_A^i = c_A^f + x$$
$$c_B^i = c_B^f + x \tag{V.7}$$
$$c_C^i = c_C^f - x$$

From equation V.3 and equation V.7, we have:

$$-\frac{dc_A^i}{dt} = -\frac{dc_B^i}{dt} = \frac{dc_C^i}{dt} = \frac{d(c_C^f - x)}{dt} = \frac{dc_C^f}{dt} - \frac{dx}{dt} = -\frac{dx}{dt} \tag{V.8}$$

Notes that at equilibrium state d[A]/dt = 0, equation V.2 can be expressed as:

$$-\frac{dx}{dt} = k_1(c_A^f + x)(c_B^f + x) - k_{-1}(c_C^f - x) \tag{V.9}$$

$$= k_1[c_A^f c_B^f + (c_A^f + c_B^f)x + x^2] - k_{-1}(c_C^f - x)$$

$$= (k_1 c_A^f c_B^f - k_{-1}c_C^f) + [k_1(c_A^f + c_B^f)x + k_{-1}x] + k_1 x^2$$

$$= [k_1(c_A^f + c_B^f)x + k_{-1}x] + k_1 x^2 \tag{V.10}$$

If only small equilibrium perturbations are considered, that means $|x| \ll c_i^f$, the term $k_1 x^2$ is negligibly small compared to the other terms and equation V.10 becomes:

$$-\frac{dx}{dt} = [k_1(c_A + c_B) + k_{-1}]x \tag{V.11}$$

Or:
$$-\frac{dx}{dt} = \frac{1}{\tau}x \tag{V.12}$$

With
$$\tau^{-1} = k_1(c_A + c_B) + k_{-1} \tag{V.13}$$

τ is called the relaxation time of the system. Integration of equation V.12

$$\int_{xo}^{x} x^{-1}dx = -\tau^{-1}\int_0^t dt$$

leads to:
$$\ln\left(\frac{x}{x_o}\right) = -\frac{t}{\tau}$$

Or.
$$x = x_o e^{-t/\tau} \tag{V.14}$$

With
$$x_o = c_A^i - c_A^f$$

As is evident from equation V.13 k_1 and k_{-1} can be evaluated from the concentration dependence of τ^{-1} being a linear function of $(c_A + c_B)$ (Figure V.10).
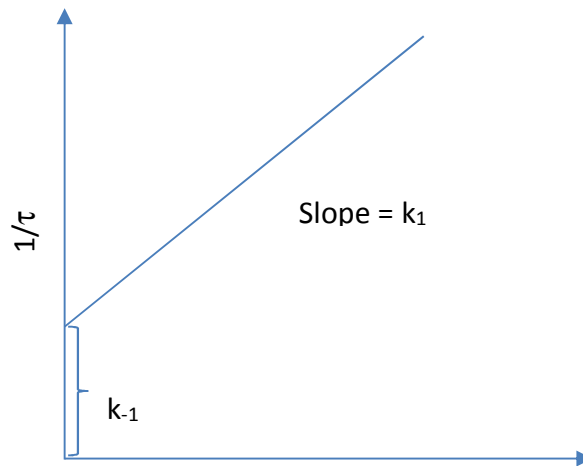

*Figure V.10: **Determination of rate constants from the concentration dependence of τ^{-1} for the $A+B \Leftrightarrow C$ system**.*

5. Enzymatic activity study
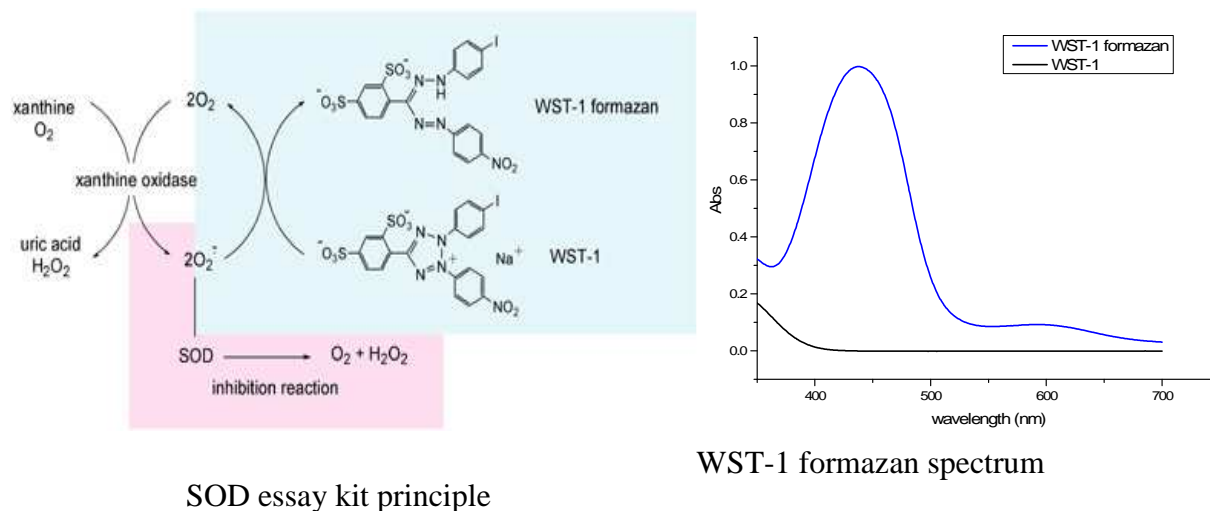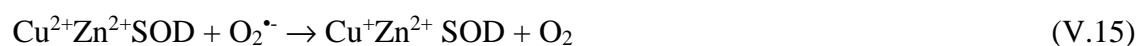
5.1. Superoxide dismutase enzymatic activity essay

SOD essay kit principle

WST-1 formazan spectrum

*Figure V.11: **Superoxide dismutase activity assay.***

$$Cu^{2+}Zn^{2+}SOD + O_2^{\bullet-} \rightarrow Cu^+Zn^{2+} SOD + O_2 \qquad (V.15)$$

$$Cu^+Zn^{2+} SOD + O_2^{\bullet-} + 2H^+ \rightarrow Cu^{2+}Zn^{2+} SOD + H_2O_2 \qquad (V.16)$$

To investigate the influences of Yfh1 on enzymatic activity of SOD, we used the SOD assay kit, which uses a tetrazolium salt to detect the superoxide radicals generated by xanthine oxidase (XO) and hypoxanthine. SOD essay kit contains WST-1 (2-(4-Iodophenyl) - 3-(4-nitrophenyl)-5-(2,4-disulfophenyl)-2H-tetrazolium, monosodium salt), which produces a highly water-soluble formazan dye (WST-1 formazan) upon reduction with a superoxide anion $O_2^{\bullet-}$ (Figure V.11). Xanthine oxidase (XO) has been used to generate $O_2^{\bullet-}$. At 37°C, SOD catalyzed the dismutation of $O_2^{\bullet-}$ to O_2 and H_2O_2 as described in equations V.15 and V.16 with the rate approaches the diffusion-controlled limit (1.6×10^9 M^{-1} s^{-1}) (Culotta et al. 2006). By disproportioning $O_2^{\bullet-}$, SOD reduced the rate of WST-1 oxidation. By measuring the rate of WST-1 formazan production in presence of SOD, we can evaluate its activity. The absorbance at 450 nm is proportional to the amount WST-1 formazan.

In a 200 µL cuvette, the reaction was initialized by adding XO, the absorption 450 nm was measured each 0.01 s during 20 mins. The initial rate of WST-1 oxidation reaction by $O_2^{\bullet-}$ generated from XO was measured and considered as total 100 % (v_o), the rate in presence of SOD was determined as v_i. The percentage of inhibition is calculated as following equation:

$$\%inhibition = \frac{(v_o - v_i) \times 100}{v_o} \quad (\%)$$

The IC50 of SOD in presence or absence of Yfh1 was determined by tracing a regression linear of percentage of inhibition against log[SOD]. IC50 corresponds to the concentration of SOD that inhibits 50 % total activity of working enzyme (XO).

5.2. Yhb1 enzymatic activity essay

The NADH oxydase activity of Yhb1 was evaluated indirectly by the reduction of cytochrome c oxidase based on the reaction (equation V.17). The product has a typical absorption band at 550 nm (Figure V.12) with molar coefficient extinction of $\varepsilon_{550} = 21\ 100\ M^{-1}.cm^{-1}$ (El Hammi et al. 2012).

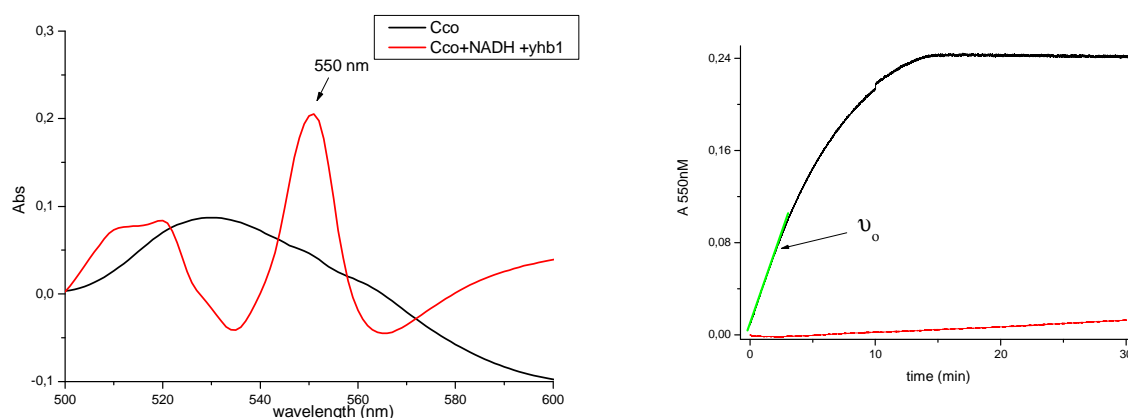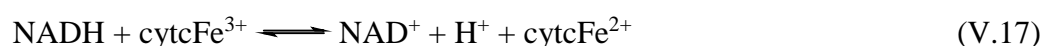$$NADH + cytcFe^{3+} \longrightarrow NAD^+ + H^+ + cytcFe^{2+} \quad (V.17)$$

*Figure V.12: (a) **Absorbance spectrum of cytochrome c before** (black) **and after** (red) **the reduction by NADH and Yhb1**. (b) **Variation of $A_{550\ nm}$ during 30 min in presence of Yhb1** (black) **or not** (red).*

The initial rate of cytochrome c reduction is proportional to the initial rate of NADH oxidation. Thus, the initial rates of NADH oxidation at different concentrations of NADH were measured. The Michealis Menten model was applied to determine *Vmax* and *Km* and *kcat*.

REFERENCES

Barr I, Guo F. 2015. Pyridine Hemochromagen Assay for Determining the Concentration of Heme in Purified Protein Solutions. Bio-protocol 5: e1594.

Binstead RA, Zuberbühler AD, Jung B. 2003. SPECFIT global analysis system version 3.04.34. SPECFIT global analysis system version 3.04.34.

Broyles RH, Pack BM, Berger S, Dorn AR. 1979. Quantification of small amounts of hemoglobin in polyacrylamide gels with benzidine. Analytical Biochemistry 94: 211-219.

Buisson. N, Labbe-Bois R. 1997. Flavohemoglobin Expression and Function in Saccharomyces cerevisiae: no relationship with respiration and complex response to oxidative stress. The journal of Biological chemistry 273: 9527–9533.

Ciriolo MR, Desideri A, Paci M, Rotilio G. 1990. Reconstitution of Cu,Zn-superoxide dismutase by the Cu(I).glutathione complex. J Biol Chem 265: 11030-11034.

Culotta VC, Yang M, O'Halloran TV. 2006. Activation of superoxide dismutases: putting the metal to the pedal. Biochim Biophys Acta 1763: 747-758.

El Hage Chahine JM, Fain D. 1994. The mechanism of iron release from transferrin. Slow-proton-transfer-induced loss of nitrilotriacetatoiron(III) complex in acidic media. Eur J Biochem 223: 581-587.

El Hammi E, Warkentin E, Demmer U, Marzouki NM, Ermler U, Baciou L. 2012. Active site analysis of yeast flavohemoglobin based on its structure with a small ligand or econazole. FEBS J 279: 4565-4575.

Gardner PR. 2008. Assay and Characterization of the NO Dioxygenase Activity of Flavohemoglobins. 436: 217-237.

Hanna PM, Tamilarasan R, McMillin DR. 1988. Cu(I) analysis of blue copper proteins. Biochem J 256: 1001-1004.

Paul KG, Theorell H, Akeson A. 1953. The molar light absorption of Pyridine Ferroprotoporphyrine (Pyridine haemochromogen). Acta Chemica Scandinavica 7: 1284-1287.

Schenk PM, Baumann S, Mattes R, Steinbiss HH. 1995. Improved high-level expression system for eukaryotic genes in Escherichia coli using T7 RNA polymerase and rare (Arg)tRNAs. BioTechniques 19.

Yergey AL, Coorssen JR, Backlund Jr PS, Blank PS, Humphrey GA, Zimmerberg J, Campbell JM, Vestal ML. 2002. De novo sequencing of peptides using MALDI/TOF-TOF. Journal of the American Society for Mass Spectrometry 13: 784-791.

Zheng X, Bi C, Li Z, Podariu M, Hage DS. 2015. Analytical methods for kinetic studies of biological interactions: A review. Journal of Pharmaceutical and Biomedical Analysis 113: 163-180.

Résumé

La frataxine est une protéine mitochondriale bien conservée de la bactérie à l'homme. La déficience de la frataxine chez l'homme entraine une maladie neurodégénérative grave, appelée Ataxie de Friedreich. Cette protéine a été découverte dans les années 90s et depuis sa fonction physiologique exacte n'est toujours pas connue. La frataxine joue un rôle important dans la biosynthèse des centres Fe-S dans l'homéostasie du fer et/ou dans la protection contre le stress oxydant. Dans cette thèse, nous nous intéressons aux interactions entre la protéine et d'autres molécules, comme certains métaux mitochondriaux ou protéines pour mieux comprendre la fonction de la frataxine dans la cellule. Lors de ce travail, la frataxine de levure (Yfh1) a été synthétisée par la technique de l'ADN recombinant, puis purifiée pour les études physico-chimiques. La flavohémoglobine (Yhb1) qui joue le rôle important dans la détoxification de NO (un agent du stress oxydatif et nitrosatif) a été aussi exprimée et purifiée selon le même principe. Ensuite, nous avons étudié la thermodynamique et la cinétique de la complexation de Yfh1 par les métaux mitochondriaux comme Fe, Cu, Mn, Zn, ainsi qu'avec les protéines impliquées dans le système antioxydant comme les superoxydes dismutases, CuZnSOD et MnSOD, et la flavohémoglobine. Ces résultats montrent tout d'abord que Yfh1 interagit avec tous les métaux mitochondriaux, néanmoins elle présente une meilleure affinité pour le cuivre et le manganèse. Par la suite, nous mettons en évidence le rôle remarquable de la frataxine dans le système antioxydant. Nous attribuons ainsi à la frataxine un rôle de protéine multifonctionnelle : « régulateur » dans le métabolisme des métaux.

Resume

The frataxin is a mitochondrial protein which is highly conserved during the evolution. The deficiency of frataxin in human induces a neurodegenerative disease: Friedreich's ataxia. This protein was discovered in the nineties. However, its functions are always opened questions. It has been shown that frataxin participates in the assembly of Fe-S cluster, as well as the iron homeostasis and cellular antioxidant system. The interactions between frataxin and others molecules, such as metals or proteins, are necessary for a better understanding of protein's functions. In this work, we synthesized a yeast frataxin homologue (Yfh1) by DNA recombinant technique, and then purified it for cell free studies. Yeast flavohemoglobin (Yhb1), which is responsible for the detoxification of NO (an oxidative and nitrosative stress agent), was also isolated. We started by determining the thermodynamics and kinetics of the physiological interaction between Yfh1 and mitochondrial metals, such as Fe, Cu, Mn and Zn, as well as the interaction with the gatekeepers in the anti-oxidative stress such as superoxide dismutases, CuZnSOD & MnSOD, and Yhb1. We underline here, in the first part the unspecific interaction of Yfh1 with mitochondrial metals, and more especially the higher affinity of Yfh1 for copper and manganese than for iron. We also confirm the remarkable participation of Yfh1 in the antioxidant system. Based on these observations, we assume that frataxin plays the role of a "regulator" in metal metabolism.